QUANTUM LIGHT FOR IMAGING, SENSING AND SPECTROSCOPY

EDITED BY: Roberto de J. León-Montiel, Mario Alan Quiroz-Juarez, Omar Magana-Loaiza and Juan Torres

PUBLISHED IN: Frontiers in Physics

frontiers Research Topics

ISSN 1664-8714
ISBN 978-2-83250-394-2
DOI 10.3389/978-2-83250-394-2

About Frontiers

Frontiers is more than just an open-access publisher of scholarly articles: it is a pioneering approach to the world of academia, radically improving the way scholarly research is managed. The grand vision of Frontiers is a world where all people have an equal opportunity to seek, share and generate knowledge. Frontiers provides immediate and permanent online open access to all its publications, but this alone is not enough to realize our grand goals.

Frontiers Journal Series

The Frontiers Journal Series is a multi-tier and interdisciplinary set of open-access, online journals, promising a paradigm shift from the current review, selection and dissemination processes in academic publishing. All Frontiers journals are driven by researchers for researchers; therefore, they constitute a service to the scholarly community. At the same time, the Frontiers Journal Series operates on a revolutionary invention, the tiered publishing system, initially addressing specific communities of scholars, and gradually climbing up to broader public understanding, thus serving the interests of the lay society, too.

Dedication to Quality

Each Frontiers article is a landmark of the highest quality, thanks to genuinely collaborative interactions between authors and review editors, who include some of the world's best academicians. Research must be certified by peers before entering a stream of knowledge that may eventually reach the public - and shape society; therefore, Frontiers only applies the most rigorous and unbiased reviews.
Frontiers revolutionizes research publishing by freely delivering the most outstanding research, evaluated with no bias from both the academic and social point of view. By applying the most advanced information technologies, Frontiers is catapulting scholarly publishing into a new generation.

What are Frontiers Research Topics?

Frontiers Research Topics are very popular trademarks of the Frontiers Journals Series: they are collections of at least ten articles, all centered on a particular subject. With their unique mix of varied contributions from Original Research to Review Articles, Frontiers Research Topics unify the most influential researchers, the latest key findings and historical advances in a hot research area! Find out more on how to host your own Frontiers Research Topic or contribute to one as an author by contacting the Frontiers Editorial Office: frontiersin.org/about/contact

QUANTUM LIGHT FOR IMAGING, SENSING AND SPECTROSCOPY

Topic Editors:
Roberto de J. León-Montiel, National Autonomous University of Mexico, Mexico
Mario Alan Quiroz-Juarez, Autonomous Metropolitan University, Mexico
Omar Magana-Loaiza, Louisiana State University, United States
Juan Torres, The Institute of Photonic Sciences (ICFO), Spain

Citation: León-Montiel, R. d. J., Quiroz-Juarez, M. A., Magana-Loaiza, O., Torres, J., eds. (2022). Quantum Light for Imaging, Sensing and Spectroscopy. Lausanne: Frontiers Media SA. doi: 10.3389/978-2-83250-394-2

Table of Contents

frontiers | Frontiers in Physics

TYPE Editorial
PUBLISHED 20 September 2022
DOI 10.3389/fphy.2022.1029478

OPEN ACCESS

EDITED BY
Xiongfeng Ma,
Tsinghua University, China

REVIEWED BY
He Lu,
Shandong University, China

*CORRESPONDENCE
Roberto de J. León-Montiel,
roberto.leon@nucleares.unam.mx

SPECIALTY SECTION
This article was submitted to Quantum Engineering and Technology, a section of the journal Frontiers in Physics

RECEIVED 27 August 2022
ACCEPTED 06 September 2022
PUBLISHED 20 September 2022

CITATION
León-Montiel RdJ, Quiroz-Juárez MA, Magaña-Loaiza OS and Torres JP (2022), Editorial: Quantum light for imaging, sensing and spectroscopy. *Front. Phys.* 10:1029478. doi: 10.3389/fphy.2022.1029478

Editorial: Quantum light for imaging, sensing and spectroscopy

Roberto de J. León-Montiel[1]*, Mario A. Quiroz-Juárez[2], Omar S. Magaña-Loaiza[3] and Juan P. Torres[4,5]

[1]Instituto de Ciencias Nucleares, Universidad Nacional Autónoma de México, Mexico City, Mexico, [2]Centro de Física Aplicada y Tecnología Avanzada, Universidad Nacional Autónoma de México, Mexico City, Mexico, [3]Quantum Photonics Laboratory, Department of Physics and Astronomy, Louisiana State University, Baton Rouge, LA, United States, [4]ICFO—Institut de Ciencies Fotoniques, Barcelona, Spain, [5]Department of Signal Theory and Communications, Campus Nord D3, Universitat Politecnica de Catalunya, Barcelona, Spain

KEYWORDS

non-classical light sources, quantum technologies, quantum imaging, quantum-enhanced spectroscopy, atomic quantum optics, quantum metrology, structured light, machine learning

Editorial on the Research Topic
Quantum light for imaging, sensing and spectroscopy

The last two decades have witnessed an enormous progress in the development of novel ideas and technologies for sensing and imaging based on the quantum properties of light. Our ability to generate, manipulate and detect non-classical states of light has opened new avenues in experimental imaging, sensing and spectroscopy, where unprecedented levels of sensitivity and resolution can be attained. In this Research Topic, we aim at highlighting state-of-the-art research, and their potential applications, in imaging, spectroscopy and metrology. This includes the generation and control of quantum optical states, such as single-photon sources, entangled photon pairs, and structured light beams.

This Research Topic, issued within the Quantum Engineering and Technology section of Frontiers in Physics, includes one brief research report, eight original research articles, and one review article. These contributions cover applications of entangled light in metrology and spectroscopy, the generation of spatially-structured non-classical states of light, as well as imaging applications using correlated thermal light and machine learning.

Chen et al. provide a review article on both theoretical and experimental entangled-photon-enabled quantum interferometric metrology. Topics covered by the review include Hong-Ou-Mandel interferometry with frequency and time resolution, entanglement-assisted single-photon absorption and two-photon absorption spectroscopy using energy-time correlated photon pairs. Scully et al. introduce a spectroscopy technique based on the monitoring of quantum beats in the cooperative light emission from an atomic (or molecular) sample. The use of entangled photon pairs in the context of spectroscopy is discussed by Schlawin, who explores the possible role of

the sample's inhomogeneous broadening and photons' polarization degrees of freedom in the quantum enhancement that entangled two-photon absorption might offer to experimental nonlinear spectroscopy. Debnath and Rubio further show that entangled light can also be used as a probe for extracting information about dissipative cavity exciton-polariton dynamics in the ultrafast regime.

The generation and control of non-classical states of light are discussed in two contributions. Puentes discusses a method for the generation of entangled two-photon states in high-dimensional Hilbert spaces by placing multiple angular slits in the path of spontaneous parametric down-converted entangled photon pairs. This result can be relevant for quantum information protocols where high-dimensional encryption is required. Mendoza-López et al. demonstrate theoretically and experimentally the frequency conversion of multiple optical vortices by inducing a four-wave mixing process in a hot vapor of rubidium atoms. The authors' study adds to the available protocols for the generation and control of photonic orbital angular momentum in atomic ensembles.

The potential of structured light for quantum physics is discussed by Gutiérrez-Jáuregui and Jáuregui who show that nonlinear processes, at the single-photon level, might be produced in the light-matter interaction of tightly trapped atoms in the focus of vectorial waves. Furthermore, Lv et al. demonstrate that propagating spatially-structured modes of light can be identified (and reconstructed) using deep learning. This method is particularly relevant in quantum applications where structured light is susceptible to phase distortions due to propagation in noisy environments.

Wang et al. demonstrate a theoretical and experimental scheme for "fractional" ghost imaging. This is managed by symmetrically placing the object to be imaged and a fractional spiral phase filter in the test and reference pseudo-thermal beams of a lensless ghost imaging system. Finally, Fernandez-Guasti and Garcia-Guerrero demonstrate an interesting scheme that allows for two non-degenerate photon beams to exhibit first-order optical interference. These results call for a possible reformulation of the "which-way information" concept for non-degenerate photon interference.

To conclude, we would like to mention that the study of quantum light for imaging, sensing, and spectroscopy is a timely and exciting research field at the forefront of physics and technology. It has the potential to impact many areas of science and engineering, from material science to quantum communications and quantum computing. We expect this Research Topic to provide valuable information and guidance for future research along these lines.

Finally, we would like to thank all authors, reviewers and administrative staff at Frontiers, without whom this Research Topic could not have been possible.

Author contributions

All authors have made a substantial, direct, and intellectual contribution to the editorial and approved it for publication.

Acknowledgments

RJLM thankfully acknowledges financial support by DGAPA-UNAM under the project UNAM-PAPIIT IN102920. OSML acknowledges support from the National Science Foundation through Grant No. OMA MPS—2231387.

Conflict of interest

The authors declare that the research was conducted in the absence of any commercial or financial relationships that could be construed as a potential conflict of interest.

Publisher's note

frontiers in Physics

ORIGINAL RESEARCH
published: 24 January 2022
doi: 10.3389/fphy.2021.813565

Time and Space Resolved First Order Optical Interference Between Distinguishable Photon Paths

M. Fernandez-Guasti and C. García-Guerrero*

Lab. de Óptica Cuántica, Depto. de Física, Universidad Autónoma Metropolitana–Iztapalapa, Ciudad de México, Mexico

Interference between different photons occurs and has been observed under diverse experimental conditions. A necessary condition in order to obtain interference fringes is the existence of at least two possible paths and unknown which-path information. If the photon beams have different frequencies, stability of the sources and fast spatially distributed detectors are required in order to detect the time displaced interference fringes. First order optical interference between two truly independent CW laser sources is observed. In contrast with the standard quantum criterion, interference is observed although the photon beams are distinguishable and, from quantum measurements, the path is unequivocally known for each photon beam. Segments of the continuous wave wavetrains are selected with an acousto-optic modulator. Temporal and spatial interference are integrated in a single combined phenomenon via streak camera detection. The displacement of the fringes in the time versus space interferograms evince the trajectories of the labeled photons. These results suggest that in non-degenerate frequency schemes, the ontology has to be refined and the which-path criterion must be precisely formulated. On the one hand, if the query refers to the frequency labeled photons, the path of each red or blue photon is known, whereas on the other hand, if the query is performed in terms of the detected photons, the path is unknown.

Keywords: quantum interference, quantum optics, quantum measurement, monomode lasers, quantum electrodynamics

OPEN ACCESS

Edited by:
Juan Torres,
The Institute of Photonic Sciences (ICFO), Spain

Reviewed by:
Chenglong You,
Louisiana State University, United States
Jianming Wen,
Kennesaw State University, United States

****Correspondence:***
M. Fernandez-Guasti
mfg@xanum.uam.mx

Specialty section:
This article was submitted to Quantum Engineering and Technology, a section of the journal Frontiers in Physics

Received: *11 November 2021*
Accepted: *22 December 2021*
Published: *24 January 2022*

Citation:
Fernandez-Guasti M and García-Guerrero C (2022) Time and Space Resolved First Order Optical Interference Between Distinguishable Photon Paths. Front. Phys. 9:813565. doi: 10.3389/fphy.2021.813565

1 INTRODUCTION

The two manifestations of first order interference between two wave-fields are 1) spatial interference fringes and 2) temporal interference or beating. The beams in optical spatial interference setups are usually derived from the same source but traveling along separate paths. In contrast, temporal interference is commonly achieved with different sources having different frequencies. Early experiments in the laser era demonstrated the temporal [1] and spatial [2] interference of independent sources. The position-momentum uncertainty provided an explanation of these results without having to renounce to the Dirac statement that 'Interference between different photons never occur' [3]. However, later experiments where the photon source statistics were carefully controlled, showed ineluctably that independent photons can interfere [4]. Interference fringes in the visible region of the spectrum with two different frequencies have also been observed [5, 6]. For a constant frequency difference, a single laser source is commonly used. The frequency of one beam can then be shifted with an acousto optic modulator [7] or by selecting different frequencies from a spatially chirped femtosecond pulsed source [8]. If separate lasers are used, the frequency difference varies from shot to shot and so does the fringe pattern [9]. The fringes in most of these experiments with different frequencies have been observed using a streak camera and more recently, with a modulated CMOS camera [10].

First order interference comes from the correlations between the fields whereas second order interference arises from correlations between the fields' intensities. These correlations can be described with continuum field theory (CFT) or quantum field theory (QFT). The archetypal Young's two slit interference experiment displays identical first order interference patterns when produced by short exposure with a intense light source or by a long exposure with feeble light. However, the ontology in the two theories is rather different. CFT requires a stable amplitude and phase correlation between the two interfering fields during the detector integration time [11]. In contrast, QFT asserts that interference takes place only when the path of the photons is unknown [12]. Recall that the two theories do produce measurable differences in second order interference experiments [13]. Many theoretical predictions and experimental verifications without classical analogue, favor the quantum nature of electromagnetic fields.

The present experimental results are at odds with the standard formulation of the quantum which path problem: "A measurement which shows whether the photon passed through A or through B perturbs the state of the photon to such an extent that no interference fringes are detected. Thus, either we know which slit the photon passed through, or we observe interference fringes. We cannot achieve both goals: the two possibilities are incompatible ([14], p.22)." Many authors consider that the which path information problem is an example of Bohr's principle of complementarity, where the interference/which-way duality is a manifestation of the wave/particle mutually exclusive concepts [15]. However, Bohr's idea of complementarity is a much broader principle dealing with observation and the definition of quantum states [16, 17]. As we shall presently show, interference with which-path certainty is possible in non-degenerate frequency schemes if the statement is made in terms of the frequency labeled photons but without reference to a detected photon. However, the path of a detected photon in the interference region, cannot be traced back. This latter, more precise assertion, is consistent with the prevailing quantum viewpoint. Our observations are consistent with Heisenberg's uncertainty principle and Busch measurement/disturbance theorem. They are also consistent with Englert, which way detector inequality. However, they compromise certain versions of Bohr's complementary principle.

2 EXPERIMENTAL CONSIDERATIONS AND SETUP

Two photon beams were generated from two independent Nd: YAG lasers code named *cheb* and *oxeb* [1]. These continuous wave (CW), monomode lasers (AOTK 532Q) have a coherence time greater than 300 ns [18]. The operation of each laser does not rely in any way on the working of the other laser, nor are they synchronized. The temperature of each of them was monitored and controlled independently. Temperature was measured with a 100 Ω platinum resistance and controlled with a Peltier module external to the cavity but attached to its base. A temperature controller (Stanford Research SRC10) provided the electronic feedback to maintain a stable temperature within 0.01°C. The wavelengths of the two lasers, measured with an spectrometer (Spex1704 with 0.01 nm resolution), were temperature tuned so that their frequencies were sufficiently close to be resolved by a streak camera (Optronis SC-10). At sweep speeds of 10 ns/mm with the TSU-12–10 unit, fringes are comfortably observed in the streak camera for frequency differences below 1 GHz. The two laser beams were steered with mirrors into a TeO_2 acousto optic modulator (AOM) (10/10 ns, 10–90% rise/fall time for a 55 μm beam-waist). The general setup is shown in **Figure 1**. Preliminary results were reported at a PIERS conference [19]. Beam splitters were avoided (except for alignment purposes, prior to operation), so that a two slit wavefront division interferometer is emulated throughout the trajectories. The expanded collimated beams were overlapped and detected with the streak camera. The beams collimation was adjusted with the aid of a shear interferometer. A streak camera is an optical version of an electronic oscilloscope; at the entrance slit light impinges on a photocathode placed on the inner part of a vacuum tube. The photo-electrons emitted by the photocathode (8 mm × 2 mm) are accelerated and swept in the perpendicular direction to its long axis, in this way a two dimensional image is produced. Each photoelectron eventually impacts a multichannel plate (MCP) and is cascaded so that the bunch of electrons produces a bright point as it reaches a phosphor screen. The MCP amplification voltage is adjusted so that the intensity of the spot is adequately detected by a CCD camera. At low intensity levels, the streak camera operates in a spatially resolved photon counting mode. If at some spots more than one photon is detected, this information is encoded onto a level of gray, typically not more than 50 events per 0.7 ns as can be seen from **Figure 6B**. In the streak camera images, the abscissa corresponds to the time axis whereas the ordinate is a transverse spatial coordinate. The density of bright spots is proportional to the photon density in the two dimensional time and space coordinates. Streak images cannot be accumulated in this experiment because the frequency and relative phase between the two lasers vary stochastically in time from sweep to sweep. For this reason, the fringe pattern was recorded in single exposures with a time duration of the order of the coherence time. Low repetition rates between 1 and 3 Hz had to be used to acquire and save the digital images in real time. The streak camera detector performs an integration both in space and time,

$$\langle I(t,y)\rangle_{\delta t,\delta x,\delta y} = \frac{1}{\delta t \delta x \delta y}\int_{y}^{y+\delta y}\int_{x}^{x+\delta x}\int_{t}^{t+\delta t} I(\tau,\xi,\eta)d\tau d\xi d\eta,$$

where $I(\tau,\xi,\eta)$ is the light intensity incident on the photocathode as a function of time and the transverse dimensions. $I(t,y)$ is the intensity at the CCD screen as a function of the "coarse grain" time and one spatial direction. In the transverse dimensions, the x direction is limited to $x = \pm 7.5\,\mu$m using a $\delta x = 15\,\mu$m entrance slit. In the y direction, the position detection range is 15 mm with $\delta y = 70\,\mu$m resolution. The

[1]Tseltal variant of Mayan language for numbers two → *cheb* and three → *oxeb*

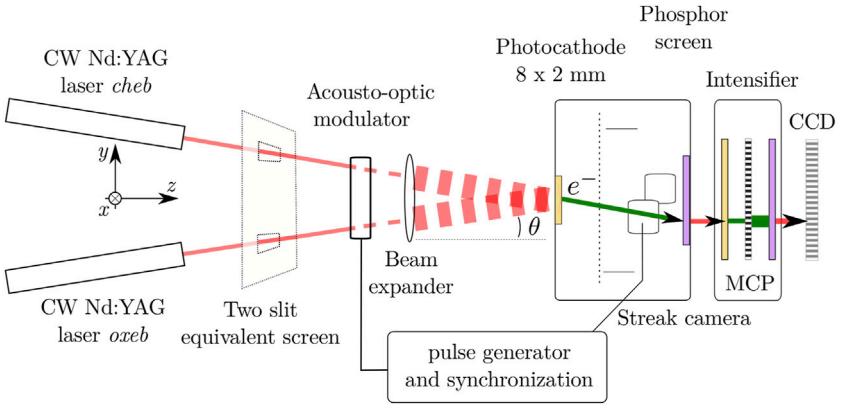

FIGURE 1 | Schematic diagram of the experimental arrangement. The setup is equivalent to a Young's two slit experiment but each 'slit' is illuminated by an independent laser. The slits can be conceived to be placed at any plane between the sources and the photocathode detector before the beams overlap. (Optical beams drawn in red, electron beams within the streak camera drawn in green.)

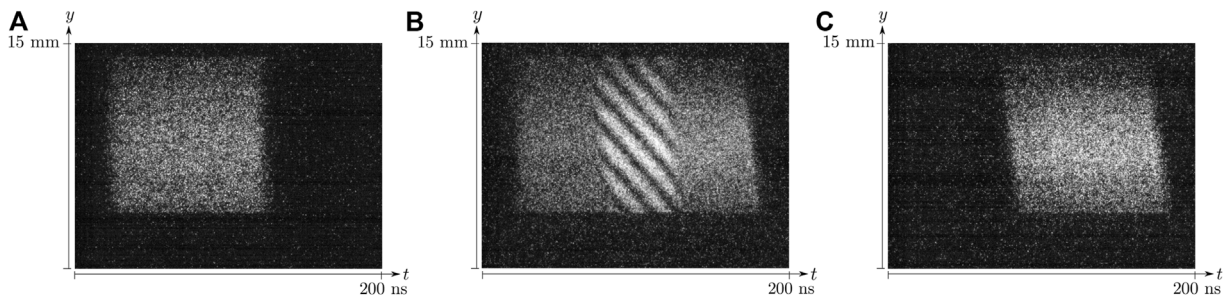

FIGURE 2 | Streak camera images. The abscissa represents time at 10 ns/mm sweep rate with δt = 1 ns temporal resolution. The ordinate depicts the beams transverse distance in the *y* direction. **(A)** 97 ns pulse from laser code named *oxeb*.; **(B)** Interferogram when both laser pulses are present; **(C)** 95 ns pulse from laser code named *cheb*.

temporal sweep is performed in the x direction with 0.34% resolution of the full sweep time. The resolution of the apparatus is given by the instrumental integration δt, δx, δy together with the image amplification and digitization bins (Anima-PX/25, 19.5 × 14.9 mm^2, 12 bit A/D CCD 1392 × 1024). The quantum efficiency (QE) of the low noise photocathode is 10.37% at 532 nm with dark noise of 100 e^-/cm^{2}s (Photek ST-LNS20). The temporal resolution at the phosphor screen placed after the image intensifier is 66 μm.

The AOM input angle was aligned with the oxeb laser beam. In our experiments, delay generator pulses with 120, 300 and 700 ns width were used. The AOM first order deflection angle is 25 mrad with a diffraction frequency shift of 210 MHz. The oxeb laser beam was diffracted in first order (210 MHz) whereas the cheb beam was operated in second order (2 × 210 MHz). There was thus a 210 MHz frequency difference that posed no problem because it was compensated by the laser's temperature tuning. Half wave retardation plates were used at the output of each laser to adjust the polarization plane in order to improve fringe visibility. A typical ≈ 100 ns output pulse is shown in **Figure 2A**. The cheb beam is a bit mismatched due to a 25 mrad oblique incidence in a displaced region of the acoustic wave within the crystal. This inclination produces a pulse delay and a pulse front tilt as may be seen in **Figure 2C**. This sweep mode neatly exhibits three regions, two to the left and right in **Figure 2B**, where only one of the pulses is present and the central area where both pulses overlap in time and interference is observed.

In a conventional single source Young's experiment, the two slits separate the wavefront into two distinct wave-fronts. Here, the waves emanate from two different truly independent sources. The physical setup can be conceived as each source illuminating a slit. The plane where the slits are placed is any arbitrary plane between the sources and the region where the beams begin to overlap just before interfering at the detection plane. Moreover, each slit could be placed at different planes, reminiscent of second order interference patterns produced by non-local objects [20].

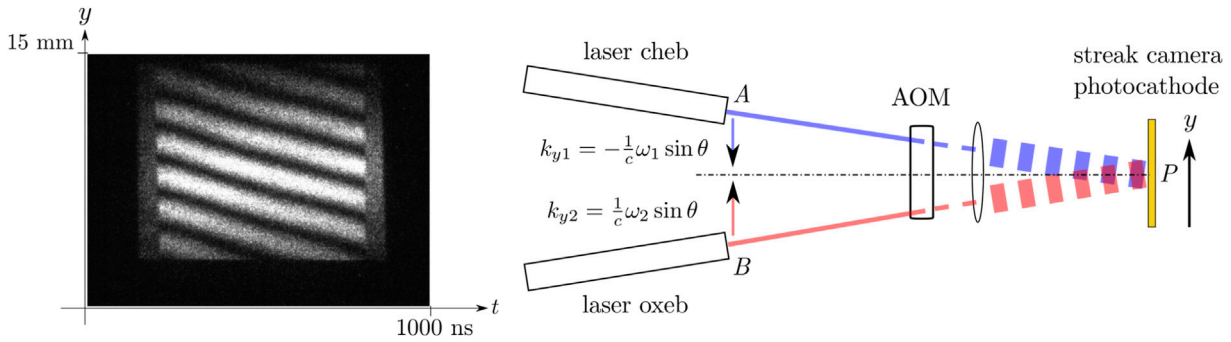

FIGURE 3 | The steak camera image (left) shows negative slope interference fringes. Therefore, the oxeb laser emitted lower frequency photons that followed the path $\overline{BP}$. The higher frequency photons from the cheb laser followed the path $\overline{AP}$.

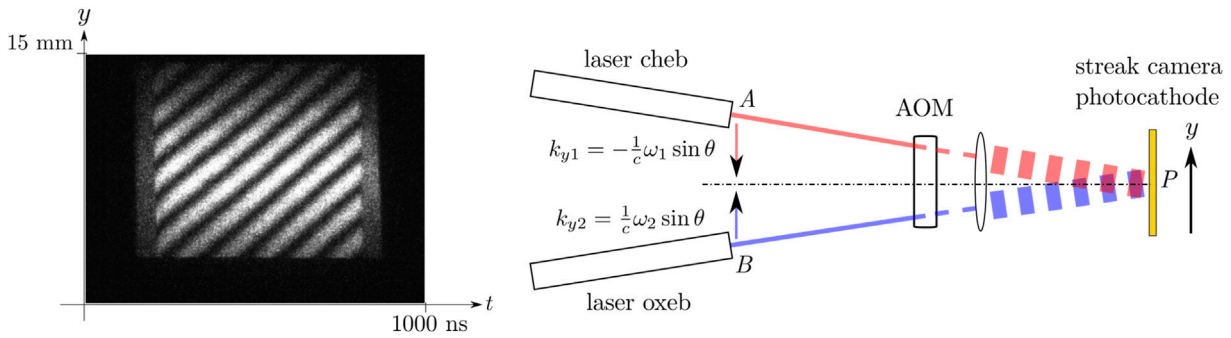

FIGURE 4 | Positive slope interference fringes, the oxeb laser emitted higher frequency photons than the cheb laser. Photons from the oxeb laser followed the lower path $\overline{BP}$ whereas photons from the cheb laser followed the upper path $\overline{AP}$.

2.1 Photon Labeling

The two beams are collimated and thereafter incident on the streak camera photocathode at an angle of 0.14 mrad between them in order to have comfortably resolved interference fringe maxima separated by 1.88 mm at the detection plane. Cartesian coordinates are set with z normal to the detector surface and the fields are linearly polarized in the x direction. The two waves propagate in the (y, z) plane, paraxially to the z direction at a small but opposite angle θ in the y axis. The wave vector of the field coming from the laser code named cheb is

$$\mathbf{k}_1 = \mathbf{k}_{y1} + \mathbf{k}_{z1} = -k_1 \sin\theta\, \hat{\mathbf{e}}_y + k_1 \cos\theta\, \hat{\mathbf{e}}_z,$$

and the wave-field coming from the laser code named oxeb is

$$\mathbf{k}_2 = \mathbf{k}_{y2} + \mathbf{k}_{z2} = k_2 \sin\theta\, \hat{\mathbf{e}}_y + k_2 \cos\theta\, \hat{\mathbf{e}}_z,$$

where the wave vector magnitudes are $|\mathbf{k}_1| = k_1 = \frac{\omega_1}{c}$ and $|\mathbf{k}_2| = k_2 = \frac{\omega_2}{c}$ and $\hat{\mathbf{e}}_y, \hat{\mathbf{e}}_z$ are unit vectors in the y and z directions. The y axis positive direction was set in the same direction of $\mathbf{k}_{y2}$, that is, the photons coming from the oxeb laser have positive momentum, $\hbar\mathbf{k}_{y2} = \hbar|\mathbf{k}_{y2}|\hat{\mathbf{e}}_y$ at the detector plane (The y axis positive direction could have been set in the opposite sense. Either convention applied consistently yields the same results). In addition to their linear momentum, the photons are also labeled by their frequency. Since each laser source has its own oscillation frequency, the wave-field coming from the *oxeb* laser with $\hbar\mathbf{k}_{y2}$ momentum projection, has frequency ω_2 and the wave-field coming from the *cheb* laser with $\hbar\mathbf{k}_{y1}$ momentum projection, has frequency ω_1. The wave vector projection in the transverse y direction and the corresponding frequency are highly correlated. This so-called photon's labeling is similar to the temporal and spatial labeling terminology in HOM second order interferometers [21]. However, the frequency of each laser is not known a priori, due to the fluctuations (albeit tiny) in the two lasers. As we shall presently see, it is only when a set of quantum tests is performed that the relative frequencies of the two lasers can be inferred.

2.2 QFT Description

In quantum field theory, the standard representation of two quantized complex electric field operators with linear polarization is $\hat{E}_1^{(+)}(\mathbf{r}) = i\mathcal{E}_1^{(1)} \exp(i\,\mathbf{k}_1 \cdot \mathbf{r})\hat{a}_1$ and $\hat{E}_2^{(+)}(\mathbf{r}) = i\mathcal{E}_2^{(1)} \exp(i\,\mathbf{k}_2 \cdot \mathbf{r})\hat{a}_2$, where $\mathcal{E}_1^{(1)}$, $\mathcal{E}_2^{(1)}$ are the one-photon amplitudes and $\hat{a}_1$, $\hat{a}_2$ are the annihilation operators for modes 1 and 2, respectively. The fields coming from each monomode laser are adequately represented by single mode coherent states $|\alpha_1\rangle$ and $|\alpha_2\rangle$ [22]. These quasi-classical states

are eigenstates of the annihilation operators $\hat{a}_1|\alpha_1\rangle = \alpha_1|\alpha_1\rangle$ and $\hat{a}_2|\alpha_2\rangle = \alpha_2|\alpha_2\rangle$ with eigenvalues α_1, α_2. Since the two fields are completely independent, their superposition is a two mode factorizable state, $|\psi_{1,2-qc}(t)\rangle = |\alpha_1 \exp(-i\omega_1 t)\rangle|\alpha_2 \exp(-i\omega_2 t)\rangle$. These states allow for the factorization of the first order coherence function [23]. The quantum photo detection probability is $w(\mathbf{r},t) = s\langle\psi_{1,2-qc}(t)|\hat{E}^{(-)}(\mathbf{r})\hat{E}^{(+)}(\mathbf{r})|\psi_{1,2-qc}(t)\rangle$, where s is the sensitivity of the detector and the operator $\hat{E}^{(-)}(\mathbf{r})$ is the Hermitian conjugate of the positive frequency part of the electric field operator $\hat{E}^{(+)}(\mathbf{r})$. This expression evaluates to

$$w(\mathbf{r},t) = s\left(\mathcal{E}_1^{(1)}\mathcal{E}_2^{(1)}\right)^2 \\ (|\alpha_1|^2 + |\alpha_2|^2 + \alpha_1^*\alpha_2 \exp[i((\mathbf{k}_2 - \mathbf{k}_1)\cdot\mathbf{r} - (\omega_2 - \omega_1)t + \varphi_2 - \varphi_1)] + c.c.), \tag{1}$$

where φ_1, φ_2 are independent stochastic functions with coherence times τ_1, τ_2 due to the laser cavities instabilities. Recall that in this experiment, the coherence time of each laser is somewhere above 300 ns.

The spatially dependent interference argument of the exponential function is $(\mathbf{k}_2 - \mathbf{k}_1)\cdot\mathbf{r} = 2\bar{k}\sin\theta\ y + \triangle k\cos\theta\ z$, where $2\bar{k} = k_1 + k_2$, $\triangle k = k_2 - k_1$. The fields superposition is observed at a detector placed at the $z = z_0$ plane, thus the term $\triangle k\cos\theta\ z_0$, only adds a constant phase shift. The phase as a function of the transverse distance y and time is

$$\phi = 2\bar{k}\sin\theta\ y + \triangle k\cos\theta\, z_0 - \triangle\omega\, t + \triangle\varphi, \tag{2}$$

where $\triangle\omega = \omega_2 - \omega_1$ and $\triangle\varphi = \varphi_2 - \varphi_1$. When the two frequencies are different, the constant phase surfaces evolve in both, time and space. In contrast, wave-fronts in frequency degenerate setups entail spatial coordinates alone. The velocity of an equal phase plane, provided that $\triangle\varphi$ varies slowly in time and space, is

$$\frac{dy}{dt} = \frac{\triangle\omega}{2\bar{k}\sin\theta}. \tag{3}$$

The fringes are therefore displaced in time with a slope $\frac{dy}{dt}$, whose sign is determined by the value of $\triangle\omega$.

3 EXPERIMENTAL RESULTS

Each point in the streak camera image represents a quantum test of whether a photon arrived at position y of the streak camera photocathode at a given time t. A streak camera image consists of two sets of quantum tests, one in the spatial domain and another in the temporal domain. In the y ordinate direction, electrons in the photocathode long axis act as a set of spatially distributed detectors. For each y position, there is another set of different consecutive quantum tests that probe the dynamical evolution of the quantum system ([24], p.33, p.237). This set is depicted in the abscissas time axis. A photoelectron is emitted with 10.37% quantum efficiency at the streak camera photocathode, if a photon is present at (y,t) where the two photon beams overlap. These events are amplified by the MCP and recorded in the $1024 \times 1392 = 1.425 \times 10^6$ detectors at the CCD. Thus, each streak camera interferogram involves 10^6 quantum tests (order of magnitude). The interferograms in **Figures 3**, **4** were registered at 50 ns/mm sweep speed with 3.4 ns temporal resolution. The transverse spatial range is 15 mm with 70 μ resolution. The 655 ns segments obtained with the AOM modulator, where the two CW lasers temporally overlap, exhibit high contrast interference fringes with visibility above 70% as shown in the figures before mentioned.

The interferogram shown in **Figure 3** exhibits fringes with negative slope. From **Eq. 3**, if the slope of the equal phase lines is negative, the frequency difference $\triangle\omega$ is negative and thus $\omega_2 < \omega_1$. Therefore, in this particular exposure, the oxeb laser emitted photons with lower energy $\hbar\omega_2$, drawn in red in **Figure 3**. Each of the photons comprising this beam have positive linear momentum projection $\hbar\mathbf{k}_{y2}$ in the y direction. These red photons ineluctably followed the path $\overline{BP}$, where B is the position of the beam at the laser oxeb output and P is a point in the streak camera photocathode screen. The converse is true for the photons that constitute the cheb laser beam. These higher energy photons drawn in blue in **Figure 3**, have negative linear momentum projection $-\hbar|\mathbf{k}_{y1}|\hat{\mathbf{e}}_y$ in the y direction at the detector plane. They followed the path $\overline{AP}$, where A is the position of the beam at the cheb laser output. From the time-space interferogram, it is of course possible to evaluate the frequency difference $\triangle\omega = -19.4$ MHz, although the specific value is irrelevant for the present discussion. Notice that the diagram drawn on the right hand side of **Figure 3** is obtained from the 10^6 quantum tests. It is the spatial and temporal distribution of these quantum tests that allow us to figure out the path that the blue or red photons followed.

Although the lasers were carefully stabilized, tiny frequency fluctuations produce quantitative and qualitative differences in the interference patterns. The interferogram shown in **Figure 4**, was acquired merely 1014 ms after the previous interferogram shown in **Figure 3**. The lasers' frequency drifted so that the slope changed sign from one scan to the next. This was of course not always the case for subsequent exposures, spatial frequency and slope varied stochastically from frame to frame. For a positive slope, the frequency difference $\triangle\omega$ is positive and then $\omega_2 > \omega_1$. Therefore, in this exposure, the oxeb laser emitted photons with higher energy $\hbar\omega_2$, drawn in blue in **Figure 4**. Each of these higher energy photons necessarily followed the path $\overline{BP}$ in this case. The photons emitted by the cheb laser beam now have lower energy and followed the path $\overline{AP}$. In this interferogram, $\triangle\omega = 54.9$ MHz. Summing up the two previous results: *The fringes are displaced, as a function of time, in the same direction of the transverse momentum projection of the photons with higher energy*. It should be stressed that the detected photons are neither blue nor red but photons with information from both sources given by the quantum photo detection probability stated in **Eq. 1**.

In the interferogram of **Figure 4**, if there were some red photons that had positive momentum but came from the lower slit and some blue ones had negative momentum but came from the upper slit, their interference would produce fringes with a negative slope. However, the interferogram in **Figure 4** does not exhibit even the faintest fringes with negative slope, thus this possibility is ruled out. Therefore, we must conclude that in either case ($\omega_2 > \omega_1$ or $\omega_2 < \omega_1$), the trajectory of the photons is well defined, yet a high contrast interference pattern is observed!

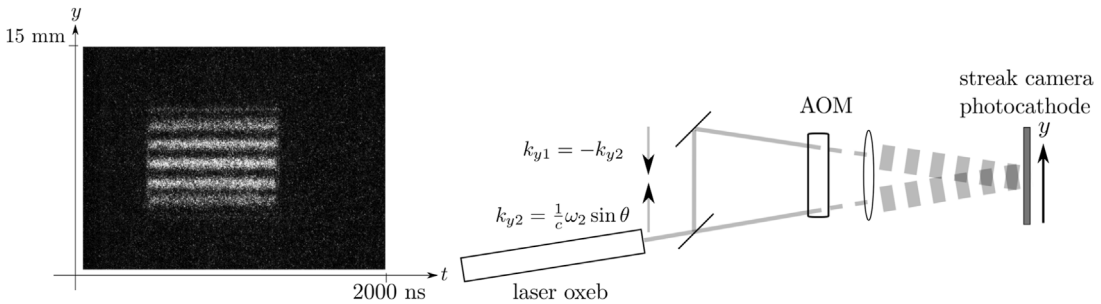

FIGURE 5 | Zero slope interference fringes. Photons are no longer frequency distinguished.

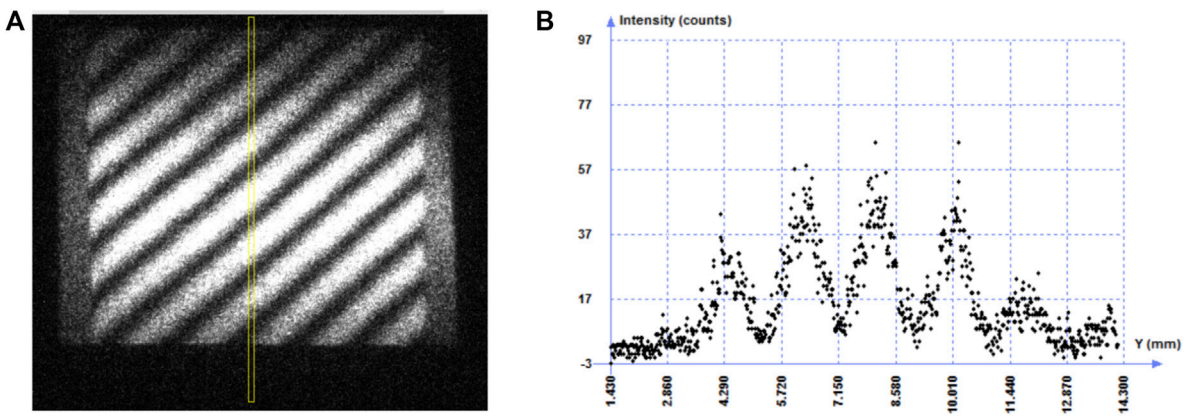

FIGURE 6 | Region of interferogram shown in **Figure 4**, limited to small range in *t* but the whole range in *y*. **(A)** Rectangle width is 0.7 ns (width is over sized in image for clarity), height encompasses the entire *y* range; **(B)** Plot of spatial profile averaged over $\triangle t$ = 0.7 ns (Optoanalyze v3.71).

In contrast, consider the case where the frequencies are equal. This degenerate frequency condition is easier to achieve experimentally using the same laser source but it could actually be accomplished with two laser sources with the appropriate stability and bandwidth or a frame where the two lasers have the same frequency within the exposure time. In this degenerate frequency case, interference fringes have zero slope and the pattern is constant in time as shown in **Figure 5**. Strictly speaking, there is no need of a streak camera. There is no frequency labeling of the photons and it is not possible to deduce which path they followed. Nonetheless, there is still a momentum labeling but, due to the position-momentum uncertainty, the sources are unresolved at the detector [25].

4 EVALUATION OF QUANTUM UNCERTAINTIES

In order to establish the path of the photons, it is sufficient to measure whether the fringes displacement is positive or negative. Nevertheless, it is reassuring to confirm that the actual numerical values of the measurements do not violate an uncertainty relationship, nor are they buried below the quantum noise.

The number of photons Φ^{ph} per unit time is given by the power Φ over the energy per photon $\hbar\omega_\ell$. The power of each laser is 50 mW but losses due to off optimal temperature operation and beam steering reduces the power roughly by a factor of 5. For a 10 mW average power with angular frequency $\omega_\ell = 3.54 \times 10^{15}$Hz, the average number of photons per nanosecond is $\Phi^{\text{ph}} = \frac{\Phi}{\hbar\omega_\ell} = 2.68 \times 10^7 \text{photons} \cdot \text{ns}^{-1}$. The δx = 15 μ horizontal entrance slit reduces the power by a factor of approximately 10^{-3} and the QE of the photodetector by 1.037×10^{-1}. The average number of photons detected per nanosecond is then $\Phi^{\text{ph}} = 2.68 \times 10^3 \text{photons ns}^{-1}$. The standard deviation in the number of photons is thus $\sqrt{\langle N_\ell \rangle} = \sqrt{\Phi^{\text{ph}}} = \sqrt{2.68 \times 10^3} = 51.7$. The phase uncertainty in the standard quantum limit (SQL) [26] in one nanosecond is then approximately

$$\triangle\phi_{\text{SQL}} = \frac{1}{2\sqrt{\langle N_\ell \rangle}} = 9.66 \times 10^{-3} \approx 10^{-2} \text{radians}. \tag{4}$$

This value of the SQL establishes the minimum achievable uncertainty in the phase of each photon beam at the detector. On the other hand, let us assess the measurement error in the interference pattern produced by the two sources. From **Figure 6**, the distance between maxima is $\triangle y_{\max} = 1.88 \pm$

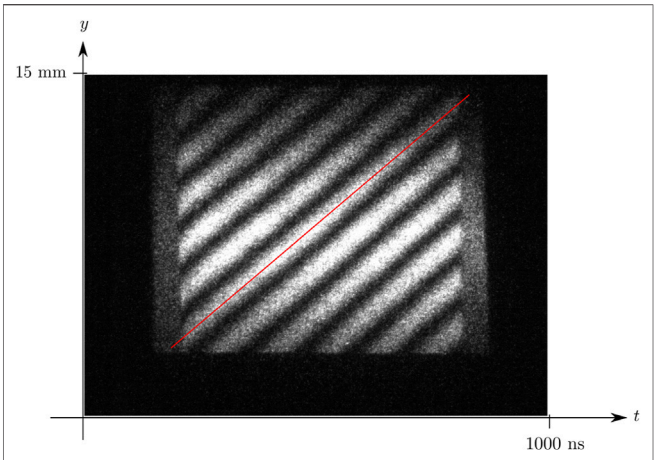

FIGURE 7 | Straight line superimposed on the interference fringes shown in **Figure 4**.

0.023 mm. The main error coming from the instrumental resolution in the y direction. The spatial resolution between maxima located 1.88 mm apart, due to the sources phase uncertainty $\triangle\phi_{\mathrm{SQL}}$ per nanosecond is 3 μm. The spatial frequency measurement uncertainty due to the interference of the two photon beams is thus about 8 times larger than the SQL of each laser source.

The fringes observed in the various interferograms presented in the paper follow straight lines, thus their slope is constant as predicted by **Eq. 3**. **Figure 7**, reproduces the positive slope interference fringes, (where the oxeb laser emits higher frequency photons than the cheb laser) together with a straight line fit. Therefore the lasers relative phase fluctuation $\triangle\varphi$ must be constant (or at most linear in time) during the ≈ 603 ns where there is temporal overlap of the two beams. Frequency fluctuations are thus smaller than the long term average $\triangle\nu$ = 3 MHz laser bandwidth in the μs timescale. For short detection times, the laser cavity fluctuations are 'frozen' and the lasers bandwidth approaches the Schawlow-Townes quantum limit, $\triangle\nu_{laser} = \frac{4\pi\hbar\omega}{\tau_{cav}^2 P}$ [27]. For these Nd:YAG monomode laser systems, the quantum limit bandwidth is of the order of a few kHz.

The existence of an energy-time uncertainty relation in quantum mechanics has been subject to much debate [28, 29]. Due to the lack of a self-adjoint time operator, there is formally no quantum uncertainty relationship of time with any other dynamical variable [30], in particular an uncertainty relationship with energy or linear momentum. Nonetheless, time and frequency are, of course, Fourier transform conjugate variables subject to the inequality, $\delta t\,\delta\omega \geq \frac{1}{2}$ for Gaussian pulses based on the mean square deviation ([31], p.623). For example, the beat frequency ($\triangle\omega$ = 54.9 MHz) in the interferogram shown in **Figure 7**, is obtained from the measurement during the beam's temporal overlap of δt = 603 ns. The frequency resolution is thus at most, $\delta\omega \geq 1/(2\delta t)$ = 0.83 MHz. In quantum parlance, photons in different modes are distinguishable if the detection time is longer than the inverse of the modes frequency separation. Photons in modes separated by $\triangle\omega$ = 54.9 MHz are distinguishable if they are detected in times longer than $1/\triangle\omega$ ≈ 18 ns. This time is considerably larger than the photolelectric response time [32] and the uncertainty in the time axis for a single temporal event. Nonetheless, the detection is performed in successive time measurements over a time span larger than 603 ns.

In the limit of macroscopic fields and small quantum fluctuations, the photon number N_ℓ and phase ϕ_ℓ fluctuations (ℓ = 1, 2), look like complementary variables in the usual sense of quantum mechanics $\triangle N_\ell \triangle\phi_\ell \geq \frac{1}{2}$ [22]. For minimum uncertainty states and in particular for coherent states, the equality is fulfilled because fluctuations are proportional to the square root of the average number of particles in a Poisson distribution,

$$\triangle\phi_\ell = \frac{1}{2\sqrt{\langle N_\ell\rangle}}. \tag{5}$$

The time-space interferograms shown here nicely depict the trend of this behavior. For a few scattered dots, $\langle N_\ell\rangle$ is small and constant phase lines are difficult to establish. However, as the number of events (dots) increase, the equal-phase lines become better delineated and the uncertainty in their slope is thus reduced. The number of detected events N_ℓ can be varied, either by attenuation of the sources or by evaluation of a limited portion of the interferometric frame. In the latter case, if the slope is evaluated from a partial region of the image, the number of dots is smaller and the uncertainty in the phase and therefore in the fringes slope, becomes larger.

5 EXPERIMENTAL RATIONALE

Many which-path experiments have been tried out: "A succession of suggestions for more and more ingenious experiments has failed to provide any method for simultaneous fringe and path observations"[33]. So called welcher weg experiments were even proposed by eminent physicists, Einstein and Feynman amongst them ([34], Sec.1.1.3). However, even in the thought experiments, monitoring the path introduces an uncertainty that disrupts the interference pattern. The less disruptive probes implemented so far involve weak measurements that provide fuzzy quantum information [35, 36]. We shall say more about this approach in the following lines. Our setup, was designed to study the dynamics of decoherence, it was not intended to undertake a which-path problem; The before mentioned facts being enough to deter almost anyone from doing so. Nonetheless, we should also mention that previous interference experiments with photons of different energy were already indicative of a well known frequency going to a specific slit [37, 38].

Why then does this experiment succeed in the measurement of path knowledge without destroying the interference pattern? From our understanding, there are three reasons:

1. The path information is obtained from measurements at the interference detection plane.

a. The trajectory is in no way perturbed since the path detection is not performed in mid trajectory but at the end plane where the fringes are observed. The Englert inequality establishes that for a given fringe visibility there is an upper bound on the amount of information that can be stored in a which-way detector (WWD) [39]. Englert inequality is derived assuming that the WWD's are placed somewhere in the way between the two alternative trajectories before the photon beams overlap. Here, the photocathode plays the role of the WWD's; However, it is placed at the interference plane where the beams overlap but not before.
b. Recall that no information can be obtained without disturbing a quantum system [40]. In the present experiment, photons are destroyed when detected at the streak camera photo-cathode where information is extracted, thus Busch theorem is not violated. Our measurement is not a weak measurement. On the contrary, each of the 10^6 quantum tests of a given frame, destroy the photons involved in each test. The system is destroyed, that is completely disturbed, by the measurement.

2. The fringes slope in the time-space coordinates is the decisive parameter in order to establish the photons path.
   a. It is necessary to accumulate a sufficiently large number of photons in order to produce a fringe pattern. Whether this pattern is obtained by intense or attenuated beam exposures does not alter the statistics of the laser light and are thus entirely equivalent [4]. It does not make sense to ask whether a single photon produces a fringe pattern. At least two dots are needed to draw a line, and if the position uncertainty of the photons (dots) is large, many dots are required to draw a line with some confidence. Nonetheless, the collection of measurements gives information about each trial even to the point of stating that "Each photon then interferes only with itself" ([41], p.9). In an analogous fashion, the trajectory of the photons is revealed here from the measurement of a large number of events. Nonetheless, information about the trajectory of each photon is obtained.
   b. Successive time measurements of the fringe pattern are recorded. This scheme follows the rationale of quantum measurements distributed in time where the path-integral formulation is particularly well suited to describe time dependent experiments [42]. Feynman's rules for combining probability amplitudes depend on whether intermediate states are measured [43]. In the present experiment no intermediate state is measured. Nonetheless, information about intermediate states is obtained from measurements at a succession of final states.
3. Photons need to be frequency labeled.

As a rule, photons need to be doubly labeled with tags that are not conjugate variables. In this experiment, labels are "photon linear momentum projection in the y axis" and "photon energy" or quantities derived thereof. Thus determination of one of them does not obstruct the determination of the other. One label, in this case its frequency, distinguishes the type of photon; while the other, describes its momentum that ultimately establishes the path that it followed.

Regarding point 2a, it could be argued that only the average behavior of the system is being probed. However, this is not the case. In the prevailing Copenhagen view of quantum mechanics, or its modern quantum Bayesian version, the theory is intrinsically probabilistic. A prediction can only be related to observation in an statistical way given by Born's rule. The larger the number of measured events, the sharper the measured property (within the uncertainty principle if complementary variables are involved). From the measurement of a large number of independent events, it is possible to infer certain properties of each event. The fundamental reason being that events independence imply that each event is not altered in any way by the other events.

The uncertainty principle has been stated as "Any determination of the alternative taken by a process capable of following more than one alternative destroys the interference between alternatives" ([44], 1–2, p.9). This assertion by Feynman and coauthors is certainly compromised by the present results. However, they do not contradict the uncertainty principle. Heisenberg's uncertainty principle is, strictly speaking, related to the uncertainty between conjugate variables, that is, operators that do not commute [24]. In **Section 4**, we have shown that the present experimental results are in full accordance with quantum uncertainties.

6 ONTOLOGY AND DISCUSSION

6.1 Which Way Query

In order to clarify the delicate conceptual difference of the which path query, let us pose two questions that are seemingly the same but have different answers:

- Do the experimental results reveal which path each photon followed?

The answer is YES. Let the outcome of the 10^6 quantum tests be positive slope fringes. Then, in the experimental layout that has been presented, each red photon came through A and each blue photon came through B. The path that each photon followed is known, yet, an interference pattern is observed. The interference pattern is built up by the accumulation single photon events. The certainty of the assertion depends on the visibility of the interference fringes, and these in turn, depend on the number of quantum events (and of course, the appropriate experimental arrangement with truly independent but stable enough sources).

- Do the experimental results reveal which path did a detected photon (a white speck on the screen) followed?

The answer is NO. When we refer to "this" photon that impinged on the screen, it is not known whether it is a red or a blue photon or even a redblue photon. In order to specify which way it followed, the color must be known but we only detect a

white speck regardless of the photon frequency. Thus interference is observed but the detected photon path is unknown.

The subtle but fundamental difference between these two queries is that the former question does not involve the category of the detected entity. In contrast, the detected entity is at the core of the latter question.

6.2 Detected Photons

A closely related but different question is the nature of the detected photons. Before embarking onto it, we should be aware of the tacit assumption that photons are considered to exist as an indivisible lump of electromagnetic energy or at least provide the best description we have so far of the EM fields. To some extent, this is a matter, as Prof. Penrose puts it, of quantum faith [45]. A faith not exempt of support and vast evidence considering the overwhelming success of quantum field theory. For this reason, the alternatives mentioned here below do not admit the possibility of a detector (say an atom) absorbing part of one photon and part of another photon, for this would destroy the photon concept altogether.

Two alternatives are envisaged regarding the nature of each detected photon:

1) Detected photons are either blue or red. One possibility is to consider that a detected photon is either blue or red but its frequency cannot be known if interference occurs. An asset of this approach is that the entities "red photon" or "blue photon" retain their identity. Thus, the photon concept remains a good concept, in the sense of good quantum numbers. However, this view has the major problem that there is then no superposition of the disturbances, but it is superposition that produces the interference phenomenon. A thought experiment has been proposed before, involving frequency sensitive photo detectors with different predictions for the expected outcome ([37], App. A). It has also been stressed that superposition actually takes place only in the presence of charges that respond to the superimposed fields [46].
2) Detected photons bear information of both frequencies (mainstream view). The other possibility is to consider that a detected photon within the interference region has information on both laser fields as expounded by Paul ([47], p.221). In the present experiment, it must bear information of both frequencies according to the superposition described in **Subsection 2.2**. The difficulty with this view is that a photon cannot give part of it to another photon because it would then loose its entity. Somehow, it has to give information to the other photon while retaining its photon identity. Photons cannot be conceived like classical particles. What is more, photons cannot even be conceived like other quantum material particles because, in general, there is no mathematical object that represents a photon wavefunction [48]. The photon notion arises naturally in number states as the elementary energy unit $\hbar\omega$. Number states are eigenstates of the Hamiltonian but their phase is random. In order to observe first order interference, a well defined phase, up to uncertainty limitations, is required. Single mode coherent states exhibit a well defined phase but are not eigenstates of the Hamiltonian. Their energy is not well defined due to the uncertainty in photon number but, being single mode states, the energy per photon is fixed. As mentioned by Paul ([47], p.221), in the detection process, "an energy packet $h\nu$ is taken from the superposition field to which both lasers contribute equally, and hence it is only natural that this photon bears information on both laser fields."

6.3 Final Remark

According to the present results, the which way assertion should be refined in order to have an unambiguous meaning: The path that each photon followed, in a non-degenerate frequency scheme, whether red or blue, can be known without destroying the interference pattern. In this formulation of the statement, the slit that each photon passed through is known, but it is not known to which detected spot it corresponds. Another, equally correct formulation is that, within the interference region, the path of a detected photon cannot be traced back. That is, if interference occurs, it is not possible to assert the path followed by a photon detected on the screen.

DATA AVAILABILITY STATEMENT

The original contributions presented in the study are included in the article/Supplementary Material, further inquiries can be directed to the corresponding author.

AUTHOR CONTRIBUTIONS

MF-G conceived and performed the experiment. MF-G wrote the manuscript, CG-G revised the text. CG-G collaborated in the setup and maintained the stringent conditions needed to stabilize the two CW lasers.

FUNDING

Part of the equipment used in these experiments was funded by CONACYT, projects CB2005-51345-F-24696 and CB2010-151137-F.

REFERENCES

1. Javan A, Ballik EA, Bond WL. Frequency Characteristics of a Continuous-Wave He-Ne Optical Maser. *J Opt Soc Am* (1962) 52:96–8. doi:10.1364/JOSA.52.000096
2. Magyar G, Mandel L. Interference Fringes Produced by Superposition of Two Independent Maser Light Beams. *Nature* (1963) 198:255–6. doi:10.1038/198255a0
3. Pfleegor RL, Mandel L. Interference of Independent Photon Beams. *Phys Rev* (1967) 159:1084–8. doi:10.1103/physrev.159.1084
4. Kaltenbaek R, Blauensteiner B, Żukowski M, Aspelmeyer M, Zeilinger A. Experimental Interference of Independent Photons. *Phys Rev Lett* (2006) 96:240502. doi:10.1103/PhysRevLett.96.240502
5. Bratescu GG, Tudor T. On the Coherence of Disturbances of Different Frequencies. *J Opt* (1981) 12:59–64. doi:10.1088/0150-536x/12/1/005
6. Lee D-I, Roychoudhuri C. Measuring Properties of Superposed Light Beams Carrying Different Frequencies. *Opt Express* (2003) 11:944–51. doi:10.1364/OE.11.000944
7. Davis LM. Interference between Resolvable Wavelengths with Single-Photon-Resolved Detection. *Phys Rev Lett* (1988) 60:1258–61. doi:10.1103/PhysRevLett.60.1258
8. Saveliev IG, Sanz M, Garcia N. Time-resolved Young$rquot$s Interference and Decoherence. *J Opt B: Quan Semiclass. Opt.* (2002) 4:S477–S481. doi:10.1088/1464-4266/4/4/343
9. Louradour F, Reynaud F, Colombeau B, Froehly C. Interference Fringes between Two Separate Lasers. *Am J Phys* (1993) 61:242–5. doi:10.1119/1.17298
10. Patel R, Achamfuo-Yeboah S, Light R, Clark M. Widefield Two Laser Interferometry. *Opt Express* (2014) 22:27094–101. doi:10.1364/OE.22.027094
11. Marathay AS. *Elements of Optical Coherence Theory*. New York: Wiley (1982).
12. Eichmann U, Bergquist JC, Bollinger JJ, Gilligan JM, Itano WM, Wineland DJ, et al. Young's Interference experiment with Light Scattered from Two Atoms. *Phys Rev Lett* (1993) 70:2359–62. doi:10.1103/physrevlett.70.2359
13. Riedmatten Hd., Marcikic I, Tittel W, Zbinden H, Gisin N. Quantum Interference with Photon Pairs Created in Spatially Separated Sources. *Phys Rev A* (2003) 67:022301. doi:10.1103/PhysRevA.67.022301
14. Esposito G, Marmo G, Miele G, Sudarshan G. *Advanced Concepts in Quantum Mechanics*. Cambridge, United Kingdom: CUP (2014).
15. Jacques V, Wu E, Grosshans F, Treussart F, Grangier P, Aspect A, et al. Delayed-choice Test of Quantum Complementarity with Interfering Single Photons. *Phys Rev Lett* (2008) 100:220402. doi:10.1103/PhysRevLett.100.220402
16. Katsumori M. *Niels Bohr's Complementarity*. Dordrecht: Springer (2011).
17. Plotnitsky A. *Niels Bohr and Complementarity*. New York: Springer (2013).
18. Fernández-Guasti M, Palafox H, Chandrasekar R. Coherence and Frequency Spectrum of a Nd:YAG Laser - Generation and Observation Devices. In: *Optics and Photonics 2011*. San Diego: SPIE (2011). p. 81211E–1–10. vol. 8121 of *The nature of light: What are photons? IV*. doi:10.1117/12.893194
19. Fernández-Guasti M, García-Guerrero C. Optical Interference between Distinguishable Photon Paths. In: *2019 PhotonIcs Electromagnetics Research Symposium - Spring (PIERS-Spring)*. Rome: IEEE Xplore (2020). p. 3634–42.
20. Vidal I, Caetano DP, Fonseca EJS, Hickmann JM. Observation of Interference Pattern in the Intensity Correlation of a Non-local Object Using a Hanbury Brown and Twiss-type experiment. *Europhys Lett* (2008) 82:34004. doi:10.1209/0295-5075/82/34004
21. Lee PSK, van Exter MP. Spatial Labeling in a Two-Photon Interferometer. *Phys Rev A* (2006) 73:063827. doi:10.1103/PhysRevA.73.063827
22. Grynberg G, Aspect A, Fabre C. *Introduction to Quantum Optics*. New York: CUP (2010).
23. Glauber R. *Quantum Theory of Optical Coherence*. Heppenheim: WILEY-VCH Verlag (2007).
24. Peres A. *Quantum Theory: Concepts and Methods*. Boston: Kluwer Academic (2002). vol. 72 of *Fundamental Theories of Physics*.
25. Mandel L. Photon Interference and Correlation Effects Produced by Independent Quantum Sources. *Phys Rev A* (1983) 28:929–43. doi:10.1103/PhysRevA.28.929
26. Clerk AA, Devoret MH, Girvin SM, Marquardt F, Schoelkopf RJ. Introduction to Quantum Noise, Measurement, and Amplification. *Rev Mod Phys* (2010) 82:1155–208. doi:10.1103/RevModPhys.82.1155
27. Schawlow AL, Townes CH. Infrared and Optical Masers. *Phys Rev* (1958) 112:1940–9. doi:10.1103/physrev.112.1940
28. Busch P. On the Energy-Time Uncertainty Relation. Part I: Dynamical Time and Time Indeterminacy. *Found Phys* (1990) 20:1–32. doi:10.1007/BF00732932
29. Miyadera T. Energy-time Uncertainty Relations in Quantum Measurements. *Found Phys* (2016) 46:1522–50. doi:10.1007/s10701-016-0027-6
30. Aharonov Y, Bohm D. Time in the Quantum Theory and the Uncertainty Relation for Time and Energy. *Phys Rev* (1961) 122:1649–58. doi:10.1103/physrev.122.1649
31. Diels JC, Rudolph W. *Ultrashort Laser Pulse Phenomena: Fundamentals, Techniques, and Applications on a Femtosecond Time Scale*. 2nd ed. Amsterdam: Academic Press, Elsevier Science Publishers (2006).
32. Liu J, Zhou Y, Zheng H, Chen H, Li F-l., Xu Z. Two-photon Interference with Non-identical Photons. *Opt Commun* (2015) 354:79–83. doi:10.1016/j.optcom.2015.05.072
33. Roychoudhuri C, Roy R. *The Nature of Light: What Is a Photon?* Boca Raton: Taylor and Francis (2003). p. S1–S35. Optics and Photonics News.
34. Ficek Z, Swain S. *Quantum Interference and Coherence: Theory and Experiments*. New York: Springer (2005).
35. Aharonov Y, Albert DZ, Vaidman L. How the Result of a Measurement of a Component of the Spin of a Spin-1/2particle Can Turn Out to Be 100. *Phys Rev Lett* (1988) 60:1351–4. doi:10.1103/PhysRevLett.60.1351
36. Kocsis S, Braverman B, Ravets S, Stevens MJ, Mirin RP, Shalm LK, et al. Observing the Average Trajectories of Single Photons in a Two-Slit Interferometer. *Science* (2011) 332:1170–3. doi:10.1126/science.1202218
37. Garcia N, Saveliev IG, Sharonov M. Time-resolved Diffraction and Interference: Young's Interference with Photons of Different Energy as Revealed by Time Resolution. *Philos Trans A Math Phys Eng Sci* (2002) 360:1039–59. doi:10.1098/rsta.2001.0980
38. Grave de Peralta L. Phenomenological Quantum Description of the Ultrafast Response of Arrayed Waveguide Gratings. *J Appl Phys* (2010) 108:103110. doi:10.1063/1.3512860
39. Englert B-G. Fringe Visibility and Which-Way Information: An Inequality. *Phys Rev Lett* (1996) 77:2154–7. doi:10.1103/PhysRevLett.77.2154
40. Myrvold WC, Christian J. *Quantum Reality, Relativistic Causality, and Closing the Epistemic Circle*. Netherlands: Springer (2009).
41. Dirac PAM. *The Principles of Quantum Mechanics*. 4th ed. Oxford: OUP (1978).
42. Caves CM. Quantum Mechanics of Measurements Distributed in Time. A Path-Integral Formulation. *Phys Rev D* (1986) 33:1643–65. doi:10.1103/PhysRevD.33.1643
43. Feynman RP. Space-time Approach to Non-relativistic Quantum Mechanics. *Rev Mod Phys* (1948) 20. doi:10.1103/revmodphys.20.367
44. Feynman R, Hibbs A, Styer D. *Quantum Mechanics and Path Integrals*. New York: Dover Books on Physics (Dover Publications) (2010).
45. Penrose R. *Fashion, Faith and Fantasy*. Woodstock: Princeton Univ. Press (2016).
46. Roychoudhuri C. *Causal Physics: Photons by Non-interactions of Waves*. Boca Raton: CRC Press, Taylor and Francis (2017).
47. Paul H. Interference between Independent Photons. *Rev Mod Phys* (1986) 58:209–31. doi:10.1103/RevModPhys.58.209
48. Scully MO, Zubairy MS. *Quantum Optics*. Cambridge: CUP (2001).

Conflict of Interest: The authors declare that the research was conducted in the absence of any commercial or financial relationships that could be construed as a potential conflict of interest.

frontiers in Physics

ORIGINAL RESEARCH
published: 30 March 2022
doi: 10.3389/fphy.2022.843932

Identification of Diffracted Vortex Beams at Different Propagation Distances Using Deep Learning

Heng Lv[1†], *Yan Guo*[1†], *Zi-Xiang Yang*[1], *Chunling Ding*[1], *Wu-Hao Cai*[1], *Chenglong You*[2*] and *Rui-Bo Jin*[1,3*]

[1]Hubei Key Laboratory of Optical Information and Pattern Recognition, Wuhan Institute of Technology, Wuhan, China, [2]Quantum Photonics Laboratory, Department of Physics and Astronomy, Louisiana State University, Baton Rouge, LA, United States, [3]Guangdong Provincial Key Laboratory of Quantum Science and Engineering, Southern University of Science and Technology, Shenzhen, China

The Orbital angular momentum (OAM) of light is regarded as a valuable resource in quantum technology, especially in quantum communication and quantum sensing and ranging. However, the OAM state of light is susceptible to undesirable experimental conditions such as propagation distance and phase distortions, which hinders the potential for the realistic implementation of relevant technologies. In this article, we exploit an enhanced deep learning neural network to identify different OAM modes of light at multiple propagation distances with phase distortions. Specifically, our trained deep learning neural network can efficiently identify the vortex beam's topological charge and propagation distance with 97% accuracy. Our technique has important implications for OAM based communication and sensing protocols.

Keywords: deep learning, vortex beams, orbital angular momentum, propagation, diffraction

OPEN ACCESS

Edited by:
Omar Magana-Loaiza,
Louisiana State University,
United States

Reviewed by:
Tao Peng,
Texas A&M University, United States
Xiangping Li,
Jinan University, China

***Correspondence:**
Chenglong You
cyou2@lsu.edu
Rui-Bo Jin
jrbqyj@gmail.com

[†]*These authors have contributed equally to this work*

Specialty section:
This article was submitted to Quantum Engineering and Technology, a section of the journal Frontiers in Physics

Received: *27 December 2021*
Accepted: *15 February 2022*
Published: *30 March 2022*

Citation:
Lv H, Guo Y, Yang Z-X, Ding C, Cai W-H, You C and Jin R-B (2022) Identification of Diffracted Vortex Beams at Different Propagation Distances Using Deep Learning. Front. Phys. 10:843932. doi: 10.3389/fphy.2022.843932

INTRODUCTION

Vortex beam generally refers to the phase vortex beam, which has a spiral wavefront, a phase singularity in the center of the beam, and ring-shaped intensity distribution [1, 2]. The beam with orbital angular momentum (OAM) has the phase term $e^{i\ell\phi}$ in the complex amplitude equation, where ϕ is the azimuthal angle and ℓ is the angular quantum number or topological charge. OAM is an inherent characteristic of vortex beam photons, and each photon carries OAM, which is $\ell\hbar$ [3, 4]. Due to the high-dimensional characteristics of the photon OAM, it is utilized in applications such as optical tweezers [5, 6], micromanipulation [7, 8], angular velocity sensing [9], quantum information [10–13], quantum computing [14–17], optical communications [18–22] and quantum cryptography [23]. Once the value of ℓ is identified, the orbital angular momentum can be calculated, allowing the features of the vortex beam to be determined. Unfortunately, the vortex beam will diffract during propagation, and its spatial profile will be easily distorted in a real-world environment [24]. Detrimentally, the information encoded in the structured beam can be destroyed by random phase distortions [25–27] and diffraction effects, resulting in mode loss and mode cross-talk [28, 29]. As a result, capturing the vortex beam and identifying its information using equipment such as a charge coupled device (CCD) camera or a complementary metal oxide semiconductor (CMOS) camera is difficult [30]. Hitherto, the traditional methods of identifying vortex beams have included methods such as the interferometer method, plane wave interferometry, and triangular aperture diffraction measurement, to name a few [31–34]. These traditional methods are much more challenging

due to the need for more equipment, as well as complicated data analysis process. In addition, some of these methods can only identify specific vortex beams [35]. Moreover, the accuracy of these methods will be greatly reduced when turbulence is considered. These aforementioned factors have significantly hampered the performance of communication, cryptography, and remote sensing. As a result, identifying OAM efficiently and correctly while accounting for diffraction and turbulence is a critical and unresolved challenge.

In recent years, methods such as deep learning algorithms [36] and transfer learning [37] have considerably increased the accuracy of automatic image recognition [38, 39]. A significant number of recent articles have proved the potential of artificial neural networks for efficient pattern recognition and spatial mode identification [40–42], and its accuracy is far superior to some traditional identification detection methods [43–45]. However, due to the complex diffraction effect in the OAM propagation process, there is little relevant work in the identification of the propagation distance value. In the related research, the propagation distance of the vortex beam ranges from the order of centimeters to the order of kilometers, and it is used as a known parameter [46, 47]. Different propagation distance z will drastically change the size of the central aperture of the vortex beam. As a result, it remains difficult to identify the z value using only the intensity pattern. Additionally, changing the value of topological charge ℓ also changes the size of the central aperture, making the identification task more challenging. Finally, turbulence in real-world applications exacerbates the difficulty of such an identification task [48].

In this report, we take advantage of the deep learning algorithm to identify vortex beams and their propagation distances while considering the effects of undesired turbulence. Through theoretical simulations and experiments, we generated vortex beams with different propagation distances and topological charges. In addition, using the transfer learning method, we designed a deep learning model to classify vortex beams. For the first time, our approach utilizes artificial intelligence to simultaneously identify the propagation distance and topological charge of a vortex beam under turbulence's effects. Our research enables the encoding of vortex beams with different propagation distances. As a result, the vortex beam propagation distance may become a new encoding variable. With the improvement of the accuracy of distance recognition, it is even possible to realize precise distance measurement based on the intensity of vortex beams. Our research opens up a new direction for OAM communication and has great significance in OAM based sensing.

THEORY AND METHODS

Generation of the Vortex Beam

The fundamental beam used to produce the vortex beam is a Gaussian beam. By applying a phase mask on the spatial light modulator (SLM), the beam amplitude on the plane of SLM becomes [49]:

$$E_1(r,\theta) = \exp\left(-\frac{r^2}{\omega_0^2}\right)\exp(-i\ell\theta), \tag{1}$$

where ℓ is the topological charge, ω_0 is the Gaussian beam waist, r and θ are radial and azimuthal coordinates, respectively.

Within the framework of paraxial approximation, the field distribution of $E_1(r,\theta)$ after propagation can be calculated using the Collins integral equation [50]:

$$E_2(r_1,\theta_1,z) = \frac{i}{\lambda B}\exp(-ikz)\int_0^{2\pi}\int_0^{\infty} E_1(r,\theta) \times \exp\left[-\frac{ik}{2B}\left(Ar^2 - 2rr_1\cos(\theta_1-\theta) + Dr_1^2\right)\right] r dr d\theta, \tag{2}$$

where r_1 and θ_1 are radial and azimuthal coordinates in the output plane, z is the propagation distance, and $k = 2\pi/\lambda$ is the wave number with λ being the wavelength. The ABCD transfer matrix of light propagation in free space of distant z is

$$\begin{pmatrix} A & B \\ C & D \end{pmatrix} = \begin{pmatrix} 1 & z \\ 0 & 1 \end{pmatrix}. \tag{3}$$

By inserting **Eq. 1** and **Eq. 3** into **Eq. 2**, we can obtain the beam amplitude as

$$E_2(r_1,\theta_1,z) = \frac{i^{\ell+1}\pi}{\lambda z}\exp(-ikz)\exp\left(-\frac{ikr_1^2}{2z}\right)\exp(-i\ell\theta_1) \frac{b_1^{\ell}}{\varepsilon_1^{1+\frac{\ell}{2}}}\frac{\Gamma\left(\frac{\ell}{2}+1\right)}{\Gamma(\ell+1)}{}_1F_1\left(\frac{\ell+2}{2},\ell+1,-\frac{b_1^2}{\varepsilon_1}\right). \tag{4}$$

Eq. 4 represents the hypergeometric Gaussian mode. ${}_1F_1(\alpha,\beta,z)$ is a confluent hypergeometric function, $\Gamma(n)$ is the Gamma function, b_1 and ε_1 are defined as:

$$b_1 = \frac{kr_1}{2z}, \quad \varepsilon_1 = \frac{1}{\omega_0^2} + \frac{ik}{2z}. \tag{5}$$

Based on the above calculations, we can obtain transverse intensity images of vortex beam with different values of ℓ after propagating different distances z.

In actual communication, turbulence can lead to phase distortion of optical mode spatial distribution. Therefore, in our experiment, we use the Kolmogorov model with Von Karman spectrum of turbulence to simulate the atmospheric turbulence in SLM to achieve a distorted communication mode [51, 52]. The degree of distortion is quantified by the Fried's parameter r_0. The expression of the turbulence phase mask we added on the SLM is [42]:

$$\Phi(x,y) = \mathbb{R}\left\{\mathcal{F}^{-1}\left(\mathbb{M}_{NN}\sqrt{\phi_{NN}(\kappa)}\right)\right\}, \tag{6}$$

with $\phi_{NN}(\kappa) = 0.023r_0^{-5/3}(\kappa^2+\kappa_0^2)^{-11/6}e^{-\kappa^2/\kappa_m^2}$ and the Fried's parameter $r_0 = (0.423k^2C_n^2z)^{-3/5}$. The symbol $\mathbb{R}$ represents the real part of the complex field, and $\mathcal{F}^{-1}$ indicates the inverse Fourier transform operation. In addition, κ, κ_0, and $\mathbb{M}_{NN}$ represent the spatial frequency, the central spatial frequency, and encoded random matrix, respectively. C_n^2 is the standard

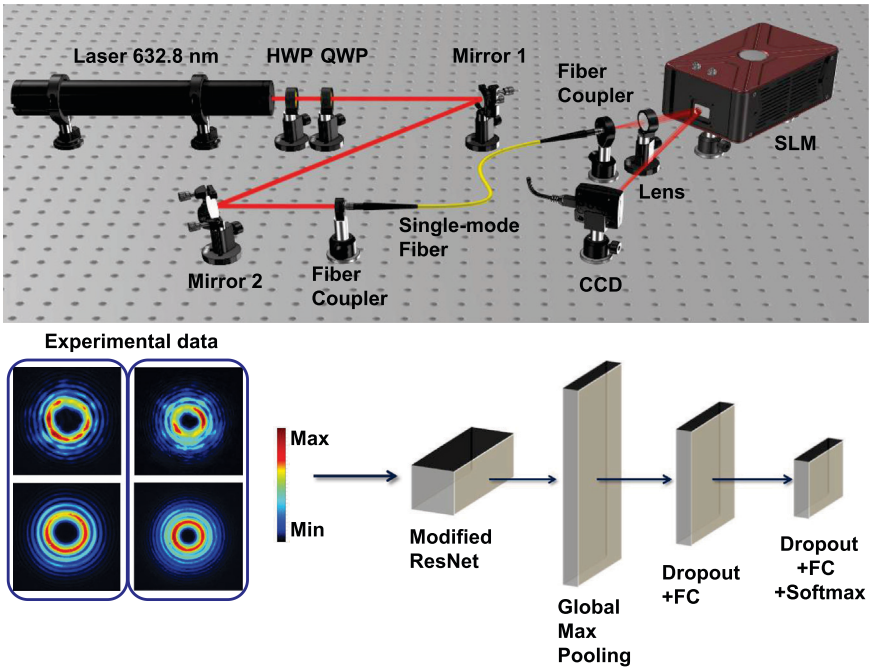

FIGURE 1 | The experimental setup (upper panel) and our customized deep learning algorithm (lower panel). We perform the experiment using a collimated He-Ne laser beam. The vortex beam is generated using an SLM with the computer-generated hologram. Finally, the intensity images are collected by a CCD and used for training and testing. Our deep learning network consists of the unaltered ResNet-101 bottom layer and our redesigned top layer.

refractive index, which is a constant representing the turbulence intensity.

After the turbulence term is added to the original phase mask and loaded on the SLM, beam amplitude on the plane of SLM becomes

$$E_1'(r,\theta) = E_1(r,\theta)\exp\left[i\Phi(x,y)\right]. \tag{7}$$

By substituting **Eq. 7** into **Eq. 2**, we can numerically obtain the field distribution of the turbulence distorted $E_2'(r_1,\theta_1,z)$ after propagation.

The experimental setup and the deep learning model are shown in **Figure 1**. In our experiment, the vortex beams are generated by using an SLM and computer-generated holograms. Utilizing the first-diffraction order of SLM, we can obtain the vortex beam of arbitrary topological charge. A laser beam from a He-Ne laser (wavelength of 632.8 nm) is coupled into a single-mode fiber for spatial mode cleaning. A half-wave plate (HWP) and a quarter-wave plate (QWP) are employed to adjust the polarization of the laser beam at the output port of the fiber. An objective lens (magnification of 10× and an effective focal length of 17 mm) is used to collimate the light from the fiber, and the beam waist after collimation is around 2 mm. By loading a computer-generated phase hologram onto the SLM, a Gaussian beam is converted into a vortex beam. In order to simulate the turbulence in an atmosphere transmission process, we can add an additional turbulence phase to the hologram. Finally, a CCD camera is used to collect the intensity images of the vortex beam, and the transmission distance is controlled by changing the distance between the CCD and the SLM. The images collected by the CCD are sent to a computer for training. Each training set, validation set, and test set contain 86, 10, and 10 images (360 × 360 pixels), in which the value of ℓ ranges from 1 to 5, and the propagation distance z ranges from 40 to 100 cm with a step of 5 cm. Totally, there are 86 × 5 × 13 = 5590 images for the training set and 10 × 5 × 13 = 650 images for the validation set and test set.

The Deep Learning Algorithm

The lower panel of **Figure 1** shows our customized deep learning algorithm model. Our model is a transfer learning network based on the ResNet-101 network design [53]. Since our obtained images have a high degree of similarity, the neural network must have enough depth to extract image features. Therefore, we adopt the CNN architecture and retrain the ResNet-101 deep learning model rather than the shallow neural networks model. More specifically, the top layer is removed from the original ResNet-101. Moreover, a global max pooling layer with a node count of 2048 is used to reduce the parameters to increase the calculation speed. Following that, a dropout layer is added to remove some parameters randomly to minimize over-fitting, and then we use a fully connected (FC) layer to connect the local features. Another dropout layer and an FC layer are added to lower the number of nodes from 1024 to 65. Finally, a softmax layer is applied for a 65 classification probability output.

To train and test the deep learning model, we utilize a computer with an Intel(R) Core(TM) i5-7300HQ CPU @2.5 GHz and an Nvidia GeForce GTX 1050 Ti GPU with

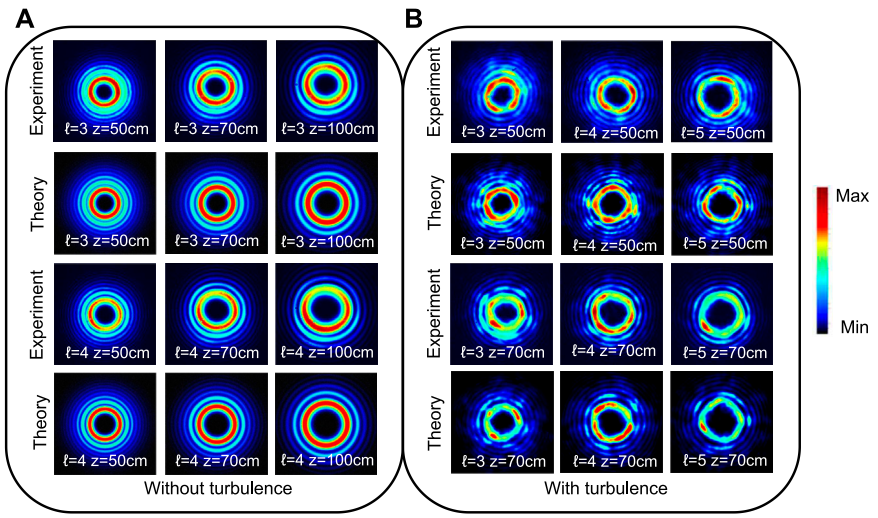

FIGURE 2 | The spatial profiles of different vortex beams. We show the experimentally measured images and simulated images for different topological charges ℓ and different propagation distances z, without turbulence in **(A)** and with turbulence in **(B)**. The first and third rows are the images acquired from the experiment, and the second and fourth rows represent the theoretically simulated images.

4 GB of video memory. We use an adaptive moment estimation (Adam) optimizer throughout the algorithm [54]. In our deep learning model, we also used the transfer learning technique (TLT) [55], which has two benefits. Firstly, it is highly efficient; for example, tasks that originally required months of training without TLT can be reduced to a few hours. The second merit of TLT is that less data is needed. This is because transfer learning requires the use of a pre-trained model, which allows us to achieve accurate recognition results with fewer datasets [56]. Generally speaking, only hundreds or thousands of training images (instead of tens of thousands or even millions of images) are enough to achieve good training results [57, 58]. Finally, the training results in each epoch are evaluated by the categorical cross-entropy loss function [59] which is given by

$$\text{Loss} = -\sum_{i=1}^{n} (\hat{y}_{i1} \ln y_{i1} + \hat{y}_{i2} \ln y_{i2} + \cdots + \hat{y}_{im} \ln y_{im}), \quad (8)$$

where n is the number of samples, m is the number of classifications, $\hat{y}_{im}$ indicates that the true label (with the value of 0 or 1), and y_{im} is the predicted value of the mth class given by the neural network.

RESULTS AND DISCUSSION

Figure 2 shows the spatial profiles of vortex beams with different propagation distances z and topological charges ℓ obtained from experiments and simulations. **Figure 2A** shows the vortex beams without turbulence, and **Figure 2B** depicts vortex beams affected by turbulence. The first and third rows depict the spatial profiles of the vortex beams acquired in the experiment, while the second and fourth rows depict the simulated ones under identical conditions. For simplicity, we define the first aperture in the center as the "center aperture" and other outer apertures as the "diffraction apertures". For a fixed value of ℓ, the size of the central aperture becomes larger as the propagation distance z value increases. At the same time, for a fixed propagation distance z, the size of the central aperture also increases as the value of ℓ increases. From **Figure 2**, we can observe that the spatial profiles obtained from the experiment match well with our simulations, therefore validating our theoretical model of the experiment. By comparing the experimental and theoretical images of $\ell = 4$ and $z = 100$ cm, we can notice that the central aperture in the experimental image is not distributed uniformly. This effect is due to the slight misalignment of the collimated beam to the center of the SLM. As a result, the brightness and shape of the center aperture can vary slightly. This kind of deviation is also included, in order to increase the diversities of the training data. We will show later that, even with such deviations, the training results remain excellent.

There are many situations where the size of the central aperture is comparable for vortex beams with different ℓ and propagation distance z. This particular effect makes the simultaneous identification of ℓ and z difficult. For example, by comparing the theoretical image of $\ell = 3$ and $z = 70$ cm (second row, second column), and the image of $\ell = 4$ and $z = 50$ cm (fourth row, first column) in **Figure 2A**, we can notice that the sizes of the center aperture are similar, making it difficult to distinguish between these two modes. In this case, the difference of the diffraction apertures provides the best characteristic value to distinguish them. More intuitively, **Figure 3** shows the cross-sectional view of the intensity for these two beams at $y = 0$. It is clear that the distance between the two main peaks in **Figure 3A** and **Figure 3B** is almost the same. However, **Figure 3A** has 4 side lobes in the diffraction apertures, while **Figure 3B** has 6 side lobes in the diffraction apertures. This subtle difference makes it possible to distinguish these two cases. Finally, we note that in

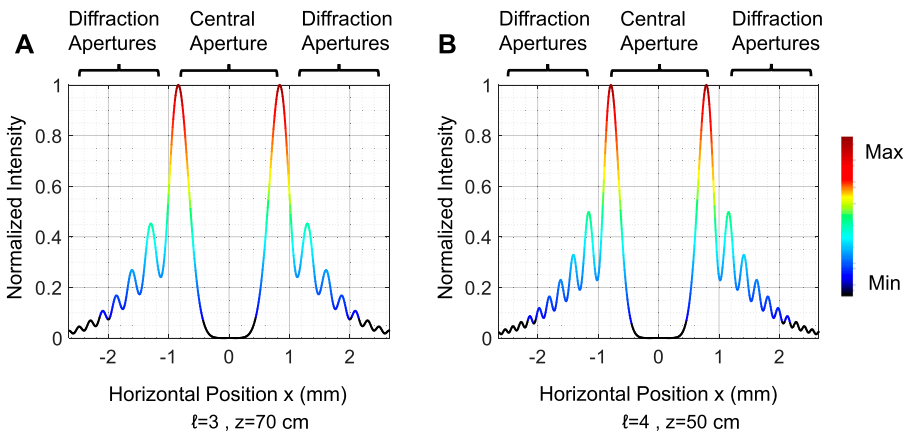

FIGURE 3 | The cross-sectional view of the intensity images at $y = 0$ for **(A)** $\ell = 3, z = 70$ cm and **(B)** $\ell = 4, z = 50$ cm. The size of the central apertures is comparable in both images. However, the number of side lobes in the diffractive apertures is different. This subtle feature enables us to distinguish these two cases.

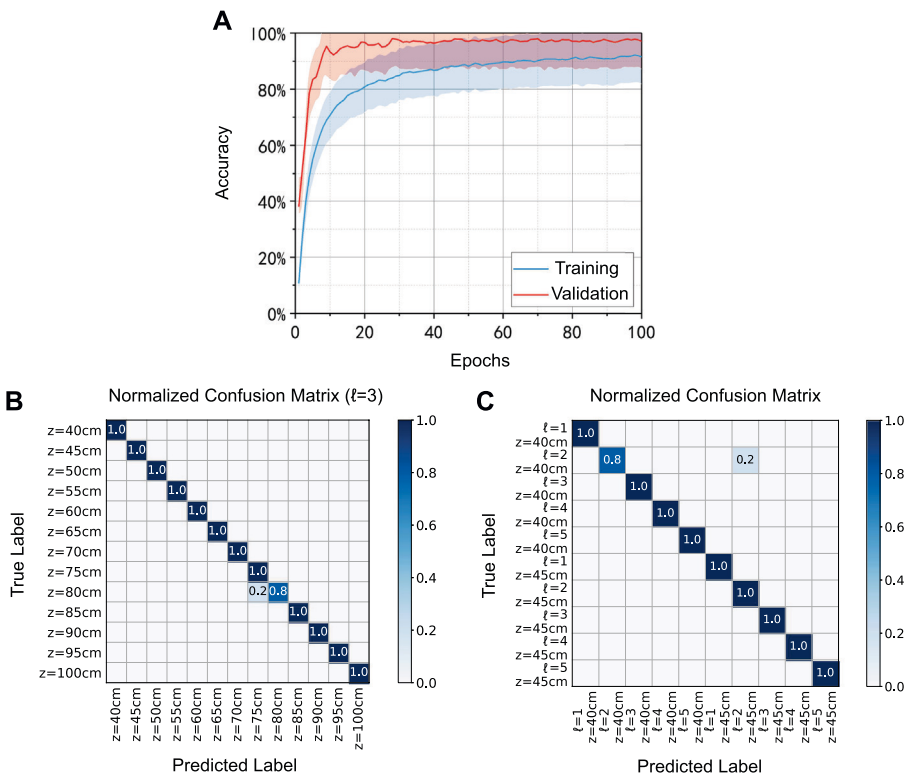

FIGURE 4 | The accuracy and confusion matrix of our trained deep learning algorithm. **(A)** The accuracy of the training set and the validation set versus the epochs. The accuracy of up to 97% is achieved in identifying vortex beams with different ℓ values and different z values after 90 epochs. All shaded areas correspond to the standard deviation of accuracy. All classification results have been tested and verified, and some test results are shown here. **(B)** The normalized confusion matrix between the predicted propagation distance and the true propagation distance for $\ell = 3$. **(C)** Normalized confusion matrix between predicted ℓ values, predicted propagation distance and true ℓ values, true propagation distance.

Figure 3 the diffraction apertures in the region of $|x| > 2.2$ mm (in black) usually cannot be well captured by a CCD in the experiment, due to low light intensity and limited resolution of the CCD.

In practical communication applications, the spatial profile of the vortex beam might be distorted due to atmospheric turbulence, underwater turbulence, or other adverse circumstances. Therefore, the turbulence should be taken into

account for the propagation of the vortex beam. **Figure 2B** shows the typical simulated and experimental diagrams with turbulence. In these theoretical (the second and fourth rows) and experimental (the first and third rows) data, a turbulence intensity parameter of $C_n^2 = 5 \times 10^{-10}$ mm$^{-2/3}$ is utilized. In these data sets, we also take into account the fact that light might not be precisely incident on the center of the SLM plane. It can be noticed that the turbulence created huge distortions on the vortex beam's center aperture and diffraction apertures. For deep learning training, we gathered 1040 distorted light intensity images.

To show the performance of our deep learning network, we plot the accuracy as a function of the training epochs in **Figure 4A**. We can see that after 90 training epochs, the accuracy is higher than 92% for the training set, while the accuracy of the validation set is greater than 97%. Since we added regularization and dropout operations during the training process. These operations will be automatically closed during the verification process, causing the accuracy of the validation set to be higher than the accuracy of the training set. A high validation accuracy of 97% indicates that our approach provides a powerful way to identify the vortex beams with different ℓ values and different z values, even under a turbulent environment. Finally, we note that the number of epochs required for convergence depends on multiple factors, including the number of cases of different vortex beams propagated and the degree of turbulence.

To show our results more comprehensibly, we calculated the normalized confusion matrix for different ℓ and z. **Figure 4B** shows a typical normalized confusion matrix from $\ell = 3$, $z = 40$ cm to $\ell = 3$, $z = 100$ cm. **Figure 4C** shows the normalized confusion matrix from $\ell = 1$, $z = 40$ cm to $\ell = 5$, $z = 45$ cm. The true propagation distance and the predicted propagation distance given by our deep learning algorithm are basically on a diagonal line. The result means almost all OAM modes and propagation distances tested are correctly identified, only two images with $\ell = 3$, $z = 80$ cm are predicted to be $\ell = 3$, $z = 75$ cm in **Figure 4B**, and only two images with $\ell = 2$, $z = 40$ cm are predicted to be $\ell = 2$, $z = 45$ cm in **Figure 4C**.

Finally, we want to emphasize that using classical methods (e.g., interferometer) to analyze the distorted intensity images in **Figure 2B** is quite challenging. However, according to training and test results, our deep learning model can accurately identify vortex beams with varying topological charges and propagation distances even under the influence of severe turbulence. This demonstrates that our approach has a high level of robustness and is very useful for practical applications. We note that our approach can be adapted to identify larger ℓ value with longer and more accurate transmission distance. However, due to the limitation of our equipment, such as the resolution of SLM and CCD, as well as the experimental error caused by the laboratory environment, we limit the size of our topological charges and the length of the propagation distance. We believe our designed deep learning neural network does not fundamentally limit the recognition accuracy, and its potential is far from being reached. Moreover, our scheme can be adapted to many vortex beam related applications. For instance, we can adapt our work to consider multiple types of vortex beams, and even the combination of them. Furthermore, the accurate identification of the propagation distance might be a novel technique for sensing related applications. Last but not least, our approach can be applied to free-space OAM communication, especially the demodulation system, to increase the robustness of the communication. We expect that by combining the unique characteristics of vortex beams with the advantages of the deep learning algorithm, more breakthroughs in vortex beams research can be made in the future.

CONCLUSION

Vortex beams have enormous potential due to their versatility and virtually unlimited quantum information resources. However, these beams are highly susceptible to undesirable experimental conditions such as propagation distance and phase distortions. In our work, we exploit the deep learning algorithm to identify a vortex beam's topological charge and propagation distance. Specifically, we focus on vortex beam with topological charge ℓ from 1 to 5, and the propagation distance z ranges from 40 to 100 cm. Additionally, we consider the effect of turbulence-induced in the propagation of the beam. We experimentally demonstrated that our customized deep learning algorithm could accurately identify the propagation distance and topological charge. Our work has important implications for the realistic implementation of OAM-based optical communications and sensing protocols in a turbulent environment.

DATA AVAILABILITY STATEMENT

The raw data supporting the conclusion of this article will be made available by the authors, without undue reservation.

AUTHOR CONTRIBUTIONS

The idea was conceived by R-BJ, CY, and HL. The experiment was designed by HL, YG, CY, and R-BJ. The experiment was performed by HL with help of R-BJ, CY, YG, Z-XY, CD, and W-HC. The theoretical description and numerical simulation were developed by YG, CY, and R-BJ. The deep learning process was carried out by HL. The data was analyzed by HL, YG, CY, and R-BJ. The project was supervised by R-BJ and CY. All authors contributed to the preparation of the manuscript.

FUNDING

This work is supported by the National Natural Science Foundations of China (Grant Nos.12074299, 91836102, 11704290) and by the Guangdong Provincial Key Laboratory (Grant No. GKLQSE202102).

ACKNOWLEDGMENTS

We thank Prof. Zhi-Yuan Zhou for the helpful discussion.

REFERENCES

1. Franke-Arnold S, Allen L, Padgett M. Advances in Optical Angular Momentum. *Laser Photon Rev* (2008) 2:299–313. doi:10.1002/lpor.200810007
2. Rubinsztein-Dunlop H, Forbes A, Berry MV, Dennis MR, Andrews DL, Mansuripur M, et al. Roadmap on Structured Light. *J Opt* (2016) 19: 013001. doi:10.1088/2040-8978/19/1/013001
3. Fickler R, Lapkiewicz R, Plick WN, Krenn M, Schaeff C, Ramelow S, et al. Quantum Entanglement of High Angular Momenta. *Science* (2012) 338:640–3. doi:10.1126/science.1227193
4. Bai Y, Lv H, Fu X, Yang Y. Vortex Beam: Generation and Detection of Orbital Angular Momentum [Invited]. *Chin. Opt. Lett.* (2022) 20:012601. doi:10.3788/col202220.012601
5. Friese MEJ, Nieminen TA, Heckenberg NR, Rubinsztein-Dunlop H. Optical Alignment and Spinning of Laser-Trapped Microscopic Particles. *Nature* (1998) 394:348–50. doi:10.1038/28566
6. Padgett M, Bowman R. Tweezers with a Twist. *Nat Photon* (2011) 5:343–8. doi:10.1038/nphoton.2011.81
7. Grier DG. A Revolution in Optical Manipulation. *Nature* (2003) 424:810–6. doi:10.1038/nature01935
8. Curtis JE, Grier DG. Structure of Optical Vortices. *Phys Rev Lett* (2003) 90: 133901. doi:10.1103/physrevlett.90.133901
9. Lavery MPJ, Speirits FC, Barnett SM, Padgett MJ. Detection of a Spinning Object Using Light's Orbital Angular Momentum. *Science* (2013) 341:537–40. doi:10.1126/science.1239936
10. Mair A, Vaziri A, Weihs G, Zeilinger A. Entanglement of the Orbital Angular Momentum States of Photons. *Nature* (2001) 412:313–6. doi:10.1038/35085529
11. Molina-Terriza G, Torres JP, Torner L. Twisted Photons. *Nat Phys* (2007) 3: 305–10. doi:10.1038/nphys607
12. Magaña-Loaiza OS, Boyd RW. Quantum Imaging and Information. *Rep Prog Phys* (2019) 82:124401. doi:10.1088/1361-6633/ab5005
13. Ding D-S, Zhang W, Zhou Z-Y, Shi S, Xiang G-Y, Wang X-S, et al. Quantum Storage of Orbital Angular Momentum Entanglement in an Atomic Ensemble. *Phys Rev Lett* (2015) 114:050502. doi:10.1103/physrevlett.114.050502
14. Langford NK, Dalton RB, Harvey MD, O'Brien JL, Pryde GJ, Gilchrist A, et al. Measuring Entangled Qutrits and Their Use for Quantum Bit Commitment. *Phys Rev Lett* (2004) 93:053601. doi:10.1103/physrevlett.93.053601
15. Zhang P, Ren X-F, Zou X-B, Liu B-H, Huang Y-F, Guo G-C. Demonstration of One-Dimensional Quantum Random Walks Using Orbital Angular Momentum of Photons. *Phys Rev A* (2007) 75:052310. doi:10.1103/physreva.75.052310
16. Nagali E, Sciarrino F, De Martini F, Marrucci L, Piccirillo B, Karimi E, et al. Quantum Information Transfer from Spin to Orbital Angular Momentum of Photons. *Phys Rev Lett* (2009) 103:013601. doi:10.1103/physrevlett.103.013601
17. Zhang P, Jiang Y, Liu R-F, Gao H, Li H-R, Li F-L. Implementing the Deutsch's Algorithm with Spin-Orbital Angular Momentum of Photon without Interferometer. *Opt Commun* (2012) 285:838–41. doi:10.1016/j.optcom.2011.11.024
18. Bozinovic N, Yue Y, Ren Y, Tur M, Kristensen P, Huang H, et al. Terabit-scale Orbital Angular Momentum Mode Division Multiplexing in Fibers. *Science* (2013) 340:1545–8. doi:10.1126/science.1237861
19. Wang J, Yang J-Y, Fazal IM, Ahmed N, Yan Y, Huang H, et al. Terabit Free-Space Data Transmission Employing Orbital Angular Momentum Multiplexing. *Nat Photon* (2012) 6:488–96. doi:10.1038/nphoton.2012.138
20. Ouyang X, Xu Y, Xian M, Feng Z, Zhu L, Cao Y, et al. Synthetic Helical Dichroism for Six-Dimensional Optical Orbital Angular Momentum Multiplexing. *Nat Photon* (2021) 15:901–7. doi:10.1038/s41566-021-00880-1
21. Zhang M, Ren H, Ouyang X, Jiang M, Lu Y, Hu Y, et al. Nanointerferometric Discrimination of the Spin-Orbit Hall Effect. *ACS Photon* (2021) 8:1169–74. doi:10.1021/acsphotonics.1c00087
22. Wang L, Jiang X, Zou L, Zhao S. Two-dimensional Multiplexing Scheme Both with Ring Radius and Topological Charge of Perfect Optical Vortex Beam. *J Mod Opt* (2018) 66:87–92. doi:10.1080/09500340.2018.1512669
23. Molina-Terriza G, Torres JP, Torner L. Management of the Angular Momentum of Light: Preparation of Photons in Multidimensional Vector States of Angular Momentum. *Phys Rev Lett* (2001) 88:013601. doi:10.1103/physrevlett.88.013601
24. Rodenburg B, Lavery MPJ, Malik M, O'Sullivan MN, Mirhosseini M, Robertson DJ, et al. Influence of Atmospheric Turbulence on States of Light Carrying Orbital Angular Momentum. *Opt Lett* (2012) 37:3735. doi:10.1364/ol.37.003735
25. Rodenburg B, Mirhosseini M, Malik M, Magaña-Loaiza OS, Yanakas M, Maher L, et al. Simulating Thick Atmospheric Turbulence in the Lab with Application to Orbital Angular Momentum Communication. *New J Phys* (2014) 16:033020. doi:10.1088/1367-2630/16/3/033020
26. Paterson C. Atmospheric Turbulence and Orbital Angular Momentum of Single Photons for Optical Communication. *Phys Rev Lett* (2005) 94:153901. doi:10.1103/physrevlett.94.153901
27. Tyler GA, Boyd RW. Influence of Atmospheric Turbulence on the Propagation of Quantum States of Light Carrying Orbital Angular Momentum. *Opt Lett* (2009) 34:142. doi:10.1364/ol.34.000142
28. Ndagano B, Mphuthi N, Milione G, Forbes A. Comparing Mode-Crosstalk and Mode-dependent Loss of Laterally Displaced Orbital Angular Momentum and Hermite-Gaussian Modes for Free-Space Optical Communication. *Opt Lett* (2017) 42:4175. doi:10.1364/ol.42.004175
29. Krenn M, Fickler R, Fink M, Handsteiner J, Malik M, Scheidl T, et al. Communication with Spatially Modulated Light through Turbulent Air across vienna. *New J Phys* (2014) 16:113028. doi:10.1088/1367-2630/16/11/113028
30. Cox MA, Maqondo L, Kara R, Milione G, Cheng L, Forbes A. The Resilience of Hermite- and Laguerre-Gaussian Modes in Turbulence. *J Lightwave Technol* (2019) 37:3911–7. doi:10.1109/jlt.2019.2905630
31. Courtial J, Dholakia K, Robertson DA, Allen L, Padgett MJ. Measurement of the Rotational Frequency Shift Imparted to a Rotating Light Beam Possessing Orbital Angular Momentum. *Phys Rev Lett* (1998) 80:3217–9. doi:10.1103/physrevlett.80.3217
32. Zhang W, Qi Q, Zhou J, Chen L. Mimicking Faraday Rotation to Sort the Orbital Angular Momentum of Light. *Phys Rev Lett* (2014) 112:153601. doi:10.1103/physrevlett.112.153601
33. Padgett M, Arlt J, Simpson N, Allen L. An experiment to Observe the Intensity and Phase Structure of Laguerre-Gaussian Laser Modes. *Am J Phys* (1996) 64: 77–82. doi:10.1119/1.18283
34. Yongxin L, Hua T, Jixiong P, Baida L. Detecting the Topological Charge of Vortex Beams Using an Annular triangle Aperture. *Opt Laser Tech* (2011) 43: 1233–6. doi:10.1016/j.optlastec.2011.03.015
35. Karimi E, Piccirillo B, Nagali E, Marrucci L, Santamato E. Efficient Generation and Sorting of Orbital Angular Momentum Eigenmodes of Light by Thermally Tuned Q-Plates. *Appl Phys Lett* (2009) 94:231124. doi:10.1063/1.3154549
36. Shin H-C, Roth HR, Gao M, Lu L, Xu Z, Nogues I, et al. Deep Convolutional Neural Networks for Computer-Aided Detection: CNN Architectures, Dataset Characteristics and Transfer Learning. *IEEE Trans Med Imaging* (2016) 35: 1285–98. doi:10.1109/tmi.2016.2528162
37. Quattoni A, Collins M, Darrell T. Transfer Learning for Image Classification with Sparse Prototype Representations. In: IEEE Conference on Computer Vision and Pattern Recognition. IEEE (2008). doi:10.1109/cvpr.2008.4587637
38. Taigman Y, Yang M, Ranzato M, Wolf L. Deepface: Closing the gap to Human-Level Performance in Face Verification. In: Proceedings of the IEEE Conference on Computer Vision and Pattern Recognition. Columbus: CVPR (2014). doi:10.1109/cvpr.2014.220
39. Melnikov AA, Poulsen Nautrup H, Krenn M, Dunjko V, Tiersch M, Zeilinger A, et al. Active Learning Machine Learns to Create New Quantum Experiments. *Proc Natl Acad Sci USA* (2018) 115:1221–6. doi:10.1073/pnas.1714936115
40. Doster T, Watnik AT. Machine Learning Approach to OAM Beam Demultiplexing via Convolutional Neural Networks. *Appl Opt* (2017) 56: 3386. doi:10.1364/ao.56.003386
41. You C, Quiroz-Juárez MA, Lambert A, Bhusal N, Dong C, Perez-Leija A, et al. Identification of Light Sources Using Machine Learning. *Appl Phys Rev* (2020) 7:021404. doi:10.1063/1.5133846
42. Bhusal N, Lohani S, You C, Hong M, Fabre J, Zhao P, et al. Spatial Mode Correction of Single Photons Using Machine Learning. *Adv Quan Tech* (2021) 4:2000103. doi:10.1002/qute.202000103

43. Gibson G, Courtial J, Padgett MJ, Vasnetsov M, Pas'ko V, Barnett SM, et al. Free-space Information Transfer Using Light Beams Carrying Orbital Angular Momentum. *Opt Express* (2004) 12:5448. doi:10.1364/opex.12.005448
44. Liao K, Chen Y, Chen Y, Yu Z, Hu X, Wang X, et al. All-optical Computing Based on Convolutional Neural Networks. *Opto-Electron Adv* 4:200060 (2021). doi:10.29026/oea.2021.200060
45. Bhusal N, Hong M, Miller NR, Quiroz-Juarez MA, de J Leon-Montiel R, You C, et al. *Smart Quantum Statistical Imaging beyond the Abbe-Rayleigh Criterion*. arXiv:2110.05446 (2021).
46. Zhang C, Zhao Y. Orbital Angular Momentum Nondegenerate index Mapping for Long Distance Transmission. *IEEE Trans Wireless Commun* (2019) 18:5027–36. doi:10.1109/twc.2019.2927672
47. Krenn M, Handsteiner J, Fink M, Fickler R, Ursin R, Malik M, et al. Twisted Light Transmission over 143 Km. *Proc Natl Acad Sci USA* (2016) 113:13648–53. doi:10.1073/pnas.1612023113
48. Zhao SM, Leach J, Gong LY, Ding J, Zheng BY. Aberration Corrections for Free-Space Optical Communications in Atmosphere Turbulence Using Orbital Angular Momentum States. *Opt Express* (2011) 20:452. doi:10.1364/oe.20.000452
49. Zhou ZY, Zhu ZH, Liu SL, Liu SK, Wang K, Shi S, et al. Generation and Reverse Transformation of Twisted Light by Spatial Light Modulator. arXiv:1612.04482 (2016).
50. Collins SA. Lens-System Diffraction Integral Written in Terms of Matrix Optics. *J Opt Soc Am* (1970) 60:1168–77. doi:10.1364/JOSA.60.001168
51. Bos JP, Roggemann MC, Rao Gudimetla VS. Anisotropic Non-kolmogorov Turbulence Phase Screens with Variable Orientation. *Appl Opt* (2015) 54:2039–45. doi:10.1364/AO.54.002039
52. Glindemann A, Lane RG, Dainty JC. Simulation of Time-Evolving Speckle Patterns Using Kolmogorov Statistics. *J Mod Opt* (1993) 40:2381–8. doi:10.1080/09500349314552401
53. He K, Zhang X, Ren S, Sun J. Deep Residual Learning for Image Recognition. In: Proceedings of the IEEE Conference on Computer Vision and Pattern Recognition. Las Vegas: CVPR (2016). doi:10.1109/cvpr.2016.90
54. Kingma DP, Ba J. *Adam: A Method for Stochastic Optimization*. arXiv:1412.6980 (2014).
55. Fernando B, Habrard A, Sebban M, Tuytelaars T. *Subspace Alignment for Domain Adaptation*. arXiv:1409.5241 (2014).
56. Patel VM, Gopalan R, Li R, Chellappa R. Visual Domain Adaptation: A Survey of Recent Advances. *IEEE Signal Process Mag* (2015) 32:53–69. doi:10.1109/msp.2014.2347059
57. Krizhevsky A, Sutskever I, Hinton GE. ImageNet Classification with Deep Convolutional Neural Networks. *Commun ACM* (2017) 60:84–90. doi:10.1145/3065386
58. Liu Z, Yan S, Liu H, Chen X. Superhigh-resolution Recognition of Optical Vortex Modes Assisted by a Deep-Learning Method. *Phys Rev Lett* (2019) 123:183902. doi:10.1103/physrevlett.123.183902
59. Zhang Z, Sabuncu MR. Generalized Cross Entropy Loss for Training DeepNeural Networks with Noisy Labels. In: Proceedings of the 32nd International Conference on Neural Information Processing Systems. NY, USA: Red HookCurran Associates Inc. (2018). p. 8792–802.

Conflict of Interest: The authors declare that the research was conducted in the absence of any commercial or financial relationships that could be construed as a potential conflict of interest.

Publisher's Note: All claims expressed in this article are solely those of the authors and do not necessarily represent those of their affiliated organizations, or those of the publisher, the editors and the reviewers. Any product that may be evaluated in this article, or claim that may be made by its manufacturer, is not guaranteed or endorsed by the publisher.

frontiers in Physics

ORIGINAL RESEARCH
published: 14 March 2022
doi: 10.3389/fphy.2022.848624

Polarization-Entangled Two-Photon Absorption in Inhomogeneously Broadened Ensembles

Frank Schlawin [1,2]*

[1]Max Planck Institute for the Structure and Dynamics of Matter, Hamburg, Germany, [2]The Hamburg Centre for Ultrafast Imaging, Hamburg, Germany

Entangled photons are promising candidates for a variety of novel spectroscopic applications. In this paper, we simulate two-photon absorption (TPA) of entangled photons in a molecular ensemble with inhomogeneous broadening. We compare our results with a homogeneously broadened case and comment on the consequences for the possible quantum enhancement of TPA cross sections. We find that, while there are differences in the TPA cross section, this difference always remains small and of the order unity. We further consider the impact of the polarization degrees of freedom and carry out the orientational average of a model system Hamiltonian. We find that certain molecular geometries can give rise to a substantial polarization dependence of the entangled TPA rate. This effect can increase the TPA cross section by up to a factor of five.

Keywords: entangled photons, two-photon absorption, quantum correlations, inhomogeneous broadening, polarization entanglement

OPEN ACCESS

Edited by:
Roberto de J. León-Montiel, National Autonomous University of Mexico, Mexico

Reviewed by:
Jiri Svozilik, Palacký University Olomouc, Czechia
Mike Mazurek, National Institute of Standards and Technology (NIST), United States

***Correspondence:**
Frank Schlawin
frank.schlawin@mpsd.mpg.de

Specialty section:
This article was submitted to Quantum Engineering and Technology, a section of the journal Frontiers in Physics

Received: *04 January 2022*
Accepted: *28 January 2022*
Published: *14 March 2022*

Citation:
Schlawin F (2022) Polarization-Entangled Two-Photon Absorption in Inhomogeneously Broadened Ensembles. Front. Phys. 10:848624. doi: 10.3389/fphy.2022.848624

1 INTRODUCTION

Entangled photons have been identified as promising new tools for spectroscopic or imaging applications [1–7]. Their strong quantum correlations could circumvent certain classical Fourier uncertainties and thus enhance the sensing capabilities of optical measurements [8–16]. The detection of quantum correlations could also provide new spectroscopic information [17–25], and the use of quantum light in interferometric setups promises additional control knobs to analyze spectroscopic information [26–29] as well as access to out-of-time correlations [30]. The main driving force behind this development of entangled photon spectroscopy, however, is the linear scaling of nonlinear optical signals such as the two-photon absorption (TPA) rate with the incident photon flux [31–34], which could enable measurements on photosensitive samples at reduced photon numbers. This linear scaling has been observed conclusively in atomic samples [33, 35, 36]. Similar experiments in molecular samples, however, have resulted in widely differing estimates for the entangled two-photon absorption (ETPA) cross section σ_e [37–47]. The reported values range from $\sigma_e \sim 10^{-17}\,\mathrm{cm}^2$ [37] or $10^{-21}\,\mathrm{cm}^2$ [43] to $\leq 10^{-23}\,\mathrm{cm}^2$ [46, 47].

In theoretical work, recent analyses predict a very small enhancement of the ETPA cross section due to spectral entanglement [48, 49]. The key assumption in these publications is that molecular resonances are broadened much more strongly than their atomic counterparts. As a consequence, spectral quantum correlations cannot enhance the absorption probability in the same way as in atomic samples. This would imply that the large absorption cross sections mentioned above cannot be explained by ETPA, and have to be attributed to other processes that remain to be clarified. In contrast, another study by Kan et al. alleges that ETPA takes place into final states with much weaker broadening [50], such that large enhancements due to quantum correlations become possible. Here

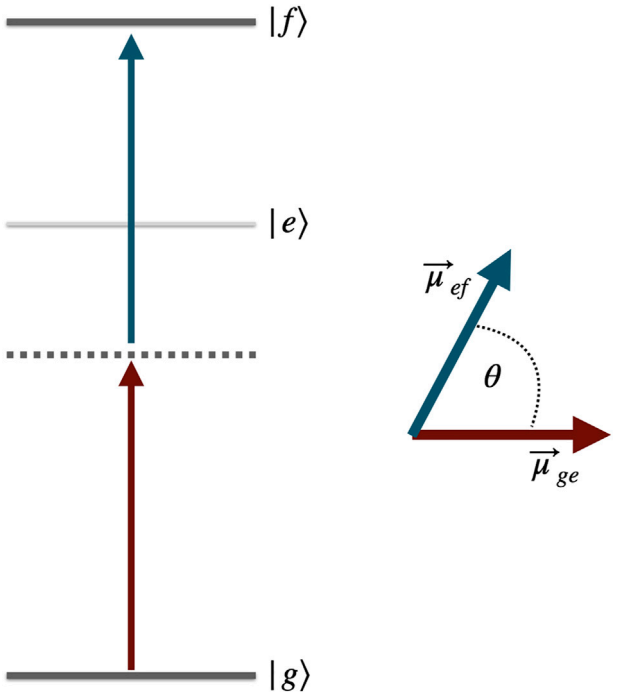

FIGURE 1 | Level scheme and dipole orientation considered in this paper: We consider two-photon excitation from the ground state $|g\rangle$ to the final state $|f\rangle$. The intermediate state $|e\rangle$ is far-off-resonant from the carrier frequencies of the two photons. The dipoles between ground and intermediate state, $\vec{\mu}_{ge}$, and between intermediate and final state, $\vec{\mu}_{ef}$, form a relative angle θ.

we investigate whether these two scenarios can give rise to vastly different absorption cross sections. In particular, we consider ETPA in an ensemble of inhomogeneously broadened molecules, where sharp absorption resonances are distributed randomly within a certain frequency distribution (see **Figure 2**). This enables us to interpolate between these two scenarios mentioned above. We will investigate whether strongly enhanced absorption in a subset of molecules that can be excited resonantly can overcompensate the reduced absorption probabilities in the remaining molecules.

In addition, we will scrutinize the impact of the polarization degrees of freedom on the ETPA cross section. By carrying out an orientational average of the molecular dipoles, we will explore how the relative orientation of the two dipoles affects the ETPA process. A recent study [43] detected no discernible dependence on the photon polarization. Here we show that this is true only for certain molecular dipole orientations.

2 THE MODEL

We consider the interaction of broadband entangled photons with matter. For a quantum light field propagating in a fixed spatial direction (without loss of generality, we here consider the z-direction), the electric field operator in the interaction picture with respect to the field Hamiltonian reads [51]

$$\mathbf{E}(z,t) = \mathbf{E}^{(+)}(z,t) + \mathbf{E}^{(-)}(z,t), \tag{1}$$

with the positive frequency component

$$\mathbf{E}^{(+)}(z,t) = i\sum_{\nu=1,2}\hat{e}_\nu\int_0^\infty\frac{d\omega}{2\pi}\sqrt{\frac{\hbar\omega}{2\epsilon_0 n A_0}}e^{i\omega(z/c-t)}a_\nu(\omega) \tag{2}$$

$$= \sum_{\nu=1,2}\hat{e}_\nu E_\nu^{(+)}(z,t) \tag{3}$$

and $E^{(-)}$ its hermitian conjugate. Here, ϵ_0 denotes the vacuum permittivity, and A_0 is the quantization area perpendicular to the propagation direction of the field. The photon annihilation and creation operators obey the usual permutation relations $[a_\nu(\nu), a^\dagger_{\nu'}(\omega')] = 2\pi\delta_{\nu,\nu'}\delta(\omega-\omega')$. The polarization vector $\hat{e}_\nu$ distinguishes horizontal or vertical polarization. In the second line, we define the scalar fields E_ν. In the following, we will consider a sample, which is placed at the origin of our coordinate system and set $z = 0$.

We will investigate the ETPA probability of a multilevel system with ground state g, an off-resonant intermediate states e, and a final state f. This is shown in **Figure 1**. The probability to excite the final state f can be derived with perturbation theory with respect to the light-matter interaction Hamiltonian, which reads within the rotating-wave approximation for a sample placed at the origin of our coordinate system

$$H_{int} = \mathbf{E}^{(+)}(t)\cdot\mathbf{V}^{(-)}(t) + h.c. \tag{4}$$

Here, $\mathbf{V}^{(-)}(t)$ denotes the negative frequency component of the dipole operator, i.e. it creates a molecular excitation, and we have dropped the spatial dependence of the operators. A detailed account for the derivation of the ETPA probability can be found, e.g., in [49, 52]. Here, we only present the final result which, neglecting the polarization degrees of freedom at first, reads

$$P^{\mathrm{TPA}}_{\mathrm{hom}} = \sigma^{(2)}\frac{\gamma_{fg}}{A_0^2}\Re\int\frac{d\omega'}{2\pi}\int\frac{d\omega'}{2\pi}\int\frac{d\omega''}{2\pi} \times\frac{\langle a^\dagger(\omega')a^\dagger(\omega+\omega''-\omega')a(\omega)a(\omega'')\rangle}{\gamma_{fg}-i\omega_{fg}+i\omega+i\omega''}, \tag{5}$$

with the classical TPA cross section given by

$$\sigma^{(2)} = \left(\frac{\omega_0}{\hbar\epsilon_0 nc}\right)^2\frac{1}{2\gamma_{fg}}\left|\frac{d_{ef}d_{ge}}{\omega_{eg}-\omega_0}\right|^2. \tag{6}$$

Here, we have defined the transition frequency to the final state of the molecule, ω_{fg}, as well as the inverse lifetime γ_{fg}. The intermediate state transition frequency is denoted ω_{eg}, and d_{ge} and d_{ef} are the dipole matrix elements connecting ground and intermediate, or intermediate and final states, respectively. In **Eq. 5**, we also included the so-called entanglement area A_0, which could be a function of the entanglement of the two-photon state [44]. Here, we will not consider this effect and treat A_0 as a constant. We further introduced the four-point correlation function of the field in the numerator of the second line of **Eq. 5**. It is evaluated with respect to the initial state of the light field, which we will specify later in **Section 2.3**. In writing **Eq. 5**, we require the intermediate states to be far off-resonant from the

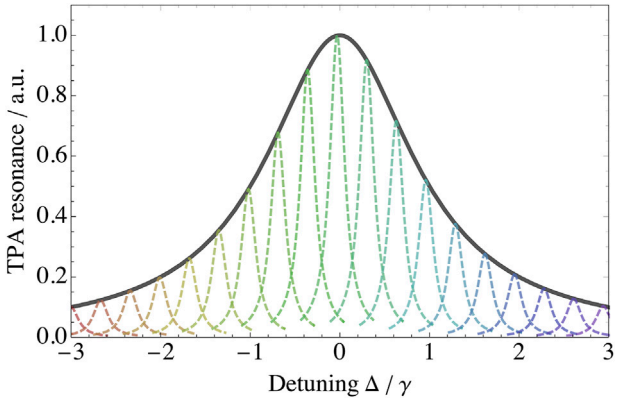

FIGURE 2 | Inhomogeneously broadened two-photon absorption resonance, $(\Delta^2+\gamma^2)^{-1}$, vs. the detuning $\Delta=\omega_{fg}^{(0)}-\omega$. The gray solid line corresponds to an homogenously broadened ensemble, whereas the small dashed Lorentzians indicate an inhomogeneously broadened ensemble which creates the same broad absorption feature.

entangled photons' centre frequency ω_0. If this condition is violated the intermediate state resonances cannot be taken out of the frequency integrations and need to be considered separately [2]. In this resonant regime, which will not be considered here, we could already show how quantum correlations can enhance the absorption probability [53–55].

2.1 Inhomogeneous Broadening

Two-photon transitions in the presence of inhomogeneous broadening were already discussed in [56]. Here we model it by assuming that the resonance of the final state ω_{fg} is distributed around a central value $\omega_{fg}^{(0)}$ with a Gaussian distribution with width σ_D, i.e.

$$p\left(\omega_{fg}\right)=\frac{1}{\sigma_D\sqrt{2\pi}}e^{-\left(\omega_{fg}-\omega_{fg}^{(0)}\right)^2/\left(2\sigma_D^2\right)}. \tag{7}$$

The TPA probability is then given by the average with respect to this ensemble,

$$P_{\text{inh}}^{\text{TPA}}=\langle P^{\text{TPA}}\rangle_{\text{ensemble}} \tag{8}$$

$$=\int d\omega_{fg}\; p\left(\omega_{fg}\right)P^{\text{TPA}}\left(\omega_{fg}\right), \tag{9}$$

where $P^{\text{TPA}}(\omega_{fg})$ is given by **Eq. 5** at frequency ω_{fg}. This situation is illustrated is **Figure 2**, where we plot the two-photon resonance in **Eq. 5**, i.e., $\Re\left(\gamma_{fg}-i\omega_{fg}+i\omega\right)$ vs. the detuning $\Delta=\omega_{fg}^{(0)}-\omega$. In an inhomogeneously broadened ensemble, the broad resonance is in fact composed of the incoherent mixture of much more narrow resonances of the ensemble constituents. We note that the role of the Lorentzian width γ_{fg} changes between the homogeneously and inhomogeneously broadened samples. In the former case, **Eq. 5**, γ_{fg} denotes the width that one would measure in a spectroscopic experiment. In the latter case, it is the narrow linewidth of an individual molecule, but experiments would detect the much broader distribution described by **Eq. 8**. To distinguish the two situations, we will call the Lorentzian width in the inhomogeneously broadened sample the intrinsic width of the resonance, γ_{inh} in the following. In contrast, we will call it the homogeneous width γ_{hom} in the homogeneously broadened case.

2.2 Orientational Average

We next discuss how to carry out an orientational average of the molecular absorption. To this end, the dipole elements in **Eq. 5** have to be treated as vectors, i.e. $d_{ij}\to\vec{d}_{ij}$. More specifically, we consider dipole vectors in the molecular reference frame,

$$\vec{d}_{eg}=d_{eg}\begin{pmatrix}1\\0\\0\end{pmatrix},\qquad \vec{d}_{ef}=d_{ef}\begin{pmatrix}\cos\theta\\\sin\theta\\0\end{pmatrix}. \tag{10}$$

We further take the polarization of the light fields into account, see **Equation 2**. We then generalize **Eq. 5** to

$$P_{\text{hom}}^{\text{TPA}}=\sum_{\nu_1,\nu_2,\nu_3,\nu_4}\sigma^{(2)}_{\nu_1,\nu_2,\nu_3,\nu_4}\frac{\gamma_{fg}}{A_0^2}\Re\int\frac{d\omega'}{2\pi}\int\frac{d\omega'}{2\pi}\int\frac{d\omega''}{2\pi}\times\frac{\langle a^\dagger_{\nu_1}(\omega')a^\dagger_{\nu_2}(\omega+\omega''-\omega')a_{\nu_4}(\omega)a_{\nu_3}(\omega'')\rangle}{\gamma_{fg}-i\omega_{fg}+i\omega+i\omega''}, \tag{11}$$

where the TPA tensor is given by

$$\sigma^{(2)}_{\nu_1,\nu_2,\nu_3,\nu_4}=\left(\frac{\omega_0}{\hbar\epsilon_0 nc}\right)^2\frac{1}{2\gamma_{fg}}\left\langle\frac{\left(\vec{d}^{\,\star}_{ge}\cdot\hat{e}_{\nu_1}\right)\left(\vec{d}^{\,\star}_{ef}\cdot\hat{e}_{\nu_2}\right)}{\omega_{eg}-\omega_0}\,\frac{\left(\vec{d}_{ge}\cdot\hat{e}_{\nu_3}\right)\left(\vec{d}_{ef}\cdot\hat{e}_{\nu_4}\right)}{\omega_{e'g}-\omega_0}\right\rangle_{\text{ens}}. \tag{12}$$

Here, we denote $\langle\ldots,\rangle_{\text{ens}}$ the orientational average which accounts for the random orientation of the molecules in the sample with respect to the lab frame. To evaluate this average, we have to transform from the lab frame into the molecular frame. This orientational average was first carried out in [57]. The application to nonlinear spectroscopy can be found, e.g., in [58]. The result is that we can straightforwardly relate the dipole elements in the lab frame with the corresponding dipole vectors in the molecular frame using the transformation

$$\left\langle\left(\vec{d}^{\,\star}_{ge}\cdot\hat{e}_{\nu_1}\right)\left(\vec{d}^{\,\star}_{ef}\cdot\hat{e}_{\nu_2}\right)\left(\vec{d}_{ge'}\cdot\hat{e}_{\nu_3}\right)\left(\vec{d}_{e'f}\cdot\hat{e}_{\nu_4}\right)\right\rangle_{\text{ens}}=\sum_{\alpha_1,\alpha_2,\alpha_3,\alpha_4}T^{(4)}_{\nu_1,\nu_2,\nu_3,\nu_4;\alpha_1,\alpha_2,\alpha_3,\alpha_4}d^{\alpha_1}_{ge}d^{\alpha_2}_{ef}d^{\alpha_3}_{ge'}d^{\alpha_4}_{e'f}, \tag{13}$$

where the indices $\alpha_i=x,y,z$ label the components of the dipole operator in the molecular frame. The transformation tensor is given by

$$T^{(4)}_{\nu_1,\nu_2,\nu_3,\nu_4;\alpha_1,\alpha_2,\alpha_3,\alpha_4}=\frac{1}{30}\left(\delta_{\nu_4,\nu_3}\delta_{\nu_2,\nu_1},\;\delta_{\nu_4,\nu_2}\delta_{\nu_3,\nu_1},\;\delta_{\nu_4,\nu_1}\delta_{\nu_3,\nu_1}\right)\times\begin{pmatrix}4&-1&-1\\-1&4&-1\\-1&-1&4\end{pmatrix}\begin{pmatrix}\delta_{\alpha_4,\alpha_3}\delta_{\alpha_2,\alpha_1}\\\delta_{\alpha_4,\alpha_2}\delta_{\alpha_3,\alpha_1}\\\delta_{\alpha_4,\alpha_1}\delta_{\alpha_3,\alpha_2}\end{pmatrix}. \tag{14}$$

2.3 The Field Correlation Function

We finally have to evaluate the field correlation function in **Eqs 5**, **11**, respectively. For an initial two-photon state, which we will denote $|\psi\rangle$, this function factorizes as

$$\begin{aligned}&\langle a^\dagger_{\nu_1}(\omega_1)a^\dagger_{\nu_2}(\omega_2)a_{\nu_4}(\omega_4)a_{\nu_3}(\omega_3)\rangle\\&=\langle\psi|a^\dagger_{\nu_1}(\omega_1)a^\dagger_{\nu_2}(\omega_2)|0\rangle\langle 0|a_{\nu_4}(\omega_4)a_{\nu_3}(\omega_3)|\psi\rangle\\&=\Psi^*_{\nu_1,\nu_2}(\omega_1,\omega_2)\Psi_{\nu_3,\nu_4}(\omega_3,\omega_4).\end{aligned}\tag{15}$$

Here, we have inserted an identity in between $a^\dagger_{\nu_2}(\omega_2)$ and $a_{\nu_4}(\omega_4)$. For a two-photon state, the only non-vanishing contribution stems from the vacuum. In our discussion of the inhomogeneous broadening, where we do not account for the polarization degree of freedom, we simply drop the indices ν_i. With the entangled field propagating along the z-direction, see **Eq. 2**, we consider the horizontal polarization to be along the x-direction and the vertical polarization along the y-direction. In the third line, we defined the function $\Psi_{\nu,\nu'}(\omega,\omega')=\langle 0|a_\nu(\omega)a_{\nu'}(\omega')|\psi\rangle$, which is often called the two-photon wavefunction. Its absolute square is referred to as the joint spectral intensity. As explained in detail in [52], in the situation described by **Eq. 5** where the intermediate states are far off-resonant and can be subsumed into $\sigma^{(2)}$, the marginal of the two-photon wavefunction along the anti-diagonal is what is relevant for the TPA process, and we can write **Eq. 5** as

$$P^{\mathrm{TPA}}_{\mathrm{hom}}=\sigma^{(2)}\frac{\gamma_{fg}}{A_0^2}\Re\int\frac{dx}{2\pi}\frac{\gamma_{fg}|K_\Psi(x)|^2}{\omega_{fg}^2+(\Delta+x)^2},\tag{16}$$

where the marginal is given by

$$K_\Psi(x)=\int\frac{dz}{2\pi}\Psi_{\nu,\nu'}(\omega_0+z,\omega_0+x-z).\tag{17}$$

We further defined the detuning $\Delta=\omega_{fg}-2\omega_0$. In the homogeneously broadened case, we simply set this to zero (i.e. we assume that the entangled pair is resonant with the transition), but in the inhomogeneous case, this detuning will be weighted by the ensemble's frequency distribution **(7)** below. In this paper, we will focus on bi-Gaussian two-photon wavefunctions, i.e. we write

$$\psi(\omega,\omega')=\frac{1}{\sqrt{2}}\left(\frac{\sigma_N\sigma_B}{2\pi}\right)^{-1/2}e^{-(\omega-\omega')^2/(4\sigma_N^2)}e^{-(\omega+\omega'-2\omega_0)^2/(4\sigma_B^2)},\tag{18}$$

where σ_N is the spectral width of the individual photon wavepackets and σ_B is the width of the sum frequency $\omega+\omega'$. Please note the factor $1/\sqrt{2}$ in front of the wavefunction, which accounts for the fact that in the case of indistinguishable photons we have the normalization $\langle\psi|\psi\rangle=2\int d\omega\int d\omega'|\Psi(\omega,\omega')|^2/(2\pi)^2=1$. In a strongly entangled state, we will typically have $\sigma_N\gg\sigma_B$. This regime is dominated by strong frequency anti-correlations between the entangled photons, as well as strong correlations in their respective arrival times [2]. We further write the full two-photon wavefunction as

$$|\psi\rangle=\int d\omega\int d\omega'\ \psi(\omega,\omega')f\left(a^\dagger_\nu,a^\dagger_{\nu'}\right)|0\rangle,\tag{19}$$

where we consider specifically the two cases

$$f_1\left(a^\dagger_\nu,a^\dagger_{\nu'}\right)=\sqrt{2}a^\dagger_H(\omega)a^\dagger_V(\omega'),\tag{20}$$

$$f_2\left(a^\dagger_\nu,a^\dagger_{\nu'}\right)=a^\dagger_H(\omega)a^\dagger_H(\omega')\tag{21}$$

$$f_3\left(a^\dagger_\nu,a^\dagger_{\nu'}\right)=\frac{1}{\sqrt{2}}\left(a^\dagger_H(\omega)a^\dagger_H(\omega')+e^{i\phi}a^\dagger_V(\omega)a^\dagger_V(\omega')\right)\tag{22}$$

Please not that the factor $\sqrt{2}$ is included in **Eq. 20** to ensure normalization with respect to the frequency wavefunction **(18)**. In the first two cases, f_1 and f_2, the two-photon state is not polarization entangled, as **Eq. 18** is symmetric with respect to the exchange of its frequency arguments. In the latter case, the state is polarization entangled. We note that, as pointed out in [52], within the current model the molecular response is symmetric with respect to the exchange of the frequency arguments in **Eq. 15**, because any photon can excite either the $g\rightarrow e$ or the $e\rightarrow f$ transition. Consequently, even if the initial two-photon frequency wavefunction $\Psi(\omega,\omega')$ is not symmetric (as is the case, e.g., for type-II downconversion), the correlation function **(15)** selects the symmetric superposition $\sim\Psi(\omega,\omega')+\Psi(\omega',\omega)$. As a consequence, a photonic singlet state of the form $(|H_s\rangle|V_i\rangle-|V_s\rangle|H_i\rangle)/\sqrt{2}$ will not give rise to a TPA signal within the current model due to the destructive interference between the two terms. This situation would change, for instance, in the presence of near-resonant intermediate states or any other process that breaks the abovementioned symmetry between the $g\rightarrow e$ and $e\rightarrow f$ transitions.

3 RESULTS

3.1 Inhomogeneous Broadening

We now compare how inhomogeneously broadened ensembles can affect the two-photon absorption probability. In this part of our investigation, we will neglect the polarization degrees of freedom at first. For simplicity, we divide the ETPA probability, **Eq. 5**, by its constant prefactor $\sigma^{(2)}\gamma_{fg}/A_0^2$. For each combination of intrinsic linewidth γ_{inh} and inhomogeneous broadening σ_D, we calculate the full width at half maximum of the f-state distribution as shown in **Figure 3A**. We also calculate the ETPA probability from **Eq. 8**. As shown in **Figure 3B**, its behaviour inversely follows the broadening of the f-state in the sense that a broader f-distribution in panel (a) results in a reduced ETPA probability. There is however a noticeable asymmetry between the two plots. The ETPA probability appears to be reduced more rapidly with increasing intrinsic linewidth γ_{inh} compared to an increase of the inhomogeneous broadening σ_D. This behaviour could be a consequence of the photonic entanglement and in the following we investigate it more closely.

To compare ETPA in homogeneously and inhomogeneously broadened ensembles, we define the ratio between the absorption probability in an inhomogeneously broadened sample, **Eq. 8**, and in a homogeneously broadened sample, **Eq. 5**,

$$r_{\mathrm{rel}}\equiv\frac{P^{\mathrm{TPA}}_{\mathrm{inh}}(\gamma_{\mathrm{inh}},\sigma_D)}{P^{\mathrm{TPA}}_{\mathrm{hom}}(\gamma_{\mathrm{hom}})}.\tag{23}$$

where we use as homogeneous broadening γ_{hom} the width of the f-state distribution, which we determined in **Figure 3A**. We note, however, that the convolution of an intrinsic Lorentzian broadening with a Gaussian as in **Eq. 8** gives rise to a Voigt line profile. This is

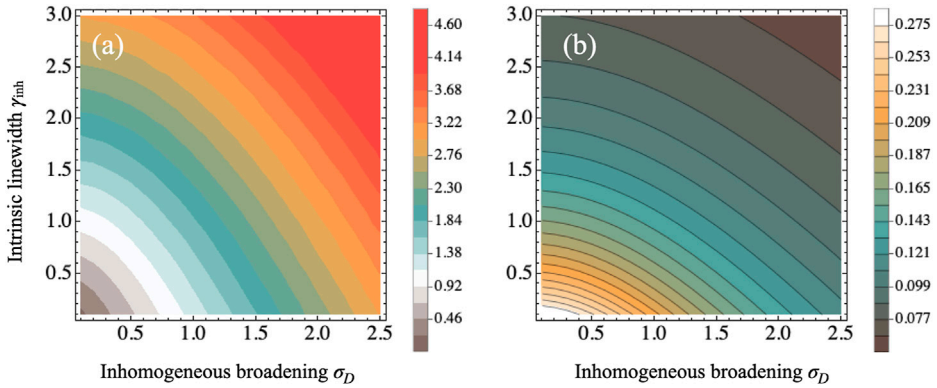

FIGURE 3 | (A) Full width half maximum of the *f*-state resonance as a function of the intrinsic linewidth γ_{inh} and the inhomogeneous broadening σ_D. **(B)** ETPA probability according to **Eq. 8** in units of $\sigma^{(2)}\gamma_{fg}/A_0^2$ as a function of the intrinsic linewidth γ_{inh} and the inhomogeneous broadening σ_D. We use an frequency-anticorrelated, entangled state with $\sigma_N = 1$ and $\sigma_B = 1$.

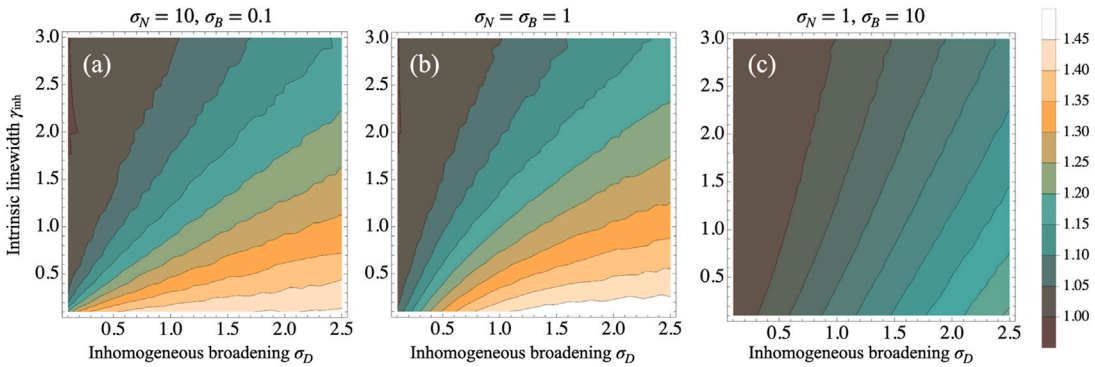

FIGURE 4 | Ratio of the absorption probability **(23)** between ETPA in an inhomogeneously broadened sample and in a homogeneously broadened sample with the same linewidth broadening is plotted for three different input states vs. the intrinsic linewidth and the inhomogeneous broadening. As indicated above the contour plots, the parameters are chosen as **(A)** $\sigma_N = 10$ and $\sigma_B = 0.1$, i.e. a two-photon state featuring strong frequency anti-correlations, **(B)** $\sigma_N = \sigma_B = 1$, i.e. almost separable photon pairs, and **(C)** $\sigma_N = 1$ and $\sigma_B = 10$, i.e. a state featuring strong positive frequency correlations.

markedly different from the Lorentzian resonance of the homogeneous case. As a consequence, one should keep in mind that the ratio (23) compares two slightly different situations.

We plot the ratio **(23)** in **Figure 4** as a function of both γ_{inh} and σ_D for three different two-photon states. In **Figure 4A**, the entangled photons show very strong frequency anti-correlations, in panel (b) they are separable, and in panel (c) the show strong positive frequency correlations. We see that, even though there are notable differences between these cases, the general trend is identical. The ratio of the two excitation probabilities can be enhanced, and the effect increases with increasing inhomogeneous broadening σ_D and with decreasing intrinsic linewidth γ_{inh}. This effect is stronger when the exciting photon pair is entangled with strong frequency anti-correlations as in panel (a). In contrast, positive frequency correlations which are nevertheless associated with an entangled wave function, have the opposite effect and reduce this enhancement.

Still we also find that this enhancement saturates to increasing inhomogeneity of the distribution. This is shown in **Figure 5** for different entanglement strengths. The broadening at which the saturation is reached depends strongly on the degree of entanglement. However, the ratio r_{rel} always remains of order unity, as the enhanced resonant excitation probability is balanced by an increase in the number of molecules which can not be excited resonantly and thus become dark. Therefore, inhomogeneous broadening cannot account for the enormous disparity in the reported ETPA cross sections in the literature.

3.2 Orientational Average

With our choice of the Gaussian two-photon wavefunction **(18)**, which is symmetric with respect to its frequency arguments, we can separate the orientational average from the frequency integrations. Thus, using the definition of our molecular dipoles (10), their transformation to the laboratory frame in **Eqs. 13**, **14**, we can carry out the index summations $\nu_1, \ldots, \nu_4$ and $\alpha_1, \ldots, \alpha_4$. Note that this orientational average will always reduce the ETPA rate, since the dipole vectors in **Eqs. 11** are chosen normalized. As a consequence, their orientationally

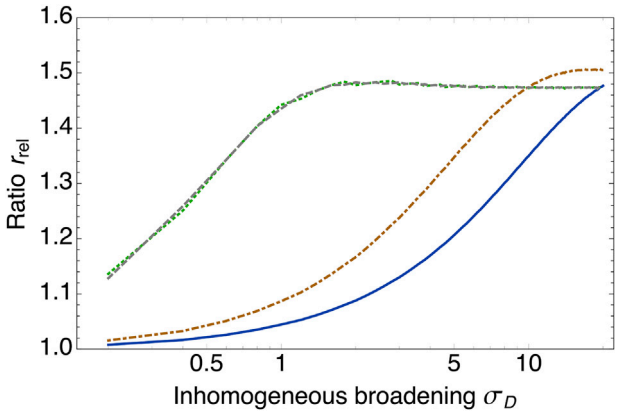

FIGURE 5 | Ratio r_{rel}, **Eq. 23**, is plotted vs. the inhomogeneous broadening σ_D and entangled states with $\sigma_B = 20$, $\sigma_N = 1$ (solid, blue), $\sigma_B = 10$, $\sigma_N = 1$ (dot-dashed, red), $\sigma_N = \sigma_B = 1$ (dotted, green), and $\sigma_B = 1$, $\sigma_N = 10$ (dashed, gray). The intrinsic broadening is fixed at $\gamma_{inh} = 0.1$.

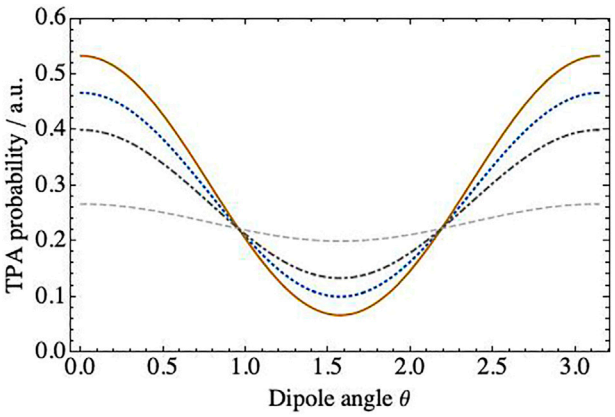

FIGURE 6 | Polarization dependence of ETPA probability on the angle between the molecular dipoles according to **Eq. 10**. The gray, dashed line depicts the dependence **(24)** which is created by the input state **(20)**. The black, dot-dashed line is given by **Eq. 25**, created by the state **(21)**. The polarization dependence **(26)**, which is created by the state **(22)**, is shown as a solid, yellow line for $\phi = 0$, and as a blue, dotted line for $\phi = \pi/3$.

averaged overlap with any polarization mode will be smaller than unity.

For the polarization state **(20)**, we obtain

$$P_1^{\mathrm{TPA}} = P_{\mathrm{iso}}^{\mathrm{TPA}} \times \frac{1}{15}\left(7 + cos\left(2\theta\right)\right). \tag{24}$$

Here, $P_{\mathrm{iso}}^{\mathrm{TPA}}$ denotes the isotropic result where the vectorial nature of the dipoles and the photons has been neglected. Likewise, we obtain from **Eq. 21**

$$P_2^{\mathrm{TPA}} = P_{\mathrm{iso}}^{\mathrm{TPA}} \times \frac{4}{15}\left(2 + cos\left(2\theta\right)\right), \tag{25}$$

and for the entangled polarization state **(22)**, we arrive at

$$P_3^{\mathrm{TPA}} = P_{\mathrm{iso}}^{\mathrm{TPA}} \times \frac{1}{15}\left(4cos^2\left(\theta\right)\left(1 + \cos\phi\right) - 2\sin^2\left(\theta\right)\left(-4 + \cos\phi\right)\right). \tag{26}$$

These results are shown in **Figure 6**. The separable states, **Eqs 24**, **25**, show a weaker dependence on the dipole angle compared to the entangled state **(26)**. The latter shows the largest dependence at an angle $\phi = 0$, i.e. for a symmetric superposition state, where it also takes its maximal value. This is consistent with our discussion in **Section 2.3**, where we pointed out that the molecular response projects onto a symmetric superposition. Hence, such a state is optimal for the ETPA cross section. Conversely, the entangled state shows the smallest variation at $\phi = \pi/2$ (not shown), where it coincides with the product state **(25)**.

The polarization dependence of ETPA in rhodamine 6G molecules was carefully examined in [43], and no discernable dependence on the interphoton polarization angle was reported. This can be reconciled with our simulations provided the dipole angle is around $\theta \simeq \pi/3$ or $2\pi/3$. Indeed, as we see in **Figure 6**, in such a case the polarization state should not affect the ETPA probability regardless of the polarization state of the light. This appears broadly consistent with measurements in [59], where an angle of around 40° was reported, thus implying a rather weak ETPA polarization dependence. A further possibility, which we have not discussed here, would be the interference between different excitation pathways. Such a situation could wash out the strong polarization dependence observed here for a single excitation pathway.

4 CONCLUSION

In summary, we have extended the existing theory of entangled two-photon absorption to describe excitation in inhomogeneously broadened molecular ensembles, and to investigate the influence of the polarization degrees of freedom on ETPA.

In our investigation of inhomogeneously broadened samples, we showed that ETPA can be enhanced compared to homogeneously broadened samples. However, this enhancement always remains relatively small, of order unity. It cannot explain the several orders of magnitudes in difference among the various measured ETPA cross sections in the literature. The presence of near-resonant intermediate states could change this conclusion. As shown in [53–55], optimized entangled states of light can substantially enhance the ETPA probability. It remains an open question, however, how these conclusions would be affected by inhomogeneous broadening. Furthermore, entangled states with large spectral tails in their single-photon spectrum also affect the present conclusion. As shown in the context of virtual state spectroscopy [60], these large frequency tails render the key assumption in the current theoretical model - that intermediate states are far detuned from the photonic states (see **Eq. 5**) - problematic and further emphasize the need for the investigation of near-resonant intermediate states in ETPA.

In our simulation of the orientationally averaged absorption of polarization entangled photon pairs, we showed that polarization entanglement can have a substantial influence on the ETPA

absorption probability. It can increase or reduce the absorption probability by as much as a factor of five, provided the molecular dipoles are aligned in parallel or perpendicular. These findings rely on a single excitation pathway, i.e. a single intermediate molecular state. In case there are several, competing excitation pathways, the pronounced angular dependence of the ETPA rate could be washed out by the mixing of these pathways. Furthermore, it is one of the consequences of the employed theoretical model, as observed already by Landes et al. in [60], that the molecular response projects the entangled photon wavefunction onto a symmetrized superposition. As a consequence, the present model predicts a vanishing ETPA probability for a photonic singlet state due to destructive interference. This effect could be tested experimentally, e.g., in atomic ETPA measurements. It could further provide an experimental test in molecular ETPA experiments to gauge the strength of single-photon losses, which should not be suppressed by destructive interference.

DATA AVAILABILITY STATEMENT

The original contributions presented in the study are included in the article/supplementary material, further inquiries can be directed to the corresponding author.

AUTHOR CONTRIBUTIONS

The author confirms being the sole contributor of this work and has approved it for publication.

FUNDING

The author acknowledges support from the Cluster of Excellence "Advanced Imaging of Matter" of the Deutsche Forschungsgemeinschaft (DFG) - EXC 2056 - project ID 390 715 994.

REFERENCES

1. Dorfman KE, Schlawin F, Mukamel S Nonlinear Optical Signals and Spectroscopy with Quantum Light. *Rev Mod Phys* (2016) 88:045008. doi:10.1103/RevModPhys.88.045008
2. Schlawin F Entangled Photon Spectroscopy. *J Phys B: Mol Opt Phys* (2017) 50:203001. doi:10.1088/1361-6455/aa8a7a
3. Schlawin F, Dorfman KE, Mukamel S Entangled Two-Photon Absorption Spectroscopy. *Acc Chem Res* (2018) 51:2207–14. doi:10.1021/acs.accounts.8b00173
4. Gilaberte Basset M, Setzpfandt F, Steinlechner F, Beckert E, Pertsch T, Gräfe M Perspectives for Applications of Quantum Imaging. *Laser Photon Rev* (2019) 13:1900097. doi:10.1002/lpor.201900097
5. Szoke S, Liu H, Hickam BP, He M, Cushing SK Entangled Light-Matter Interactions and Spectroscopy. *J Mater Chem C* (2020) 8:10732–41. doi:10.1039/D0TC02300K
6. Mukamel S, Freyberger M, Schleich W, Bellini M, Zavatta A, Leuchs G, et al. Roadmap on Quantum Light Spectroscopy. *J Phys B: At Mol Opt Phys* (2020) 53:072002. doi:10.1088/1361-6455/ab69a8
7. Ma Y-Z, Doughty B Nonlinear Optical Microscopy with Ultralow Quantum Light. *The J Phys Chem A* (2021) 125:8765–76. doi:10.1021/acs.jpca.1c06797
8. Schlawin F, Dorfman KE, Fingerhut BP, Mukamel S Suppression of Population Transport and Control of Exciton Distributions by Entangled Photons. *Nat Commun* (2013) 4:1782. doi:10.1038/ncomms2802
9. Raymer MG, Marcus AH, Widom JR, Vitullo DLP Entangled Photon-Pair Two-Dimensional Fluorescence Spectroscopy (Epp-2dfs). *The J Phys Chem B* (2013) 117:15559–75. doi:10.1021/jp405829n
10. Lever F, Ramelow S, Gühr M Effects of Time-Energy Correlation Strength in Molecular Entangled Photon Spectroscopy. *Phys Rev A* (2019) 100:053844. doi:10.1103/PhysRevA.100.053844
11. Debnath A, Rubio A Entangled Photon Assisted Multidimensional Nonlinear Optics of Exciton–Polaritons. *J Appl Phys* (2020) 128:113102. doi:10.1063/5.0012754
12. Ishizaki A Probing Excited-State Dynamics with Quantum Entangled Photons: Correspondence to Coherent Multidimensional Spectroscopy. *J Chem Phys* (2020) 153:051102. doi:10.1063/5.0015432
13. Oka H Entangled Two-Photon Absorption Spectroscopy for Optically Forbidden Transition Detection. *J Chem Phys* (2020) 152:044106. doi:10.1063/1.5138691
14. Fujihashi Y, Ishizaki A Achieving Two-Dimensional Optical Spectroscopy with Temporal and Spectral Resolution Using Quantum Entangled Three Photons. *J Chem Phys* (2021) 155:044101. doi:10.1063/5.0056808
15. Chen F, Mukamel S Vibrational Hyper-Raman Molecular Spectroscopy with Entangled Photons. *ACS Photon* (2021) 8:2722–7. doi:10.1021/acsphotonics.1c00777
16. Cutipa P, Chekhova MV Bright Squeezed Vacuum for Two-Photon Spectroscopy: Simultaneously High Resolution in Time and Frequency, Space and Wavevector. *Opt. Lett.* (2022) 47:465. doi:10.1364/OL.448352
17. Schlawin F, Dorfman KE, Mukamel S Pump-probe Spectroscopy Using Quantum Light with Two-Photon Coincidence Detection. *Phys Rev A* (2016) 93:023807. doi:10.1103/PhysRevA.93.023807
18. Li H, Piryatinski A, Jerke J, Kandada ARS, Silva C, Bittner ER Probing Dynamical Symmetry Breaking Using Quantum-Entangled Photons. *Quan Sci Technology* (2017) 3:015003. doi:10.1088/2058-9565/aa93b6
19. Zhang Z, Saurabh P, Dorfman KE, Debnath A, Mukamel S Monitoring Polariton Dynamics in the Lhcii Photosynthetic Antenna in a Microcavity by Two-Photon Coincidence Counting. *J Chem Phys* (2018) 148:074302. doi:10.1063/1.5004432
20. Li H, Piryatinski A, Srimath Kandada AR, Silva C, Bittner ER Photon Entanglement Entropy as a Probe of many-body Correlations and Fluctuations. *J Chem Phys* (2019) 150:184106. doi:10.1063/1.5083613
21. Sánchez Muñoz C, Schlawin F Photon Correlation Spectroscopy as a Witness for Quantum Coherence. *Phys Rev Lett* (2020) 124:203601. doi:10.1103/PhysRevLett.124.203601
22. Gu B, Mukamel S Manipulating Two-Photon-Absorption of Cavity Polaritons by Entangled Light. *J Phys Chem Lett* (2020) 11:8177–82. doi:10.1021/acs.jpclett.0c02282
23. Schlawin F, Dorfman KE, Mukamel S Detection of Photon Statistics and Multimode Field Correlations by Raman Processes. *J Chem Phys* (2021) 154:104116. doi:10.1063/5.0039759
24. Yang Z, Saurabh P, Schlawin F, Mukamel S, Dorfman KE Multidimensional Four-Wave-Mixing Spectroscopy with Squeezed Light. *Appl Phys Lett* (2020) 116:244001. doi:10.1063/5.0009575
25. Dorfman K, Liu S, Lou Y, Wei T, Jing J, Schlawin F, et al. Multidimensional Four-Wave Mixing Signals Detected by Quantum Squeezed Light. *Proc Natl Acad Sci* (2021) 118. doi:10.1073/pnas.2105601118
26. Ye L, Mukamel S Interferometric Two-Photon-Absorption Spectroscopy with Three Entangled Photons. *Appl Phys Lett* (2020) 116:174003. doi:10.1063/5.0004617
27. Eshun A, Gu B, Varnavski O, Asban S, Dorfman KE, Mukamel S, et al. Investigations of Molecular Optical Properties Using Quantum Light and Hong–Ou–Mandel Interferometry. *J Am Chem Soc* (2021) 143:9070–81. doi:10.1021/jacs.1c02514
28. Asban S, Mukamel S Distinguishability and "Which Pathway"information in Multidimensional Interferometric Spectroscopy with a Single Entangled Photon-Pair. *Sci Adv* (2021) 7:eabj4566. doi:10.1126/sciadv.abj4566

29. Dorfman KE, Asban S, Gu B, Mukamel S Hong-ou-mandel Interferometry and Spectroscopy Using Entangled Photons. *Commun Phys* (2021) 4:49. doi:10.1038/s42005-021-00542-2
30. Asban S, Dorfman KE, Mukamel S Interferometric Spectroscopy with Quantum Light: Revealing Out-Of-Time-Ordering Correlators. *J Chem Phys* (2021) 154:210901. doi:10.1063/5.0047776
31. Gea-Banacloche J Two-photon Absorption of Nonclassical Light. *Phys Rev Lett* (1989) 62:1603–6. doi:10.1103/PhysRevLett.62.1603
32. Javanainen J, Gould PL Linear Intensity Dependence of a Two-Photon Transition Rate. *Phys Rev A* (1990) 41:5088–91. doi:10.1103/PhysRevA.41.5088
33. Georgiades NP, Polzik ES, Edamatsu K, Kimble HJ, Parkins AS Nonclassical Excitation for Atoms in a Squeezed Vacuum. *Phys Rev Lett* (1995) 75:3426–9. doi:10.1103/PhysRevLett.75.3426
34. Georgiades NP, Polzik ES, Kimble HJ Atoms as Nonlinear Mixers for Detection of Quantum Correlations at Ultrahigh Frequencies. *Phys Rev A* (1997) 55:R1605–R1608. doi:10.1103/PhysRevA.55.R1605
35. Dayan B, Pe'er A, Friesem AA, Silberberg Y Two Photon Absorption and Coherent Control with Broadband Down-Converted Light. *Phys Rev Lett* (2004) 93:023005. doi:10.1103/PhysRevLett.93.023005
36. Dayan B, Pe'er A, Friesem AA, Silberberg Y Nonlinear Interactions with an Ultrahigh Flux of Broadband Entangled Photons. *Phys Rev Lett* (2005) 94:043602. doi:10.1103/PhysRevLett.94.043602
37. Lee D-I, Goodson T Entangled Photon Absorption in an Organic Porphyrin Dendrimer. *J Phys Chem B* (2006) 110:25582–5. doi:10.1021/jp066767g
38. Guzman AR, Harpham MR, Süzer O, Haley MM, Goodson TG Spatial Control of Entangled Two-Photon Absorption with Organic Chromophores. *J Am Chem Soc* (2010) 132:7840–1. doi:10.1021/ja1016816
39. Upton L, Harpham M, Suzer O, Richter M, Mukamel S, Goodson T Optically Excited Entangled States in Organic Molecules Illuminate the Dark. *J Phys Chem Lett* (2013) 4:2046–52. doi:10.1021/jz400851d
40. Villabona-Monsalve JP, Calderón-Losada O, Nuñez Portela M, Valencia A Entangled Two Photon Absorption Cross Section on the 808 Nm Region for the Common Dyes Zinc Tetraphenylporphyrin and Rhodamine B. *J Phys Chem A* (2017) 121:7869–75. doi:10.1021/acs.jpca.7b06450
41. Villabona-Monsalve JP, Varnavski O, Palfey BA, Goodson T Two-photon Excitation of Flavins and Flavoproteins with Classical and Quantum Light. *J Am Chem Soc* (2018) 140:14562–6. doi:10.1021/jacs.8b08515
42. Li T, Li F, Altuzarra C, Classen A, Agarwal GS Squeezed Light Induced Two-Photon Absorption Fluorescence of Fluorescein Biomarkers. *Appl Phys Lett* (2020) 116:254001. doi:10.1063/5.0010909
43. Tabakaev D, Montagnese M, Haack G, Bonacina L, Wolf J-P, Zbinden H, et al. Energy-time-entangled Two-Photon Molecular Absorption. *Phys Rev A* (2021) 103:033701. doi:10.1103/PhysRevA.103.033701
44. Burdick RK, Schatz GC, Goodson T Enhancing Entangled Two-Photon Absorption for Picosecond Quantum Spectroscopy. *J Am Chem Soc* (2021) 143:16930–4. doi:10.1021/jacs.1c09728
45. Lerch S, Stefanov A Experimental Requirements for Entangled Two-Photon Spectroscopy. *J Chem Phys* (2021) 155:064201. doi:10.1063/5.0050657
46. Landes T, Allgaier M, Merkouche S, Smith BJ, Marcus AH, Raymer MG Experimental Feasibility of Molecular Two-Photon Absorption with Isolated Time-Frequency-Entangled Photon Pairs. *Phys Rev Res* (2021) 3:033154. doi:10.1103/PhysRevResearch.3.033154
47. Parzuchowski KM, Mikhaylov A, Mazurek MD, Wilson RN, Lum DJ, Gerrits T, et al. Setting Bounds on Entangled Two-Photon Absorption Cross Sections in Common Fluorophores. *Phys Rev Appl* (2021) 15:044012. doi:10.1103/PhysRevApplied.15.044012
48. Landes T, Raymer MG, Allgaier M, Merkouche S, Smith BJ, Marcus AH Quantifying the Enhancement of Two-Photon Absorption Due to Spectral-Temporal Entanglement. *Opt Express* (2021) 29:20022–33. doi:10.1364/OE.422544
49. Raymer MG, Landes T, Allgaier M, Merkouche S, Smith BJ, Marcus AH How Large Is the Quantum Enhancement of Two-Photon Absorption by Time-Frequency Entanglement of Photon Pairs? *Optica* (2021) 8:757–8. doi:10.1364/OPTICA.426674
50. Kang G, Nasiri Avanaki K, Mosquera MA, Burdick RK, Villabona-Monsalve JP, Goodson T, et al. Efficient Modeling of Organic Chromophores for Entangled Two-Photon Absorption. *J Am Chem Soc* (2020) 142:10446–58. doi:10.1021/jacs.0c02808
51. Loudon R *The Quantum Theory of Light*. Oxford, UK: Oxford science publications (1979) Clarendon Press.
52. Raymer MG, Landes T, Marcus AH Entangled Two-Photon Absorption by Atoms and Molecules: A Quantum Optics Tutorial. *J Chem Phys* (2021) 155:081501. doi:10.1063/5.0049338
53. Schlawin F, Buchleitner A Theory of Coherent Control with Quantum Light. *New J Phys* (2017) 19:013009. doi:10.1088/1367-2630/aa55ec
54. Carnio EG, Buchleitner A, Schlawin F Optimization of Selective Two-Photon Absorption in Cavity Polaritons. *J Chem Phys* (2021) 154:214114. doi:10.1063/5.0049863
55. Carnio EG, Buchleitner A, Schlawin F How to Optimize the Absorption of Two Entangled Photons. *Scipost Phys Core* (2021) 4:28. doi:10.21468/SciPostPhysCore.4.4.028
56. Ben-Reuven A, Jortner J, Klein L, Mukamel S Collision Broadening in Two-Photon Spectroscopy. *Phys Rev A* (1976) 13:1402–10. doi:10.1103/PhysRevA.13.1402
57. Andrews DL, Thirunamachandran T On Three-Dimensional Rotational Averages. *J Chem Phys* (1977) 67:5026–33. doi:10.1063/1.434725
58. Abramavicius D, Mukamel S Coherent Third-Order Spectroscopic Probes of Molecular Chirality. *J Chem Phys* (2005) 122:134305. doi:10.1063/1.1869495
59. Kauert M, Stoller PC, Frenz M, Rička J Absolute Measurement of Molecular Two-Photon Absorption Cross-Sections Using a Fluorescence Saturation Technique. *Opt Express* (2006) 14:8434–47. doi:10.1364/OE.14.008434
60. de J León-Montiel R, Svozilík J, Salazar-Serrano LJ, Torres JP Role of the Spectral Shape of Quantum Correlations in Two-Photon Virtual-State Spectroscopy. *New J Phys* (2013) 15:053023. doi:10.1088/1367-2630/15/5/053023

Conflict of Interest: The author declares that the research was conducted in the absence of any commercial or financial relationships that could be construed as a potential conflict of interest.

Publisher's Note: All claims expressed in this article are solely those of the authors and do not necessarily represent those of their affiliated organizations, or those of the publisher, the editors, and the reviewers. Any product that may be evaluated in this article, or claim that may be made by its manufacturer, is not guaranteed or endorsed by the publisher.

frontiers | Frontiers in Physics

BRIEF RESEARCH REPORT
published: 12 April 2022
doi: 10.3389/fphy.2022.878478

Distributed Edge-Enhanced Imaging With a Fractional Spiral Phase Filter Using Random Light

Huahua Wang[1,2,3], Jian Ma[1,2], Zhixin Yang[1], Haoran Du[1,2], Xingwang Kang[2], Hengzhi Su[2,4], Lu Gao[1,2] and Ze Zhang[2,3,4,5]**

[1]School of Science, China University of Geosciences, Beijing, China, [2]Aerospace Information Research Institute, Chinese Academy of Sciences, Beijing, China, [3]Science and Technology on Solid-State Laser Laboratory, Beijing, China, [4]School of Electronic Engineering, Beijing University of Posts and Telecommunications, Beijing, China, [5]Qilu Aerospace Information Research Institute, Jinan, China

A gradual edge-enhanced ghost imaging method with pseudo-thermal light is proposed in both the theory and experiment. In the experiment, a phase object and fractional spiral phase filter are placed symmetrically in the imaging plane of the pseudo-thermal light source in the distributed test and reference beams of the lensless ghost imaging system. The procedure of gradual edge-enhanced ghost imaging is carried out by modulating the fractional topological charge from 0 to 1. We observe that the brightness of the object edge increases with the increase of the fractional topological charge. It is also found that the intensity distribution is uniform and isotropic when the topological charge is an integer; otherwise, the intensity distribution is not uniform. Theoretical analysis is also provided. The proposed gradual edge-enhanced ghost imaging scenario releases the position limitation in the Fourier plane for the filter of the traditional phase filtering imaging process. The method is believed to have prospective applications in microscopic imaging and biomedical detection.

Keywords: spiral phase contrast imaging, second-order correlation, edge enhancement, orbital angular momentum, fractional-order spiral filtering

OPEN ACCESS

Edited by:
Omar Magana-Loaiza, Louisiana State University, United States

Reviewed by:
Chenglong You, Louisiana State University, United States
Yanfeng Bai, Hunan University, China

****Correspondence:***
Lu Gao
gaolu@cugb.edu.cn
Ze Zhang
zhangze@aircas.ac.cn

Specialty section:
This article was submitted to Quantum Engineering and Technology, a section of the journal Frontiers in Physics

Received: *18 February 2022*
Accepted: *14 March 2022*
Published: *12 April 2022*

Citation:
Wang H, Ma J, Yang Z, Du H, Kang X, Su H, Gao L and Zhang Z (2022) Distributed Edge-Enhanced Imaging With a Fractional Spiral Phase Filter Using Random Light. Front. Phys. 10:878478. doi: 10.3389/fphy.2022.878478

1 INTRODUCTION

As early as the 1930s, Zernike first proposed the phase contrast imaging method and won the Nobel Prize for employing this technology to observe the structure of living cells in 1953 [1]. Different from the traditional optical microscopy, the phase contrast method can convert the invisible phase distributions into visible optical field intensity [2–4] to highlight the edges of an object with phase changes, which is called edge enhancement [5–7]. Edge-enhanced imaging, a kind of image processing, can extract the contour features of an image, so that the boundary of the target can be displayed more clearly, and the position of the target can be determined. Since then, the phase contrast technology has been further developed to expand its applications from the initial differential interference phase contrast microscopy and interference reflection contrast microscopy to the later spiral phase contrast (SPC) microscopy [8, 9]. In the 1990s, researchers realized the imaging of one-dimensional (1D) and two-dimensional (2D) phase objects by employing the SPC technology [10, 11]. In 2006, the homogeneous enhancement of the amplitude and phase objects was achieved using SPC technology combined with optical microscopy [12]. In 2015, Prof. Lixiang Chen's research group used a fractional spiral phase filter (SPF) in the Fourier plane of the lens to achieve the isotropic edge enhancement with laser [13, 14].

SPC was applied in quantum imaging in 2009 by Jack et al. [15]. The entangled two-photon was separated using a beam splitter (BS). The pure phase object and the SPF were symmetrically placed in the

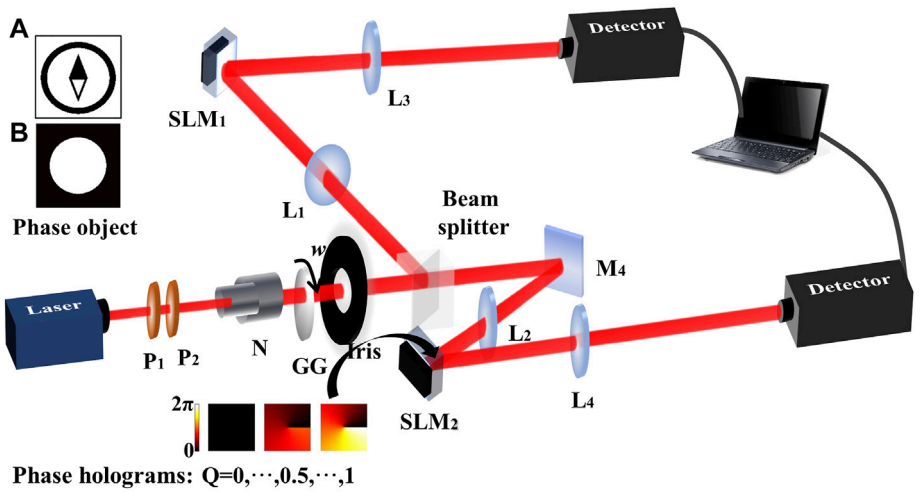

FIGURE 1 | Schematic diagram of the experimental setup. Phase objects in the upper left corner are the sketch of a compass **(A)** and a circle **(B)** which are loaded by SLM_1, and the dynamic phase hologram in the lower left corner is loaded by SLM_2.

image plane of the entangled two photons. The phase objects can be recognized through edge enhancement through the two-photon coincident measurement. However, ghost imaging can not only be implemented with an entangled two-photon light source but also be achieved with incoherent thermal light [16–20]. The quantum entangled source behaves like a mirror, whereas the classical thermal source acts like a phase-conjugate mirror in the ghost imaging [21]. It has been demonstrated that intensity fluctuations give rise to the formation of correlations in the OAM components and angular positions of random light in [22]. It was then proved that the spatial signatures and phase information of an object with rotational symmetries can be identified using classical OAM correlations in random light [23]. Furthermore, an experimental scenario of distributed angular double-slit interference based on the OAM correlations of pseudo-thermal light was accomplished in [24]. In 2020, we proved the classical physical essence of the spatial dimension of the non-local edge-enhanced ghost imaging system by making use of orientated SPF [25]. Inspired by the previous research, we proposed the scenario here to observe the phase object edge-enhanced imaging with a fractional-order spiral phase filter based on the OAM components of incoherent random light. The experimental results proved that the enhanced edge intensity of the image increased with the increase of the topological charge from 0 to 1. The reason why the edge brightness increases with the increase of the fractional orbital angular momentum (OAM) is due to the pseudo-thermal light OAM correlation and eigenvalue decomposition of the fractional topological charge of the SPF. The theoretical analysis finds good agreement with the experimental results. The proposed scenario can accomplish the continuously modulated edge-enhanced ghost imaging even with the incoherent light source.

2 EXPERIMENT

A schematic diagram of the experimental setup is shown in **Figure 1**. The input light is a Gaussian beam derived from a 632.8 *nm* He–Ne laser (THORLABS, HNL225RB). The light beam illuminates a slowly rotating glass (RG) with the rotation angular velocity of 0.013 *rad/s* to produce a pseudo-thermal light beam. P_1 and P_2 are polarizers to modulate the intensity of the laser beam. N is a telescope (×2 magnification) to collimate and expand the transverse size of the laser beam. Radiation from a chaotic pseudo-thermal source *via* an Iris is then divided into two optical paths, namely, a test beam and a reference beam, by a 50:50 non-polarizing BS. The pseudo-thermal light source is imaged, by two convex lenses L_1 and L_2, to the transverse planes of the spatial light modulators (SLMs, HOLOEYE, PLUTO-2-VIS-016), a device with full high-definition resolutions of 1920 × 1080 square pixels. The focal length of the convex lens is 25 cm. Then, the SLM_1 and SLM_2, located at a distance of 50 cm from the biconvex lens, are re-imaged to the charge-coupled devices (CCDs, MTV-1881EX) with the resolution of 575 × 767 square pixels placed at the end of each light beam, respectively. Two beams are connected with a data acquisition card embedded in a personal computer, and the intensity correlation calculation can be carried out.

The role of the SLMs is loading phase objects and fractional SPF instead of the spiral phase plate, so that the gradual edge enhancement by varying the fractional OAM value from 0 to 1 with a step length of 0.1 can be observed conveniently. The phase object and the phase hologram are symmetrically loaded on SLM_1 and SLM_2 in the distributed beams. The size of the phase object compass is 150 × 150 square pixels. The phase mutation along the pointer and the dial is π. The black part of the phase object presents the phase of 0, and the white part presents the phase of π. The phase hologram placed on the SLM_2 is 10 × 10 square pixels. Correspondingly, the black part of each phase filter presents the phase of 0, whereas the white part presents the phase of 2π. The correlation detection is carried out through scanning measurement. 10 × 10 square pixel points of the data obtained from CCD_2 are taken as a unit to traverse line by line to implement the second-order correlation with the data of CCD_1.

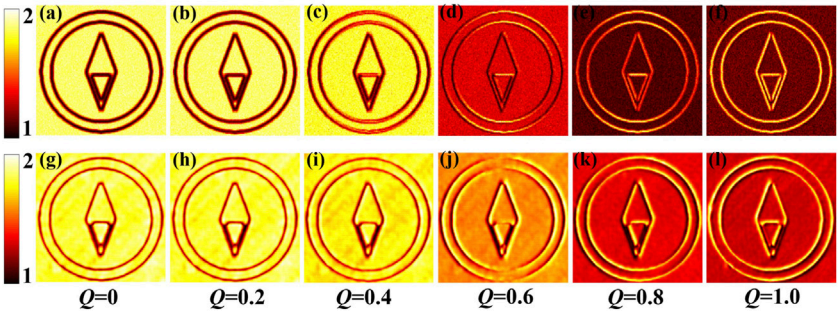

FIGURE 2 | Simulation and experimental results of the non-local edge-enhanced imaging with a fractional spiral phase filter. **(a–f)** in the upper row show the simulation results, and **(g–k)** in the lower row show the experimental results.

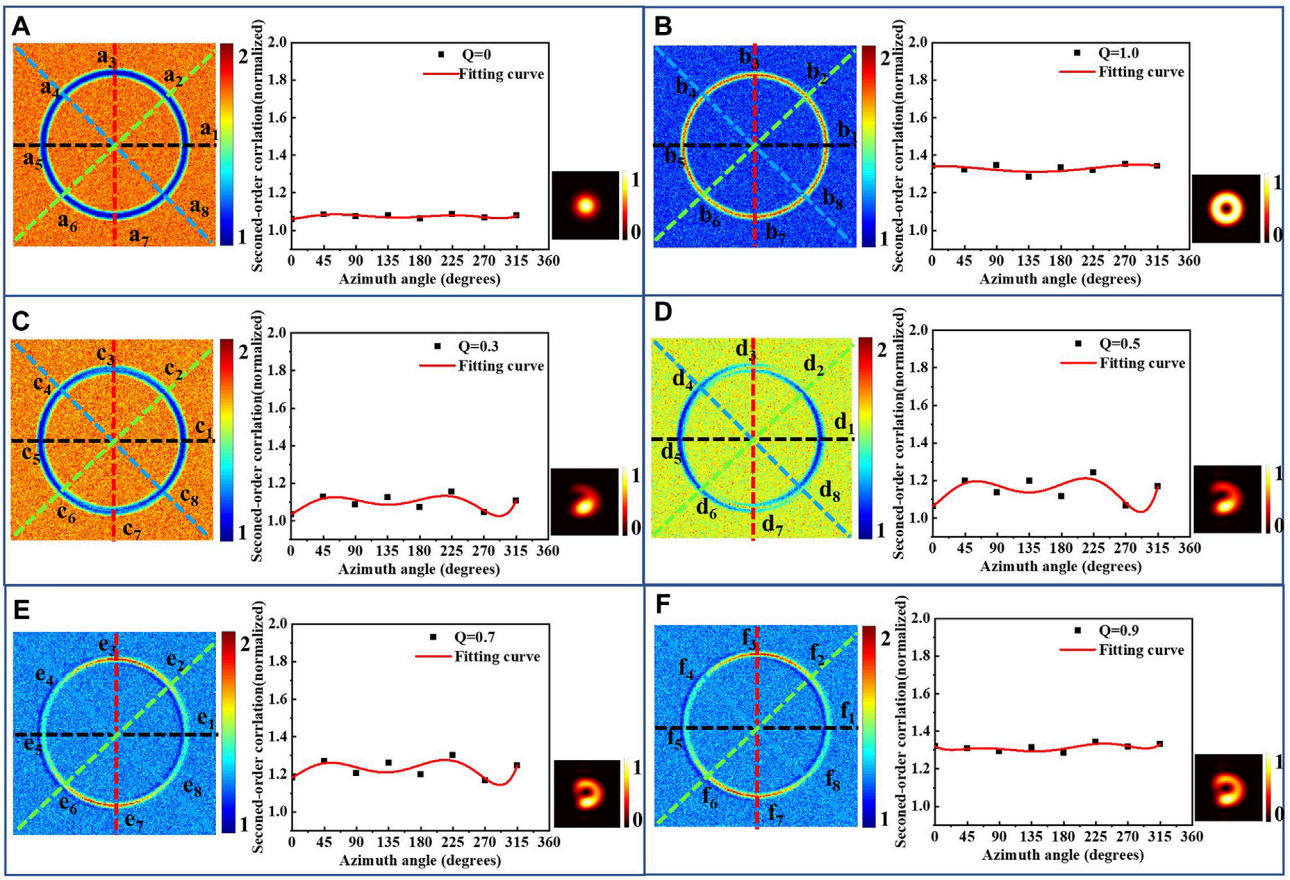

FIGURE 3 | Experimental results of the circle phase with the integer and fractional vortex filters. **(A–F)** show the 2D edge-enhanced images and the fitted curves of some special azimuth corresponding to different *Q*.

3 RESULTS

The process of simulation calculation is as follows: first, a random thermal light field of Gaussian distribution in both the amplitude and phase is generated by a calculation program, which has the same size as the phase object to be detected. Then, the thermal light field is multiplied with the phase object and the vortex phase filter, respectively, in the reference and test beams to obtain the light field distributions in the detection planes. Finally, the correlation calculation is carried out to achieve the edge-enhanced imaging, as shown in **Figure 2**.

We can find in **Figure 2** that the intensity at the position where the phase gradient existed is lower than that where the phase gradient did not exist when the fractional OAM topological

charge Q is lower than 0.5. It is because when Q is less than 0.5, the vortex has not formed yet, as shown in the lower right corner of each subgraph of **Figure 3**. However, when Q is greater than 0.5, a black hole at the center of the vortex appears. Thus, the contrast of the edge and background gradually reversed with the increase of Q. The intensity distribution of the fractional-order vortex light is not uniform along the radial direction, so the edge enhancement is not isotropic as the integer-order condition.

Furthermore, we take a simple circular phase object as the detected phase object to analyze the isotropic feature of the SPC ghost imaging. The phase circle is shown in the upper left corner of **Figure 1B**, whose dimension is 200 × 200 pixels and diameter is 130 pixels. The black part of the circle presents the phase of 0, whereas the white part presents the phase of π. **Figures 3A–F** show the 2D edge-enhanced intensity distribution and the fitted edge-enhanced intensity curves of some special azimuth corresponding to the Q-value of 0, 1.0, 0.3, 0.5, 0.7, and 0.9. The lower right corner of each subgraph shows the vortex map of each fractional OAM. **Figures 3C–F** show that edge enhancement is non-isotropic of fractional Q.

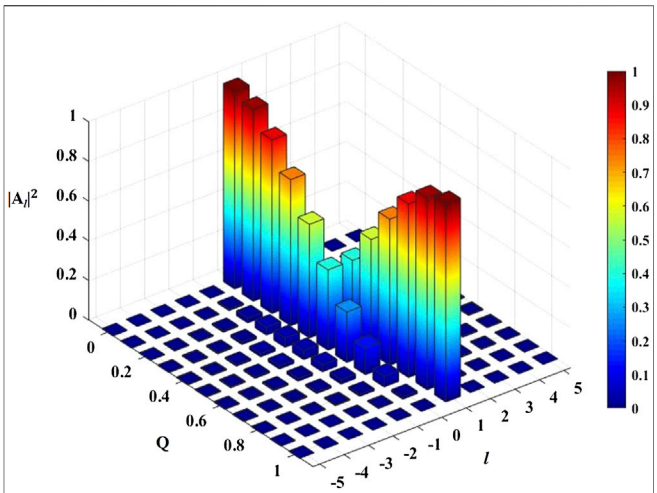

FIGURE 4 | OAM spectra of fractional SPF.

4 THEORETICAL ANALYSIS

The aforementioned experimental results are based on SPC imaging methods which are sensitive to the phase gradients by making use of SPF. SPF is a common device to generate helical wave fronts and vortex beams with an azimuthal structure exp ($jl\phi$), in which the topological charge l is an integer and $0 \leqslant \phi < 2\pi$. Light with this phase structure carries OAM of $l\hbar$ per photon, and the most commonly used filter in the SPC imaging is the SPF with the integer topological charge of $l = 1$. All phase edges of a sample object can be enhanced isotropically as a result of the directional symmetry of an integer SPF.

In our case, H_i presents the impulse response functions during the free transmission in the reference beam between RG and D_1 while $i = 1$ and in the test beam between RG and D_2 while $i = 2$, respectively,

$$H_i(r_i, r_0) = \exp\left\{jk\left[8f + \frac{1}{2f}\left(r_0^2 + r_i^2\right)\right] - j\pi\right\}\delta(r_i - r_0)\,(i = 1, 2), \tag{1}$$

where $k = \omega/c$ is the wave number, f is the focal length of the convex lens, r_0 is the 2D transverse plane position vector of the incident plane, and r_i presents the 2D transverse plane position vector of the output plate of the reference and test beams.

Then, the SPF function of the polar coordinates (r, ϕ) is written as $S(r_1) = \exp[jQ\phi(r_1)]$, where Q is a fraction varying from 0 to 1 and $\phi(r_1)$ is an angular function of the filter. The amplitude transmittance of the input object is described by the function of $T(r_2) = \exp[j\phi'(r_2)]$. Consequently, from the cascade relationship, the optical field in the transverse plane of the detectors D_1 and D_2 can be described as follows:

$$E_i(r_i, r_0) = E_0(r_0)H_i(r_i, r_0)F_i \quad (i = 1, 2), \tag{2}$$

where F_i represents the SPF function $S(r_1)$ when the value of i is 1; otherwise, it represents the amplitude transmittance $T(r_2)$ of the object.

The second-order correlation function of the thermal light ghost imaging is given by [26].

$$\langle I_1(r_1)I_2(r_2)\rangle = \langle I_1(r_1)\rangle\langle I_2(r_2)\rangle + |\langle E_1^*(r_1)E_2(r_2)\rangle|^2, \tag{3}$$

where the cross-spectral density function is

$$\langle E_1(r_1)E_2(r_2)\rangle = \iint E_1^*(r_1)\cdot E_2(r_2)dr_1dr_2. \tag{4}$$

The classical incoherent light source is characterized by the cross-spectral density function as $I(r_0, r_0') = E_0(r_0)\cdot E_0^*(r_0') = I_0\delta(r_0 - r_0')$, where r_0 and r_0' are the 2D transverse plane position vectors. Inserting **Eqs. 1** and **2** into **Eq. 4**, we find that

$$\langle E_1^*(r_1)E_2(r_2)\rangle = I_0^2|S^*(r_1)T(r_2)|^2. \tag{5}$$

It was demonstrated that the integer OAM eigenstates form a complete and infinite basis [27–29]. A fractional vortex can be expressed in terms of the OAM eigenstates as $S(r_1) = \exp(jQ\phi) = \sum_{l=-\infty}^{\infty} A_l \exp(jl\phi)$, where $|A_l|^2 = |\exp[j\pi(Q-l)]\frac{\sin[\pi(Q-l)]}{\pi(Q-l)}|^2$ represents the weight of each OAM component [30] and $\exp(jl\phi)$ is the eigenstate. **Figure 4** shows the spectra of the fractional OAM spread on its integer-order eigenstates.

In the same way, $T(r_2) = \exp(j\phi') = \sum_{m=-\infty}^{\infty} A_m \exp(jm\phi)$, where $|A_m|^2$ represents the weight of each OAM component [30].

Hence, substituting the functions of the filter and object in **Eq. 5**, the second-order correlation function can be given as

$$\langle I_1(r_1)I_2(r_2)\rangle = I_0^2\left\{1 + \left|\sum_{l=-\infty}^{\infty}\sum_{m=-\infty}^{\infty} A_m A_l \exp[j(m-l)\phi]\right|^2\right\}. \tag{6}$$

Equation 6 provides a clear understanding of the edge-enhanced effect of the fractional SPF. It indicates that the edge-enhanced image can be considered a coherent superposition of all images that are individually picked out by

employing integer OAM filters. The OAM spectra of the phase platform of the object only have the composition of $m = 0$, so that the second-order correlation value represented by **Eq. 6** will reach the maximum with $l = 0$ of the SPF and the minimum with $l = 1$. When the value of Q varies from 0 to 1, the OAM spectra composition of $l = 0$ decreases while $l = 1$ increases, as shown in **Figure 4**. Thus, the correlation value of the phase platform decreased as the value of Q increased. However, the situation of the edge part of the object is opposite to the phase platform. The second-order correlation value will reach the maximum with $l = 1$ and the minimum with $l = 0$, and the correlation value of the edge of the object increases as the value of Q increases.

5 CONCLUSION

In summary, a fractional phase filtering ghost imaging method with pseudo-thermal light is proposed. The experimental results show that the edge of the phase object can be gradually enhanced by the fractional SPF spatially distributed to the object with incoherent light beam illumination. The non-local gradual edge enhancement is also theoretically analyzed through correlation in the OAM components of the random fluctuations of the incoherent light beam. This effect is very important in a situation when entanglement is not required and when correlations in OAM suffice. The physical explanations of the gradual edge enhancement with the fractional topological charge change are the coherent superposition of the images filtered out by an integer vortex filter. The proposed scenario here provided a new edge enhancement imaging technology releasing the position of the filter in the Fourier plane with incoherent pseudo-thermal light. It is believed that the proposed non-locally fractional SPF imaging scenario may find potential applications in the field of micro-detection of quantum imaging and bioengineering.

DATA AVAILABILITY STATEMENT

The original contributions presented in the study are included in the article/supplementary material; further inquiries can be directed to the corresponding authors.

AUTHOR CONTRIBUTIONS

LG put forward the initial idea and supervised the project. HW further developed and confirmed the idea through analysis, experiment, and simulation. JM, ZY, and HD provided methodology and resources. HW analyzed the results with the assistance of JM, and ZY drew the figures. LG and HW wrote the manuscript. All authors contributed to manuscript revision and read and approved the submitted version.

FUNDING

This work was supported by the National Natural Science Foundation of China (No. 12074350 and No. 62105341), the Fundamental Research Funds for the Central Universities (No. 2652021046), the National Science Foundation of Shandong Province, China (No. ZR2021QF126), and the National College Students Innovation and Entrepreneurship Training Program (No. S202111415184).

ACKNOWLEDGMENTS

The authors thank Hanquan Song for the meaningful advice and discussions.

REFERENCES

1. Zernike F. Phase Contrast, a New Method for the Microscopic Observation of Transparent Objects Part Ii. *Physica* (1942) 9:974–86. doi:10.1016/s0031-8914(42)80079-8
2. Torre V, Poggio TA. On Edge Detection. *IEEE Trans Pattern Anal Mach Intell* (1986) PAMI-8:147–63. doi:10.1109/TPAMI.1986.4767769
3. Kohlmann K. Corner Detection in Natural Images Based on the 2-d hilbert Transform. *Signal Process.* (1996) 48:225–34. doi:10.1016/0165-1684(95)00138-7
4. Zhu T, Zhou Y, Lou Y, Ye H, Qiu M, Ruan Z, et al. Plasmonic Computing of Spatial Differentiation. *Nat Commun* (2017) 8:15391. doi:10.1038/ncomms15391
5. Zhou Y, Feng S, Nie S, Ma J, Yuan C. Image Edge Enhancement Using Airy Spiral Phase Filter. *Opt Express* (2016) 24:25258. doi:10.1364/OE.24.025258
6. Li D, Feng S, Nie S, Ma J, Yuan C. Scalar and Vectorial Vortex Filtering Based on Geometric Phase Modulation with a Q-Plate. *J Opt* (2019) 21:065702–5171. doi:10.1088/2040-8986/ab18e3
7. Han Y-J, Guo C-S, Rong Z-Y, Chen L-M. Radial hilbert Transform with the Spatially Variable Half-Wave Plate. *Opt Lett* (2013) 38:5169–71. doi:10.1364/OL.38.005169
8. Fürhapter S, Jesacher A, Bernet S, Ritsch-Marte M. Spiral Phase Contrast Imaging in Microscopy. *Opt Express* (2005) 13:689–94. doi:10.1364/OPEX.13.000689
9. Ritsch-Marte M. Orbital Angular Momentum Light in Microscopy. *Phil Trans R Soc A* (2017) 375:20150437. doi:10.1098/rsta.2015.0437
10. Khonina SN, Kotlyar VV, Shinkaryev MV, Soifer VA, Uspleniev GV. The Phase Rotor Filter. *J Mod Opt* (1992) 39:1147–54. doi:10.1080/09500349214551151
11. Jaroszewicz Z, Koɵdziejczyk A. Zone Plates Performing Generalized Hankel Transforms and Their Metrological Applications. *Opt Commun* (1993) 102:391–6. doi:10.1016/0030-4018(93)90410-7
12. Bernet S, Jesacher A, Fürhapter S, Maurer C, Ritsch-Marte M. Quantitative Imaging of Complex Samples by Spiral Phase Contrast Microscopy. *Opt Express* (2006) 14:3792–805. doi:10.1364/oe.14.003792
13. Wang J, Zhang W, Qi Q, Zheng S, Chen L. Gradual Edge Enhancement in Spiral Phase Contrast Imaging with Fractional Vortex Filters. *Sci Rep* (2015) 5:15826. doi:10.1038/srep15826
14. Xu D, Ma T, Qiu X, Zhang W, Chen L. Implementing Selective Edge Enhancement in Nonlinear Optics. *Opt Express* (2020) 28:32377–85. doi:10.1364/OE.404594
15. Jack B, Leach J, Romero J, Franke-Arnold S, Ritsch-Marte M, Barnett SM, et al. Holographic Ghost Imaging and the Violation of a bell Inequality. *Phys Rev Lett* (2009) 103:083602. doi:10.1103/PhysRevLett.103.083602
16. Bennink RS, Bentley SJ, Boyd RW. "Two-Photon" Coincidence Imaging with a Classical Source. *Phys Rev Lett* (2002) 89:113601. doi:10.1103/PhysRevLett.89.113601

17. Valencia A, Scarcelli G, D'Angelo M, Shih Y. Two-photon Imaging with thermal Light. *Phys Rev Lett* (2005) 94:063601. doi:10.1103/PhysRevLett.94.063601
18. Scarcelli G, Berardi V, Shih Y. Can Two-Photon Correlation of Chaotic Light Be Considered as Correlation of Intensity Fluctuations? *Phys Rev Lett* (2006) 96:063602. doi:10.1103/PhysRevLett.96.063602
19. Ferri F, Magatti D, Gatti A, Bache M, Brambilla E, Lugiato LA. High-resolution Ghost Image and Ghost Diffraction Experiments with thermal Light. *Phys Rev Lett* (2005) 94:183602. doi:10.1103/PhysRevLett.94.183602
20. Zhang D-J, Tang Q, Wu T-F, Qiu H-C, Xu D-Q, Li H-G, et al. Lensless Ghost Imaging of a Phase Object with Pseudo-thermal Light. *Appl Phys Lett* (2014) 104:121113. doi:10.1063/1.4869959
21. Cao D-Z, Xiong J, Wang K. Geometrical Optics in Correlated Imaging Systems. *Phys Rev A* (2005) 71:013801. doi:10.1103/PhysRevA.71.013801
22. Magaña-Loaiza OS, Mirhosseini M, Cross RM, Rafsanjani SMH, Boyd RW. Hanbury Brown and Twiss Interferometry with Twisted Light. *Sci Adv* (2016) 2:e1501143. doi:10.1126/sciadv.1501143
23. Yang Z, Magaña-Loaiza OS, Mirhosseini M, Zhou Y, Gao B, Gao L, et al. Digital Spiral Object Identification Using Random Light. *Light Sci Appl* (2017) 6:e17013. doi:10.1038/lsa.2017.13
24. Gao L, Hashemi Rafsanjani SM, Zhou Y, Yang Z, Magaña-Loaiza OS, Mirhosseini M, et al. Distributed Angular Double-Slit Interference with Pseudo-thermal Light. *Appl Phys Lett* (2017) 110:071107. doi:10.1063/1.4976575
25. Song H, Zhang Y, Ren Y, Yuan Z, Zhao D, Zheng Z, et al. Non-local Edge Enhanced Imaging with Incoherent thermal Light. *Appl Phys Lett* (2020) 116:174001. doi:10.1063/5.0002069
26. Shirai T, Setälä T, Friberg AT. Ghost Imaging of Phase Objects with Classical Incoherent Light. *Phys Rev A* (2011) 84:2669–74. doi:10.1103/PhysRevA.84.041801
27. Götte JB, Franke-Arnold S, Zambrini R, Barnett SM. Quantum Formulation of Fractional Orbital Angular Momentum. *J Mod Opt* (2007) 54:1723–38. doi:10.1080/09500340601156827
28. Oemrawsingh SSR, Aiello A, Eliel ER, Nienhuis G, Woerdman JP. How to Observe High-Dimensional Two-Photon Entanglement with Only Two Detectors. *Phys Rev Lett* (2004) 92:217901. doi:10.1103/PhysRevLett.92.217901
29. Chen L, Lei J, Romero J. Quantum Digital Spiral Imaging. *Light Sci Appl* (2014) 3:e153. doi:10.1038/lsa.2014.34
30. Berry MV. Optical Vortices Evolving from Helicoidal Integer and Fractional Phase Steps. *J Opt A: Pure Appl Opt* (2004) 6:259–68. doi:10.1088/1464-4258/6/2/018

Conflict of Interest: The authors declare that the research was conducted in the absence of any commercial or financial relationships that could be construed as a potential conflict of interest.

Publisher's Note: All claims expressed in this article are solely those of the authors and do not necessarily represent those of their affiliated organizations, or those of the publisher, the editors, and the reviewers. Any product that may be evaluated in this article, or claim that may be made by its manufacturer, is not guaranteed or endorsed by the publisher.

frontiers | Frontiers in Physics

ORIGINAL RESEARCH
published: 26 April 2022
doi: 10.3389/fphy.2022.868522

High-Dimensional Entanglement of Photonic Angular Qudits

Graciana Puentes[1,2]*

[1]Departamento de Fsica, Facultad de Ciencias Exactas y Naturales, Universidad de Buenos Aires, Ciudad Universitaria, Buenos Aires, Argentina, [2]CONICET-Universidad de Buenos Aires, Instituto de Fisica de Buenos Aires (IFIBA), Ciudad Universitaria, Buenos Aires, Argentina

We propose a method for generation of entangled photonic states in high dimensions, the so-called qudits, by exploiting quantum correlations of Orbital Angular Momentum (OAM) entangled photons, produced via Spontaneous Parametric Down Conversion. Diffraction masks containing N angular slits placed in the path of twin photons define a qudit space of dimension N^2, spanned by the alternative pathways of OAM-entangled photons. We quantify the high-dimensional entanglement of path-entangled photons by the Concurrence, using an analytic expression valid for pure states. We report numerical results for the Concurrence as a function of the angular aperture size for the case of high-dimensional OAM entanglement and for the case of high-dimensional path entanglement, produced by $N \times M$ angular slits. Our results provide additional means for preparation and characterization of entangled quantum states in high-dimensions, a fundamental resource for quantum simulation and quantum information protocols.

Keywords: parametric down conversion, orbital angular momentum, qudits, entanglement, angular diffraction, quantum optics

OPEN ACCESS

Edited by:
Mario Alan Quiroz-Juarez, Autonomous Metropolitan University, Mexico

Reviewed by:
Nicolò Spagnolo, Sapienza University of Rome, Italy
Alfred U'Ren, National Autonomous University of Mexico, Mexico

***Correspondence:**
Graciana Puentes
gpuentes@df.uba.ar

Specialty section:
This article was submitted to Quantum Engineering and Technology, a section of the journal Frontiers in Physics

Received: *02 February 2022*
Accepted: *09 March 2022*
Published: *26 April 2022*

Citation:
Puentes G (2022) High-Dimensional Entanglement of Photonic Angular Qudits. Front. Phys. 10:868522. doi: 10.3389/fphy.2022.868522

1 INTRODUCTION

In recent years, Spontaneous Parametric Down Conversion (SPDC) has become a fundamental process for generation of entangled photonic states, allowing for preparation of quantum states entangled in several degrees of freedom, such as position and momentum, time and energy, polarization or angular position and Orbital Angular Momentum (OAM), thus providing for a key resource in fundamentals of quantum physics and quantum information. Quantum correlations of SPDC photons in a given domain give rise to interference phenomena resulting from two-photon coherence [1–8]. These phenomena are routinely used in fundamental tests of quantum physics [9–11] and are a key ingredient for the implementation of quantum communication and information protocols, including quantum teleportation and quantum cryptography [12–14]. Fourier relations link angular position and OAM of photons, leading to angular interference in the OAM-mode distribution, as photons diffract through angular apertures, resulting in two-photon quantum interference [15–22].

In this article, we quantify entanglement of such high-dimensional angular qudits, in a scheme in which OAM-entangled photons produced by SPDC are transmitted through multiple angular apertures, in the form of $N \times M$ angular slits in the path of signal and idler photons, which results in path entanglement in a space of dimension $D = N \times M$. Using this scheme, we demonstrate high-dimensional entanglement based on angular-position correlations of down-converted photons. Our results suggest that violations of Bell's inequalities in even higher dimensions could in principle be achieved. Moreover, in contrast to previous approaches [16, 17] relying on the Fourier limit only, our results shine light on the quantum interpretation, providing new insights. Adding to the novelty of

our work, we consider the case of asymmetric angular slits N and M for signal and idler, which can lead to high-dimensional angular interference phenomena. We note that linear qudits have previously been proposed [24]. Here we propose and characterize angular qudits, which due to their shape can enable generation of entanglement in a larger Hilbert space than linear qudits. In order to quantify entanglement, we derive an analytic expression for calculation of the Concurrence, valid for pure states. The results reported here extend the notion of angular qudits to an arbitrary number of angular slits $N \times M$, which not only demonstrates two-photon coherence effects in the angular domain but also provide additional means for preparation and characterization of entangled quantum states in a high-dimensional Hilbert space. This is a fundamental resource for quantum communication [23–40] and quantum information protocols [12, 16, 19, 41–57].

The article is organized as follows: In **Section 2** we introduce the concept of high-dimensional path-entanglement of angular qudits [56]. Next, in **Section 3** we present an overview of angular diffraction in the position basis [57] and we derive an analytic expression for the Concurrence of high-dimensional qudits, valid for pure states. In **Section 4** we present numerical results in two specific scenarios, (IVA) high-dimensional OAM entanglement and (IVB) high-dimensional path entanglement. Finally, in **Section 5** we outline the conclusions.

2 HIGH-DIMENSIONAL ANGULAR QUDITS

Consider the experimental scheme depicted in **Figure 1**. A Gaussian pump beam produces signal (s) and idler (i) entangled twin photons by the non-linear process of SPDC. In the simplest scenario of a Gaussian pump beam with zero OAM ($l = 0$), phase matching conditions determine the two-photon down-converted state $|\psi_0\rangle$, which can be expressed in the following form [56]:

$$|\psi_0\rangle = \sum_{l=-\nu}^{\nu} c_l |l\rangle_s |-l\rangle_i, \tag{1}$$

where s and i label signal and idler photons, $|l\rangle$ refers to the OAM eigen-mode of order l, and $D = 2\nu + 1$ is the dimension of the OAM Hilbert space under consideration. Such OAM modes are characterized by an helical phase front typically expressed as $e^{il\phi}$. For $|\psi_0\rangle$ to represent a quantum state, the normalization condition imposes $\sum_{l=-\nu}^{\nu} |c_l|^2 = 1$. Subsequently, signal and idler photons are transmitted through N angular slits, as shown in **Figure 1**. The transmission functions $A_{j,n}$ of the individual angular slits are given by [56]:

$$A_{j,n}\left(\phi_j\right) = 1 \;\text{ if }\; n\beta - \alpha/2 \le \phi_j \le n\beta + \alpha/2 \;\text{ else }\; 0, \tag{2}$$

where $n = 0, \ldots, N-1$ is the angular slit label, α represents the aperture of the angular slits, and β represents the separation between consecutive angular slits. For the simplest case $N = 2$ slits, we recover the results reported in [49]. Considering N slits in both arms, there are in principle N^2 alternative pathways by

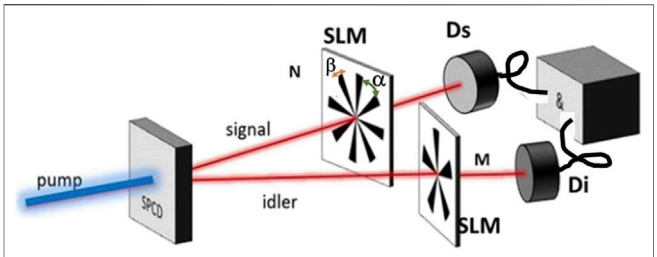

FIGURE 1 | Proposed experimental scheme for generation of high-dimensional OAM-entangled photon pairs via SPDC. Spatial Light Modulators (SLMs) containing (N, M) angular slits are placed in the path of signal and idler photons, generating high-dimensional angular qudits. Further details are in the text. The figure was modified from Ref. [56].

which the down-converted photons can pass through the apertures and get detected in coincidence at single-photon avalanche detectors D_s and D_i. The N^2 alternative paths, here labelled by the sub-index $q = 1, \ldots, N^2$, can be expressed as the outer product of the sub-spaces corresponding to each photon (s, i) passing through the slits $n = 0, \ldots, N-1$, respectively, in the following form [56]:

$$\begin{aligned} &|s,0\rangle \otimes \{|i,0\rangle, |i,1\rangle, \ldots, |i,N-1\rangle\}; \\ &|s,1\rangle \otimes \{|i,0\rangle, |i,1\rangle, \ldots, |i,N-1\rangle\}; \ldots . \\ &|s,N-1\rangle \otimes \{|i,0\rangle, |i,1\rangle, \ldots, |i,N-1\rangle\}. \end{aligned} \tag{3}$$

Spatial quantum correlations between the twin photons can be controlled so that only paths of the form $|i, n\rangle|s, n\rangle$ will have a significant contribution. We note there is a one to one mapping between the path-way basis and the OAM-mode basis. For a given path n, the two-photon state can be written in the OAM-mode basis as [49]:

$$\begin{aligned} |s,n\rangle|i,n\rangle = C \sum_l c_l \sum_{l'} \frac{1}{2\pi} \int_{-\pi}^{\pi} d\phi_s A_{s,n}(\phi_s) e^{i(l'-l)\phi_s} |l'\rangle \\ \times \sum_{l''} \frac{1}{2\pi} \int_{-\pi}^{\pi} d\phi_i A_{i,n}(\phi_i) e^{i(l''+l)\phi_i} |l''\rangle. \end{aligned} \tag{4}$$

In this notation, the single-photon quantum state with OAM of order l diffracted by the k-th slit, with OAM momentum l, can be expressed as [56]:

$$|\psi_l^k\rangle_{s,i} = \frac{\alpha}{2\pi} \sum_{l'} e^{-i(l'-l)\beta k} \mathrm{sinc}\left[\frac{\alpha(l'-l)}{2}\right] |l'\rangle_{s,i}, \tag{5}$$

where $\mathrm{sinc}[x] = \frac{\sin[x]}{x}$. In the most general case, the overlap between the diffracted states by slits k and j, with OAM labels m and l, results in:

$$\begin{aligned} \langle \psi_m^j | \psi_l^k \rangle = \left(\frac{\alpha}{2\pi}\right)^2 \sum_{l'} \sum_{l''} e^{-i(l'-l)\beta k} e^{i(l''-m)\beta j} \times \\ \mathrm{sinc}\left[\frac{\alpha(l'-l)}{2}\right] \mathrm{sinc}\left[\frac{\alpha(l''-m)}{2}\right] \langle l''|l'\rangle, \end{aligned} \tag{6}$$

where $\langle l''|l'\rangle = \delta_{l'',l'}$ due to orthonormality of OAM modes.

For the simple case of a single slit, we have $j = k = 1$, the mode overlap $\langle \psi_m | \psi_l \rangle$ can be expressed as:

$$\langle \psi_m | \psi_l \rangle = \left(\frac{\alpha}{2\pi}\right)^2 \sum_{l'} e^{i(l-m)\beta} \times \operatorname{sinc}\left[\frac{\alpha(l'-l)}{2}\right] \operatorname{sinc}\left[\frac{\alpha(l'-m)}{2}\right]. \tag{7}$$

3 HIGH-DIMENSIONAL SPATIAL MODE ENTANGLEMENT AND DIFFRACTION

In this Section we derive expressions for twin photons angular diffracted states in the position basis. As already anticipated in **Section 2**, we focus on D − dimensional ($D = 2\nu + 1$) entangled biphoton pure states of the form [57].

$$|\psi_0\rangle = \sum_{l=-\nu}^{\nu} c_l |l\rangle |-l\rangle, \tag{8}$$

where

$$|l\rangle = \int d^2\mathbf{r} u_l(\mathbf{r}) |\mathbf{r}\rangle \tag{9}$$

are single photon states in the spatial modes defined by the orthonormal transverse functions $u_l(\mathbf{r})$, i.e., $\int d^2\mathbf{r} u_l^\dagger(\mathbf{r}) u_l(\mathbf{r}) = \delta_{l,l'}$, and $\sum_{l=-\nu}^{\nu} |c_l|^2 = 1$ to ensure normalization [57, 58].

We are interested in how the entanglement of such states is modified by diffraction of the two photons on two independent opaque screens of different shapes and forms. Moreover, we focus on the case where both photons are detected after the diffracting screens. In this post-selection scenario, entanglement is only modified by the change of the spatial profile of the modes occupied by the photons due to diffraction on the screens. Under these assumptions, the quantum state of the diffracted photons can be written [57, 58].

$$|\psi\rangle = \sum_{l=-\nu}^{\nu} \tilde{c}_l |\psi_l\rangle |\psi_{-l}\rangle, \tag{10}$$

with

$$|\psi_l\rangle = \int d^2\mathbf{r} \psi_l(\mathbf{r}) |\mathbf{r}\rangle, \tag{11}$$

where the modes $\psi_l(\mathbf{r})$ are the images of the modes $u_l(\mathbf{r})$ that can be computed using standard diffraction theory [57], and $\tilde{c}_l = c_l/\sqrt{\mathcal{K}}$ with ν a renormalization constant needed to compensate for the non orthogonality of the diffracted modes $\psi_l(\mathbf{r})$, which we can express as [57, 58].

$$\mathcal{K} = \sum_{lk=-\nu}^{\nu} c_l^* c_k b_{lk} b_{-l-k}, \tag{12}$$

with

$$b_{lk} = \int d^2 \psi_l^*(\mathbf{r}) \psi_k(\mathbf{r}), \tag{13}$$

the mutual overlaps between pairs of diffracted modes [57]. We note that since the single photon states $|\psi_l\rangle$ are fully determined by the modes they occupy, we also have that $\langle \psi_l | \psi_k \rangle = b_{lk}$.

We now set to characterize the entanglement of such states developing a high-dimensional generalization of the method presented in [56, 57]. Following this path, we quantify the entanglement of the diffracted state using the Concurrence, that for pure states in arbitrary dimensions can be expressed as a function of the purity $\mathrm{Tr}[\rho^2]$ of the reduced density matrix $\rho = \mathrm{Tr}_2[|\psi\rangle\langle\psi|]$ [57].

$$C(|\psi\rangle) = \sqrt{2(1 - \mathrm{Tr}[\rho^2])}. \tag{14}$$

The reduced density matrix can be computed using the expression (11) for the quantum state of single photons in the diffracted modes and the mutual overlap (13)

$$\rho = \int d^2\mathbf{r}_2 \langle \mathbf{r}_2 | \psi \rangle \langle \psi | \mathbf{r}_2 \rangle = \sum_{kl=-\nu}^{\nu} \tilde{c}_l^* \tilde{c}_k b_{-l-k} |\psi_l\rangle \langle \psi_k|. \tag{15}$$

In a similar fashion, we can determine the purity of the reduced density matrix

$$\begin{aligned} \mathrm{Tr}[\rho^2] &= \int d^2\mathbf{r}_1 \langle \mathbf{r}_1 | \rho^2 | \mathbf{r}_1 \rangle \\ &= \sum_{l,k,p,q=-\nu}^{\nu} \tilde{c}_l^* \tilde{c}_k \tilde{c}_p^* \tilde{c}_q b_{-l-k} b_{-p-q} b_{kp} b_{lq}, \\ &= \frac{\sum_{l,k,p,q=-\nu}^{\nu} c_l^* c_k c_p^* c_q b_{-l-k} b_{-p-q} b_{kp} b_{lq}}{\left(\sum_{lk=-\nu}^{\nu} c_l^* c_k b_{lk} b_{-l-k}\right)^2} \end{aligned} \tag{16}$$

which fully determines the Concurrence **Eq. 14**. From **Eq. 16**, we see that the entanglement of diffracted biphoton states is fully characterized by the entanglement of the input state (encoded in the coefficients c_l), and by the diffraction induced overlaps of the states $|\psi_l\rangle$ (quantified by the coefficients b_{lk}).

We note that the goal of the scheme presented in **Figure 1** is to provide an alternative means for generation of entangled quantum states in high dimensions, using only two photons. It should be mentioned that the operations introduced by the SLMs are local and cannot increase the total amount of entanglement, which is given by the entanglement content present in the initial state generated by the SPDC process, as quantified by the Concurrence (**Eq. 14**). In particular, for a maximally entangled pure input state in D-dimensions, the Concurrence is given $C_D = \sqrt{2(1 - 1/D)}$ whose upper bound is $\sqrt{2}$, since the reduced density matrix of a bipartite maximally entangled state is a maximally mixed state, proportional to the Identity operator.

4 EXAMPLES

In the following, we will apply the theoretical framework presented in **Sections 2**, **3** to two particular examples. In particular, in **Section 4A**, we will consider high-dimensional OAM-entangled biphotons diffracted on screens containing a single angular aperture, while in **Section 4B** we will consider initial biphotons entangled in few OAM modes impinging on screens containing multiple apertures.

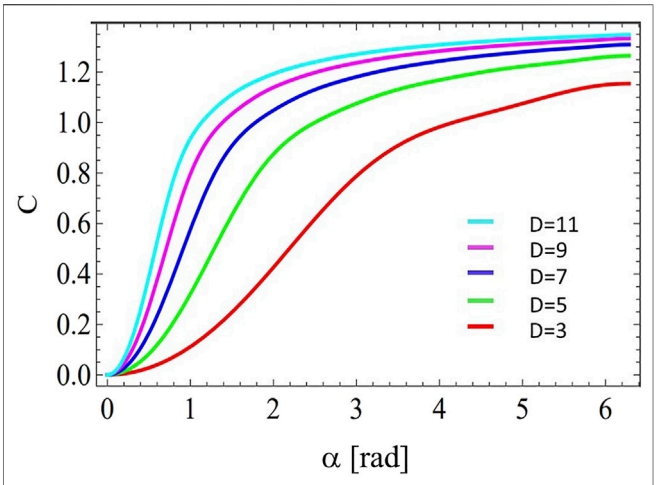

FIGURE 2 | Concurrence vs. angular aperture size for different OAM subpsace dimension ($D = 2\nu + 1$) as indicated in the label, considering a single angular slit for both signal and idler photons ($M = N = 1$). Details are in the text.

A. High-Dimensional OAM Entanglement on Angular Apertures

We now specialize to the study of maximally entangled states, i.e., we set $c_l = 1/\sqrt{2\nu+1}\ \forall l$ in **Eq. 8**. Moreover, we assume the spatial modes carrying OAM to be fully characterized by their helical phase front so that we have

$$|l\rangle = \frac{1}{\sqrt{2\pi}}\int_{-\pi}^{\pi} d\phi e^{il\phi}|\phi\rangle, \tag{17}$$

where $|\phi\rangle = \int r dr u_l(\vec{r})|\vec{r}\rangle$. After transmission through an angular aperture of size α, $|l\rangle$ becomes:

$$|\psi_l\rangle = \frac{1}{\sqrt{\alpha}}\int_{-\alpha/2}^{\alpha} d\phi e^{il\phi}|\phi\rangle. \tag{18}$$

Using **Eq. 18**, we can calculate the mutual overlaps (13) which results into

$$b_{lk} = \frac{1}{\alpha}\int_{-\alpha/2}^{\alpha} d\phi e^{i(k-l)\phi} = \mathrm{sinc}\left[\frac{(l-k)\alpha}{2}\right]. \tag{19}$$

Eq. 19 implies that $b_{lk} = b_{-l-k}$, accordingly in this case the purity (16) can be rewritten as

$$\mathrm{Tr}[\rho^2] = \frac{\sum_{lkpq=-\nu}^{\nu} b_{lk}b_{pq}b_{lp}b_{kq}}{\left(\sum_{lk=-\nu}^{\nu} b_{lk}^2\right)^2}. \tag{20}$$

Combining **Eqs 19**, **20** into **Eq. 14** we can compute the concurrence of the diffracted state, which is plotted in **Figure 2**.

B. High-Dimensional Path-Entanglement on Angular Apertures

We now consider an alternative scenario for generation of high-dimensional entanglement relying on path-entangled modes generated by multiple angular apertures in the path of signal and idler photons (s, i). For simplicity, we consider twin photons initially prepared in a OAM qubit state of the form:

$$|\psi_0\rangle = |l_0\rangle_s|-l_0\rangle_i. \tag{21}$$

When masks with (N, M) angular slits for (s, i) photons are placed in each spatial mode (seen **Figure 1**), the biphoton state immediately after the apertures can be expressed as [36]:

$$|\psi'\rangle \propto \sum_{k=-\frac{(N-1)}{2}}^{\frac{(N-1)}{2}} \sum_{k'=-\frac{(M-1)}{2}}^{\frac{(M-1)}{2}} \phi(x_s, x_i, z)|\psi^k\rangle_s|\psi^{k'}\rangle_i, \tag{22}$$

where $x_{s,i}$ denote the position of signal and idler photons at the crystal plane (z). $\phi(x_s, x_i, z)$ indicates the biphoton amplitude at z, which can be regarded as a product of the pump transverse amplitude and phase matching function [36]. For simplicity, in what follows we consider the biphoton amplitude to be approximately constant. $|\psi^{k,k'}\rangle$ describe the quantum state of signal and idler photons diffracted by angular apertures (k, k'), respectively.

In the notation introduced in **Section 2**, for an initial state of the form $|l_0\rangle_s| - l_0\rangle_i$, the quantum state of ($s$, i) photons diffracted by angular apertures (k, k'), respectively, can be expressed as:

$$|\psi^k_{l_0}\rangle_s = \frac{\alpha}{2\pi}\sum_{l'} e^{-i(l'-l_0)\beta k}\mathrm{sinc}\left[\frac{\alpha(l'-l_0)}{2}\right]|l'\rangle_s, \tag{23}$$

$$|\psi^{k'}_{-l_0}\rangle_i = \frac{\alpha}{2\pi}\sum_{l''} e^{-i(l''+l_0)\beta k'}\mathrm{sinc}\left[\frac{\alpha(l''+l_0)}{2}\right]|l''\rangle_i. \tag{24}$$

The biphoton path-entangled state diffracted by $N \times M$ angular slits results in:

$$\begin{aligned}|\psi'\rangle = &\sum_{k=-\frac{(N-1)}{2}}^{\frac{(N-1)}{2}} \sum_{k'=-\frac{(M-1)}{2}}^{\frac{(M-1)}{2}} \left(\frac{\alpha}{2\pi}\right)^2 \times \\ &\sum_{l'}\sum_{l''} e^{-i(l'-l_0)\beta k}e^{-i(l''+l_0)\beta k'} \times \\ &\mathrm{sinc}\left[\frac{\alpha(l'-l_0)}{2}\right]\mathrm{sinc}\left[\frac{\alpha(l''+l_0)}{2}\right]|l'\rangle_s|l''\rangle_i.\end{aligned} \tag{25}$$

A compact expression for the biphoton diffracted state can be cast in the form:

$$|\psi'\rangle = \sum_{l'}\sum_{l''} c_{l',l''}|l'\rangle_s|l''\rangle_i, \tag{26}$$

where the coefficients in the summation $c_{l',l''}$ are given by:

$$\begin{aligned}c_{l',l''} = &\sum_{k=\frac{-(N-1)}{2}}^{\frac{(N-1)}{2}} \sum_{k'=\frac{-(M-1)}{2}}^{\frac{(M-1)}{2}} \left(\frac{\alpha}{2\pi}\right)^2 \times \\ &e^{-i(l'-l_0)\beta k}e^{-i(l''+l_0)\beta k'} \times \\ &\mathrm{sinc}\left[\frac{\alpha(l'-l_0)}{2}\right]\mathrm{sinc}\left[\frac{\alpha(l''+l_0)}{2}\right].\end{aligned} \tag{27}$$

The Concurrence for the path-entangled biphoton states can be derived considering the generalized overlap (b_{lm}) of the form:

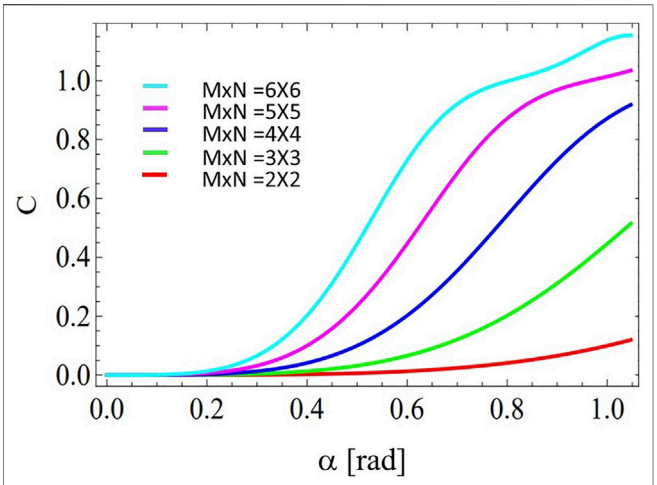

FIGURE 3 | Concurrence vs. angular aperture size for different path dimensions ($M \times N$) and aperture sizes in the range $[0, 2\pi/N_{\max}]$ with $N_{\max} = 6$. Details are in the text.

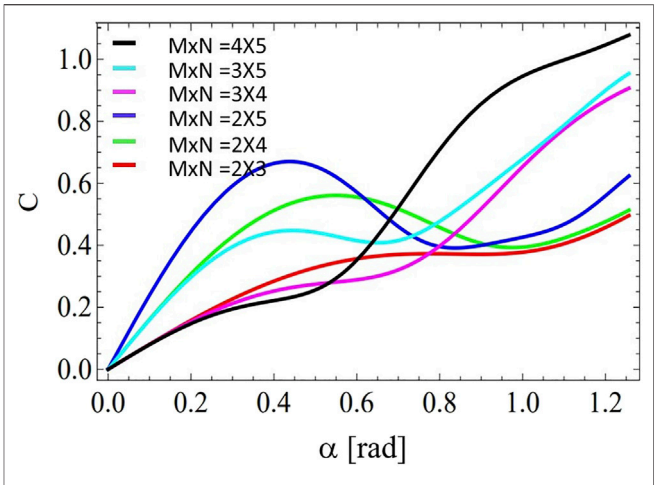

FIGURE 4 | Concurrence vs. angular aperture size for different path dimensions ($M \times N$) and aperture sizes in the range $[0, 2\pi/N_{\max}]$ with $N_{\max} = 5$. Details are in the text.

$$b_{lm} = \sum_{k,k'} \int_{-\pi}^{\pi} d\phi e^{i(m-l)\phi} A_k A_{k'}, \tag{28}$$

where $A_{k,k'}$ describe the angular aperture functions introduced in **Section 2**.

Figures 3–5 present numerical simulations of the Concurrence (C) vs. Aperture Size (in radians), for different angular slit dimensions $M \times N$ for signal and idler photons, respectively. For the case of N and M angular slits the maximum angular aperture size per slit is $2\pi/N$ and $2\pi/M$, respectively. Taking this limit into consideration, we performed numerical simulations for aperture sizes in the range $2\pi/N_{\max}$, where $N_{\max}$ is the maximum number of slits between the values of N and M considered in the specific numerical simulations. All angular dimensions considered are experimentally feasible in view of the resolution of state-of-the-art Spatial Light Modulators (SLMs) [56]. Different curves in **Figure 3** correspond to symmetric path-dimensions $M \times N$ given by 2×2, 3×3, 4×4, 5×5, and 6×6 angular silts, for aperture sizes in the range $[0, 2\pi/N_{\max}]$, with $N_{\max} = 6$. Different curves in **Figure 4** correspond to asymmetric path-dimensions $M \times N$ given by 2×2, 2×4, 2×5, 3×4, 3×5 and 4×5 angular silts, for aperture sizes in the range $[0, 2\pi/N_{\max}]$, with $N_{\max} = 5$. Different curves in **Figure 5** correspond to asymmetric path-dimensions $M \times N$ given by 5×6, 5×7, 5×8, 6×7, 6×8 and 7×8 angular silts, for aperture sizes in the range $[0, 2\pi/N_{\max}]$, with $N_{\max} = 8$. Interestingly, within our approximation, for a sufficiently large number of angular apertures ($M \times N$) it is possible to reach the same amount of entanglement as with high-dimensional OAM.

Figure 2 indicates that for the case of OAM-entangled modes in D-dimensions, it is possible to reach the maximal amount of entanglement present in the initial state for a sufficiently large angular aperture size (nearly equal to 2π). On the other hand, a similar amount of entanglement can be achieved with path-entangled states using smaller angular apertures, by introducing a sufficiently large number of angular slits (**Figures 3–5**). Therefore, we can conclude that the advantage of high-dimensional path-entangled states is that they can enable to achieve the maximal entanglement present in the initial state at reduced angular aperture sizes, by increasing the number of angular slits.

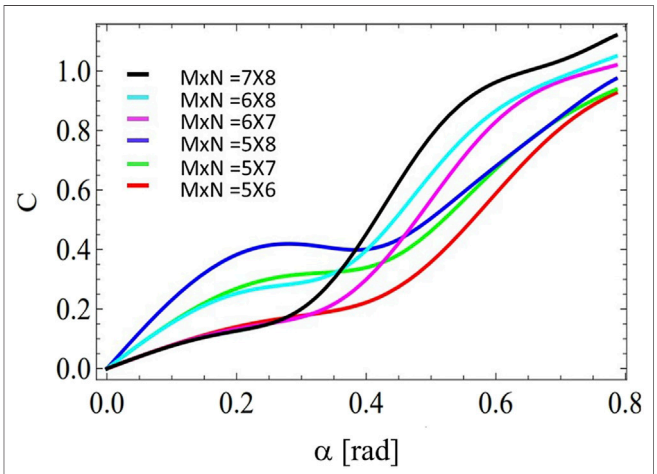

FIGURE 5 | Concurrence vs. angular aperture size for different path dimensions ($M \times N$) and aperture sizes in the range $[0, 2\pi/N_{\max}]$ with $N_{\max} = 8$. Details are in the text.

Close inspection of **Figures 2–5** reveals that the monotonicity in the Concurrence is directly linked to a symmetric slit configuration ($M = N$), as depicted in **Figures 2**, **3**. While non-monotonicity can be ascribed to high-dimensional interference phenomena associated with an asymmetric slit configurations ($M \neq N$), as depicted in **Figures 4**, **5**. Therefore, a tunable slit configuration can be

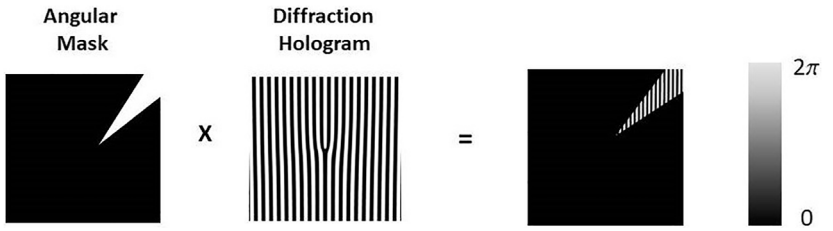

FIGURE 6 | Angular masks used to create path-entanglement and diffraction holograms used to analyze the OAM spectrum. Both the angular mask and the diffraction hologram can be programmed using the same Spatial Light Modulator. Details are in the text.

regarded as an alternative means for tailoring the entanglement content in the angular qudit state. This could prove a promising solution for instance for improving the performance of next generation function-integrated quantum circuits, among other relevant applications [50–57].

5 EXPERIMENTAL IMPLEMENTATION

The proposed experimental scheme envisioned to characterize high-dimensional entanglement using (N, M) angular slits is depicted in **Figure 1**. It is based on the experimental setup described in Ref. [49]. In this experimental scenario, a Gaussian pump laser beam with zero OAM is customarily prepared by spatial filtering using single-mode fibers. The pump power is typically in the range of $100\,mW$ and typical operational wavelength is at $\lambda = 413\,nm$. Degenerate down-converted photons at $\lambda = 826\,nm$ are created by the non-linear process of Spontaneous Parametric Down Conversion (SPDC), where a pump beam is normally incident on a non-linear crystal, for either type-I or type-II phase matching conditions. Conservation of OAM for the twin photons is granted by the SPDC process itself, for the given pump and phase matching conditions [49]. The novel element introduced in the setup is given by the angular masks containing (N, M) angular slits, for signal and idler photons, respectively. Such angular slits are programmed using state-of-the-art Spatial Light Modulators (SLMs). The OAM spectrum of the diffracted states can be analyzed in terms of OAM spiral harmonics, typically over a range from $l = 12$ to $l = 12$. This is routinely accomplished in the laboratory using diffraction holograms, which for ease of implementation can be programmed in the same SLM used for the angular masks (**Figure 6**). Such OAM projective measurements are registered via Coincidence Counts (R_{si}), in the (l_s, l_i) OAM basis. The Coincidence Count (CC) rate R_{si} of single-photon detectors $D_{s(i)}$ gives the probability that signal(idler) photons are detected at single-photon detector $D_{s(i)}$ in mode $|ls(i)\rangle$, in a given fixed-time coincidence window. Specifically, the CC rate is given by $R_{si} = \langle\, l_i|\langle l_s\|\rho\|l_i|\rangle l_s|$ [49].

An alternative, more exciting, detection approach would consist of implementing a detection scheme that could resolve the angular slits taken by the photons and enable to reconstruct the density matrix directly in the path-way basis. We envision that such complex detection schemes could in principle be implemented by means of N-arm interferometers in combination with spatial multiplexing techniques. More specific, spatial multiplexing could enable active stabilization of such complex interferometers, which is a key experimental challenge in the context [59].

As mentioned, SLMs are used both for preparation of angular masks, and for analysis of the transmitted state in the OAM basis via diffraction holograms. As it is well known in the literature, SLMs are programmable refractive elements which enable full control of the amplitude of the diffracted beams. In the standard technique, if the index of the analysis l-forked hologram is opposite to that of the incoming mode, planar wave-fronts with on-axis intensity are generated in the first diffraction order. The on-axis intensity can be coupled to single-mode fibers with high efficiency, and can be measured with single-photon detectors $D_{s,i}$, using a coincidence count circuit (**Figure 1**). The maximum number of angular slits that can be implemented in a realistic experimental situation will be fundamentally limited by the finite spatial and angular correlation width of signal and idler photons, as well as by the resolution of the SLM itself [56].

6 DISCUSSION

We presented a method to generate entangled photonic states in high-dimensional quantum systems, the so-called qudits, by exploiting quantum correlations of OAM-entangled photons produced by the non-linear process of Spontaneous Parametric Down Conversion. Diffraction masks containing N angular slits in the path of twin photons define a qudit space of dimension N^2, spanned by the alternative pathways of the entangled photons. We quantify the entanglement of path-entangled photons by an explicit calculation of the Concurrence, valid for pure states. We reported numerical results for the Concurrence as a function of the angular aperture size for the case of high-dimensional OAM-entangled photons and for the case the case of high-dimensional entanglement produced by $N \times M$ angular slits. Interestingly, within our approximation, it is possible to reach the same amount of entanglement using either high-dimensional OAM-entangled

photons or path-entangled photons. Our results shine light into the fundamental quantum aspects of two-photon angular interference, and provide alternative means for preparation of entangled quantum states in high-dimensions, a fundamental resource for quantum information and quantum simulation protocols [12, 16, 19, 25–57].

DATA AVAILABILITY STATEMENT

Data supporting the conclusion of this article will be made available by the authors upon request.

AUTHOR CONTRIBUTIONS

GP conceived the idea, developed the theory, performed numerical simulations, and wrote the manuscript.

ACKNOWLEDGMENTS

The authors gratefully acknowledge Giacomo Sorelli for the derivation of **Eq. 15**. GP acknowledges Sonja Franke-Arnold, Antonio Zelaquett-Khoury, and Leonardo Neves for helpful discussions. GP acknowledges financial support via PICT Startup.

REFERENCES

1. Hong CK, Ou ZY, Mandel L. Measurement of Subpicosecond Time Intervals between Two Photons by Interference. *Phys Rev Lett* (1987) 59:2044–6. doi:10.1103/physrevlett.59.2044
2. Brendel J, Gisin N, Tittel W, Zbinden H. Pulsed Energy-Time Entangled Twin-Photon Source for Quantum Communication. *Phys Rev Lett* (1999) 82:2594–7. doi:10.1103/physrevlett.82.2594
3. Thew RT, Tanzilli S, Tittel W, Zbinden H, Gisin N. Experimental Investigation of the Robustness of Partially Entangled Qubits Over 11 km. *Phys Rev A* (2002) 66:062304. doi:10.1103/physreva.66.012303
4. Herzog TJ, Rarity JG, Weinfurter H, Zeilinger A. Frustrated Two-Photon Creation via Interference. *Phys Rev Lett* (1994) 72:629–32. doi:10.1103/physrevlett.72.629
5. Jha AK, O'Sullivan MN, Clifford Chan KW, Boyd RW. Temporal Coherence and Indistinguishability in Two-Photon Interference Effects. *Phys Rev A* (2008) 77:021801(R). doi:10.1103/physrevc.77.045801
6. Neves L, Lima G, Aguirre Gómez JG, Monken CH, Saavedra C, Pádua S, et al. Generation of Entangled States of Qudits Using Twin Photons. *Phys Rev Lett* (2005) 94:100501.
7. Fonseca EJS, Machado da Silva JC, Monken CH, Pádua S. Generation of Entangled States of Qudits using Twin Photons. *Phys Rev A* (2000) 61:023801. doi:10.1103/physreve.61.1550
8. Neves L, Lima G, Fonseca EJS, Davidovich L, Pádua S. Characterizing Entanglement in Qubits Created With Spatially Correlated Twin Photons. *Phys Rev A* (2007) 76:032314. doi:10.1103/physreva.76.032314
9. Aspect A, Grangier P, Roger G. Experimental Realization of Einstein-Podolsky-Rosen-BohmGedankenexperiment: A New Violation of Bell's Inequalities. *Phys Rev Lett* (1982) 49:91–4. doi:10.1103/physrevlett.49.91
10. Mandel L. Quantum Effects in One-Photon and Two-Photon Interference. *Rev Mod Phys* (1999) 71:S274–S282. doi:10.1103/revmodphys.71.s274
11. Zeilinger A. Experiment and the Foundations of Quantum Physics. *Rev Mod Phys* (1999) 71:S288–S297. doi:10.1103/revmodphys.71.s288
12. Ekert AK. Quantum Cryptography Based on Bell's Theorem. *Phys Rev Lett* (1991) 67:661–3. doi:10.1103/physrevlett.67.661
13. Bennett CH, Wiesner SJ. Communication via One- and Two-Particle Operators on Einstein-Podolsky-Rosen States. *Phys Rev Lett* (1992) 69:2881–4. doi:10.1103/physrevlett.69.2881
14. Jack B, Padgett MJ, Franke-Arnold S. Angular Diffraction. *New J Phys* (2008) 10:103013. doi:10.1088/1367-2630/10/10/103013
15. Jha AK, Mishra H. Constraints on Nuclear Matter Parameters of an Effective Chiral Model. *Phys Rev A* (2008) 78:043810. doi:10.1103/physrevc.78.065802
16. Bennett CH, Brassard G, Crépeau C, Jozsa R, Peres A, Wootters WK. Teleporting an Unknown Quantum State via Dual Classical and Einstein-Podolsky-Rosen Channels. *Phys Rev Lett* (1993) 70:1895–9. doi:10.1103/physrevlett.70.1895
17. Barnett SM, Pegg DT. Quantum Theory of Rotation Angles. *Phys Rev A* (1990) 41:3427–35. doi:10.1103/physreva.41.3427
18. Franke-Arnold S, Barnett SM, Yao E, Leach J, Courtial J, Padgett M. Uncertainty Principle for Angular Position and Angular Momentum. *New J Phys* (2004) 6:103. doi:10.1088/1367-2630/6/1/103
19. Vaziri A, Weihs G, Zeilinger A. Experimental Two-Photon, Three-Dimensional Entanglement for Quantum Communication. *Phys Rev Lett* (2002) 89:240401. doi:10.1103/physrevlett.89.240401
20. Langford NK, Harvey MD, O'Brien JL, Pryde GJ, Gilchrist A, Bartlett SD, et al. Measuring Entangled Qutrits and Their Use for Quantum Bit Commitment. *Phys Rev Lett* (2004) 93:053601.
21. Leach J, Jack B, Romero J, Ritsch-Marte M, Boyd RW, Jha AK, et al. Violation of a Bell Inequality in Two-Dimensional Orbital Angular Momentum State-Spaces. *Opt Express* (2009) 17:8287. doi:10.1364/oe.17.008287
22. Dadda A, Leach J, Buller GS, Padgett MJ, Andersson E. Experimental Highdimensional Two-Photon Entanglement and Violations of Generalized Bell Inequalities. *Nat Phys* (2011) 7:677–80.
23. Kwiat PG, Mattle K, Weinfurter H, Zeilinger A, Sergienko AV, Shih Y. New High-Intensity Source of Polarization-Entangled Photon Pairs. *Phys Rev Lett* (1995) 75:4337–41. doi:10.1103/physrevlett.75.4337
24. Ramelow S, Ratschbacher L, Fedrizzi A, Langford NK, Zeilinger A. Discrete Tunable Color Entanglement. *Phys Rev Lett* (2009) 103:253601. doi:10.1103/physrevlett.103.253601
25. Rarity JG, Tapster PR. Experimental Violation of Bell's Inequality Based on Phase and Momentum. *Phys Rev Lett* (1990) 64:2495–8. doi:10.1103/physrevlett.64.2495
26. O'Sullivan-Hale MN, Ali Khan I, Boyd RW, Howell JC. Pixel Entanglement: Experimental Realization of Optically Entangled d=3 and d=6 Qudits. *Phys Rev Lett* (2005) 94:220501.
27. Walborn SP, de Oliveira AN, Thebaldi RS, Monken CH. Entanglement and Conservation of Orbital Angular Momentum in Spontaneous Parametric Down-Conversion. *Phys Rev A* (2004) 69:023811. doi:10.1103/physreva.69.023811
28. Franke-Arnold S, Barnett SM, Padgett MJ, Allen L. Two-photon Entanglement of Orbital Angular Momentum States. *Phys Rev A* (2002) 65:033823. doi:10.1103/physreva.65.033823
29. Torres JP, Alexandrescu A, Torner L. *Phys Rev A* (2003) 68:050301(R). doi:10.1103/physreva.68.050301
30. Wootters WK. Entanglement of Formation of an Arbitrary State of Two Qubits. *Phys Rev Lett* (1998) 80:2245–8. doi:10.1103/physrevlett.80.2245
31. Jack B, Leach J, Ritsch H, Barnett SM, Padgett MJ, Franke-Arnold S. Precise Quantum Tomography of Photon Pairs with Entangled Orbital Angular Momentum. *New J Phys* (2009) 11:103024. doi:10.1088/1367-2630/11/10/103024
32. Molina-Terriza G, Torres JP, Torner L. Orbital Angular Momentum of Photons in Noncollinear Parametric Downconversion. *Opt Commun* (2003) 228:155–60. doi:10.1016/j.optcom.2003.09.071
33. Mair A, Vaziri A, Weihs G, Zeilinger A. Entanglement of the Orbital Angular Momentum States of Photons. *Nature* (2001) 412:313–6. doi:10.1038/35085529
34. Leach J, Dennis MR, Courtial J, Padgett MJ. Vortex Knots in Light. *New J Phys* (2005) 7:55. doi:10.1088/1367-2630/7/1/055
35. Tyler GA, Boyd RW. Influence of Atmospheric Turbulence on the Propagation of Quantum States of Light Carrying Orbital Angular Momentum. *Opt Lett* (2009) 34:142. doi:10.1364/ol.34.000142
36. Machado P, Slooter RJ, Blanter YM. Quantum Signatures in Quadratic Optomechanics. *Phys Rev A* (2019) 99:063839. doi:10.1103/physreva.99.053801

37. Puentes G, Voigt D, Aiello A, Woerdman JP. *Opt Lett* (2005) 31:2057–9.
38. Ling A, Han PY, Lamas-Linares A, Kurtsiefer C. Preparation of bell States with Controlled white Noise. *Laser Phys* (2006) 16:1140–4. doi:10.1134/s1054660x06070206
39. Wei T-C, Altepeter JB, Branning D, Goldbart PM, James DF, Jeffrey E, et al. Synthesizing Arbitrary Two-Photon Mixed States. *Phys Rev A* (2005) 71: 032329. doi:10.1103/physreva.71.032329
40. Kaslikowski D, Gnaciński P, Żukowski M, Miklaszewski W, Zeilinger A. Violations of Local Realism by Two Entangled N-Dimensional Systems Are Stronger than for Two Qubits. *Phys Rev Lett* (2000) 85:4418.
41. Collins D, Gisin N, Linden N, Massar S, Popescu S. Bell Inequalities for Arbitrarily High-Dimensional Systems. *Phys Rev Lett* (2002) 88:040404.
42. Bechmann-Pasquinucci H, Peres A. Quantum Cryptography with 3-State Systems. *Phys Rev Lett* (2000) 85:3313–6. doi:10.1103/physrevlett.85.3313
43. Durt T, Cerf NJ, Gisin N, Zukowski M. *Phys Rev A* (2003) 67:012311. doi:10.1103/physreva.67.012311
44. Bourennane M, Karlsson A, Bjork G. *Phys Rev A* (2001) 64:012306. doi:10.1103/physreva.64.012306
45. Cerf NJ, Bourennane M, Karlsson A, Gisin N. Security of Quantum Key Distribution Usingd-Level Systems. *Phys Rev Lett* (2002) 88:127902. doi:10.1103/physrevlett.88.127902
46. Howell JC, Lamas-Linares A, Bouwmeester D. *Phys Rev Lett* (2002) 85:030401.
47. Thew RT, Acın A, Zbinden H, Gisin N. *Phys Rev Lett* (2004) 93:010503. doi:10.1103/physrevlett.93.010503
48. de Riedmatten H, Marcikic I, Zbinden H, Gisin N. Creating High-Dimensional Time-Bin Entanglement Using Mode-Locked Lasers. *Qic* (2002) 2:425–33. doi:10.26421/qic2.6-1
49. Kumar Jha A, Leach J, Jack B, Franke-Arnold S, Barnett S, Boyd R, et al. *Phys Rev Lett* (2010) 104:010501. doi:10.1103/physrevlett.104.010501
50. Puentes G, Datta A, Feito A, Eisert J, Plenio MB, Walmsley IA. Entanglement Quantification from Incomplete Measurements: Applications Using Photon-Number-Resolving Weak Homodyne Detectors. *New J Phys* (2010) 12:033042. doi:10.1088/1367-2630/12/3/033042
51. Puentes G, Waldherr G, Neumann P, Balasubramanian G, Wrachtrup J. *Scientific Rep* (2014) 4:1–6. doi:10.1038/srep04677
52. Puentes G, Aiello A, Voigt D, Woerdman JP. *Phys Rev A* (2007) 75:032319. doi:10.1103/physreva.75.032319
53. Puentes G, Colangelo G, Sewell RJ, Mitchell MW. Planar Squeezing by Quantum Non-demolition Measurement in Cold Atomic Ensembles. *New J Phys* (2013) 15:103031. doi:10.1088/1367-2630/15/10/103031
54. Takayama O, Sukham J, Malureanu R, Lavrinenko AV, Puentes G. Photonic Spin Hall Effect in Hyperbolic Metamaterials at Visible Wavelengths. *Opt Lett* (2018) 43:4602–5. doi:10.1364/ol.43.004602
55. Moulieras S, Lewenstein M, Puentes G. Entanglement Engineering and Topological protection by Discrete-Time Quantum Walks. *J Phys B: Mol Opt Phys* (2013) 46:104005. doi:10.1088/0953-4075/46/10/104005
56. Puentes G. High-dimensional Angular Two-Photon Interference and Angular Qudit States. *OSA Continuum* (2020) 3:1616. doi:10.1364/osac.392178
57. Sorelli G, Shatokhin VN, Buchleitner A. Universal Entanglement Loss Induced by Angular Uncertainty. *J Opt* (2020) 22:024002. doi:10.1088/2040-8986/ab66d0
58. Sorelli G, Shatokhin VN, Roux FS, Buchleitner A. *Phys Rev A* (2019) 97: 013849.
59. de Riedematten H, Marcikic I, Scarani V, Tittel W, Zbinden H, Gisin N. Tayloring Photonic Entanglement in High-Dimensional Hilbert Spaces. *Phys Rev A* (2003) 69:050304.

Conflict of Interest: The author declares that the research was conducted in the absence of any commercial or financial relationships that could be construed as a potential conflict of interest.

Publisher's Note: All claims expressed in this article are solely those of the authors and do not necessarily represent those of their affiliated organizations, or those of the publisher, the editors and the reviewers. Any product that may be evaluated in this article, or claim that may be made by its manufacturer, is not guaranteed or endorsed by the publisher.

frontiers | Frontiers in Physics

ORIGINAL RESEARCH
published: 16 June 2022
doi: 10.3389/fphy.2022.896174

Nonlinear Quantum Optics With Structured Light: Tightly Trapped Atoms in the 3D Focus of Vectorial Waves

R. Gutiérrez-Jáuregui[1]* *and R. Jáuregui*[2]*

[1]Department of Physics, Columbia University, New York, NY, United States, [2]Departamento de Física Cuántica y Fotónica, Instituto de Física, Universidad Nacional Autónoma de México, Circuito de la Investigación Científica s/n, Ciudad Universitaria, Ciudad de México, Mexico

Atomic gases tightly trapped near the focus of an electromagnetic wave interact with photons that exhibit a complex structure, displaying strong gradients of field amplitude and local polarization that can lead to topological phase singularities. We illustrate the consequences of this structure on a paradigmatic nonlinear optical process: three-wave mixing. The process begins by proper selection of the pump field, whose spatial structure is tailored to present huge gradients of the EM field that enhance atomic excitations through forbidden transitions. Atoms can then be depopulated *via* two electric dipole decays in a cascade configuration, thus providing the three necessary waves. The properties of the down-converted photons are conditioned to those of the pump field through phase matching conditions. It is emphasized that the expression of the photons must incorporate both the structure of the vectorial EM modes and the spatial configuration of the atomic trap. Due to the three-dimensional focusing, the slowly varying envelope approximation becomes inadequate when describing the scattered EM field. We discuss an alternative using a Green function formalism valid for any configuration of the field that also allows to identify the phase matching conditions. Spherical vectorial waves exemplify most concepts here discussed, including the possibility of observing nonlinear quantum phenomena at the single photon level.

Keywords: quantum optics and applications, nonlinear optics and laser properties, structured light (SL), three-wave mixing (TWM), forbidden transition

OPEN ACCESS

Edited by:
Omar Magana-Loaiza, Louisiana State University, United States

Reviewed by:
Blas Manuel Rodriguez Lara, Instituto de Tecnología y Educación Superior de Monterrey (ITESM), Mexico
Jose Javier Sanchez Mondragon, National Institute of Astrophysics, Optics and Electronics (INAOE), Mexico

***Correspondence:**
R. Jáuregui
rocio@fisica.unam.mx
R. Gutiérrez-Jáuregui
r.gutierrez.jauregui@gmail.com

Specialty section:
This article was submitted to Quantum Engineering and Technology, a section of the journal Frontiers in Physics

Received: *14 March 2022*
Accepted: *19 April 2022*
Published: *16 June 2022*

Citation:
Gutiérrez-Jáuregui R and Jáuregui R (2022) Nonlinear Quantum Optics With Structured Light: Tightly Trapped Atoms in the 3D Focus of Vectorial Waves. Front. Phys. 10:896174. doi: 10.3389/fphy.2022.896174

It is now 60 years from publication of the emblematic work: *Interaction between light waves in a nonlinear dielectric* where Bloembergen and collaborators set out to connect the radiative response of electrons in atomic gases to the nonlinear optical properties of macroscopic dielectrics [1]. The connection was based on the collective, coherent scattering of light from atoms inside the gas and its relation to the incident electromagnetic field. The authors showed that the coherence between scattered and incident fields induces electric moments on the atoms that can yield nonlinear terms in the field strength, thus coupling waves of different frequencies. To unearth these effects a quasimonochromatic light source of high-brightness, directionality, and stable intensity as that given by the laser was required [1]. As modern technologies delve deeper into miniaturization, we need to look back at this connection but now placing emphasis on an efficient transfer of light at low intensities. An efficiency that can be reached by tailoring spatial and temporal profiles of light and matter through light-shaping techniques [2] and versatile atomic traps [3, 4].

Considered most broadly, the nonlinear process arises from the underlying interaction between light and matter. An illuminated atom probes and modifies the surrounding electromagnetic (EM) field, acquiring information on field intensities, gradients, and temporal correlations as it scatters photons between populated and vacuum modes. When the illuminating field is tailored to match the spatial and temporal profiles of the atomic radiation pattern, it can create a strong nonlinear response. Three-wave mixing represents the most simple response where fields of different frequencies couple and the potential of structured light is made apparent. Its implementation requires for three waves to induce a cycling transition in an atomic medium: moving up *via*, for instance, an electric quadrupole transition and cascading down *via* two electric dipole transitions through an intermediate level. Under adequate phase matching conditions an incident beam inducing the quadrupole transition gives rise to lower frequency waves, thus acting as a parametric amplifier. This example was chosen in Ref. [1] to show how symmetry constraints affect the nonlinear coupling. The experimental challenges to induce this process in atomic gases at the time were, however, formidable, with the conditions for observing quadrupole transitions being found in astrophysical or laboratory plasmas mostly [5]. Experiments searching to create correlated photons whose frequencies matched the atomic transition moved towards next order [1]. The first sources of correlated photon pairs were based on a cascade decay in a four-wave mixing process [6, 7] and led to enabling technologies in lithography [8], tomography [9], cryptography [10] and imaging [11, 12] with multiple physics [13] and transdisciplinary [14, 15] applications.

Atomic electric quadrupole transitions require large gradients in the amplitude of the incoming field. It is now possible to meet the experimental challenges to induce these transitions and explore three-wave mixing in atomic gases. On the one hand, further development of high-intensity lasers allows for the observation of quadrupole transitions even using thermal atomic samples and paraxial pump beams [16–18]. On the other hand, a quadrupole transition can be induced by large gradients in the amplitude of the incident EM field down to the limit of weak intensities. For this, spatial gradients are generated by shaping light using either phase singularities [19, 20] or evanescent waves [21] for which even micro-Watt intensity lasers can suffice [22].

In this manuscript we look back at the three-wave mixing process following ideas of light shaping and monitoring mechanisms that have been developed since the early days of nonlinear optics. Deep down this work is driven by the following thought: transitions with a single photon can trigger strong nonlinear optical processes when the spatial profile of the photon is tailored. The ideal scenario involves spherical vectorial waves, whose implementation remains challenging as they require control of the full 4π angle surrounding the atom. There are, however, experimental platforms where this control is achieved to a good approximation. In particular a single ion trapped at the focus of a parabolic mirror [23, 24] is a feasible set-up for achieving nonlinear strong coupling between few photons associated to vectorial modes. It has already been shown that a single photon can induce an electric dipole transition with high-probability in this set-up due to the similarities between parabolic and spherical waves [25]. Here, we study a three-wave mixing process based on ideal spherical vectorial modes [26]. We consider tightly trapped atoms in the Lamb-Dicke regime where the spatial confinement approaches the typical transition wavelengths. Through this ideal scenario we identify the theoretical tools necessary to understand the nonlinear process in detail, and establish a route to perform theoretical and experimental realizations of nonlinear optics events with a minimum number of photons.

The manuscript is organized as follow. In **Section 1** we introduce our model where a tightly trapped atom is coupled to a structured EM field. Emphasis is placed on the vectorial structure of the field and effects related to the spatial extent of the trap on the atom-light coupling. We show that the trap strength can alter the atomic multipole decay rates through a form factor. At the end of this Section we revisit spherical vectorial waves and their relevance for the system under study. **Section 2** concerns the connection between atomic transitions and nonlinear optics. We consider the specific example of an atom in a cascade configuration driven *via* an electric quadrupole transition by an incoming spherical wave. The nonlinear susceptibilities and collective responses of atomic systems are worked out for tightly trapped atoms. The mesoscopic densities of electric dipole and quadrupole polarization as sources of scattered photons are discussed. In **Section 3** we introduce a dyadic Green function formalism that can be used to overcome the theoretical challenges that rise for deeply focused modes, such as, non-applicability of the slowly varying envelope approximation and the identification of the phase matching conditions. We conclude in **Section 4** with a recapitulation of our results and the scope of our analyses.

1 ELECTRODYNAMICS BEYOND THE ELECTRIC DIPOLE APPROXIMATION

We consider an atomic gas coupled to a free electromagnetic field. The dynamics of this composite system are given by the Hamiltonian

$$\hat{\mathcal{H}} = \hat{\mathcal{H}}_{\text{atom}} + \hat{\mathcal{H}}_{\text{field}} + \hat{\mathcal{H}}_{\text{int}}, \tag{1}$$

where $\hat{\mathcal{H}}_{\text{field}}$ describes the free electromagnetic field, $\hat{\mathcal{H}}_{\text{atom}}$ the center-of-mass and electronic state of the atomic gas in the absence of the EM field, and $\hat{\mathcal{H}}_{\text{int}}$ links atom and field.

The gas is assumed to be tightly trapped and formed by atoms with three relevant electronic states $|s\rangle (s = a, b, c)$ in a cascade configuration sketched in **Figure 1**. It is described by the Hamiltonian

$$\hat{\mathcal{H}}_{\text{atom}} = \sum \hbar\omega_A |\Phi_A\rangle\langle\Phi_A| + \sum \hbar\omega_s |s\rangle\langle s|, \tag{2}$$

where the operator $\hat{\sigma}_{ss'} = |s\rangle\langle s'|$ acts over electronic states while $|\Phi_A\rangle\langle\Phi_A|$ acts over vibrational states that describe the atomic motion inside the trap; the parameters ω_s and ω_A refer to electronic and vibrational frequencies, respectively. These

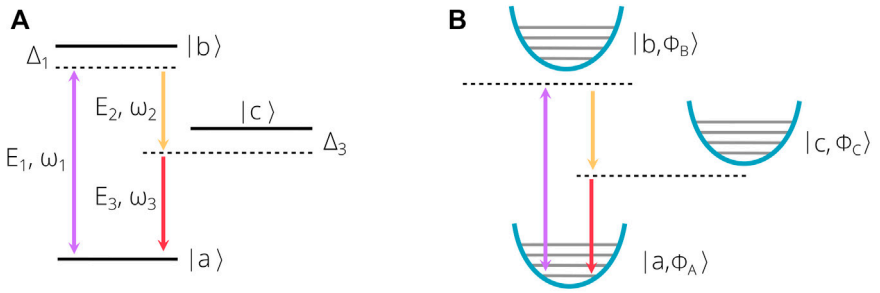

FIGURE 1 | (A) A three-level atom mediates the interaction between different waves. It is considered to be excited *via* a quadrupole transition connecting levels $|a\rangle$ and $|b\rangle$ and decays through cascade dipole transitions along level $|c\rangle$. **(B)** Since the atomic system is trapped in a region comparable to the involved radiative wavelengths, vibrational motion effects must be included.

states are connected by the free EM field, whose evolution is described by

$$\hat{\mathcal{H}}_{\text{field}} = \sum_{\gamma} \hbar\omega_{\gamma}\hat{a}_{\gamma}^{\dagger}\hat{a}_{\gamma} \tag{3}$$

with $\hat{a}_{\gamma}$ the annihilation operator for an EM mode of frequency ω_{γ}. The index γ denotes a set of parameters that characterize the mode, e.g., in a plane wave $\gamma = \{\mathbf{k}, \epsilon_{\mathbf{k},\lambda}\}$ refers to modes of wavevector $\mathbf{k}$ and polarization $\epsilon_{\mathbf{k},\lambda}$. The evolution of the EM field is given by Maxwell equations for the electric $\hat{\mathbf{E}}$ and magnetic $\hat{\mathbf{B}}$ field operators that, when expanded within a normal mode basis, read

$$\hat{\mathbf{E}}(\mathbf{x},t) = \sum_{\gamma} \mathbf{E}_{\gamma}^{(+)}(\mathbf{x})\hat{a}_{\gamma}e^{-i\omega_{\gamma}t} + h.c., \tag{4}$$

$$\hat{\mathbf{B}}(\mathbf{x},t) = \sum_{\gamma} i\frac{\omega_{\gamma}}{c}\nabla\times\mathbf{E}_{\gamma}^{(+)}(\mathbf{x})\hat{a}_{\gamma}e^{-i\omega_{\gamma}t} + h.c.. \tag{5}$$

It is convenient to write the mode amplitudes $\mathbf{E}_{\gamma}$ inside a restricted Fourier space where the free-space dispersion relation $|\mathbf{k}|^2 = \omega^2/c^2$ has been imposed. In this space the amplitudes are

$$\mathbf{E}_{\gamma}^{(+)}(\mathbf{x}) = \int d\Omega_{\mathbf{k}} e^{i\mathbf{k}\cdot\mathbf{x}}\mathbf{f}_{\gamma}(\theta_{\mathbf{k}},\varphi_{\mathbf{k}}), \tag{6}$$

with $d\Omega_{\mathbf{k}}$ a solid angle element and $\mathbf{f}_{\gamma}$ the angular spectrum of the mode. **Equation 6** gives a direct connection between plane waves and general structured modes.

The interaction between atom and field supports a multipole description due to the small size of the atom as compared to the wavelengths involved in most radiative transitions [27]. For extremely 3D-focused structured light, large gradients of the field amplitude and spatial-dependent polarization are found [28]. If the atom is trapped nearby the focus of the light mode it is necessary to move beyond the dipole approximation, done here through an interaction Hamiltonian

$$\hat{\mathcal{H}}_{\text{int}} = -\left[\hat{\mathbf{E}}\left(\hat{\mathbf{X}},t\right)\cdot\hat{\mathbf{d}} + \hat{\mathbf{B}}\left(\hat{\mathbf{X}},t\right)\cdot\hat{\mathbf{m}} + \frac{1}{2}\nabla\hat{\mathbf{E}}\left(\hat{\mathbf{X}},t\right):\hat{\mathbf{q}}\right], \tag{7}$$

written in terms of the atomic electric dipole $\hat{\mathbf{d}} = e\hat{\mathbf{r}}$, magnetic dipole $\hat{\mathbf{m}} = \frac{e}{2m}\hat{\mathbf{l}} + (\mu/s)\hat{\mathbf{s}}$, and electric quadrupole $\hat{\mathbf{q}}_{ij} = e(3\hat{r}_i\hat{r}_j - |\hat{\mathbf{r}}|^2\delta_{ij})$, operators. These operators act over the internal states of the atom with $\hat{\mathbf{r}}$, $\hat{\mathbf{l}}$, $\hat{\mathbf{s}}$, refering, respectively, to the relative electronic position, orbital angular momentum, and spin angular momentum; while parameters e, m, and μ refer to the electron charge, mass, and magnetic moment. The vibrational states are accounted for through the operator $\hat{\mathbf{X}}$ that denotes the atomic center-of-mass position where field operators are evaluated. Notice the double product of two range tensors defined as $\mathbf{F}$: $\mathbf{G} = \sum_{i,j}\mathbf{F}_{ij}\mathbf{G}_{ij}$.

Equation 7 illustrates how an atom probes an electromagnetic field by correlating its internal states to the state of the field. Through the electric and magnetic dipole moments it probes local field amplitudes and quadratures, through the quadrupole moment it gains information of spatial gradients of the field. By moving past the dipole moment it is possible to acquire a better landscape of the EM field. Furthermore, the theoretical tools used to describe this extended landscape resemble those commonly used under the dipole approximation. The similarity is made transparent by inserting **Eq. 4** into **Eq. 7** and applying the rotating-wave approximation, such that—in a reference frame oscillating with $\hat{\mathcal{H}}_{\text{atom}}$—the interaction Hamiltonian takes the form

$$\hat{\mathcal{H}}_{\text{int}} = \sum_{\gamma}\sum_{s,s'} e^{i(\omega_{ss'}-\omega_{\gamma})t}\hbar\kappa_{ss'}^{\gamma}\left(\tilde{\mathbf{X}}\right)\hat{a}_{\gamma}\hat{\sigma}_{s,s'} \tag{8}$$

where $\tilde{\mathbf{X}}$ is evaluated in the rotating frame and the coupling strength contains electric dipole, magnetic dipole, and electric quadrupole contributions

$$\kappa_{ss'}^{\gamma}(\mathbf{x}) = \kappa_{ss';\gamma}^{(\text{ed})}(\mathbf{x}) + \kappa_{ss';\gamma}^{(\text{md})}(\mathbf{x}) + \kappa_{ss';\gamma}^{(\text{eq})}(\mathbf{x}). \tag{9}$$

The contributions read explicitly as

$$\kappa_{ss';\gamma}^{(\text{ed})}(\mathbf{x}) = \mathbf{E}_{\gamma}^{(+)}(\mathbf{x})\cdot\mathbf{d}_{ss'}, \tag{10a}$$

$$\kappa_{ss';\gamma}^{(\text{md})}(\mathbf{x}) = \mathbf{B}_{\gamma}^{(+)}(\mathbf{x})\cdot\mathbf{m}_{ss'}, \tag{10b}$$

$$\kappa_{ss';\gamma}^{(\text{eq})}(\mathbf{x}) = \frac{1}{2}\nabla\mathbf{E}_{\gamma}^{(+)}(\mathbf{x}):\hat{\mathbf{q}}_{ss'}. \tag{10c}$$

Here, the matrix elements $\mathcal{O}_{ss'} = \langle s|\hat{\mathcal{O}}|s'\rangle$ that connect two electronic states $|s\rangle$ and $|s'\rangle$ are used.

From **Eq. 7** it is possible to obtain Rabi oscillations, decay rates, and radiative shifts caused by higher multipole terms following standard techniques used in quantum optics. There is, however, a difference that has to be emphasized. The coupling depends on the trapping strength through the operator $\hat{\mathbf{X}}$, which can induce transitions among vibrational states ruled by the matrix element

$$\langle \Phi_A | \kappa^{(\mathrm{ed})}_{ss';\gamma}\big(\tilde{\mathbf{X}}\big) | \Phi_B \rangle = \mathbf{d}_{nm} \cdot \left[\int \mathrm{d}^3\mathbf{X} \Phi^*_A(\mathbf{X}) \boldsymbol{E}^{(+)}_\gamma(\mathbf{X}) \Phi_B(\mathbf{X}) \right] e^{i\omega_{AB}t}, \tag{11}$$

plus two analogue terms for the magnetic dipole and electric quadrupole moments. With vibrational states defining the strength at which EM field an atom interact, a natural question is raised: Is it possible to alter the decay rate of an atom in an structured environment by changing the location and strength of the trap? While the effect of the location has been studied at length in the past, where tests of the Purcell enhancement factor depend on the location of an atom with respect to a boundary that alters the field distribution [29], the effect of trap strength is less explored. We answer this question in the affirmative below, where we show that for localized environments the spontaneous decay rate can be reduced (enhanced) for weaker (tighter) traps. The change is attributed to the extension of the atomic trap, which leads to an average over regions where field intensity and gradient change.

1.1 Spontaneous Emission of Tightly Trapped Atoms in Structured Environments

To describe the spontaneous emission of an atomic gas inside a structured environment, we consider the probability that an excited atom emits a photon into a free mode during a time interval τ. From **Eq. 8** the probability for this process to occur, regardless of the final vibrational state, is given by the integral

$$P^{\gamma}_{s\to s'} = \left| \int_0^\tau dt \sum_B e^{i\left(\omega_{ss'}+\omega_{AB}-\omega_\gamma\right)t} \langle \Phi_B | \kappa^{\gamma}_{ss'}(\mathbf{X}) | \Phi_A \rangle \right|^2, \tag{12}$$

thus posing frequency missmatch conditions on the modes the atom interacts most strongly with. In general these conditions depend on a vibrational shift ω_{AB}, but, when the electronic transition frequency is much larger than the relevant CM transition frequencies $\omega_{ss'} \gg \omega_{AB}$, this shift can be neglected [30]. By removing these shifts from the equation the states $|\Phi_B\rangle$ can be averaged out using the completeness of the vibrational states, leading to

$$P^{\gamma}_{s\to s'} \simeq \mathcal{S}\big(\omega_{ab}-\omega_\gamma\big) \langle \Phi_A | \kappa^{\gamma\dagger}_{ss'}(\mathbf{X}) \kappa^{\gamma}_{ss'}(\mathbf{X}) | \Phi_A \rangle, \tag{13}$$

with $\mathcal{S}(\omega_{ab}-\omega_\gamma)$ a sharp spectral function that satisfies $\mathcal{S}(\omega) \sim 2\pi\tau\delta(\omega)$ as $\tau \to \infty$ [31].

Equation 13 should be read as a probability distribution that weights the decay process. The atom interacts with many modes of the environment such that the spontaneous decay rates is obtained from the sum

$$\Gamma_{ss';A} = \sum_\gamma \frac{\partial}{\partial\tau} P^{\gamma}_{s\to s'} \tag{14}$$

consistent with the Born and Markov approximations. By removing the correlations that build-up between field and atom we have made the Born approximation, and by extending the time integral without accounting for selfconsistent exchanges we have performed the Markov approximation. In this sense, the spread $\omega_{ss} + \omega_{AB}$ introduced by vibrational states has to be much smaller than the free mode density in order to be neglected. This is usually achieved in free space, and is a good approximation to half cavities where modes acquire a linewidth.

It is now possible to identify the decay rate of an atom inside an structured environment. The transition rates between electronic states incorporate information about the spatial region explored by the atom and the vectorial nature of the radiated field. By using the angular spectrum of the field defined in **Eq. 6** the spontaneous rates are found to be [25].

$$\Gamma^{(\mathrm{ed})}_{ab;A} = \sum_{\sigma=,\pm,0} \sum_\gamma \mathcal{S}\big(\omega_{ab}-\omega_\gamma\big) \big[\mathbf{d}^*_{ab}\big]_{-\sigma} \Big[\mathcal{T}^{(\mathrm{ed})}_{\gamma;A}\Big]_{\sigma\sigma} \big[\mathbf{d}_{ab}\big]_{-\sigma}, \tag{15a}$$

$$\Gamma^{(\mathrm{md})}_{ab;A} = \sum_{\sigma=,\pm,0} \sum_\gamma \mathcal{S}\big(\omega_{ab}-\omega_\gamma\big) \big[\mathbf{m}^*_{ab}\big]_{-\sigma} \Big[\mathcal{T}^{(\mathrm{md})}_{\gamma;A}\Big]_{\sigma\sigma} \big[\mathbf{m}_{ab}\big]_{-\sigma}, \tag{15b}$$

$$\Gamma^{(\mathrm{eq})}_{ab;A} = \sum_{\sigma,\sigma'=,\pm,0} \sum_\gamma \mathcal{S}\big(\omega_{ab}-\omega_\gamma\big) \big[\mathbf{q}^*_{ab}\big]_{-\sigma-\sigma'} \Big[\mathcal{T}^{(\mathrm{eq})}_{\gamma;A}\Big]_{\sigma\sigma'\sigma\sigma'} \big[\mathbf{q}_{ab}\big]_{-\sigma-\sigma'}, \tag{15c}$$

where we have used square brackets $[\mathbf{x}]_\sigma$ to denote the σ component of vectors and tensors and adopted the circular polarization basis $\{\mathbf{e}_\sigma\} = \{\mathbf{e}_\pm = \mathbf{e}_x \pm i\mathbf{e}_y, \mathbf{e}_0 = \mathbf{e}_z\}$. The contribution of each mode becomes

$$\Big[\mathcal{T}^{(\mathrm{ed})}_{\gamma;A}\Big]_{\sigma\sigma} = \frac{2\pi}{\hbar^2} \int d\Omega_{\mathbf{k}} \int d\Omega_{\mathbf{k}'} g_A\big(\mathbf{k},\mathbf{k}';\omega_\gamma\big) \Big[\mathbf{f}^*_\gamma(\theta_{\mathbf{k}},\varphi_{\mathbf{k}})\Big]_\sigma \Big[\mathbf{f}_\gamma(\theta_{\mathbf{k}'},\varphi_{\mathbf{k}'})\Big]_\sigma, \tag{16a}$$

$$\Big[\mathcal{T}^{(\mathrm{md})}_{\gamma;A}\Big]_{\sigma\sigma} = \frac{2\pi c^2}{\hbar^2\omega^2_\gamma} \int d\Omega_{\mathbf{k}} \int d\Omega_{\mathbf{k}'} g_A\big(\mathbf{k},\mathbf{k}';\omega_\gamma\big) \Big[\mathbf{k}\times\mathbf{f}^*_\gamma(\theta_{\mathbf{k}},\varphi_{\mathbf{k}})\Big]_\sigma \Big[\mathbf{k}'\times\mathbf{f}_\gamma(\theta_{\mathbf{k}'},\varphi_{\mathbf{k}'})\Big]_\sigma, \tag{16b}$$

$$\Big[\mathcal{T}^{(\mathrm{eq})}_{\gamma;A}\Big]_{\sigma\sigma'\sigma\sigma'} = \frac{2\pi c^2}{\hbar^2\omega^2_\gamma} \int d\Omega_{\mathbf{k}} \int d\Omega_{\mathbf{k}'} g_A\big(\mathbf{k},\mathbf{k}';\omega_\gamma\big) [\mathbf{k}]_\sigma \Big[\mathbf{f}^*_\gamma(\theta_{\mathbf{k}},\varphi_{\mathbf{k}})\Big]_{\sigma'} [\mathbf{k}']_\sigma \Big[\mathbf{f}_\gamma(\theta_{\mathbf{k}'},\varphi_{\mathbf{k}'})\Big]_{\sigma'}. \tag{16c}$$

The effect of the vibrational states for all multiple moments is given entirely by a form factor

$$g_A\big(\mathbf{k},\mathbf{k}';\omega_\gamma\big) = \int d^3\mathbf{X} \Phi^*_A(\mathbf{X}) e^{i\left(\hat{\mathbf{k}}-\hat{\mathbf{k}}'\right)\cdot\left(\omega_\gamma \mathbf{X}/c\right)} \Phi_A(\mathbf{X}). \tag{17}$$

The form factor shows that the center-of-mass motion performs an average over the field distributions. The average depends on the atomic center of mass initial state. For an atom prepared in the ground state of an harmonic trap with angular frequency components $\Lambda_{x,y,z}$ centered at the position $\mathbf{X}_0$—which does not need to coincide with the origin used to describe the EM field—the form factor is

$$g_A\big(\mathbf{k},\mathbf{k}';\omega_\gamma\big) = e^{i\left(\hat{\mathbf{k}}-\hat{\mathbf{k}}'\right)\cdot\left(\omega_\gamma \mathbf{X}_0/c\right)} \prod_{i=x,y,z} e^{-\frac{2\pi\eta_i\left(\hat{\mathbf{k}}_i-\hat{\mathbf{k}}'_i\right)^2}{2}} \tag{18}$$

The average carries information on the trap through the Lamb-Dicke parameters $\eta_i = \sqrt{\hbar\omega^2_\gamma/2Mc^2\Lambda_i} = l_i/\lambda_\gamma$ relating the

ground-state size of the trap $l_i = 2\pi\sqrt{\hbar/2M\Lambda_i}$ to the wavelength of the electromagnetic mode λ_γ. In the Lamb-Dicke limit $\eta_i < 1$, the atoms are confined below the photon wavelength and will not be heated by light scattering [32]. Notice that even if $\omega_\gamma \gg \Lambda_i$, the condition is achieved for $\omega_\gamma \ll \sqrt{2Mc^2/\hbar}$ taking into account the value of the atom rest energy Mc^2. The Lamb-Dicke regime has been achieved for trapped ions [33] and neutral atoms [34].

Through **Eqs 15a**, **15b**, **15c**, **16a**, **16b**, **16c**, **Eq. 17** we have shown that decay rates depend on the EM mode density evaluated at the atomic resonance frequency and also on the average value determined by the vibrational states. The electromagnetic modes γ that participate in **Eqs 15a**, **15b**, **15c** can be constrained by imposing physical boundaries, as done in experiments with optical cavities. Then, the enhancement [29] or inhibition [35, 36] of the spontaneous emission rate depends on the electromagnetic structure of the environment and the location and trapping strength of the atom. Notice that this control is expected not only for electric dipole transitions, but for any multipole transition as we have just illustrated for electric quadrupole and magnetic dipole cases.

It is worth mentioning that for atoms in free-space the EM field is homogeneous and the dipolar and quadrupolar spontaneous emission decay rates are

$$\Gamma_{ss'}^{(\mathrm{ed})} = \frac{4|\mathbf{d}_{ss'}|^2\omega_{ss'}^3}{3\hbar c^3}, \tag{19a}$$

$$\Gamma_{ss'}^{(\mathrm{md})} = \frac{4|\mathbf{m}_{ss'}|^2\omega_{ss'}^3}{3\hbar c^3}, \tag{19b}$$

$$\Gamma_{ss'}^{(\mathrm{eq})} = \frac{|\mathbf{q}_{ss'}|^2\omega_{ss'}^5}{15\hbar c^5}. \tag{19c}$$

This can be shown by evaluating the $\mathcal{T}_{\gamma;A}^{(\mathrm{mult})}$ integrals with angular spectrum

$$f_\gamma^{\mathrm{free}}(\theta_\mathbf{k}, \phi_\mathbf{k}) = \frac{1}{|\sin\theta_\mathbf{k}|}\delta\big(\theta_\mathbf{k} - \theta_\gamma\big)\delta\big(\phi_\mathbf{k} - \phi_\gamma\big)$$

for each polarization, and using the completeness relation of polarizations $\epsilon_{\mathbf{k},\lambda}$ and wavevectors $\mathbf{k}$. For a systematic approach beyond the quadrupolar interaction, however, it is more convenient to use the spherical modes.

1.2 Spherical Vector Waves: Atomic Radiation Patterns

The structure of the radiated field incorporates the atomic symmetries that arise from the central field model. In the mean field scheme, individual radiative electronic transitions involve a single electron that changes its orbital and yields a non-null electromagnetic multipole for the atom as a whole. An EM multipole transition of an atom can be either described as the emission or absorption of a *single* photon in an appropriate spherical vectorial mode, or as divided along multiple photon channels with wavevectors $\mathbf{k}$ and specific angular distribution probabilities. Spherical vectorial modes then lead to a more efficient transfer than their wavevector counterparts.

This efficient transfer is already suggested by the form of the spherical vectorial modes. In free space a monochromatic spherical wave of frequency ω and amplitude $\mathcal{A}$ has an angular spectrum

$$\mathbf{f}_\gamma = \mathcal{A}\tilde{\mathbb{Y}}_{jm}^{(P)}(\theta_\mathbf{k}, \varphi_\mathbf{k}). \tag{20}$$

The spectrum describes the coupling of orbital and polarization angular momenta of photons to yield a total angular momentum $\{jm\}$ as described by the functions $\tilde{\mathbb{Y}}_{jm}^{(P)}$ where $P = E, M$ refers to either transverse magnetic or transverse electric waves. These functions are written explicitly in the **Supplementary Appendix SAI** in terms of standard spherical harmonic functions $Y_{\ell m}(\theta, \varphi)$—that account for the orbital angular momentum—and spherical polarizations $\mathbf{e}_\pm = \mathbf{e}_x \pm i\mathbf{e}_y$, $\mathbf{e}_0 = \mathbf{e}_z$. Spherical vectorial modes are then characterized by the parameters γ: $\{\omega/c = k, j, m, P\}$ that can be compared to the electronic degrees-of-freedom involved during a transition. In particular to the atomic angular momentum that includes both orbital and spin contributions of the electronic configurations and the angular momentum of the nucleus. Note that the electronic and electromagnetic fields should be described in the same reference frame. In particular, the same quantization z-axis, which is either arbitrarily selected or predetermined by anisotropic environments. The latter can be, e.g., external electric and magnetic fields selected to manipulate the internal or external degrees of the atom, or they could refer to the geometry of cavities designed to control the classical or quantum features of the electromagnetic field.

The radiative transitions that connect two-atomic states are ruled by strict conservation laws for energy, linear momentum, and angular momentum of the atom-radiation system as a whole. These conservation laws are naturally satisfied by spherical modes where electric and magnetic multipole transitions involve a *single* $\mathbb{Y}_{jm}^{(E)}$ or $\mathbb{Y}_{jm}^{(M)}$ photon [37]. As such, they can be used to connect the atomic internal state to the most probable decay processes and the specific EM modes involved. For example, the spatial pattern of magnetic spherical waves $\mathbb{Y}_{jm}^{(M)}$ is obtained from **Eq. 6** as

$$\int d\Omega_\mathbf{k} e^{-i\mathbf{k}\cdot\mathbf{r}}\tilde{\mathbb{Y}}_{jm}^{(M)}(\theta_\mathbf{k}, \varphi_\mathbf{k}) = 4\pi i^{-j}\mathrm{j}_j(kr)\mathbb{Y}_{jm}^{(M)}(\theta, \varphi), \tag{21}$$

with $\mathrm{j}_j(kr)$ the spherical Bessel functions with $k = \omega/c$ and the position $\mathbf{r} = \{r, \theta, \phi\}$. This form was used to obtain the radiative decay of Eqs **19a**, **19b**, **19c**, but, by portraying the wave as a single vectorial mode, there is no need to account for the contribution of each wavevector and polarization. Similar descriptions are found for the spherical electric modes. Relevant, well-known mathematical properties of spherical vectorial modes are summarized in **Supplementary Appendix SAI** including a connection to vectorial plane waves. We show explicitly the simple structure of the modes in $\mathbf{k}$-space that is used to define a scalar product from which the EM field can be quantized. These properties emphasize that the mode structure results from the direct coupling of orbital and polarization angular momenta of the field.

Figures 2–4 are used to illustrate the rich spatial patterns of vectorial modes. In an effort to show the symmetries involved, isointensity surfaces are drawn for each polarization $\mathbf{e}_{\pm,0}$, and for the total intensity of the spherical waves. As anticipated in the Introduction, the polarization and configuration structure in this

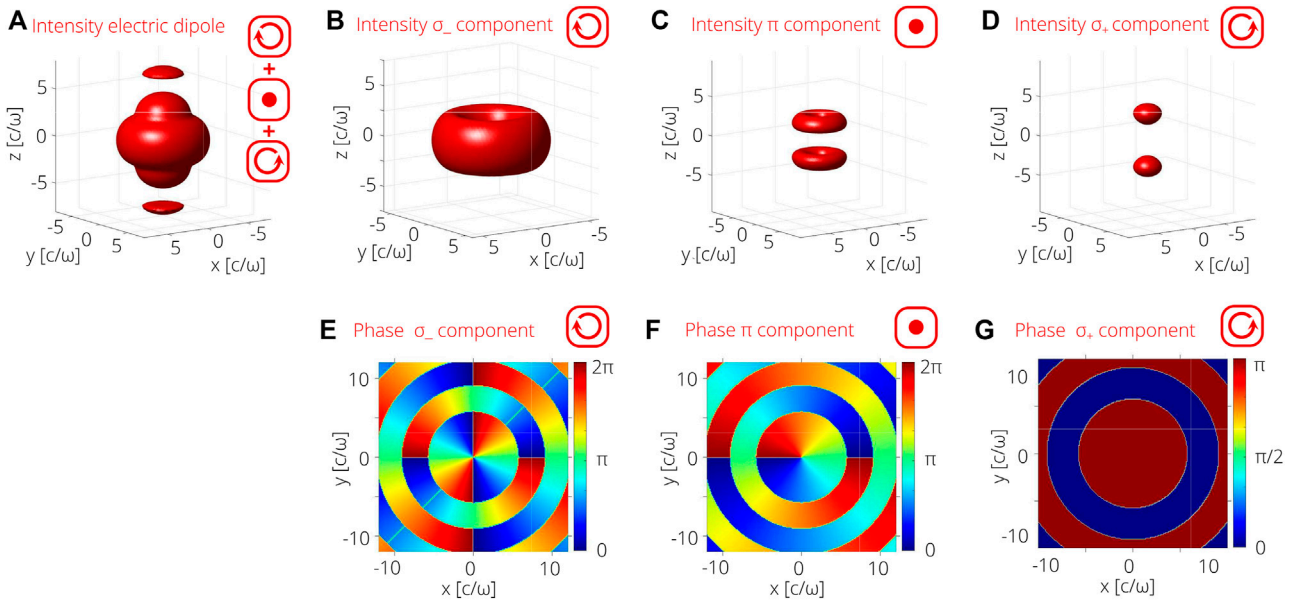

FIGURE 2 | Isosurfaces of an electric dipole $\mathbb{Y}_{11}^{(E)}$ spherical wave at 40% of the intensity divided into: **(A)** total intensity; **(B)** σ_- polarization component; **(C)** π polarization component; and **(D)** σ_+ componentsof the polarization. In **(E–G)** the phase distributions at the $z = 0$ plane are plotted for different polarization components.

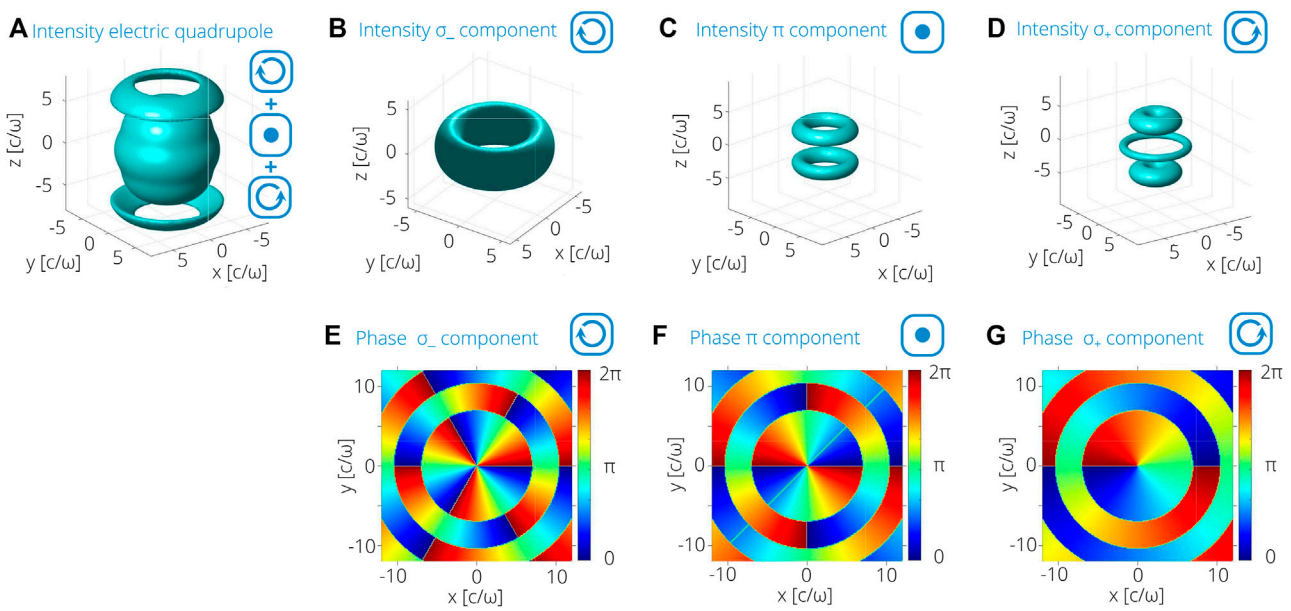

FIGURE 3 | Isosurfaces of an electric quadrupole $\mathbb{Y}_{22}^{(E)}$ spherical wave at 40% of the intensity divided into: **(A)** total intensity; **(B)** σ_- polarization component; **(C)** π polarization component; and **(D)** σ_+ components of the polarization. In **(E–G)** the phase distributions at the $z = 0$ plane are plotted for different polarization components.

subwavelength region is complex. High gradients of the intensity and vortices along a dislocation line for certain polarizations can be found as shown by the phase structure in the XY plane.

We begin with **Figure 2** where each polarization component of the electric dipole spherical wave is described by a combination of spherical functions $Y_{\ell m}$ with $\ell = 0$ and 2, as we now discuss. **Figure 2** shows the $\mathbb{Y}_{11}^{(E)}$ spherical wave. The σ_+ polarization component is a combination of both Y_{20} and Y_{00}, the latter being independent of θ and φ and not null at $r = 0$. Neither Y_{20} nor Y_{00} components exhibit orbital vortices. For comparison, the σ_- component is proportional Y_{22} and displays an optical vortex with topological charge 2 along the Z-axis. The π component is proportional to Y_{21} with a unit

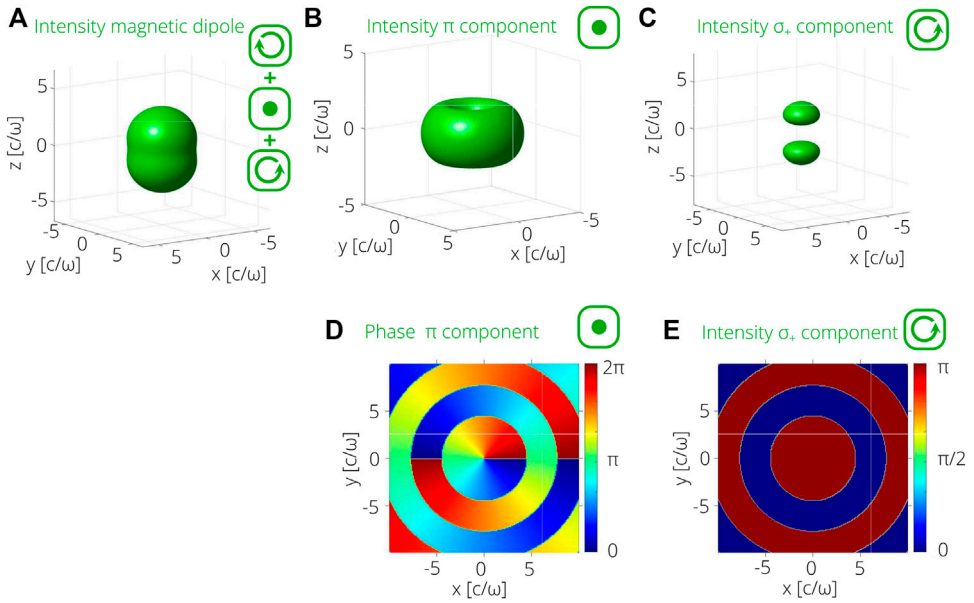

FIGURE 4 | Isosurfaces of an magnetic dipole $\mathbb{Y}_{11}^{(M)}$ spherical wave at 40% of the intensity divided into: **(A)** total intensity; **(B)** σ_- polarization component; **(C)** π polarization component; and **(D)** σ_+ components of the polarization. In **(E)**–**(G)** the phase distributions at the $z = 0$ plane are plotted for different polarization components.

topological charge vortex. Consider next the quadrupole electric spherical wave $\mathbb{Y}_{22}^{(E)}$ shown in **Figure 3**. An analogous description follows but through a combination of $Y_{\ell m}$ functions with $\ell = 1$ and 3. This implies an odd behavior for quadrupole waves in contrast to the even behavior of dipole electric waves with respect to the parity transformation. Finally, **Figure 4** illustrates a $\mathbb{Y}_{11}^{(M)}$ spherical wave. In general, each circular polarization $\sigma_\pm(\pi)$ component of $\mathbb{Y}_{jm}^{(M)}$ is proportional to the $Y_{jm\mp1}(Y_{jm})$ spherical harmonic. The parity of magnetic spherical modes is even (odd) for even (odd) values of j.

The results are to be compared with standard paraxial optics. For paraxial optics, light polarization is approximately a global concept. There is a main direction of propagation and the polarization vectors are approximately perpendicular to it. This facilitates the identification of processes where only either σ_+, σ_- or π transitions occur; π-transitions require a main direction of propagation perpendicular to a quantization-axis defined by the environment as mentioned in the beginning of this Subsection. For each type of transition the atomic internal states experience a change of the internal magnetic number $\Delta m = 1, -1, 0$ respectively. If a realization of a few atomic levels model is desired, a search of an atomic- EM field configuration is performed to maximize the relevance of predetermined internal atomic sublevels that participate in the nonlinear optical process.

2 THREE-WAVE MIXING INDUCED BY A FORBIDDEN TRANSITION

Having described how light can be tailored to induce particular transitions with high probability, we now move to the nonlinear response of an atomic gas. For this we are going to consider the case drawn in **Figure 1** where a three-level atomic gas is driven by a structured EM mode. States $|a\rangle$ and $|b\rangle$ are connected through two paths: one *via* a quadrupole transition with moment $\mathbf{q}_{ab}$; and the other *via* two electric dipole transitions through an intermediate level $|c\rangle$ with moments $\mathbf{d}_{ac}$ and $\mathbf{d}_{bc}$. All other moments are considered negligible. The incident mode $\hat{a}_1$ is tailored to display a large spatial gradient, it presents the adequate polarization to connect a and b states, and is slightly detuned from the quadrupole transition. It provides the conditions for modes $\hat{a}_2$ and $\hat{a}_3$ to become populated as the atom descends down the dipole ladder, thus describing a three-wave mixing process. Most studies in the literature do not consider the possibility of the quadrupole transition and focus only on the two-photon electric dipole processes associated to the ladder configuration of a three level atom-EM field system [38]. Nevertheless, those studies illustrate a plethora of interesting phenomena whose analogs and extensions when three-wave mixing is allowed deserve further analyses.

Three-wave mixing relies on the coherent scattering from mode $\hat{a}_1$ to modes $\hat{a}_2$ and $\hat{a}_3$. To account for this scattering we divide the total Hamiltonian of **Eq. 1** as

$$\hat{\mathcal{H}} = \sum_{i=1,2,3} \hbar\omega_i \hat{a}_i^\dagger \hat{a}_i + \sum_{s,s'} \left\{ \hbar\kappa_{ss'}^i \left(\tilde{\tilde{\mathbf{X}}} \right) \hat{a}_i \hat{\sigma}_{s,s'}^{(n)} + H.c. \right\} + \hat{\mathcal{H}}_{\text{atom}} + \hat{\mathcal{H}}'_{\text{field}} + \hat{\mathcal{H}}'_{\text{int}} \tag{22}$$

where we separated the three EM modes $\hat{a}_1, \hat{a}_2, \hat{a}_3$ from other environment modes accounted for in the primed terms. The evolution of the mode operators

$$\dot{\hat{a}}_j = -i\omega_j \hat{a}_j - i\sum_{ss'} \kappa_{ss'}^{j*} \hat{\sigma}_{ss'}, \tag{23}$$

naturally divides into free and scattered components. The electromagnetic $\hat{\mathbf{E}}$ and $\hat{\mathbf{B}}$ field operators are then obtained by solving the self-consistent equations for field and atom operators and performing a sum over all the modes (see **Eq. 4** above). Equivalently, we could define atomic polarizabilities and obtain the evolution of the field from Maxwell equations. To do so we consider first a density matrix for the atomic state

$$\rho^{\mathrm{tw}} = \rho^{\mathrm{CM}} \otimes \rho \tag{24}$$

where ρ^{CM} describes the vibrational motion of the atom and ρ describes its electronic state. This form requires that center of mass and internal states are not correlated at an initial time, and remain so throughout the nonlinear process. This condition could be valid in the Lamb-Dicke regime. From **Eqs 23**, **24** dipole and quadrupole moment densities $\mathbf{P}$ and $\mathbf{Q}$ of the three-level atomic gas can be defined as

$$\mathbf{P}(\mathbf{X},t) = N\rho^{CM}(\mathbf{X})\left(\mathbf{d}_{ac}\rho_{ac} + \mathbf{d}_{cb}\rho_{cb} + h.c.\right), \tag{25a}$$

$$\mathbf{Q}(\mathbf{X},t) = N\rho^{CM}(\mathbf{X})\left(\mathbf{q}_{ab}\rho_{ab} + \mathbf{q}_{ab}^{\dagger}\rho_{ba}\right), \tag{25b}$$

where the total number of trapped atoms N is first introduced.

Non-linearities enter the picture through the internal state of the atom. They result from the participation of photons inside γ modes at different orders in the coupling strength κ

$$\rho = \sum_n g_n(\kappa)\rho^{(n)}. \tag{26}$$

The series converges for κ lower than the detunings Δ and decay rates $\Gamma^{(\mathrm{mult})}$. Three-wave mixing appears at second order in the series, the details are described in the **Supplementary Appendix SAII** following a semiclassical approach equivalent to an adiabatic elimination of the atomic variables in the fully quantum regime [39]. The final expression for the atomic polarization at a position $\mathbf{X}$ is

$$\hat{\mathbf{P}}(\mathbf{X},t) = \sum_{\ell} \hat{\mathbf{P}}_{\ell}(\mathbf{X},\omega_{\ell})e^{-i\omega_{\ell}t}, \tag{27}$$

where the leading terms are shown to be

$$\hat{\mathbf{P}}_2(\mathbf{X},-\omega_2) = \frac{N}{\hbar^2}\rho^{CM}(\mathbf{X})\frac{\left(\mathbf{q}_{ab}\colon \nabla\mathbf{E}_{\gamma_1}a_{\gamma_1}\right)^{\dagger}\left(\mathbf{d}_{cb}\cdot\mathbf{E}_{\gamma_2}a_{\gamma_2}\right)\mathbf{d}_{ac}}{\Delta_3\left[\Delta_1 - i\frac{1}{2}\Gamma_{ab}^{(\mathrm{eq})}\right]}, \tag{28}$$

$$\hat{\mathbf{P}}_3(\mathbf{X},-\omega_3) = \frac{N}{\hbar^2}\rho^{CsM}(\mathbf{X})\frac{\left(\mathbf{q}_{ab}\colon \nabla\mathbf{E}_{\gamma_1}a_{\gamma_1}\right)^{\dagger}\left(\mathbf{d}_{ac}\cdot\mathbf{E}_{\gamma_3}a_{\gamma_3}\right)\mathbf{d}_{cb}}{\Delta_2 - i\frac{1}{2}\left(\Gamma_{ab}^{(\mathrm{eq})} + \Gamma_{cb}^{(\mathrm{ed})}\right)}\left(\frac{1}{\Delta_1 - i\frac{1}{2}\Gamma_{ab}^{(\mathrm{eq})}} + \frac{1}{\Delta_3 + i\frac{1}{2}\Gamma_{ac}^{(\mathrm{ed})}}\right) \tag{29}$$

Meanwhile, the quadrupole densities oscillate as

$$\hat{\mathbf{Q}}(\mathbf{X},-\omega_1) = \frac{N}{\hbar^2}\rho^{CM}(\mathbf{X})\frac{\left(\hat{\mathbf{d}}_{cb}\cdot\mathbf{E}_{\gamma_2}a_{\gamma_2}\right)^{\dagger}\left(\hat{\mathbf{d}}_{ac}\cdot\mathbf{E}_{\gamma_3}a_{\gamma_3}\right)^{\dagger}\hat{\mathbf{q}}_{ab}}{\left[\Delta_1 - i\frac{1}{2}\Gamma_{ab}^{(\mathrm{eq})}\right]\left[\Delta_3 - i\frac{1}{2}\Gamma_{ac}^{(\mathrm{ed})}\right]} \tag{30}$$

Once the electronic states are adiabatically eliminated, the field evolution of **Eq. 23** is equivalent to an effective Hamiltonian density of the atomic gas interacting with the EM field

$$\hat{H}_{\mathrm{eff}} = \sum_{\gamma_1}\frac{1}{2}\hat{\mathbf{Q}}(\omega_1,\mathbf{X})\colon\nabla\mathbf{E}^{(\gamma_1)}(\mathbf{X},t) + \sum_{\gamma_2}\hat{\mathbf{P}}(-\omega_2,\mathbf{X})\cdot\mathbf{E}^{(\gamma_2)}(\mathbf{X},t) + \sum_{\gamma_3}\hat{\mathbf{P}}(-\omega_3,\mathbf{X})\cdot\mathbf{E}^{(\gamma_3)}(\mathbf{X},t). \tag{31}$$

Here, the summation is performed over free modes γ_i whose frequency ω_i close to the transition frequency $\omega_{ss'}$ and their polarization and angular momentum $j_i m_i$ are adequate to induce the atomic transition with the corresponding multipole moment. That is, rapidly oscillating terms derived from far from resonance conditions or an spatial configuration out of the expected spherical vector mode one have been discarded.

2.1 Multipole Densities as Sources of Radiation

Having revisited the connection between electronic processes and nonlinear optical processes, we can now exploit the connection to Maxwell equations. For localized sources which admit an efficient multipole expansion, the radiated field operator $\hat{\mathbf{E}}$ is known to satisfy the equation [31, 37, 40]

$$\left[-\boldsymbol{\nabla}\cdot\boldsymbol{\nabla} + \frac{1}{c^2}\frac{\partial^2}{\partial t^2}\right]\hat{\mathbf{E}} = \frac{4\pi}{c}\frac{\partial}{\partial t}\hat{\mathbf{J}} \tag{32}$$

where the sources

$$\hat{\mathbf{J}} = \hat{\mathbf{J}}^{(\mathrm{ed})} + \hat{\mathbf{J}}^{(\mathrm{eq})} \tag{33}$$

divide into electric dipole $\hat{\mathbf{J}}^{(\mathrm{ed})}$ and quadrupole $\hat{\mathbf{J}}^{(\mathrm{eq})}$ operators that satisfy

$$\mathbf{J}^{(\mathrm{ed})} = \frac{1}{c}\frac{\partial\hat{\mathbf{P}}}{\partial t}, \qquad \mathbf{J}^{(\mathrm{eq})} = -\frac{1}{c}\frac{\partial}{\partial t}\boldsymbol{\nabla}\cdot\hat{\mathbf{Q}}. \tag{34}$$

It is possible to extend the formalism to include magnetic dipole transitions through a magnetization term

$$\hat{\mathbf{J}}^{(md)} = \boldsymbol{\nabla}\times\hat{\mathbf{M}}. \tag{35}$$

In our case, **Eq. 32** stems from the interaction Hamiltonian beyond the dipole approximation written in **Eq. 7** and the decomposition of the electric fields [4]. The form of the interaction led naturally to the vectorial spherical waves associated to each atomic radiative transition and then to source terms of this form. The particular atomic evolution follows from a master equation evolution (as defined in **Supplementary Appendix SAII**), but the form is universal.

Note that radiation can also be generated by so-called "free" sources. An example is radiation scattered by structureless ideal charges such as electrons, i.e., the Compton effect, which has frequently been described using a plane wave expansion of the quantized EM field [31]. Recent theoretical studies concern the Compton effect with photons associated to structured beams

[41], and the implementation of the inverse Compton effect for twisted electron beams is an active area of research [42].

For the three-wave mixing process considered here, the induced moments oscillate at frequencies ω_1, ω_2 and ω_3. As such, the evolution of the field amplitudes can be decomposed into a Fourier series that leads to

$$\left[-\boldsymbol{\nabla}\cdot\boldsymbol{\nabla}-\frac{\omega_1^2}{c^2}\right]\mathbf{E}^{(\gamma_1)}=-\frac{4\pi\omega_1^2}{c^2}\boldsymbol{\nabla}\cdot\mathbf{Q}(-\omega_1), \tag{36a}$$

$$\left[-\boldsymbol{\nabla}\cdot\boldsymbol{\nabla}-\frac{\omega_i^2}{c^2}\right]\mathbf{E}^{(\gamma_i)}=\frac{4\pi\omega_i^2}{c^2}\mathbf{P}_s(-\omega_i),\quad i=2,3 \tag{36b}$$

whenever the temporal phase matching condition is imposed $\omega_1 = \omega_2 + \omega_3$. From them, conditions yielding a high efficiency of parametric processes based on atomic coherence can be obtained [43]. Note that the full quantum treatment implicit in **Eq. 32** allows to study correlations of the quadrature equations of the EM modes, including squeezing conditions [44].

Most implementations of nonlinear optics processes consider input paraxial beams driving the atomic gas. The set of paraxial modes $\{\gamma_i^{px}\}$ neither matches the atomic symmetry nor provides any guarantee of an adequate description of the EM field in the radiation zone [45]. Within the paraxial regime, the theoretical description of the classical and quantum properties of light is incorporated using the slowly varying amplitude approximation [1]. It states that the relative change in the amplitude per wavelength is small and there is a main direction of propagation z of the light fields so that the dominant spatial variation of the amplitude can be approximated by $(\omega/c)\partial_z\mathbf{E}^{(\gamma_i)}$. This is not valid when the electromagnetic beams are focused, but, as we now show, the vectorial waves provide a form to describe the evolution.

3 DYADIC GREEN FUNCTIONS

Schwinger [46] introduced an elegant formalism to evaluate the response function between the electromagnetic field and a polarization source using the Green function dyadic. As Maxwell equation, **Eq. 32**, can be worked out using this formalism for generalized multipole sources we now revisit this formalism.

The Green dyadic $\mathbf{\Gamma}$ is a tensor with r, s components

$$\mathbf{G}_{rs}(\mathbf{X},t;\mathbf{X}',t')=\langle\hat{\mathcal{T}}\hat{\mathbf{E}}_r^{(-)}(\mathbf{X},t)\hat{\mathbf{E}}_s^{(+)}(\mathbf{X}',t')\rangle \tag{37}$$

with $\hat{\mathcal{T}}$ a time ordering operator that, in field theory applications, leads to Feynman symmetric order; and, in optical studies, is chosen to guarantee the retarded scheme. By being written in normal order it also provides a natural connection to photon detection theory and real time monitoring of the emitted field. This tensor is responsible of the propagation of fields. It then allows us to write the free and scattered fields discussed above as

$$\hat{\mathbf{E}}_r(\mathbf{X},t)=\hat{\mathbf{E}}_r^{\text{free}}(\mathbf{X},t)+\hat{\mathbf{E}}_r^{\text{scatt}}(\mathbf{X},t) \tag{38a}$$

$$\hat{\mathbf{E}}_r^{\text{scatt}}(\mathbf{X},t)=\sum_{s=1,2,3}\int d^3\mathbf{X}'dt'\mathbf{G}_{rs}(\mathbf{X},t;\mathbf{X}',t')(\partial_{ct'}\mathbf{J})_s(\mathbf{X}',t'). \tag{38b}$$

Where the free field $\hat{\mathbf{E}}^{\text{free}}$ is, by construction, the adequate quantum field solution of the Maxwell equations with no sources, and may include the incident EM field. And the scattered EM field $\hat{\mathbf{E}}^{scatt}$ is created by the atomic multipole densities.

For a retarded scheme and a vectorial spherical expansion of the electric field operators in free space, the tensor is decomposed as

$$\mathbf{G}_{rs}(\mathbf{X},t;\mathbf{X}',t')=\int d\omega\,\mathbf{G}_{rs}(\mathbf{X},\mathbf{X}';\omega)e^{-i\omega(t-t')}$$

$$\mathbf{G}_{rs}(\mathbf{X},\mathbf{X}';\omega)=\omega^2\sum_{P=E,M}\sum_{\ell,m}j_\ell\left(\frac{\omega r_<}{c}\right)h_\ell^{(1)}\left(\frac{\omega r_>}{c}\right)\left(\tilde{\mathbb{Y}}_{\ell m}^{(P)}\right)_r(\theta,\varphi)\left(\tilde{\mathbb{Y}}_{\ell m}^{(P)*}\right)_s(\theta',\varphi') \tag{39}$$

with j_ℓ and $h_\ell^{(1)}$ the spherical Bessel functions.

3.1 Spatial Phase Matching Conditions

We can now use this formalism to describe the phase matching conditions that rule the underlying nonlinear processes. For plane waves phase matching conditions establish the relations between the wave vectors of the involved EM modes that guarantee the highest efficiency of an optical nonlinear process. In the quantum realm, these equations are interpreted as the conservation of linear momentum of the participating photons. For a homogeneous atomic gas, the three-wave mixing phase matching conditions are

$$\mathbf{k}_1=\mathbf{k}_2+\mathbf{k}_3. \tag{40}$$

For beams exhibiting a common dislocation line—and correspondingly a non-trivial local orbital momentum along that line—the phase matching conditions correlate the topological charge of the vortices so that the angular momentum of the photons is conserved [47, 48]. For an isotropic atomic sample and for modes exhibiting optical vortices of topological charge m_i along a common axes, for our process

$$m_1=m_2+m_3. \tag{41}$$

In this Section we show how they naturally emerge from the dyadic treatment of the scattered field. To that end it is just necessary the integrate the Maxwell Equation **Eqs 38a**, **38b** over the spatial variables of the localized source

$$\int d^3\mathbf{X}'\,j_\ell(\omega r/c)\tilde{\mathbb{Y}}_{\ell m}^{(P)*}(\theta',\varphi')\cdot\mathbf{J}(\mathbf{X}',t') \tag{42}$$

If the 3D sample is in an isotropic trap, the angular integration acquires an analytic expression (some formulae useful for the calculation of the spatial derivatives of the spherical waves can be found in the **Supplementary Appendix SAI**). The integrals are, in general, a linear combination of the Wigner 3-j symbols

$$\int d\Omega Y_{\ell_1 m_1}(\theta,\varphi) Y_{\ell_2 m_2}(\theta,\varphi) Y_{\ell_3 m_3}(\theta,\varphi) = \sqrt{\frac{(2\ell_1+1)(2\ell_2+1)(2\ell_3+1)}{4\pi}} \begin{pmatrix} \ell_1 & \ell_2 & \ell_3 \\ 0 & 0 & 0 \end{pmatrix} \begin{pmatrix} \ell_1 & \ell_2 & \ell_3 \\ m_1 & m_2 & m_3 \end{pmatrix} \quad (43)$$

available in most numerical platforms. The phase matching conditions result from the identification of non-null Wigner 3-j symbols,

$$m_i \epsilon \{-\ell_i, \ldots, \ell_i\}, \qquad i = 1,2,3,$$
$$m_1 + m_2 + m_3 = 0, \qquad |\ell_1 - \ell_2| \le \ell_3 \le \ell_1 + \ell_2.$$

These phase matching conditions can be interpreted as a conservation of the total angular momentum and not just its z-component for the photons involved in the three-wave mixing process.

3.1.1 Scattered Field

Since just a constrained set of γ_{pm} modes satifies the phase matching conditions, the scattered field is given by

$$\hat{\mathbf{E}}_r^{scatt}(\mathbf{X},t) = \int d^3\mathbf{X}' dt' \Gamma_{rs}(\mathbf{X},t;\mathbf{X}',t') (\partial_{ct'}\mathbf{J})_s(\mathbf{X}',t') \quad (44a)$$

$$= \sum_{\gamma_{pm}} \sum_s \boldsymbol{\alpha}_{rs}^{\gamma_{pm}} h_{\ell_{pm}}^{(1)}\left(\frac{\omega_{pm} r}{c}\right) \left(\tilde{\mathbb{Y}}_{\ell_{pm} m_{pm}}^{(P)}\right)_r (\theta,\varphi), \quad \omega_1 = \omega_2 + \omega_3 \quad (44b)$$

$$\boldsymbol{\alpha}_{rs}^{\gamma_{pm}} = \int d^3\mathbf{X}' \rho^{CM}(\mathbf{X}') j_{\ell_{pm}}\left(\frac{\omega_{pm} r'}{c}\right) \left(\tilde{\mathbb{Y}}_{\ell_{pm} m_{pm}}^{(P)}\right)_r (\theta',\varphi') \mathbf{J}_s(\mathbf{X}') \quad (44c)$$

An advantage of working with spherical vectorial modes is that any set of three modes γ_{ab}, γ_{bc} and γ_{ca} with $\omega_1 = \omega_2 + \omega_3$ must be considered as usual, but the phase angular matching conditions select a discrete set of few modes specified by the polarization P and the $j_{ss'}$ and $m_{ss'}$ values that satisfy the angular phase matching conditions. This is a basic difference with standard studies where the spatial phase matching is satisfied by a continuous set of spatial modes.

Once few of these modes are identified one could now apply, e.g., the semiclassical approximation or other standard techniques [49–51] to work out the behavior of the quantum quadratures of the field and their correlation to the atomic degrees of freedom. The modes, of course, depend on the experimental conditions.

4 DISCUSSION

We have presented a description of three-wave mixing inside an atomic cloud. We began by showing how this process could be efficiently induced by properly shaping the light field and then moved to the description of the free and scattered field that are ultimately measured in an experiment. For this, we went beyond the dipole approximation and showed that the system is naturally described by multipole spherical waves. Multipole spherical waves yield the optimal description of the basic radiative atomic processes. As such, they are paradigmatic structured light fields. Yet, their use in the description of nonlinear systems is scarse. The reason is that most implementations of nonlinear processes employ laser beams and assume a paraxial regime. Nowadays technological developments go in a different direction. Optimal coupling to minimize energy costs in, e.g., quantum information protocols require the realization of nonlinear processes triggered by single photons [52]. A natural scheme to achieve such a coupling is by trapping atoms nearby the focus of spherical vectorial waves.

The main task in this work was to emphasize both the effects of trapping on the radiative responses of an atom and present a way to surmount the difficulties that arise. These included moving beyond dipolar approximation, and the breakdown of commonly used approximations as the slowly varying envelope one. We showed how the dyadic Green function formalism is easily implemented and allows for the identification of a discrete set of modes that would participate in the nonlinear process once the relevant atomic states are identified.

The calculations were described by a paradigmatic process that can now be reached in experiments with atomic gases: three-wave mixing. Notice, however, that the general concepts introduced in our work can be extended to any nonlinear process. In addition the dyadic formalism can be directly applied for other symmetries; yielding a direct route for the identication of the phase matching condition. While standard techniques were developed with dipolar transitions and plane waves in mind, the extension to structured light can be readily done with the appropriate basis in mind.

DATA AVAILABILITY STATEMENT

The original contributions presented in the study are included in the article/**Supplementary Material**, further inquiries can be directed to the corresponding authors.

AUTHOR CONTRIBUTIONS

RG-J and RJ contributed with conceptual ideas, methodology strategies and writing of the manuscript.

FUNDING

This work was partially supported by PAPIIT-DGAPA-UNAM IN-103020. RG-J acknowledges financial support by the National Science Foundation QII-TAQS (Award No. 1936359).

SUPPLEMENTARY MATERIAL

The Supplementary Material for this article can be found online at: https://www.frontiersin.org/articles/10.3389/fphy.2022.896174/full#supplementary-material

REFERENCES

1. Armstrong JA, Bloembergen N, Ducuing J, Pershan PS. Interactions Between Light Waves in a Nonlinear Dielectric. *Phys Rev* (1962) 127:1918–39. doi:10.1103/physrev.127.1918
2. Rubinsztein-Dunlop H, Forbes A, Berry MV, Dennis MR, Andrews DL, Mansuripur M, et al. Roadmap on Structured Light. *J Opt* (2016) 19:013001. doi:10.1088/2040-8978/19/1/013001
3. Monroe C, Campbell WC, Duan LM, Gong ZX, Gorshkov AV, Hess PW, et al. Programmable Quantum Simulations of Spin Systems with Trapped Ions. *Rev Mod Phys* (2021) 93:025001. doi:10.1103/revmodphys.93.025001
4. Navon N, Smith RP, Hadzibabic Z. Quantum Gases in Optical Boxes. *Nat Phys* (2021) 17:1334–41. doi:10.1038/s41567-021-01403-z
5. Biémont E, Zeippen CJ. Probabilities for Forbidden Transitions in Atoms and Ions: 1989-1995. A Commented Bibliography. *Phys Scr* (1996) T65:192–7. doi:10.1088/0031-8949/1996/t65/029
6. Fry ES. Two-Photon Correlations in Atomic Transitions. *Phys Rev A* (1973) 8:1219–32. doi:10.1103/physreva.8.1219
7. Aspect A, Grangier P, Roger G. Experimental Realization of Einstein-Podolsky-Rosen-Bohm *Gedankenexperiment*: A New Violation of Bell's Inequalities. *Phys Rev Lett* (1982) 49:91–4. doi:10.1103/physrevlett.49.91
8. D'Angelo M, Chekhova MV, Shih Y. Two-Photon Diffraction and Quantum Lithography. *Phys Rev Lett* (2001) 87:013602.
9. Nasr MB, Saleh BE, Sergienko AV, Teich MC. Demonstration of Dispersion-Canceled Quantum-Optical Coherence Tomography. *Phys Rev Lett* (2003) 91:083601. doi:10.1103/PhysRevLett.91.083601
10. Gisin N, Ribordy G, Tittel W, Zbinden H. Quantum Cryptography. *Rev Mod Phys* (2002) 74:145–95. doi:10.1103/revmodphys.74.145
11. Pittman TB, Shih YH, Strekalov DV, Sergienko AV. Optical Imaging by Means of Two-Photon Quantum Entanglement. *Phys Rev A* (1995) 52:R3429–R3432. doi:10.1103/physreva.52.r3429
12. Pepe FV, Di Lena F, Mazzilli A, Edrei E, Garuccio A, Scarcelli G, et al. Diffraction-Limited Plenoptic Imaging with Correlated Light. *Phys Rev Lett* (2017) 119:243602. doi:10.1103/physrevlett.119.243602
13. Agarwal G. *Nonlinear Fiber Optics*. 5th ed. Cambridge, MA, USA: Academic Press (2012).
14. Zipfel WR, Williams RM, Webb WW. Nonlinear Magic: Multiphoton Microscopy in the Biosciences. *Nat Biotechnol* (2003) 21:1369–77. doi:10.1038/nbt899
15. Hell SW. Toward Fluorescence Nanoscopy. *Nat Biotechnol* (2003) 21:1347–55. doi:10.1038/nbt895
16. Weber K-H, Sansonetti CJ. Accurate Energies of *nS, nP, nD, nF,* and *nG* levels of Neutral Cesium. *Phys Rev A* (1987) 35:4650–60. doi:10.1103/physreva.35.4650
17. Vadla C, Horvatic V, Niemax K. Oscillator Strength of the Strongly "forbidden" Pb 6 P^2 $^3P_0$↦6 P^2 $^3P_1$ Transition at 1278.9 Nm. *Eur Phys J D* (2001) 14:23–5. doi:10.1007/s100530170229
18. Ponciano-Ojeda F, Hernández-Gómez S, López-Hernández O, Mojica-Casique C, Colín-Rodríguez R, Ramírez-Martínez F, et al. Observation of the $5P_{3/2} \rightarrow 6P_{3/2}$ Electric-Dipole-Forbidden Transition in Atomic Rubidium Using Optical-Optical Double-Resonance Spectroscopy. *Phys Rev A* (2015) 92:042511. doi:10.1103/physreva.92.042511
19. Jáuregui R. Rotational Effects of Twisted Light on Atoms Beyond the Paraxial Approximation. *Phys Rev A* (2004) 70:033415. doi:10.1103/physreva.70.033415
20. Schmiegelow CT, Schulz J, Kaufmann H, Ruster T, Poschinger UG, Schmidt-Kaler F. Transfer of Optical Orbital Angular Momentum to a Bound Electron. *Nat Commun* (2016) 7:12998. doi:10.1038/ncomms12998
21. Tojo S, Hasuo M, Fujimoto T. Absorption Enhancement of an Electric Quadrupole Transition of Cesium Atoms in an Evanescent Field. *Phys Rev Lett* (2004) 92:053001. doi:10.1103/PhysRevLett.92.053001
22. Ray T, Gupta RK, Gokhroo V, Everett JL, Nieddu T, Rajasree KS, et al. Observation of the 87Rb 5S1/2 to 4D3/2 Electric Quadrupole Transition at 516.6 Nm Mediated via an Optical Nanofibre. *New J Phys* (2020) 22:062001. doi:10.1088/1367-2630/ab8265
23. Alber G, Bernád JZ, Stobińska M, Sánchez-Soto LL, Leuchs G. QED with a Parabolic Mirror. *Phys Rev A* (2013) 88:023825. doi:10.1103/physreva.88.023825
24. Wang Z, Wang BR, Ma QL, Guo JY, Li MS, Wang Y, et al. Design of a Novel Monolithic Parabolic-Mirror Ion-Trap to Precisely Align the RF Null Point with the Optical Focus. *ArXiv:quant-ph/0408845* (2020).
25. Gutiérrez-Jáuregui R, Jáuregui R. Spontaneous Transition Rates Near the Focus of a Parabolic Mirror with Identification of the Vectorial Modes Involved. *Sci Rep* (2020) 10:17383. doi:10.1038/s41598-020-74377-2
26. Gutiérrez-Jáuregui R, Jáuregui R. Photons in the Presence of Parabolic Mirrors. *Phys Rev A* (2018) 98:043808. doi:10.1103/physreva.98.043808
27. Anderson SE, Raithel G. Ionization of Rydberg Atoms by Standing-Wave Light Fields. *Nat Commun* (2013) 4:2967. doi:10.1038/ncomms3967
28. Smirnova D, Smirnov AI, Kivshar YS. Multipolar Second-Harmonic Generation by Mie-Resonant Dielectric Nanoparticles. *Phys Rev A* (2018) 97:013807. doi:10.1103/physreva.97.013807
29. Purcell EM. Proceedings of the American Physical Society: Spontaneous Emission Probabilities at Ratio Frequencies. *Phys Rev* (1946) 69:681.
30. Cohen-Tannoudji C, Dupont-Roc J, Grynberg G. *Atom-Photon Interactions: Basic Processes and Applications*. Hoboken: Wiley (1989). p. 518.
31. Messiah A. *Quantum Mechanics*. New York: Wiley (1961).
32. Dicke RH. The Effect of Collisions Upon the Doppler Width of Spectral Lines. *Phys Rev* (1953) 89:472–3. doi:10.1103/physrev.89.472
33. Itano WM, Bergquist JC, Bollinger JJ, Gilligan JM, Heinzen DJ, Moore FL, et al. Quantum Projection Noise: Population Fluctuations in Two-Level Systems. *Phys Rev A* (1993) 47:3554–70. doi:10.1103/physreva.47.3554
34. Ido T, Katori H. Recoil-Free Spectroscopy of Neutral Sr Atoms in the Lamb-Dicke Regime. *Phys Rev Lett* (2003) 91:053001. doi:10.1103/PhysRevLett.91.053001
35. Kleppner D. Inhibited Spontaneous Emission. *Phys Rev Lett* (1981) 47:233–6. doi:10.1103/physrevlett.47.233
36. Haroche S, Kleppner D. Cavity Quantum Electrodynamics. *Phys Today* (1989) 42:24–30. doi:10.1063/1.881201
37. Berestetvkii VB, Lifshhitz EM, Pitaevskii LP. *Relativistic Quantum Theory I*. Oxford: Pergamonn Press Ltd. (1971).
38. Yoo H, Eberly JH. Dynamical Theory of an Atom with Two or Three Levels Interacting with Quantized Cavity Fields. *Phys Rep* (1985) 118:239–337. doi:10.1016/0370-1573(85)90015-8
39. Reid MD, Walls DF. Generation of Squeezed States via Degenerate Four-Wave Mixing. *Phys Rev A* (1985) 31:1622–35. doi:10.1103/physreva.31.1622
40. Jackson JD. *Classical Electrodynamics*. New York: John Wiley & Sons (1975).
41. Jentschura UD, Serbo VG. Generation of High-Energy Photons with Large Orbital Angular Momentum by Compton Backscattering. *Phys Rev Lett* (2011) 106:013001. doi:10.1103/PhysRevLett.106.013001
42. Seipt D, Surzhykov A, Fritzsche S. Structured X-Ray Beams From Twisted Electrons by Inverse Compton Scattering of Laser Light. *Phys Rev A* (2014) 90:012118. doi:10.1103/physreva.90.012118
43. Zibrov AS, Lukin MD, Hollberg L, Scully MO. Efficient Frequency Up-Conversion in Resonant Coherent Media. *Phys Rev A* (2002) 65:051801(R). doi:10.1103/physreva.65.051801
44. Kumar P, Shapiro JH. Squeezed-State Generation via Forward Degenerate Four-Wave Mixing. *Phys Rev A* (1984) 30:1568(R). doi:10.1103/physreva.30.1568
45. Nieminen TA, Rubinsztein-Dunlop H, Heckenberg NR. Vector Spherical Wavefunction Expansion of a Strongly Focussed Laser Beam. In: B. Gustafson, L. Kolokolova, G. Videen, editors. *Electromagnetic and Light Scattering by Nonspherical Particles*. Adelphi, Maryland: Army Research Laboratory (2002). p. 243–6.
46. Schwinger J, DeRaad LL, Milton KA. Casimir Effect in Dielectrics. *Ann Phys* (1978) 115:1–23. doi:10.1016/0003-4916(78)90172-0
47. Mair A, Vaziri A, Weihs G, Zeilinger A. Entanglement of the Orbital Angular Momentum States of Photons. *Nature* (2001) 412:313–6. doi:10.1038/35085529
48. Walker G, Arnold AS, Franke-Arnold S. Trans-spectral Orbital Angular Momentum Transfer via Four-Wave Mixing in Rb Vapor. *Phys Rev Lett* (2012) 108:243601. doi:10.1103/physrevlett.108.243601
49. Boyd R. *Nonlinear Optics*. 3rd ed. Amsterdam, Netherlands: Elsevier (2008).

50. Agarwal GS, Adam G. Photon-Number Distributions for Quantum Fields Generated in Nonlinear Optical Processes. *Phys Rev A* (1988) 38:750–3. doi:10.1103/physreva.38.750
51. Bloemberger N. *Nonlinear Optics : A Lecture Note and Reprint Volume*. New York: W. A. Benjamin Inc. (1965).
52. Chang DE, Vuletić V, Lukin MD. Quantum Nonlinear Optics — Photon by Photon. *Nat Phot* (2014) 8:635. doi:10.1038/nphoton.2014.192
53. Barrera RG, Estevez GA, Giraldo J. Vector Spherical Harmonics and Their Application to Magnetostatics. *Eur J Phys* (1985) 6:287–94. doi:10.1088/0143-0807/6/4/014

Conflict of Interest: The authors declare that the research was conducted in the absence of any commercial or financial relationships that could be construed as a potential conflict of interest.

frontiers | Frontiers in Physics

ORIGINAL RESEARCH
published: 04 July 2022
doi: 10.3389/fphy.2022.879113

Entangled Biphoton Enhanced Double Quantum Coherence Signal as a Probe for Cavity Polariton Correlations in Presence of Phonon Induced Dephasing

Arunangshu Debnath[1]* *and Angel Rubio*[1,2]*

[1]Max Planck Institute for the Structure and Dynamics of Matter, Center for Free-Electron Laser Science, Hamburg, Germany, [2]Center for Computational Quantum Physics (CCQ), The Flatiron Institute, New York, NY, United States

OPEN ACCESS

Edited by:
Juan Torres,
The Institute of Photonic Sciences (ICFO), Spain

Reviewed by:
Che-Ming Li,
National Cheng Kung University, Taiwan
Bin Fang,
University of Texas at Austin, United States

***Correspondence:**
Arunangshu Debnath
arunangshu.debnath@desy.de
Angel Rubio
angel.rubio@mpsd.mpg.de

Specialty section:
This article was submitted to Quantum Engineering and Technology, a section of the journal Frontiers in Physics

Received: 18 February 2022
Accepted: 06 May 2022
Published: 04 July 2022

Citation:
Debnath A and Rubio A (2022) Entangled Biphoton Enhanced Double Quantum Coherence Signal as a Probe for Cavity Polariton Correlations in Presence of Phonon Induced Dephasing. Front. Phys. 10:879113. doi: 10.3389/fphy.2022.879113

We theoretically propose a biphoton entanglement-enhanced multidimensional spectroscopic technique as a probe for the dissipative polariton dynamics in the ultrafast regime. It is applied to the cavity-confined monomeric photosynthetic complex that represents a prototypical multi-site excitonic quantum aggregate. The proposed technique is shown to be particularly sensitive to inter-manifold polariton coherence between the two and one-excitation subspaces. It is demonstrated to be able to monitor the dynamical role of cavity-mediated excitonic correlations, and dephasing in the presence of phonon-induced dissipation. The non-classicality of the entangled biphoton sources is shown to enhance the ultra-fast and broadband correlation features of the signal, giving an indication about the underlying state correlations responsible for long-range cavity-assisted exciton migration.

Keywords: entanglement, exciton-polaritons, photosynthetic complex, nonlinear optics, multidimensional spectroscopy, quantum cavity electrodynamics, dissipation

1 INTRODUCTION

The quantum aggregates consisting of multiple centers of electronic excitations, e.g., the naturally occurring light-harvesting photosynthetic complexes, artificially designed molecular light-harvesters offer a uniquely favorable testing ground for the entangled photon-induced dynamics. These systems intrinsically host collective excitations, frequently termed as molecular excitons, extending over several excitation centers/sites and often within the coherence domain of the spatial (temporal) length (time) scales. Thus, it provides opportunities for the external modulation of delocalized excitons and testing the limits of coherent dynamics. Further, the vibrational motions associated with these structures often give rise to a collective dephasing mechanism for the delocalized excitons. Additionally, the vibrational motions modulate the energy gradient of the kinetics, leading to situations where coherent excitons undergo inter-site transport and eventually localize. The spectroscopic investigation and control of such exciton kinetics offers insights into the microscopic nature of the coherent energy transfer mechanism and prescribes guidelines for bio-mimetic engineering which builds on the operational equivalence [1–6]. In a separate line of development, there have been a series of studies that have demonstrated the effective role of external electromagnetic cavities in manipulating material excitations. These studies range from the control of electronic excitations [7–16], vibrational modes [17, 18], collective mode responses [19, 20] to the

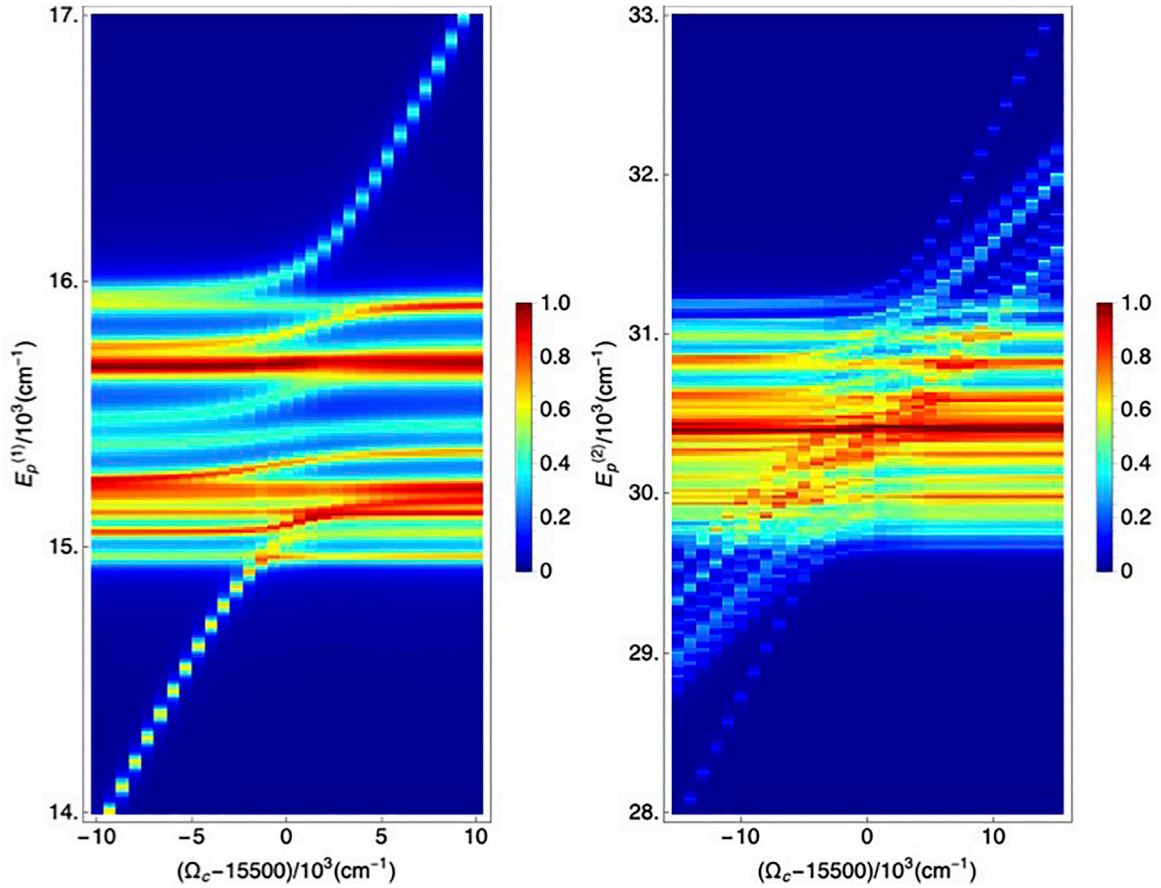

FIGURE 1 | The progression of dephasing-broadened bare polariton band with the cavity frequencies and a fixed value of cavity coupling strength are presented. For the dephasing a representative set of values (generated from a random Gaussian distribution of mean and variance of $\mu_1 = 25$, $\sigma_1 = 10$ and $\mu_2 = 35$ respectively) are chosen for clarity. In the displayed one-polariton (left panel) and the two-polariton band (right panel), the increase in the density of states in the latter within a comparable energy-window (e.g., ≈ 10, ×, $10^3 cm^{-1}$) is noticeable. The fundamental cavity frequencies along the *x*-axis are given in terms of detuning from the central region of the one-polariton band.

cavity mode-assisted modulation of dynamical resonances [21–25]. Cavity mode interacting resonantly with narrow-band of excitons and off-resonantly with the rest may modulate the excitation dispersal by tuning the delocalization properties and influence the dephasing properties via the spectral weight modulation [26–28]. Hence, combining these two developments to the case of light-harvesting quantum aggregates offers an opportunity to investigate the role of the cavity in controlling a prototypical, extended yet aperiodic system that hosts collective excitons.

Previous spectroscopic studies of the cavity-modulated dynamics [29–35] have increasingly focused their attention on the ultrafast, nonlinear techniques analogs e.g. pump-probe here. In the majority of these studies, participation of the higher-order excitations remain relatively unexplored. The dynamics involving the higher-order nonlinear excitations introduce possibilities for cavity-modulated exciton-exciton annihilation, cavity-assisted exciton fusion, and many more correlated mechanisms of practical interest. On a fundamental level, the external dielectric modification of the Coulomb interaction between different excitons underlies all of these coherent mechanisms. However, the nonlinear spectroscopic signatures studied so far depend dominantly on the associated vibrational (or vibronic) processes [37, 38]. Therefore, in order to explore the complexity of cavity-modulated nonlinear exciton dynamics, it is desirable to combine ultrafast spectroscopic tools that are sensitive to high-order exciton correlations in the presence of collective vibrational dephasing. Among the multi-pulse nonlinear spectroscopic techniques available for mapping out the correlation between two excitons and probing the two-exciton state-specific dephasing in the ultrafast regime, double-quantum multidimensional correlation spectra (DQC) have been proven useful [39–42]. The ultrafast nature of the exciton dynamics in aggregates results in difficulty in measuring the role of energetically-distant states even without the presence of the cavity mode. These delocalized multi-exciton states often participate in dynamics within the same timescale due to dynamical dephasing properties. Associated with the normal exciton-number conserving dephasing process, one encounters a dephasing mechanism that couples the energy-manifolds with the different number of excitons. The presence of cavity adds additional cavity-exciton hybrid states, introduces multiple

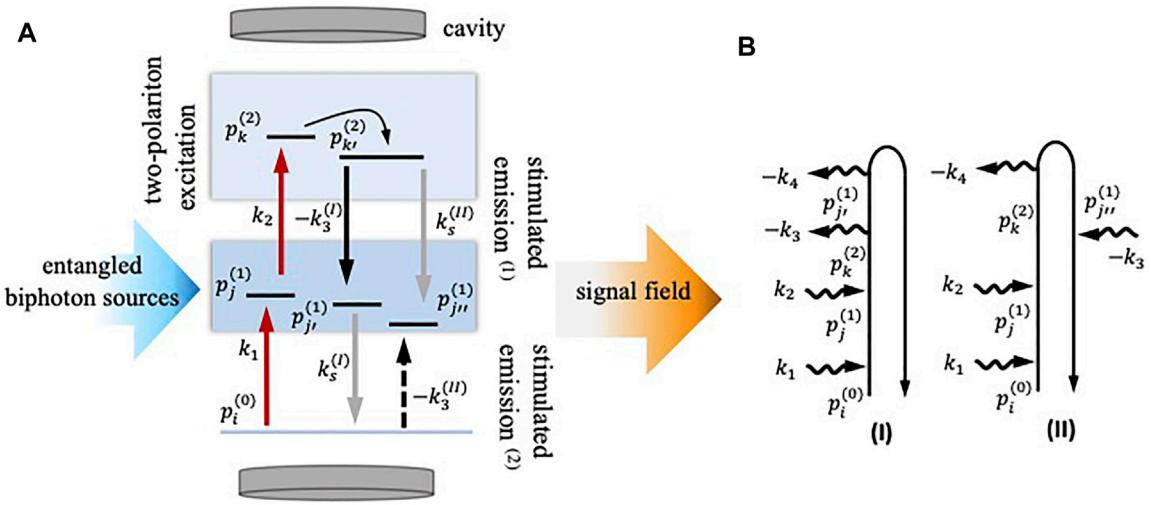

FIGURE 2 | (A) Schematic description of the dynamical phenomena (in WMEL diagrammatic convention [36]) that can be addressed by the proposed DQC signal measurement technique. The first two interactions (in red) are common to both the pathways. The last two interactions (in black and gray) are distinguished by two alternative possibilities indicated by $\{k_s^{(I)}, -k_3^{(I)}\}$, $\{k_s^{(II)}, -k_3^{(II)}\}$ pair. Entangled photons affect both these pair interactions $\{k_1, k_2\}$ and $\{-k_3, k_s\}$. **(B)** Associated Keldysh-Schwinger diagrams that describe the corresponding dynamical pathways in the multi-polariton basis contributing to the signal and which are distinct in the last two interactions in time.

dynamical timescales, and gives rise to novel cavity-exciton-phonon coupling mechanisms. These excitations are of principal interest in this communication. The investigation of them requires the deployment of probes that specifically excite spectrally narrow-band states (creation of non-linear polarization), allow the associated dynamics to evolve in time in the presence of dephasing (evolution of the polarization), and project them to desired frequency components of interest (projection of polarization to signal components). Robust, correlated state excitation can be controllably achieved by deploying the entangled photon pairs, namely entangled biphotons, via a scheme being referred to as entangled two-photon absorption [43–47]. In comparison to the shaped laser pulses, the entangled biphotons have been shown to improve the spectral resolution while scaling favorably with the intensity of the sources. The non-classical correlation properties can also be utilized to obtain favorable spectral-temporal resolution in the probing via selective state projections of the nonlinear polarization [29, 33, 48–55]. The latter requires the selection of a few states whose correlation properties are of particular interest from a manifold. In this regard, a combination of the aforementioned DQC signal measurement scheme with the entangled photon sources may provide a technique that studies cavity-modulated correlated exciton kinetics in the ultrafast regime with higher spectral resolution.

In what follows, in **Section 2**, we introduce the Frenkel exciton Hamiltonian and describe the underlying model. It will be used to describe the dissipative exciton-polariton phenomenology and obtain the relevant Green's functions. Subsequently, in **Section 2** we introduce the DQC signal in a modular manner, discuss the nature of the signal and present the simulation results in the relevant parameter regime. **Section 4** discusses limitations, the scope of the presented signal within the broader scope of entangled photon-enhanced spectroscopies, and the outlook.

2 DISSIPATIVE EXCITON-POLARITON PHENOMENOLOGY

Here we present the exciton Hamiltonian concurrently interacting with a cavity mode and the phonon reservoir, which will be used to build up the phenomenology using a quasi-particle picture. It is given by,

$$\begin{aligned} H = & \sum_{m,\ n=1}^{N_s} (E_m\delta_{mn} + J_{mn})B_m^\dagger B_n + \sum_{m,\ n=1}^{N_s} \frac{U_m^{(2)}}{2} B_m^\dagger B_m^\dagger B_m B_m \\ & + \frac{U_{mn}^{(2)}}{2} B_m^\dagger B_n^\dagger B_m B_n \quad + \sum_\alpha \omega_c \left(a_\alpha^\dagger a_\alpha + 1/2\right) \\ & + \sum_{m,\alpha} g_{c,m,\alpha}\left(a_\alpha B_m^\dagger + a_\alpha^\dagger B_m\right) + \sum_j \omega_j \left(b_j^\dagger b_j + \frac{1}{2}\right) \\ & + \sum_{m,j} g_{m,j}\left(b_j^\dagger + b_j\right) B_m^\dagger B_m \end{aligned} \tag{1}$$

where we set the $\hbar$ to unity. The components of the Hamiltonian are explained below.

2.1 Exciton, Cavity and Exciton-Cavity Interactions

The first three terms constitute the bare exciton Hamiltonian where $B_m\,(B_m^\dagger)$ are the m-th site exciton creation (annihilation) operators with the respective commutation relation, $[B_m, B_n] = [B_m^\dagger, B_n^\dagger] = 0$ and $[B_m, B_n^\dagger] = \delta_{mn}(1 - (2 - \kappa_m^2))B_m^\dagger B_m^\dagger)$ (where $\kappa_m = \mu_{21}/\mu_{10}$, is given in terms of ratio of transition dipoles of *ij*-

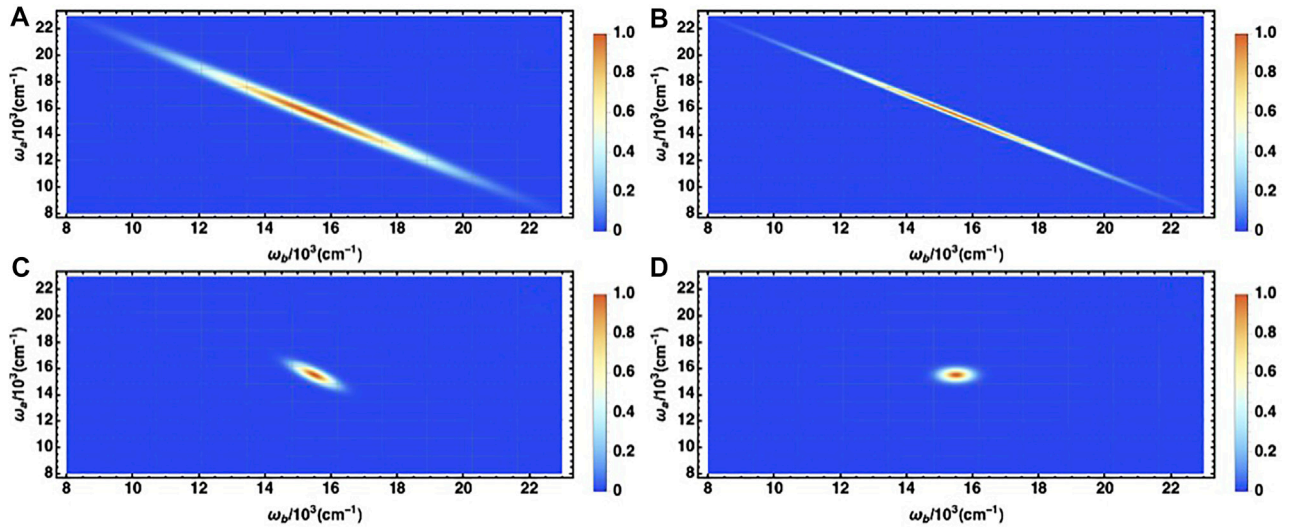

FIGURE 3 | Field correlation functions for different entangled photon states corresponding to parameter variation of temporal entanglement parameter T_{ent} (fs) and pump width τ_p (fs) for uniform pump frequency 31.0, ×, $10^3 cm^{-1}$ and biphoton frequencies $\omega_1 = \omega_2 = 15.5 \times 10^3 cm^{-1}$. The bottom right corresponds to the typical case of a classical field two-photon pulse **(A)** corresponds to the $T_{ent} = 10$; $\tau_p = 20$ **(B)** corresponds to $T_{ent} = 10$; $\tau_p = 50$ while **(C)** assumes values $T_{ent} = 50$; $\tau_p = 20$. The **(D)** corresponds to a Gaussian pair-pulse with τ_g (fs) = 10 with $\omega_{1,g} = \omega_{2,g} = 15.5 \times 10^3 cm^{-1}$.

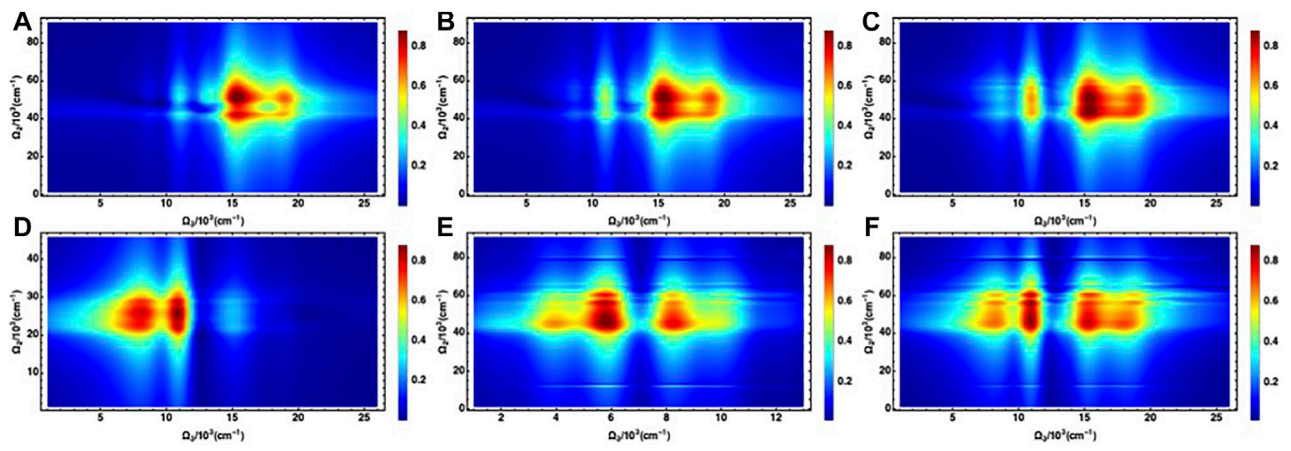

FIGURE 4 | Multidimensional correlation plots **(A–F)** for signal with parametric variation of the frequencies and the temporal entanglement parameters of the entangled biphotons. The short-lived, intermediate one-polariton resonances along the Ω_3 axis can be explored and associated with the two-polariton resonances along the Ω_2 axis. For parameters corresponding to each plot see text.

th level of the m-th site) [56–58]. $E_m^{(1)}$ is the on-site excitation energies and J_{mn} is the inter-site Coulomb-mediated hopping. The presence of the interacting terms in the exciton Hamiltonian indicates that the single and two exciton states are delocalized over sites. The two-excitation manifold which is composed of permutable composition of pure local and non-local two-exciton, pure two cavity excitations and joint one exciton-one photon excitation is given by, $H_{mnkl}^{(2)} = H_{mn}^{(1)}\delta_{kl} + \delta_{mn}H_{kl}^{(1)}$. The terms $U_m^{(1)}, U_{mn}^{(2)}$ further dictates the interaction among higher-order excitonic states which gives rise to static, local energy shifts, exciton-exciton scattering. The values of $U_m^{(1)}$ is taken as $U_m^{(1)} = 2(\kappa_n^{-2}E_n^{(2)} - E_n^{(1)})$, with $\kappa = \mu_{21}/\mu_{10}$ which accounts for the local energy shifts for two-exciton states and $U_{mn}^{(2)} = 0$. Bare two-exciton energy is given by $E_m^{(2)} = 2E_m^{(1)} + \Delta_m$ (where the Δ_m is the two-exciton state anharmonicity from the Harmonic limit). The parameter values for the Hamiltonian are obtained from the semi-empirical simulation in [59–62] where these data-set have been shown to simultaneously fit the spectral data obtained from the linear absorption, fluorescence, and circular dichroism spectra. The combined cavity and the cavity-exciton interaction Hamiltonian is be

given by the fourth and fifth term where the $g_{c;m,\alpha}$ is the cavity-exciton coupling strengths describing the resonant dipolar interaction. The effects arising from the non-resonant cavity-exciton interaction could be significant in the static limit if the exciton-cavity coupling strengths are comparable to the bare Rabi frequencies of the multi-exciton system [63–66]. The cavity-exciton parameter considered in this communication corresponds to moderately weak and within the close to resonant regime which allows this term being neglected. The cavity photonic modes are described in the oscillator basis with the corresponding creation (annihilation) operators denoted as $a_\alpha^\dagger(a_\alpha)$, for the α-th mode. Within the scope of this study, a single-mode limit (i.e. $\alpha = 1$) and two-excitation per-mode (with he fundamental frequency denoted by ω_c) has been considered. Furthermore, we assume an uniform cavity-exciton coupling strengths for all sites, i.e. $g_{c;m,\alpha} = g_c = 100\text{cm}^{-1}$ is independent of index m, although the analysis presented is not limited by that choice. We note that a detailed estimation of the cavity-exciton couplings requires investigation regarding the mode volume of the cavity and the quality factor which is beyond the scope of the article. The Coulombic origin inter-site hopping in the Hamiltonian is of different magnitude, indicating a different propensity for delocalization in the absence of cavity interaction. The cavity coupling modulates site-delocalization at different extents for one-exciton, local and non-local two-excitons. This gives rise to the possibility of creating a different admixture of cavity-matter excitations. In addition, it offers cavity mediates coupling between these configurations, thereby coupling diverse sets of excitations and inter-site processes. Since the cavity accommodates two-photon excitations, the analysis is capable of describing resonant two-polariton processes.

2.2 Phonon and Exciton-Phonon Interactions

The exciton-phonon interactions originate from the inter and intra-molecular vibrational motions associated with the relative nuclear motions of the aggregate. Normal modes of the low-energy vibrational degrees of freedom related to the collective vibrational coordinates are assigned as phonon modes and are mapped onto an infinite set of Harmonic oscillators. It is given by the free phonon Hamiltonian appearing in the sixth term where υ_k is the mode frequency associated with the k-th normal mode whose creation (annihilation) operators are denoted via $b_j^\dagger(b_j)$. The phonon operators follow the free-boson commutation relations, $[b_j, b_{j'}] = [b_j^\dagger, b_{j'}^\dagger] = 0$ and $[b_j, b_{j'}^\dagger] = \delta_{jj'}$. The seventh term presenting the exciton-phonon interactions is taken in the site-uncorrelated, local form and is characterized by the distribution of the corresponding coupling functions, $\bar{g}_{m,j}$. These phonon modes are responsible for exciton dephasing, relaxation and exciton-transport phenomena. The extent of these phenomena are governed by the site-dependent exciton-phonon coupling strengths $g_{m,j}$ which are taken as 1 (1.4) for the sites identified to represent Chl-A (Chl-b). While constructing the two-exciton phonon interaction Hamiltonian these coupling strengths are taken as 0.6 ($g_{m,j} + g_{n,j}$). Due to the differential coupling strengths, the excitations undergo dephasing at different rates, the one and two-exciton transport occur to a different extent over the sites leading to time-windowed interferences at a broader energy window. The inter-band dephasing, a quantity of particular interest in this article has contributions from the elements of the relaxation tensor that also participates in the cavity mediated one-exciton and two-exciton transport. Within this model, the single and the double excitons are coupled to a common set of phonon modes which can be characterized by the discrete distribution function, $J_0(\omega) = \pi\sum_j |\bar{g}_j|^2(\delta(\omega - \upsilon_j) - \delta(\omega + \upsilon_j))$ from which the spectral density function is obtained in the continuum frequency limit. The spectral density function, presented as, $J(\omega) = 2\lambda_0(\gamma_0\omega)/(\omega^2 + \gamma_0^2) + \sum_{j=1}^{N_b} 2\lambda_j(\upsilon_j^2\gamma_j\omega)/((\upsilon_j^2 - \omega^2)^2 + \omega^2\gamma_j^2)$ describes $N_b = 48$ multi-mode Brownian oscillator modes and one over-damped oscillator mode. The number of multi-mode Brownian oscillators (N_b), the respective spectral shift parameters (λ_0, $\lambda_j = \upsilon_j\Upsilon_j$ where υ_j and Υ_j are the j-th oscillator frequencies and Huang-Rhys parameters respectively), and the damping parameter (γ_0, γ_j) which are required to optimally describe the equilibrium spectral density function have been obtained from the work of [35, 59–61]. The numerical values corresponding to those parameters are enlisted in **Appendix A2**.

2.3 Polariton Manifolds

The polariton states are obtained as number-conserving manifolds via exact-diagonalization of the field-free Hamiltonian subspaces, $\tilde{H}_p^{(n)} = \tilde{H}_s + \tilde{H}_c + \tilde{H}_{sc}$ by using $T_p^{(n),-1}\tilde{H}_p^{(n)}T_p^{(n)} = H_p^{(n)} = \sum_{n=0,1,2} E_{p^{(n)}} X_{p^{(n)}p^{(n)}}$, where we define operators $X_{p^{(n)}p^{(n)}} = |p^{(n)}\rangle\langle p^{(n)}|$ as projectors onto the eigenstates of the polariton Hamiltonian $H_p^{(n)}$ (denoted by index n). The three distinct manifolds thus obtained corresponds to ground $n = 0$, single $n = 1$ and double $n = 2$ polariton manifolds with $N_{p^{(0)}} = 1$, $N_{p^{(1)}} = 15$, $N_{p^{(2)}} = 120$ polariton states respectively (**Figure 1**). The manifolds are composed of the cluster of states which depend on an interplay of the hopping and cavity coupling parameters. The proposed spectroscopic technique utilizing entangled biphotons, in the parameter regime of interest, interact only via two-quantum interactions, which allows the joint-excitation manifold to be truncated at the level of the double polaritons. For the simulation, we have chosen the cavity mode frequency and the coupling strength parameters as ω_c (cm^{-1}) = 15.4×10^3 and g_c (cm^{-1}) = 0.1×10^3. The cavity frequency is resonant with the narrow frequency band around the frequency and off-resonant with the rest of the cluster of states in the bare absorption spectra of the excitonic system. The cavity coupling results in the polariton states to encompass a wider range than the cavity-free counterpart with the close-to-resonance states becoming affected to a greater degree. It can also be noted that the two-polariton states accommodate more states within the comparable bandwidth which is determined by the cavity coupling parameter. These two observations, combined, affirm that the exciton-cavity hybridization dominantly takes around the resonances, as expected. The spectral weights of the resultant delocalized polariton states have respective contributions from both the exciton and cavity modes, as determined by the exciton-cavity coupling matrix elements.

2.4 Polariton-Laser Interactions

The interaction between the external field i.e. biphoton sources and polaritons are treated within the optical dipolar interaction limit and within the rotating wave approximation. Corresponding Hamiltonian is given by,

$$H_{\rm int}(t) = \sum_j \sum_{n,n'=0,1,2;n\neq n'} \left(\sqrt{2\pi\omega_j/V}\right) a_j e^{-i\omega_j t} d_{p^{(n)}p^{(n')}} X_{p^{(n)}p^{(n')}} \exp\left(i\omega_{p^{(n')}p^{(m)}} t\right) + \text{h.c.} \tag{2}$$

where external photon mode creation operators a_j and dipole-weighted inter-manifold polariton transition operators, $X_{p^{(n)}p^{(n')}}$ were defined. Also, the mode quantization volume V and the Fourier expansion frequency ω_j for the photon modes have been introduced. These operators will be used to derive the signal expressions in the next sections. It is notable that in the spirit of the weak laser driving limit suitable for spectroscopy only the one-photon transition operators had been employed.

2.5 Phonon Induced State Broadening and Polariton Green's Functions

In this section, we introduce the framework to obtain the state-dependent dephasing timescales and obtain the polariton Green's functions required for the signal expressions. It is carried out by seeking an integral solution of the generalized master equation (written in the multi-polariton basis) obtained in the Markovian and the secular limit (often termed as the Redfield equation). The secular approximation limits the polariton-phonon mode interactions to be describable within the resonant cases only. The latter suffices our treatment of acoustic phonons mediate interactions are mediated by displacive perturbations of exciton states simultaneously dressed by the cavity interactions that are comparatively much stronger. The kinetic equation is given by, $\dot{\sigma}^{(n)}(t) = -iL_S^{(n)}\sigma^{(n)}(t) + \int_0^\infty d\tau \Sigma^{(n)}(t,\tau)\sigma^{(n)}(t)$ where we denote $\sigma^{(n)}$ as number resolved reduced multi-polariton density operator. We defined the super-operator as, $L_s^{(n)}O = [H_p^{(n)}, O]$. The polariton-phonon memory kernel capable of describing the phonon-induced polariton relaxation and dephasing (neglecting the effects of the driving field on the relaxation) is given by, $\Sigma^{(n)}(t,\tau)\sigma^{(n)}(t) = -\lambda^2[X, D(t)\sigma_s(t) - \sigma_s(t)D^\dagger(t)]$. The kernel contains the dissipation operator $D(t) = X(t-t')$ $C_b(t-t')$ where we have the convolution of polariton-phonon coupling operator $X(\tau) = \sum_{p^{(n)}} X_{p^{(n)}p^{(n)}}(\tau)$ and time-domain correlation function given by,

$$\begin{aligned} C_b(\tau) = {} & (\lambda_0\gamma_0/2)\cot(\beta\gamma_0/2)\exp(-\gamma_0\tau) \\ & + \sum_{j=1}^{N_b} \frac{\lambda_j}{2\zeta_j}\left(\coth\left(i\beta\phi_j^+/2\right)\exp\left(-\phi_j^+\tau\right) - \coth\left(i\beta\phi_j^-/2\right)\exp\left(-\phi_j^-\tau\right)\right) \\ & + (-i\lambda_0\gamma_0/2)\exp(-\gamma_0\tau) + \frac{i\lambda_j v_j^2}{2\zeta_j}\left(\exp\left(-\phi_j^+ t\right) - \exp\left(-\phi_j^- t\right)\right) \\ & - \sum_{n=1}^{\infty}\left(\left(4\lambda_j\gamma_j v_j^2/\beta\right)\left(\nu_n/\left(v_j^2+\nu_n^2\right)^2 - \nu_n^2\gamma_j^2\right)\right. \\ & \left. + (2\lambda_0\gamma_0/\beta)\left(\nu_n/\left(\nu_n^2-\gamma_0^2\right)\right)\right)\exp(-i\nu_n\tau) \end{aligned} \tag{3}$$

In the above we have $\zeta_j = \sqrt{(v_j^2 - \gamma_j^2/4)}$, $\phi_j^\pm = (\gamma_j/2) \pm i\zeta_j$, and, matsubara frequencies, $\nu_n = n\,(2\pi/\beta)$ (with $n_m = 20$). Furthermore, we defined $\beta = 1/\kappa T$ where the Boltzmann constant κ and temperature T is denoted. The energy domain version of the relaxation kernel was used to extract the dephasing parameters. We define the line-broadening functions as, $\gamma_{p_1^{(n)}}(t) = \theta(t)\sum_{p_2,p_s} C_b(\omega_{p_1p_2}) T^{(n)}_{p_sp_2} T^{(n)}_{p_sp_2} T^{(n)}_{p_sp_1} T^{(n)}_{p_sp_1}$ where we have $C_b(\Omega) = \int dt \exp i\Omega t C^\pm(t)$ and $C_b^\pm(t) = \int (d\omega/2\pi)(\coth\beta\omega/2)\cos\omega t \mp i\sin\omega t)$ which can be evaluated using the previous expressions. With the help of the line-broadening functions we estimate the inter-manifold dephasing parameters as, $\gamma_{p_1^{(n)}p_2^{(m)}} = (\gamma_{p_1^{(n)}} + \gamma_{p_2^{(m)}})/2$. Finally, we obtain the inter-manifold Greens functions relevant for dephasing as, $G_{p_1^{(n)}p_2^{(m)}}(\omega) = i(\omega - \omega_{p_1^{(n)}p_2^{(m)}} - i\gamma_{p_1^{(n)}p_2^{(m)}})^{-1}$. The advanced Green's functions are defined likewise.

3 MULTIDIMENSIONAL DOUBLE-QUANTUM COHERENCE SIGNAL WITH ENTANGLED BIPHOTON SOURCES

The theoretical development mentioned in the preceding sections provides us the ingredients to introduce the Double Quantum Coherence (DQC) signal. The DQC signal, as hinted earlier, involves excitation of state-selective (or narrow-band around the selected state) two-polariton coherence that is followed by projection of the oscillating polarization components onto two plausible sets of inter-manifold coherence. Provided that the participant two-polariton states are sufficiently correlated with the states onto which they are being projected, the desired nonlinear polarization have dominant component in the phase-matched direction $k_s = k_1 + k_2 - k_3$. Below we present a modular derivation of the signal starting from the time-dependent dual-perturbation scheme, corroborate the derivation to the Keldysh-Schwinger loop diagrams **Figure 2** and introduce the entangled biphoton sources that serves as probe.

3.1 Double Quantum Coherence Signal

The DQC signal is typically generated by inducing four external field-matter interactions. In the case of time-domain (frequency-domain) classical field sources, three external fields with controllable delays (relative phases) are allowed to interact with the matter. The radiation field emitted by the time-dependent nonlinear polarization is registered, typically, via suitable heterodyning after another delay (spectrally dispersing) the signal. Typically, the deployment of quantum fields e.g., the biphoton sources to the measurement of DQC signals requires considerable care. These field sources are often parametrically scanned via schemes akin to multi-pulse phase-cycling. An involved discussion regarding the details of the deployment and measurement scheme is beyond the scope of the article [67, 68]. However, we assume that the biphoton generation scheme is capable of producing two sets of entangled photon pairs that lend themselves to external manipulation via central frequencies and delays. Before

proceeding further, we introduce the two sets of pathways involved in the DQC signal generation as,

$$\Pi_a(\tau_4,\tau_3,\tau_2,\tau_1) = d_{p_i^{(0)}p_{j'}^{(1)}}(\tau_4)d_{p_{j'}^{(1)}p_k^{(2)}}(\tau_3)d_{p_k^{(2)}p_j^{(1)}}(\tau_2)d_{p_j^{(1)}p^{(0)}}(\tau_1)$$
$$\Pi_b(\tau_4,\tau_3,\tau_2,\tau_1) = d_{p_i^{(0)}p_{j'}^{(1)}}(\tau_3')d_{p_{j'}^{(1)}p_k^{(2)}}(\tau_4')d_{p_k^{(2)}p_j^{(1)}}(\tau_2')d_{p_j^{(1)}p^{(0)}}(\tau_1') \tag{4}$$

where the first and the second one have been written in the Heisenberg representation and correspond to diagrams in **Figure 2**). These pathways, notably, differing in the last two components signify dynamical spectral weights. Interference features between these pathway components depend on the nature of the polariton correlation and dephasing properties. We also introduce the time-domain, four-point external field correlation function as $D(\tau_4, \tau_3, \tau_2, \tau_1)$ which is capable of incorporating the generalized nature of the external field. With the help of these definitions, we present the signal expression in the time-domain as, $S = C_s \mathrm{Im}\prod_{i\epsilon a,b}$ $\int_\infty^\infty d\tau_4^{(i)}d\tau_3^{(i)}d\tau_2^{(i)}d\tau_1^{(i)}\theta(\tau_{43}^{(i)})\theta(\tau_{32}^{(i)})\theta(\tau_{21}^{(i)})$ $\times D^{(i)}(\tau_4^{(i)},\tau_3^{(i)},\tau_2^{(i)},\tau_1^{(i)})\Pi_i(\tau_4^{(i)},\tau_3^{(i)},\tau_2^{(i)},\tau_1^{(i)})$ where C_s represents the coefficients that arises from the perturbative expansion and have been taken as a scaling factor. The Heaviside functions are defined in reference to the interaction times denoted along the loop diagrams. In going forward, the interaction times i.e. the loop time-instance variables were transformed to the loop-delay variables and mapped onto the real-time parameters that are externally tunable using, $\theta(s_3)\theta(s_2)\theta(s_1) \rightarrow \theta(t_3)\theta(t_2)\theta(t_1)$ for the diagram I and $\theta(s_3)\theta(s_2)\theta(s_1) \rightarrow \theta(s_3)\theta(s_2 - s_3)\theta(s_1) = \theta(t_3)\theta(t_2)\theta(t_1)$ for the diagram II. These parameters are experimentally realizable. We also use the time-domain phonon-averaged Green's functions expanded in the multi-polariton basis and write the field correlation function in the frequency domain. Following these exercises, we obtain the generalized signal as,

$$S = C_s\int_{-\infty}^{\infty} dT_1dT_2dT_3F(\Omega_3,\Omega_2,\Omega_1;T_3,T_2,T_1)$$

$$\int_\infty^\infty \frac{d\tilde{\omega}_3}{2\pi}\frac{d\tilde{\omega}_2}{2\pi}\frac{d\tilde{\omega}_1}{2\pi}e^{-i\left(-\tilde{\omega}_3+\tilde{\omega}_2+\tilde{\omega}_1\right)T_3-i\left(\tilde{\omega}_1+\tilde{\omega}_2\right)T_2-i\tilde{\omega}_1T_1}$$
$$\langle E_3^\dagger(\tilde{\omega}_3)E_4^\dagger(+\tilde{\omega}_1+\tilde{\omega}_2-\tilde{\omega}_3)E_2(\tilde{\omega}_2)E_1(\tilde{\omega}_1)\rangle$$

$$\sum_{p_j^{(1)},p_{j'}^{(1)},p_k^{(2)}} w^{(1)}G_{p_k^{(2)}p_{j'}^{(1)}}(\tilde{\omega}_1+\tilde{\omega}_2-\tilde{\omega}_3)G_{p_k^{(2)}p^{(0)}}(\tilde{\omega}_2+\tilde{\omega}_1)$$

$$G_{p_j^{(1)}p^{(0)}}(\tilde{\omega}_1) + \langle E_3^\dagger(\tilde{\omega}_3)E_4^\dagger(+\tilde{\omega}_1+\tilde{\omega}_2$$

$$-\tilde{\omega}_3)E_2(\tilde{\omega}_2)E_1(\tilde{\omega}_1)\rangle \sum_{p_j^{(1)},p_{j'}^{(1)},p_k^{(2)}} w^{(2)}G_{p_{j'}^{(1)}p^{(0)}}(-\tilde{\omega}_3+\tilde{\omega}_2+\tilde{\omega}_1)$$

$$G_{p_k^{(2)}p^{(0)}}(\tilde{\omega}_2+\tilde{\omega}_1)G_{p_j^{(1)}p^{(0)}}(\tilde{\omega}_1) \tag{5}$$

This expression is valid for a general class of DQC signal measurement which may use different kinds of external field sources beyond biphotons and simple Gaussian classical fields. The field correlation function acts as a convolutional probing function for the bare signal. Additional possibilities for the external manipulation of the field correlation function extend the applicability of DQC signals to a wide range of scenarios. Further, we aim to introduce a two-dimensional frequency-domain representation of the signal in order to facilitate a visualization of the correlation features contained in the matter correlation functions. In order to allow such representations to be generated via real-time delay-scanning protocols, we introduce integral transform, $F(\Omega_3,\Omega_2,\Omega_1;T_3,T_2,T_1) = \theta(T_3)\theta(T_2)\theta(T_1)e^{i\Omega_3T_3}e^{i\Omega_2T_2}e^{i\Omega_1T_1}$. We also define the following variable mapping of the parameters, $\tilde{\tau}_{21}^0 \rightarrow T_1, \tilde{\tau}_{32}^0 \rightarrow T_2, \tilde{\tau}_{43}^0 \rightarrow T_3$, for the diagram I and $\tau_{21}^0 \rightarrow T_1, \tau_{42}^0 - \tau_{43}^0 \rightarrow T_2, \tau_{43}^0 \rightarrow T_3$, for the diagram II (the τ_{ij}^0 is the delays between the centering times). Scanning of these set of parameters and obtaining joint Fourier transforms w. r.t the delays generate the desired two-dimensional correlation plots. The final expression can be presented as the following expression.

$$S(\Omega_3,\Omega_2,\Omega_1) = C_s\sum_{p^{(0)}p_j^{(1)}p_{j'}^{(1)}p_k^{(2)}} w^{(1)}\tilde{F}_\Omega^{(1)}\langle E_4^\dagger\left(z_{p_k^{(2)}p_{j'}^{(1)}}\right)$$

$$E_3^\dagger\left(z_{p_{j'}^{(1)}p^{(0)}}\right)E_2\left(z_{p_k^{(2)}p_j^{(1)}}\right)E_1\left(z_{p_j^{(1)}p^{(0)}}\right)$$
$$+ w^{(2)}\tilde{F}_\Omega^{(2)}\langle E_4^\dagger\left(z_{p_k^{(2)}p_{j'}^{(1)}}\right)E_3^\dagger\left(z_{p_{j'}^{(1)}p^{(0)}}\right)E_2\left(z_{p_k^{(2)}p_j^{(1)}}\right)E_1\left(z_{p_j^{(1)}p^{(0)}}\right) \tag{6}$$

where the functions are specified as,

$$\tilde{F}_\Omega^{(1)} = \left\{\left(\Omega_3 - z_{p_2^{(1)}p^{(0)}}\right)\left(\Omega_2 - z_{p^{(2)}p^{(0)}}\right)\left(\Omega_1 - z_{p_1^{(1)}p^{(0)}}\right)\right\}^{-1}$$
$$\tilde{F}_\Omega^{(2)} = \left\{\left(\Omega_3 - z_{p^{(2)}p_i^{(1)}}\right)\left(\Omega_2 - z_{p^{(2)}p^{(0)}}\right)\left(\Omega_1 - z_{p^{(1)}p^{(0)}}\right)\right\}^{-1} \tag{7}$$

These functions encode the polariton dynamical resonances. These resonances show up, as predicted, during the scan of the Fourier transformed parameter. The field correlation function encodes the information about the ability to manipulate the spectral weights of the matter excitations and reveal desired dynamical resonances.

3.2 Entangled Biphoton Properties

The principal aim of using the entangled biphoton sources is to avail the non-classical relation between the joint time of arrival and frequency pairs of the biphotons. This in turn allows one to excite relatively short-lived two-polariton states (i.e., within an ultra-short time window) that are outside the excitation energy window of the classical two-photon laser pulses. These constraints remain difficult to surpass via independent variable manipulation, even in the case of multiple classical pulses. Below we present some basic features of the entangled photon source properties that were used in the simulation and describe their correlation features. The entangled biphoton field is traditionally generated via the spontaneous parametric down-conversion (SPDC) process (in the weak down-conversion limit) by pumping the source material with an

ultra-short classical laser. The pump pulse bandwidth and the central frequency determine the correlation properties and time-frequency regime of the generated pairs. An effective Hamiltonian procedure which has been used to derive the correlation properties as outlined previously [47, 69–71] is avoided here for succinctness. Following a similar derivation, the entangled biphoton field correlation function can be obtained as, $\langle E^{\dagger}(\omega_4)E^{\dagger}(\omega_4)E(\omega_2)E(\omega_1)\rangle = F_1^{\star}(\omega_4,\omega_3)F_1(\omega_2,\omega_1)$ where we have, $F_1(\omega_a,\omega_b;\omega_p) = A_0(\omega_a,\omega_b)\{\mathrm{sinc}[\phi(\omega_a,\omega_b)]\exp i\phi(\omega_a,\omega_b) + a \leftrightarrow b\}$. The function $\phi(\omega_j,\omega_k) = (\omega_j - \omega_p/2)\tilde{T}_1 + (\omega_k - \omega_p/2)\tilde{T}_2$ and the temporal entanglement parameter of the pairs $\tilde{T}_1(\tilde{T}_2)$, via $\tilde{T}_{\mathrm{ent}} = \tilde{T}_2 - \tilde{T}_1$, quantifies the spectral-temporal properties of the entangled biphotons [71–73]. The term A_0 denotes the amplitude of the pump. This form of factorization underlies the fact that the signal scales linearly with the intensity. The temporal entanglement parameter can be viewed as an estimator of upper bound of delay between the time of generation of the entangled photon pairs inside the SPDC source material. The entanglement time parameter arises from the phase matching function $\Delta k\ (\omega_1, \omega_2)$ and parametrically depends on the group velocity of propagation inside the SPDC material. The phase mismatching function under the linearization approximation around the central frequencies of the beams, for the collinear case leads to the identification of parameters, $T_j = 1/v_p - 1/v_j$ where $j \in \{1, 2\}$ and $v_{p/j}$ denotes the group velocity of the pump, and two biphotons inside the material. These values can be estimated from the inverse of the marginal distribution function of the joint spectral amplitude function in the frequency domain [51, 73]. In contrast, the classical field, in a similar weak-field limit factorizes into the product of amplitudes as, $\langle E^{\dagger}(\omega_4)E^{\dagger}(\omega_3)E(\omega_2)E(\omega_1)\rangle = A_4^{\star}(\omega_4)A_3^{\star}(\omega_3)A_1(\omega_2)A_1(\omega_1)$ and scales quadratically with the intensity. The biphoton field correlation properties for different typical parameter regimes can be examined by plotting the joint-spectral amplitude which describes the frequency-dependent correlation of the same as shown in **Figure 3**. The bottom-right plot (i.e., (d)) in **Figure 3** corresponds to a classical field scenario. The simulation has the freedom of selecting frequency pairs from the plot region where the function has finite support.

3.3 Simulation

The correlated two-polariton excitations via entangled biphoton sources may focus on several experimental configurations which will be of particular interest to the condensed phase spectroscopies. The excitation of specific two-polariton states via higher-energy sectors of the one-polariton manifold and contrasting them with those via the lower-energy sectors may give information about polariton scattering, delocalization, and dephasing. In other words, the specific two-polariton states may have dominant contributions from certain one-polariton states which are distant on the site basis but energetically closer. Alternatively for the same two-polariton excitation, projecting to the higher and lower-energy one-polariton sector offers insights into the state compositions. Combining two strategies may provide important insight into the state resolved polariton correlations. These features can be probed as shown in the upper and lower panel of **Figure 4**. Particularly the polariton states (e.g., $\omega_{p^{(2)}} = 30550\mathrm{cm}^{-1}$) that are specifically prone to phonon-induced dephasing (higher dephasing induced broadened) have been excited while the temporal entanglement parameter of the probe, projected one-polariton sector has been varied.

In the upper panel of **Figure 4**, we present, along the rows, three sets of results for the variation of the temporal entanglement parameter $\tilde{T}_{\mathrm{ent}}$ (fs. Each of them correspond to fixed $\omega_{a_1}(\mathrm{cm}^{-1}) = 15500$ and $\omega_{b_1}(\mathrm{cm}^{-1}) = 14500$ (therefore exciting the target at $\omega_p^{(2)} = 30550$) with pump width τ_p (fs) = 20.0. Therefore, the two polariton excitation occurs via the middle sector of the one-polariton band. It also projects the two-polariton coherence to the mixed-energy region of the one-polariton band by choosing the corresponding frequencies as $\omega_{a_2}(\mathrm{cm}^{-1}) = \omega_p^{(2)} - 15800$ and $\omega_{b_2}(\mathrm{cm}^{-1}) = 15800$. It is noticed that the strong entanglement between the photon pairs, as we move from (A) to (C) corresponding to $\tilde{T}_{\mathrm{ent}}$(fs) values 60.0, 50.0, 40.0 respectively, allows correlated signal features to develop. These emergent features may not be visible in the signal obtained by using classical pulse pairs of comparable spectral-temporal properties. Time-frequency correlated excitation gives the freedom of simultaneously choosing the narrow-band target while ensuring that system remains less affected by the high dephasing components of the intermediate states. The latter has the possibility of making the short-time kinetics in the one-polariton manifold more accessible. Even an individually controlled classical field two-pulse scenario may offer less advantage because the temporal and spectral components are bound.

The bottom row ((d) to (f)) accomplishes the aforementioned goal of exploring excitation via different energy sectors of the one-polariton manifold. Here the (d) and (e) allow excitation via middle-sector and (f) lower-sector while projecting all of them to the same mixed-energy sectors as the above panel. With the increase in temporal entanglement parameter in going from (d) to (e) ($\tilde{T}_{\mathrm{ent}}$(fs) values 40.0, 10.0, respectively) we find features shows distinguishable increase. The last panel (f) whose excitation via lower energy sector (excitation via $\omega_{a_1}(\mathrm{cm}^{-1}) = 15150$ and $\omega_{b_1}(\mathrm{cm}^{-1}) =$) which reveals many more correlation features. It reveals the higher participation of the particular set of one-polariton states to chosen target in the two-polariton manifold throughout the simulation. The short temporal entanglement parameter also certifies the capability of the biphoton sources to map out correlation involving energetically distant states. The success of the parameter regime and overall strategy of the simulation can be traced back to the ability to choose the frequency pairs from a broader distribution. In addition, the fact that they are also bound by the temporal constraints allow excitation via fast dephasing components in the one-polariton band (during the first time delay i.e., T_1) while simultaneously projecting the resultant two-polariton coherence to short-lived coherences (during the last time delay i.e., T_3).

4 CONCLUSION AND OUTLOOK

In this article, we have proposed a theoretical protocol that is suitable for the investigation of the inter-manifold coherence properties associated with the two-polariton manifold. We observe that the proposal exclusively focused on the cavity control of exciton correlation and modulation of exciton-phonon dephasing via the former. In other words, the cavity affects the exciton transitions directly and redistributes the excitonic spectral weights. The extent to which this redistribution occurs is encoded in the action of the polariton transformation matrices. As a result, the novel hybridized polariton states interact with the phonons rather differently than that of the cavity-free case. We demonstrated that biphoton sources are capable of studying the ultrafast signatures of the related dynamics without losing the state specificity. In the process, it is capable of mapping out the cavity modulated exciton correlation. In this direction, two further extensions namely, the detailed study involving the parametric variation of the cavity-free case and a comparison employing controlled classical fields are worth looking at. They will be part of future communication. However, we note that the signal expressions presented in this communication will be sufficient for such extended analysis.

The role of cavity coupling has been included non-perturbatively with the same quasi-particle excitation picture. Here the real-space coupling variations were neglected for convenience, in the spirit of the first simulation. Also, the role of the mean number of photons in the cavity has not been investigated and the role of the cavity has been confined to the coherence created between the states within the proposed regime of operation.

In comparing and contrasting the present technique to the transmission mode pump-probe measurements several features distinguish the present technique. DQC measures one specific component of the nonlinear polarization of the cavity polariton, unlike the pump-probe analog. The pump-probe technique also includes the pathways analogous to polaritonic Raman scattering pathways. Thus the DQC signal is more specific to the purpose of this article. The two-polariton coherence is explicitly monitored by isolating the signal components as suggested by the plausible implementation via phase-cycling schemes. It can be also highlighted that the present technique works by projecting the two-polariton coherence in two competing coherence components of lower order. The relevant processes leading to the signal occur during the last two time intervals. The degree of discrimination of the pathways, reflected in the associated dynamical spectral weights decides the magnitude of the signal. In contrast to the pump-probe studies, the off-diagonal spectral signatures in the correlation plots required to be interpreted differently. In the latter, the cooperative features appearing in the above-mentioned sector carry less specific information regarding the physical origin of the polaritonic correlation due to non-discrimination between pure two-one polariton coherence and two-polariton-one polariton coherence.

The study can be extended to accommodate the explicit two-polariton transport phenomenology by studying the fluorescence-detected phase cycling protocols [74, 75]. The latter is a four-wave mixing analog but aimed at investigating the longer-time state correlation properties in the presence of phonon-induced dynamical population redistribution. The longer-time dynamical information thereby obtained is complementary to the information provided by the short-time dynamics investigated in this article. An investigation in this direction is on the way. Furthermore, one may combine the interferometric detection schemes to separate the pathways as recently proposed [76, 77].

The theoretical description adopted for describing the dissipative polaritonic matter is formulated at the level of a quasi-particle approach. The quasi-particle Green's function was chosen to describe the signal [78]. Over the last few years, a host of promising methods have been proposed that can potentially deal with the complexity of the quantum aggregates in near future. These methods have offered several different flavors of treating the matter and the cavity modes. We have, namely, quantum electrodynamics based hybrid (density) functional formulation [79–82], cluster-expansion [21], potential-energy surface-based dynamical calculations combined with the trajectory-based propagation for the cavity quadrature modes [83, 84], path integral based unified framework for nuclear modes and the idealized cavity modes [85–87], first-principles simulations [88–92]. Incorporating these methods to describe the phenomenology described in this article will require a qualified description of exciton formation, a description of exciton-exciton scattering in the presence of a dielectric environment, and nuclear propagation.

We also note that the numerical simulation adopted the analytical expressions which have been derived under the assumption of generalized time-translational invariance. For systems driven out-of-equilibrium via additional laser pulses, one may expect to see more correlation features in the signal. The scope to add additional pulses and using the biphotons as probes, although offers a more complicated scenario, is a promising avenue for future study of nonlinear response in correlated quantum materials [93–97].

DATA AVAILABILITY STATEMENT

The raw data supporting the conclusion of this article will be made available by the authors, without undue reservation.

AUTHOR CONTRIBUTIONS

AD developed the project in consultation with AR. AD performed the research. AD and AR analyzed the results. AD wrote the manuscript with inputs from AR.

ACKNOWLEDGMENTS

We acknowledge financial support from the European Research Council (ERC-2015-AdG-694097), by the Cluster of Excellence "Advanced Imaging of Matter" (AIM), Grupos Consolidados (IT1249-19) and SFB925 "Light induced dynamics and control of correlated quantum systems." The Flatiron Institute is a division of the Simons Foundation.

REFERENCES

1. Boulais É, Sawaya NPD, Veneziano R, Andreoni A, Banal JL, Kondo T, et al.Programmed Coherent Coupling in a Synthetic DNA-Based Excitonic Circuit. *Nat Mater* (2018) 17:159–66. doi:10.1038/nmat5033
2. Romero E, Augulis R, Novoderezhkin VI, Ferretti M, Thieme J, Zigmantas D, et al.Quantum Coherence in Photosynthesis for Efficient Solar-Energy Conversion. *Nat Phys* (2014) 10:676–82. doi:10.1038/nphys3017
3. Scholes GD, Fleming GR, Chen LX, Aspuru-Guzik A, Buchleitner A, Coker DF, et al.Using Coherence to Enhance Function in Chemical and Biophysical Systems. *Nature* (2017) 543:647–56. doi:10.1038/nature21425
4. Schlau-Cohen GS, Ishizaki A, Calhoun TR, Ginsberg NS, Ballottari M, Bassi R, et al.Elucidation of the Timescales and Origins of Quantum Electronic Coherence in LHCII. *Nat Chem* (2012) 4:389–95. doi:10.1038/nchem.1303
5. Cao J, Cogdell RJ, Coker DF, Duan H-G, Hauer J, Kleinekathöfer U, et al.Quantum Biology Revisited. *Sci Adv* (2020) 6:eaaz4888. doi:10.1126/sciadv.aaz4888
6. Scholes GDPolaritons and Excitons: Hamiltonian Design for Enhanced Coherence. *Proc R Soc A* (2020) 476:20200278. doi:10.1098/rspa.2020.0278
7. Basov D, Asenjo-Garcia A, Schuck PJ, Zhu X, Rubio APolariton Panorama. *Nanophotonics* (2021) 10:549.
8. Ruggenthaler M, Tancogne-Dejean N, Flick J, Appel H, Rubio AFrom a Quantum-Electrodynamical Light–Matter Description to Novel Spectroscopies. *Nat Rev Chem* (2018) 2:1. doi:10.1038/s41570-018-0118
9. Mewes L, Wang M, Ingle RA, Börjesson K, Chergui MEnergy Relaxation Pathways between Light-Matter States Revealed by Coherent Two-Dimensional Spectroscopy. *Commun Phys* (2020) 3:1. doi:10.1038/s42005-020-00424-z
10. Garcia-Vidal FJ, Ciuti C, Ebbesen TWManipulating Matter by strong Coupling to Vacuum fields. *Science* (2021) 373:eabd0336. doi:10.1126/science.abd0336
11. Cao JGeneralized Resonance Energy Transfer Theory: Applications to Vibrational Energy Flow in Optical Cavities. arXiv preprint arXiv:2201.12117 (2022). doi:10.48550/ARXIV.2201.12117
12. Engelhardt G, Cao JUnusual Dynamical Properties of Disordered Polaritons in Micocavities. arXiv preprint arXiv:2112.04060 (2021) 105:064205.
13. Groenhof G, Toppari JJCoherent Light Harvesting through Strong Coupling to Confined Light. *J Phys Chem Lett* (2018) 9:4848–51. doi:10.1021/acs.jpclett.8b02032
14. Latini S, Shin D, Sato SA, Schäfer C, De Giovannini U, Hübener H, et al.The Ferroelectric Photo Ground State of $SrTiO_3$: Cavity Materials Engineering. *Proc Natl Acad Sci* (2021) 118. doi:10.1073/pnas.2105618118
15. Lengers F, Kuhn T, Reiter DEPhonon Signatures in Spectra of Exciton Polaritons in Transition Metal Dichalcogenides. *Phys Rev B* (2021) 104:L241301. doi:10.1103/physrevb.104.l241301
16. Autry TM, Nardin G, Smallwood CL, Silverman K, Bajoni D, Lemaître A, et al.Excitation Ladder of Cavity Polaritons. *Phys Rev Lett* (2020) 125:067403. doi:10.1103/physrevlett.125.067403
17. Sidler D, Schäfer C, Ruggenthaler M, Rubio APolaritonic Chemistry: Collective Strong Coupling Implies Strong Local Modification of Chemical Properties. *J Phys Chem Lett* (2020) 12:508–16. doi:10.1021/acs.jpclett.0c03436
18. Yang P-Y, Cao JQuantum Effects in Chemical Reactions under Polaritonic Vibrational Strong Coupling. *J Phys Chem Lett* (2021) 12:9531–8. doi:10.1021/acs.jpclett.1c02210
19. Salij A, Tempelaar RMicroscopic Theory of Cavity-Confined Monolayer Semiconductors: Polariton-Induced valley Relaxation and the prospect of Enhancing and Controlling valley Pseudospin by Chiral strong Coupling. *Phys Rev B* (2021) 103:035431. doi:10.1103/physrevb.103.035431
20. Latini S, De Giovannini U, Sie EJ, Gedik N, Hübener H, Rubio APhonoritons as Hybridized Exciton-Photon-Phonon Excitations in a Monolayer H -BN Optical Cavity. *Phys Rev Lett* (2021) 126:227401. doi:10.1103/physrevlett.126.227401
21. Haugland TS, Ronca E, Kjønstad EF, Rubio A, Koch HCoupled Cluster Theory for Molecular Polaritons: Changing Ground and Excited States. *Phys Rev X* (2020) 10:041043. doi:10.1103/physrevx.10.041043
22. Sidler D, Ruggenthaler M, Schäfer C, Ronca E, Rubio A,A Perspective on Ab Initio Modeling of Polaritonic Chemistry: The Role of Non-equilibrium Effects and Quantum Collectivity. arXiv preprint arXiv:2108.12244 (2021).
23. Schäfer C, Flick J, Ronca E, Narang P, Rubio AShining Light on the Microscopic Resonant Mechanism Responsible for Cavity-Mediated Chemical Reactivity. arXiv preprint arXiv:2104.12429 (2021).
24. Zhang Z, Scully MO, Agarwal GSQuantum Entanglement between Two Magnon Modes via Kerr Nonlinearity Driven Far from Equilibrium. *Phys Rev Res* (2019) 1:023021. doi:10.1103/physrevresearch.1.023021
25. Zhang Z, Agarwal GS, Scully MOQuantum Fluctuations in the Fröhlich Condensate of Molecular Vibrations Driven Far from Equilibrium. *Phys Rev Lett* (2019) 122:158101. doi:10.1103/physrevlett.122.158101
26. Wang D, Kelkar H, Martin-Cano D, Utikal T, Götzinger S, Sandoghdar VCoherent Coupling of a Single Molecule to a Scanning Fabry-Perot Microcavity. *Phys Rev X* (2017) 7:021014. doi:10.1103/physrevx.7.021014
27. Maser A, Gmeiner B, Utikal T, Götzinger S, Sandoghdar VFew-photon Coherent Nonlinear Optics with a Single Molecule. *Nat Photon* (2016) 10:450–3. doi:10.1038/nphoton.2016.63
28. Campos-Gonzalez-Angulo JA, Yuen-Zhou JGeneralization of the Tavis-Cummings Model for Multi-Level Anharmonic Systems: Insights on the Second Excitation Manifold (2022) 156:194308. doi:10.1063/5.0087234
29. Debnath A, Rubio AEntangled Photon Assisted Multidimensional Nonlinear Optics of Exciton-Polaritons. *J Appl Phys* (2020) 128:113102. doi:10.1063/5.0012754
30. DelPo CA, Kudisch B, Park KH, Khan S-U -Z, Fassioli F, Fausti D, et al.Polariton Transitions in Femtosecond Transient Absorption Studies of Ultrastrong Light-Molecule Coupling. *J Phys Chem Lett* (2020) 11:2667–74. doi:10.1021/acs.jpclett.0c00247
31. Ribeiro RF, Campos-Gonzalez-Angulo JA, Giebink NC, Xiong W, Yuen-Zhou JEnhanced Optical Nonlinearities under Collective strong Light-Matter Coupling. *Phys Rev A* (2021) 103:063111. doi:10.1103/physreva.103.063111
32. Renken S, Pandya R, Georgiou K, Jayaprakash R, Gai L, Shen Z, et al.Untargeted Effects in Organic Exciton-Polariton Transient Spectroscopy: A Cautionary Tale. *J Chem Phys* (2021) 155:154701. doi:10.1063/5.0063173
33. Zhang Z, Peng T, Nie X, Agarwal GS, Scully MODirectional Superradiant Emission from Statistically Independent Incoherent. arXiv preprint arXiv:2106.10988 (2021). doi:10.48550/ARXIV.2106.10988
34. Zhang Z, Wang K, Yi Z, Zubairy MS, Scully MO, Mukamel SPolariton-Assisted Cooperativity of Molecules in Microcavities Monitored by Two-Dimensional Infrared Spectroscopy. *J Phys Chem Lett* (2019) 10:4448–54. doi:10.1021/acs.jpclett.9b00979
35. Zhang Z, Saurabh P, Dorfman KE, Debnath A, Mukamel SMonitoring Polariton Dynamics in the LHCII Photosynthetic Antenna in a Microcavity by Two-Photon Coincidence Counting. *J Chem Phys* (2018) 148:74302. doi:10.1063/1.5004432
36. Lee D, Albrecht ACThe Vibronic Theory of Resonance Hyper-Raman Scattering. *Adv infrared Raman Spectrosc* (1985) 12:179.
37. Tempelaar R, Jansen TLC, Knoester JExciton-Exciton Annihilation Is Coherently Suppressed in H-Aggregates, but Not in J-Aggregates. *J Phys Chem Lett* (2017) 8:6113–7. doi:10.1021/acs.jpclett.7b02745
38. Gutiérrez-Meza E, Malatesta R, Li H, Bargigia I, Srimath Kandada AR, Valverde-Chávez DA, et al.Frenkel Biexcitons in Hybrid HJ Photophysical Aggregates. *Sci Adv* (2021) 7:eabi5197. doi:10.1126/sciadv.abi5197
39. Mukamel S*Principles of Nonlinear Optical Spectroscopy*, 6. New York: Oxford University Press on Demand (1999).
40. Lomsadze B, Cundiff STLine-shape Analysis of Double-Quantum Multidimensional Coherent Spectra. *Phys Rev A* (2020) 102:043514. doi:10.1103/physreva.102.043514
41. Gao F, Cundiff ST, Li HProbing Dipole-Dipole Interaction in a Rubidium Gas via Double-Quantum 2D Spectroscopy. *Opt Lett* (2016) 41:2954. doi:10.1364/ol.41.002954
42. Kim J, Mukamel S, Scholes GDTwo-Dimensional Electronic Double-Quantum Coherence Spectroscopy. *Acc Chem Res* (2009) 42:1375–84. doi:10.1021/ar9000795
43. Svozilík J, Peřina J, León-Montiel Rd. JVirtual-state Spectroscopy with Frequency-Tailored Intense Entangled Beams. *J Opt Soc Am B* (2018) 35:460. doi:10.1364/josab.35.000460

44. León-Montiel Rd. J, Svozilík J, Torres JP, U'Ren ABTemperature-Controlled Entangled-Photon Absorption Spectroscopy. *Phys Rev Lett* (2019) 123:023601. doi:10.1103/physrevlett.123.023601
45. Kang G, Nasiri Avanaki K, Mosquera MA, Burdick RK, Villabona-Monsalve JP, Goodson T, III, et al.Efficient Modeling of Organic Chromophores for Entangled Two-Photon Absorption. *J Am Chem Soc* (2020) 142:10446–58. doi:10.1021/jacs.0c02808
46. Schlawin F, Dorfman KE, Mukamel SEntangled Two-Photon Absorption Spectroscopy. *Acc Chem Res* (2018) 51:2207–14. doi:10.1021/acs.accounts.8b00173
47. Saleh BEA, Jost BM, Fei H-B, Teich MCEntangled-Photon Virtual-State Spectroscopy. *Phys Rev Lett* (1998) 80:3483–6. doi:10.1103/physrevlett.80.3483
48. Richter M, Mukamel SUltrafast Double-Quantum-Coherence Spectroscopy of Excitons with Entangled Photons. *Phys Rev A* (2010) 82:013820. doi:10.1103/physreva.82.013820
49. Roslyak O, Mukamel SMultidimensional Pump-Probe Spectroscopy with Entangled Twin-Photon States. *Phys Rev A* (2009) 79:063409. doi:10.1103/physreva.79.063409
50. Mukamel S, Freyberger M, Schleich W, Bellini M, Zavatta A, Leuchs G, et al.Roadmap on Quantum Light Spectroscopy. *J Phys B: Mol Opt Phys* (2020) 53:072002. doi:10.1088/1361-6455/ab69a8
51. Landes T, Raymer MG, Allgaier M, Merkouche S, Smith BJ, Marcus AHQuantifying the Enhancement of Two-Photon Absorption Due to Spectral-Temporal Entanglement. *Opt Express* (2021) 29:20022. doi:10.1364/oe.422544
52. Bittner ER, Li H, Piryatinski A, Srimath Kandada AR, Silva CProbing Exciton/exciton Interactions with Entangled Photons: Theory. *J Chem Phys* (2020) 152:071101. doi:10.1063/1.5139197
53. Schlawin F, Buchleitner ATheory of Coherent Control with Quantum Light. *New J Phys* (2017) 19:013009. doi:10.1088/1367-2630/aa55ec
54. Li H, Piryatinski A, Srimath Kandada AR, Silva C, Bittner ERPhoton Entanglement Entropy as a Probe of many-body Correlations and Fluctuations. *J Chem Phys* (2019) 150:184106. doi:10.1063/1.5083613
55. Richter M, Singh R, Siemens M, Cundiff STDeconvolution of Optical Multidimensional Coherent Spectra. *Sci Adv* (2018) 4:eaar7697. doi:10.1126/sciadv.aar7697
56. Agranovich V, Toshich BCollective Properties of Frenkel Excitons. *Sov Phys JETP* (1968) 26:104.
57. Chernyak V, Zhang WM, Mukamel SMultidimensional Femtosecond Spectroscopies of Molecular Aggregates and Semiconductor Nanostructures: The Nonlinear Exciton Equations. *J Chem Phys* (1998) 109:9587–601. doi:10.1063/1.477621
58. Abramavicius D, Palmieri B, Voronine DV, Šanda F, Mukamel SCoherent Multidimensional Optical Spectroscopy of Excitons in Molecular Aggregates; Quasiparticle versus Supermolecule Perspectives. *Chem Rev* (2009) 109:2350–408. doi:10.1021/cr800268n
59. Novoderezhkin VI, Palacios MA, Van Amerongen H, Van Grondelle RExcitation Dynamics in the LHCII Complex of Higher Plants: Modeling Based on the 2.72 Å Crystal Structure. *J Phys Chem B* (2005) 109:10493–504. doi:10.1021/jp044082f
60. Novoderezhkin VI, Palacios MA, Van Amerongen H, Van Grondelle REnergy-Transfer Dynamics in the LHCII Complex of Higher Plants: Modified Redfield Approach. *J Phys Chem B* (2004) 108:10363–75. doi:10.1021/jp0496001
61. Novoderezhkin V, Marin A, van Grondelle RIntra- and Inter-monomeric Transfers in the Light Harvesting LHCII Complex: the Redfield–Förster Picture. *Phys Chem Chem Phys* (2011) 13:17093.
62. van Amerongen H, van Grondelle R*Understanding the Energy Transfer Function of Lhcii, the Major Light-Harvesting Complex of green Plants* (2001). doi:10.1021/jp0028406
63. De Liberato SLight-Matter Decoupling in the Deep Strong Coupling Regime: The Breakdown of the Purcell Effect. *Phys Rev Lett* (2014) 112:016401. doi:10.1103/physrevlett.112.016401
64. Schäfer C, Ruggenthaler M, Rokaj V, Rubio ARelevance of the Quadratic Diamagnetic and Self-Polarization Terms in Cavity Quantum Electrodynamics. *ACS Photon* (2020) 7:975–90. doi:10.1021/acsphotonics.9b01649
65. Keeling JCoulomb Interactions, Gauge Invariance, and Phase Transitions of the Dicke Model. *J Phys Condens Matter* (2007) 19:295213. doi:10.1088/0953-8984/19/29/295213
66. Vukics A, Grießer T, Domokos PElimination of the A-Square Problem from Cavity QED. *Phys Rev Lett* (2014) 112:073601. doi:10.1103/physrevlett.112.073601
67. Dorfman KE, Mukamel SMultidimensional Spectroscopy with Entangled Light: Loop vs Ladder Delay Scanning Protocols. *New J Phys* (2014) 16:033013. doi:10.1088/1367-2630/16/3/033013
68. Raymer MG, Landes T, Marcus AHEntangled Two-Photon Absorption by Atoms and Molecules: A Quantum Optics Tutorial. *J Chem Phys* (2021) 155:081501. doi:10.1063/5.0049338
69. Cutipa P, Chekhova MVBright Squeezed Vacuum for Two-Photon Spectroscopy: Simultaneously High Resolution in Time and Frequency, Space and Wavevector. *Opt Lett* (2022) 47:465. doi:10.1364/ol.448352
70. Andersen UL, Gehring T, Marquardt C, Leuchs G30 Years of Squeezed Light Generation. *Phys Scr* (2016) 91:053001. doi:10.1088/0031-8949/91/5/053001
71. Arzani F, Fabre C, Treps NVersatile Engineering of Multimode Squeezed States by Optimizing the Pump Spectral Profile in Spontaneous Parametric Down-Conversion. *Phys Rev A* (2018) 97:033808. doi:10.1103/physreva.97.033808
72. Schlawin F, Dorfman KE, Fingerhut BP, Mukamel SSuppression of Population Transport and Control of Exciton Distributions by Entangled Photons. *Nat Commun* (2013) 4:1. doi:10.1038/ncomms2802
73. Keller TE, Rubin MHTheory of Two-Photon Entanglement for Spontaneous Parametric Down-Conversion Driven by a Narrow Pump Pulse. *Phys Rev A* (1997) 56:1534–41. doi:10.1103/physreva.56.1534
74. MalỲ P, Mančal TSignatures of Exciton Delocalization and Exciton–Exciton Annihilation in Fluorescence-Detected Two-Dimensional Coherent Spectroscopy. *J Phys Chem Lett* (2018) 9:5654. doi:10.1021/acs.jpclett.8b02271
75. MalỲ P, Brixner TFluorescence-Detected Pump–Probe Spectroscopy. *Angew Chem Int Edition* (2021) 60:18867. doi:10.1002/anie.202102901
76. Dorfman KE, Asban S, Gu B, Mukamel SHong-Ou-Mandel Interferometry and Spectroscopy Using Entangled Photons. *Commun Phys* (2021) 4:1. doi:10.1038/s42005-021-00542-2
77. Asban S, Mukamel SDistinguishability and "Which Pathway" Information in Multidimensional Interferometric Spectroscopy with a Single Entangled Photon-Pair. *Sci Adv* (2021) 7:eabj4566. doi:10.1126/sciadv.abj4566
78. Abrikosov AA, Gorkov LP, Dzyaloshinski IE*Methods of Quantum Field Theory in Statistical Physics*. New York: Courier Corporation (2012).
79. Ruggenthaler M, Flick J, Pellegrini C, Appel H, Tokatly IV, Rubio AQuantum-electrodynamical Density-Functional Theory: Bridging Quantum Optics and Electronic-Structure Theory. *Phys Rev A* (2014) 90:012508. doi:10.1103/physreva.90.012508
80. Schäfer C, Buchholz F, Penz M, Ruggenthaler M, Rubio AMaking Ab Initio QED Functional(s): Nonperturbative and Photon-free Effective Frameworks for strong Light-Matter Coupling. *Proc Natl Acad Sci* (2021) 118. doi:10.1073/pnas.2110464118
81. Flick J, Narang PCavity-Correlated Electron-Nuclear Dynamics from First Principles. *Phys Rev Lett* (2018) 121:113002. doi:10.1103/physrevlett.121.113002
82. Yang J, Ou Q, Pei Z, Wang H, Weng B, Shuai Z, et al.Quantum-electrodynamical Time-dependent Density Functional Theory within Gaussian Atomic Basis. *J Chem Phys* (2021) 155:064107. doi:10.1063/5.0057542
83. Hoffmann NM, Lacombe L, Rubio A, Maitra NTEffect of many Modes on Self-Polarization and Photochemical Suppression in Cavities. *J Chem Phys* (2020) 153:104103. doi:10.1063/5.0012723
84. Zhang Y, Nelson T, Tretiak SNon-adiabatic Molecular Dynamics of Molecules in the Presence of strong Light-Matter Interactions. *J Chem Phys* (2019) 151:154109. doi:10.1063/1.5116550
85. Li X, Mandal A, Huo PCavity Frequency-dependent Theory for Vibrational Polariton Chemistry. *Nat Commun* (2021) 12:1. doi:10.1038/s41467-021-21610-9
86. Chowdhury SN, Mandal A, Huo PRing Polymer Quantization of the Photon Field in Polariton Chemistry. *J Chem Phys* (2021) 154:044109. doi:10.1063/5.0038330
87. Mandal A, Li X, Huo PTheory of Vibrational Polariton Chemistry in the Collective Coupling Regime. *J Chem Phys* (2022) 156:014101. doi:10.1063/5.0074106
88. Schäfer C, Ruggenthaler M, Appel H, Rubio AModification of Excitation and Charge Transfer in Cavity Quantum-Electrodynamical Chemistry. *Proc Natl Acad Sci U.S.A* (2019) 116:4883–92. doi:10.1073/pnas.1814178116

89. Flick J, Ruggenthaler M, Appel H, Rubio AAtoms and Molecules in Cavities, from Weak to strong Coupling in Quantum-Electrodynamics (QED) Chemistry. *Proc Natl Acad Sci U.S.A* (2017) 114:3026–34. doi:10.1073/pnas.1615509114
90. Flick J, Welakuh DM, Ruggenthaler M, Appel H, Rubio ALight-Matter Response in Nonrelativistic Quantum Electrodynamics. *ACS Photon* (2019) 6:2757–78. doi:10.1021/acsphotonics.9b00768
91. Welakuh DM, Flick J, Ruggenthaler M, Appel H, Rubio AFrequency-dependent Sternheimer Linear-Response Formalism for Strongly Coupled Light-Matter Systems. arXiv preprint arXiv:2201.08734 (2022). doi:10.48550/ARXIV.2201.08734
92. Svendsen MK, Kurman Y, Schmidt P, Koppens F, Kaminer I, Thygesen KSCombining Density Functional Theory with Macroscopic QED for Quantum Light-Matter Interactions in 2D Materials. *Nat Commun* (2021) 12:1. doi:10.1038/s41467-021-23012-3
93. Rostami H, Katsnelson MI, Vignale G, Polini MGauge Invariance and Ward Identities in Nonlinear Response Theory. *Ann Phys* (2021) 431:168523. doi:10.1016/j.aop.2021.168523
94. Parameswaran SA, Gopalakrishnan SAsymptotically Exact Theory for Nonlinear Spectroscopy of Random Quantum Magnets. *Phys Rev Lett* (2020) 125:237601. doi:10.1103/physrevlett.125.237601
95. Rostami H, Cappelluti EDominant Role of Two-Photon Vertex in Nonlinear Response in Two-Dimensional Dirac Systems. *npj 2D Mater Appl* (2021) 5:1. doi:10.1038/s41699-021-00217-0
96. Choi W, Lee KH, Kim YBTheory of Two-Dimensional Nonlinear Spectroscopy for the Kitaev Spin Liquid. *Phys Rev Lett* (2020) 124:117205. doi:10.1103/physrevlett.124.117205
97. Grankin A, Hafezi M, Galitski VMEnhancement of Superconductivity with External Phonon Squeezing. *Phys Rev B* (2021) 104:L220503. doi:10.1103/physrevb.104.l220503

Conflict of Interest: The authors declare that the research was conducted in the absence of any commercial or financial relationships that could be construed as a potential conflict of interest.

Publisher's Note: All claims expressed in this article are solely those of the authors and do not necessarily represent those of their affiliated organizations, or those of the publisher, the editors and the reviewers. Any product that may be evaluated in this article, or claim that may be made by its manufacturer, is not guaranteed or endorsed by the publisher.

APPENDIX

In this appendix, we provide two sets of supplementary information that aid the main text. It is composed of a relevant figure of merit for entanglement in the biphoton source and a description of parameters regarding the phonon spectral density.

A1 Singular Value Decomposition of the Biphoton Spectral Function

The singular value decomposition of the joint spectral amplitude of the biphoton sources provides an estimate for the number of effective modes that participated in mode-squeezing. It can be analyzed by obtaining the singular value decomposition of the said function at different parameter regimes. It can be seen in **Figure A1** that the cases involving the shorter temporal entanglement parameters increase the number of effectively squeezed modes. Also, a decrease in the pump bandwidth decreases the modal amplitudes for a case with comparable temporal entanglement parameters. The classical two-photon pulse, unsurprisingly, presents a plot reminiscent of the uncorrelated feature.

A2 Phonon Parameters

The site-independent spectral function is composed of discrete frequencies which primarily induce multiple timescales Markovian dissipation. Here we enlist the parameter values for the 48 structured phonon modes used in the simulation [59–62]. Along with these values, the values of other parameters are given as, γ_j (cm^{-1}) = 30.0 for all the multimode Brownian oscillators. Corresponding **Figure A2** illustrates the spectral density distribution. The parameter values for the overdamped oscillator are given by, λ_0 (cm^{-1}) = 37.0 and γ_0 (cm^{-1}) = 30.0.

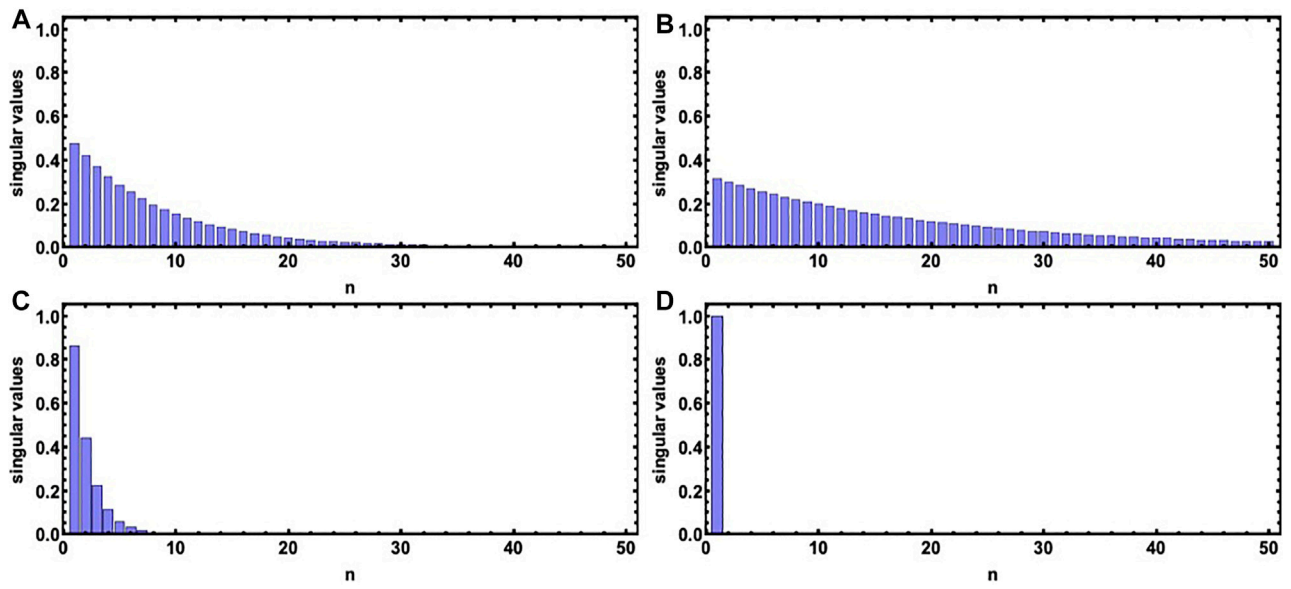

FIGURE A1 | Singular values for the three sets of entangled biphoton sources corresponding to a similar parameter regime of the ones used in the simulations of **Figure 3**. For the first two plots [i.e., in **(A,B)**] the values are truncated at n_{svd} = 50, and for the third one [i.e., in **(C)**], at n = 25 (after normalization). The classical two-photon pulse yields, as expected, n_{svd} = 1.

A

97.	604.	1143.
1354.	138.	700.
1181.	1382.	213.
722.	1190.	1439.
260.	742.	1208.
1487.	298.	752.
1216.	1524.	342.
795.	1235.	1537.
388.	916.	1252.
1553.	425.	986.
1260.	1573.	518.
995.	1286.	1580.
546.	1052.	1304.
1612.	573.	1069.
1322.	1645.	585.
1110.	1338.	1673.

B

2.32412	1.17176	46.7944
7.79904	3.97578	1.379
20.7738	9.21794	6.39426
2.84468	7.9373	9.59813
6.9394	29.2496	22.348
11.7176	7.95362	19.3866
21.3894	9.69264	20.6397
3.85575	8.60795	33.5527
9.64956	19.4467	7.96272
14.1168	6.3155	10.1657
8.0136	7.14142	20.4196
22.6263	5.83844	7.1732
1.46874	12.7608	7.51104
7.31848	4.86477	6.79884
40.083	5.97135	1.77255
12.4542	5.27172	1.62281

C

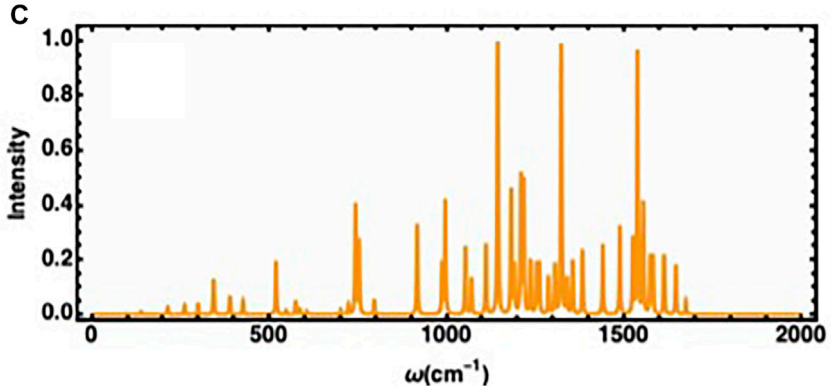

FIGURE A2 | (A,B) The list of the υ_j (cm^{-1}) parameters corresponding to the multi-mode Brownian oscillators.The list of the λ_j (cm^{-1}) parameters corresponding to the multi-mode Brownian oscillators. **(C)** The spectral function of the structured phonon modes (corresponding to the multi-mode Brownian oscillators) used in the simulation.

frontiers | Frontiers in Physics

ORIGINAL RESEARCH
published: 11 July 2022
doi: 10.3389/fphy.2022.895023

Frequency Conversion of Optical Vortex Arrays Through Four-Wave Mixing in Hot Atomic Gases

L. A. Mendoza-López, J. G. Acosta-Montes, J. A. Bernal-Orozco, Y. M. Torres, N. Arias-Téllez, R. Jáuregui and D. Sahagún Sánchez**

Departamento de Física Cuántica y Fotónica, Instituto de Física, Circuito de la Investigación Científica s/n, Universidad Nacional Autónoma de México, Ciudad Universitaria, Ciudad de México, México

Arrays of multiple vortices were transferred from infrared to the blue region of the optical spectrum. This demonstration was achieved by inducing four-wave mixing in an atomic gas with a Gaussian beam and a quasi-invariant propagation beam of the Mathieu type. The latter structure was analyzed in the Fourier space for the pump and the generated light. In both cases, the phase structure can be written with a compact mathematical expression by using the same parameters within experimental error bars. A Michelson–Morley interferometer was used to confirm that a phase singularity was present at each site as predicted by the theory. These studies add to the available control over orbital angular momentum in photons generated by atoms, which has a broad span of applications in quantum and classical information management.

Keywords: four-wave mixing, atomic gases, quantum light, structured beams, orbital angular momentum, hot atoms, Mathieu beams, up-conversion

OPEN ACCESS

Edited by:
Mario Alan Quiroz-Juarez, Autonomous Metropolitan University, Mexico

Reviewed by:
Jietai Jing, East China Normal University, China
Jianming Wen, Kennesaw State University, United States

****Correspondence:***
R. Jáuregui
rocio@fisica.unam.mx
D. Sahagún Sánchez
sahagun@fisica.unam.mx

Specialty section:
This article was submitted to Quantum Engineering and Technology, a section of the journal Frontiers in Physics

Received: *12 March 2022*
Accepted: *16 May 2022*
Published: *11 July 2022*

Citation:
Mendoza-López LA, Acosta-Montes JG, Bernal-Orozco JA, Torres YM, Arias-Téllez N, Jáuregui R and Sánchez DS (2022) Frequency Conversion of Optical Vortex Arrays Through Four-Wave Mixing in Hot Atomic Gases. Front. Phys. 10:895023. doi: 10.3389/fphy.2022.895023

1 INTRODUCTION

The angular momentum of light has been the subject of fundamental discussions about its analogies with atomic variables for nearly one century [1]. In 1993, Beijersbergen and colleagues demonstrated that, indeed, laser light can carry orbital angular momentum (OAM) by means of an appropriate preparation [2]. Thereafter, the OAM of light has been employed for a vast quantity of classical applications covering from microscopy and micro-manipulation to astrophysics and medicine [3]. This variable became an additional resource of quantum engineering once researchers were able to transfer it to correlated photons through spontaneous parametric down conversion (SPDC) [4, 5]; large Hilbert spaces became available for the subsequent treatment of entangled-photon pairs [6–8].

Since OAM can be transferred to and retrieved from atoms [9], it is also possible to generate quantum light-carrying OAM by inducing four-wave mixing (FWM). Controlling the electromagnetic degrees of freedom through this non-linear process makes it possible to generate light correlated in the time [10], useful to build, for example, quantum memories [11]. Ladder-type schemes of FWM in the alkali elements allow to convert light from one end to the other end of the optical spectrum, and even beyond. For example, exciting applications arose from generating and detecting electromagnetic fields at terahertz frequencies through FWM [12–15]. Here, we drive attention to the double transition $5S_{1/2} \rightarrow 5P_{3/2} \rightarrow 5D_{5/2}$ of Rb^{87}, which yields a beam at 420 nm during the second step of its cascade decay that can be readily detected [12] (**Figure 1**). This scheme has been a workhorse to those interested in developing the usage of OAM on light with atomic origin because the up-converted beam is relatively simple to collimate and optimize in setups where FWM is induced on hot atoms [16, 17]. Thus, the experiments involving this collimated blue

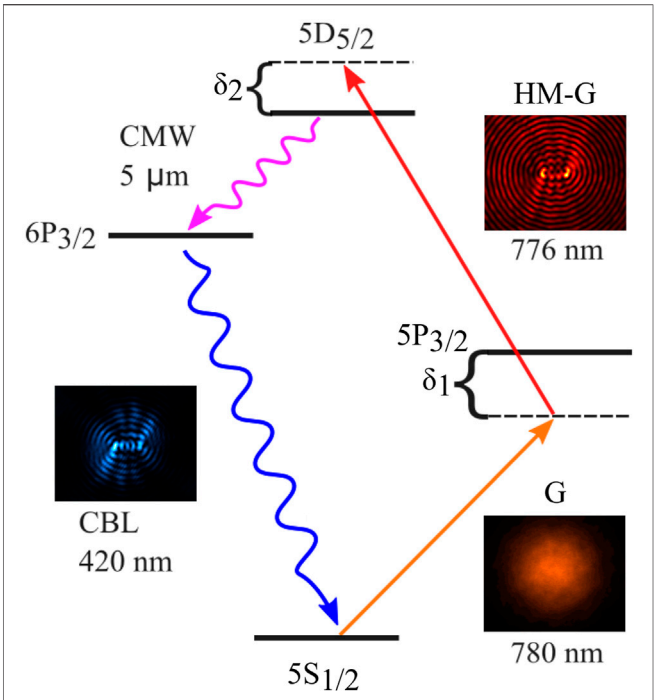

FIGURE 1 | Set of Rb^{87} transitions yielding collimated blue light through its second decay during four-wave mixing. Here, the $5S_{1/2} \rightarrow 5P_{3/2}$ was excited by a helical Mathieu–Gauss beam, whilst the $5P_{3/2} \rightarrow 5D_{5/2}$ was induced with light carrying a Gaussian profile.

light (CBL) are suitable for building scalable and robust devices, as desirable for practical applications. Quantum technologies are included since phase matching during the FWM process indicates that the OAM entanglement should be present between the CBL and the electromagnetic field at 5 μm (CMW), emitted during the cascade decay, whenever the appropriate choice in the parameters of the pump beams is carried out, especially if the total topological charge of the pump beams is large enough [18].

Single, optical vortices were first up-converted by [19]. In [20], it was shown that it is possible to perform arithmetic operations with the OAM traveling on both pump beams through FWM. Moreover, optical vortices with a helicity up to ±30 are transferable to the CBL as well [21]. In those experiments, the FWM process was pumped with Laguerre–Gauss beams that carry one phase singularity along a straight dislocation line. However, since 2002, it has been possible to generate arrays of optical vortices on laser light using Mathieu modes [22], members of the quasi-propagation invariant beam family [23]. This family of structured beams has given birth to numerous scientific discoveries through micro-manipulation of biological materials [see for example [24]]. More recently, they have yielded new methods to control the spatial and the correlation properties of photon pairs generated by SPDC [25].

In a recent publication, we reported the up-conversion of quasi-propagation invariant Mathieu beams through an FWM process in hot atoms [26]. There, the light-mode analysis was performed by studying in detail the Fourier and configuration spaces of the electromagnetic fields. These are well-established methods for experiments using non-linear crystals. However, they were introduced to the context of atomic gases in [26]. For those experiments neither the pump beams nor the CBL exhibited vortices. In this article, we report that modes containing arrays of optical vortices are also inherited *via* FWM. We also show that Michelson–Morley interferometry is a suitable tool to confirm this fact. A simulation of the classical interference pattern serves as a reference to locate the phase singularities. We induced FWM as depicted in **Figure 1**: with a Gaussian beam (G) resonant to the $5S_{1/2} \rightarrow 5P_{3/2}$ transition and a helical Mathieu–Gauss beam (HM-G) exciting the $5P_{3/2} \rightarrow 5D_{5/2}$ second step. We demonstrated that a non-trivial density of OAM was transferred from the pumping HM-G beam to the generated CBL. Our findings complement studies of non-linear processes, where the local density of angular momentum of light is connected to a spatially dependent polarization [27]. The results that we present here add two tools to experiments of this kind: conversion of light with a quasi-propagation invariant structure and several dislocation lines; and an extraordinary control over the properties of the generated light based on manipulating the atomic states involved in the non-linear process.

2 HELICAL MATHIEU BEAMS

In this section, we describe a few basic features of the structured light fields used in the experiment. We start with the elementary Mathieu modes that do not exhibit vortices but are the basis from which helical Mathieu beams—which may have more than one dislocation line—are built.

Elementary Mathieu modes are written in terms of scalar functions $\Psi(\vec{r}, t)$ that solve the following wave equation:

$$\left[\nabla^2 - \frac{1}{c^2}\frac{\partial^2}{\partial t^2}\right]\Psi(\vec{r}, t) = 0, \tag{1}$$

in elliptic-cylindrical coordinates $\{\xi, \eta, z\}$. These coordinates are related to the Cartesian space $\{x, y, z\}$ by the transformations:

$$x + iy = h\cosh(\xi + i\eta), \quad \xi\epsilon[0, \infty), \quad \eta\epsilon[0, 2\pi); \quad \text{and} \quad z = z, \tag{2}$$

where the constant h corresponds to half the inter-focal distance of the ellipses defining the coordinate system. The wave-equation in elliptic-cylindrical coordinates can be solved by the separation of variable method. By demanding the solutions to have a well-defined parity with respect to reflections through the z-plane, and to take finite value as $\xi \rightarrow \infty$, the following expressions for the scalar wave function $\Psi(\vec{r}, t)$ are found [28]:

$$\begin{aligned}\Psi_{\kappa}^{(e)}(\vec{r}, t) &= A_{\kappa}\mathrm{Je}_n(\xi, q)\mathrm{ce}_n(\eta, q)e^{i(k_z z - \omega t)},\\ \Psi_{\kappa}^{(o)}(\vec{r}, t) &= B_{\kappa}\mathrm{Jo}_n(\xi, q)\mathrm{se}_n(\eta, q)e^{i(k_z z - \omega t)}.\end{aligned} \tag{3}$$

Here, $\mathrm{ce}_n(\eta, q)$ and $\mathrm{se}_n(\eta, q)$ are the real even and odd ordinary solutions of the Mathieu equation:

$$\left[\frac{d^2}{d\eta^2} + a_n - 2q\cos 2\eta\right] f_n^{(p)}(\eta, q) = 0, \quad q = \left(\frac{h\kappa_\perp}{2}\right)^2, \quad \kappa_\perp^2 = (\omega/c)^2 - k_z^2; \tag{4}$$

and $\mathrm{Je}_n(\eta, q)$ and $\mathrm{Jo}_n(\eta, q)$ solve its modified analog as follows:

$$\left[\frac{d^2}{d\xi^2} + a_n - 2q\cosh 2\xi\right] F_n^{(p)}(\xi, q) = 0. \tag{5}$$

In general, the characteristic values a_n and b_n, for even and odd Mathieu functions, respectively, are ordered by the progressive parameter n. For a given n, $a_n \neq b_n$. The label κ in **Eq. 3** denotes a set of separation constants ω, k_z, n.

The wave function $\Psi(\vec{r}, t)$ satisfies the following eigenvalue equations [29],

$$i\frac{\partial}{\partial t}\Psi(\vec{r}, t) = \omega\Psi(\vec{r}, t), \qquad -i\frac{\partial}{\partial z}\Psi(\vec{r}, t) = k_z\Psi(\vec{r}, t), \tag{6a}$$

$$\frac{1}{2}\left[\left(\hat{\vec{l}}_+\right)_z\left(\hat{\vec{l}}_-\right)_z + \left(\hat{\vec{l}}_-\right)_z\left(\hat{\vec{l}}_+\right)_z\right]\Psi(\vec{r}, t) = a_n\Psi(\vec{r}, t), \quad \hat{\vec{l}}_\pm = \left(\vec{r} - (0, 0, \pm h)\right) \times \left(-i\vec{\nabla}\right); \tag{6b}$$

$(\hat{l}_\pm)_z$ is the z–component of the $\hat{\vec{l}}_\pm$ vector.

As a consequence, once the generalization to vectorial electromagnetic waves is carried out and the standard quantization is performed [30], in the quantum realm, the parameters $\{\omega, k_z, a_n\}$ are assigned to a photon described by these EM modes, an energy $\hbar\omega$, a linear momentum along the main propagation axis $\hbar k_z$, and an algebraic mean value of the z-component of the angular momentum with respect to the axis passing through the foci of the elliptic coordinate system, $\hbar^2 a_n$.

The angular spectrum of Mathieu fields,

$$\mathcal{S}_n^{(p)}(\theta_{\vec{k}}, \varphi_{\vec{k}}; a, q) = f_n^{(p)}(\varphi_{\vec{k}}, q)\delta\left(\sin\theta_{\vec{k}} - \kappa_\perp c/\omega\right)\frac{|\cos\theta_{\vec{k}}|}{\sin\theta_{\vec{k}}}, \tag{7}$$

allows them to be written as the superposition of plane waves,

$$\Psi^{(p)}(\vec{r}, t) = \int d\omega\,\alpha(\omega)\int d^3k\,\delta\left(\omega - c|\vec{k}|\right)e^{i\vec{k}\cdot\vec{r} - i\omega t}\mathcal{S}^{(p)}(\theta_{\vec{k}}, \varphi_{\vec{k}}). \tag{8}$$

The delta factor in **Eq. 7** guarantees cylindrical symmetry on the field by restricting the participating plane waves to those sharing a common modulus $\kappa_\perp$ of their transverse wave vector. Nevertheless, actual realizations of Mathieu beams involve a conic-shell volume within the wave-vector space derived from replacing the delta distribution by a properly normalized Gaussian distribution [31]:

$$\delta(\sin\theta - \kappa_\perp c/\omega) \to \frac{1}{(c\sigma/\omega)\sqrt{2\pi}}e^{-\frac{(\sin\theta - \kappa_\perp c/\omega)^2}{2(c\sigma/\omega)^2}} \tag{9}$$

with waist σ. This spectrum can be codified in a spatial light modulator (SLM) to generate electromagnetic Mathieu modes in the paraxial regime ($\kappa_\perp \ll |k_z|$) with a polarization determined by the quasi-plane waves that impinge the SLM. Transfer of the elementary Mathieu modes described here from infrared to blue light via FWM in atomic gases has recently been reported [26].

Optical vortices in scalar fields are locations where the phase is not well defined and exhibits a change of $2m\phi$ along any closed loop around them; the integer m is called topological charge. Close to a vortex, the field magnitude is zero, but the density of orbital angular momentum is not null. Even though the phase structure of scalar solutions $\Psi_\kappa^{(e)}(\vec{r}, t)$ and $\Psi_\kappa^{(o)}(\vec{r}, t)$ do not exhibit this kind of singularity, a proper superposition of them can give rise to one or more optical vortices with topological charges ±1. This happens for generalized-helical Mathieu beams with angular spectrum

$$\mathcal{S}_\kappa^{(h)}(\theta_{\vec{k}}, \varphi_{\vec{k}}) = \mathcal{I}_n^{(e)}\mathrm{ce}_n(\varphi_{\vec{k}}, q) + i\mathcal{I}_n^{(o)}\mathrm{se}_n(\varphi_{\vec{k}}, q). \tag{10}$$

Most studies in the literature consider the case for which the real constants $\mathcal{I}_n^{(e)}$ and $\mathcal{I}_n^{(o)}$ have the same absolute value [32].

By varying the plane of observation, optical vortices create the so-called dislocation lines. In the ideal case ($\sigma \to 0$), helical Mathieu beams are propagation invariant, and the dislocation lines are straight and parallel to the main direction of propagation. For actual helical Mathieu–Gauss beams, the dislocation lines are open but exhibit a slight curvature due to the unavoidable partial focusing of any Gaussian-like beam.

For the experiments reported here, we used a helical Mathieu–Gauss mode with $n = 4$, $\mathcal{I}_n^{(e)} = \mathcal{I}_n^{(o)}$, $\kappa_\perp = 11\ \mathrm{mm}^{-1}$, $\sigma = 0.038\kappa_\perp$, and $q = 21.78$ as an illustrative example. A simulation of its intensity profile on the $z = 0$ plane is shown in **Figure 2A**; some vortices are highlighted with blue circles where the intensity is null. The corresponding phase diagram is shown in **Figure 2A**. There, one can corroborate that the phase changes by 2π around the neighborhood highlighted in (A), so that the topological charge is unitary. **Figures 2C,D** show this beam in the Fourier space. **Figure 2C** depicts its intensity in the $k_x - k_y$ plane, and **Figure 2D** plots its angular dependence along the central $\kappa_\perp$ circle.

2.1 Phase-Matching Conditions Involving Gaussian and Helical Mathieu–Gaussian Pump Beams in FWM

Our experiment concerns the four-wave mixing process illustrated in **Figure 1**, where the $5D_{5/2}$ state of Rb^{87} is populated through a ladder transition excited by G and HM-G. Both pump beams satisfy the paraxial condition $k_z \sim \omega/c$. The cascade route explored in this work involves an electric-dipole decay in the microwave region, $5D_{5/2} \to 6P_{3/2}$, and a blue photon arising from the $6P_{3/2} \to 5S_{1/2}$ relaxation. A standard perturbative analysis of the steady-state amplitude for spontaneous emission of microwaves with electric fields $\vec{E}_{CMW}(\vec{r})e^{-i\omega_{CMW}t}$ and blue photons with $\vec{E}_{CBL}^{\,\star}(\vec{r})e^{-i\omega_{CBL}t}$ shows that it is proportional to

$$\mathfrak{F}\left[\vec{E}_{CMW}, \vec{E}_{CBL}\right] = \int_{-\infty}^{\infty} dt e^{i(\omega_{CM} + \omega_{CBL})t}\int d^3r\vec{d}_{CMW}^{\,*}\cdot\vec{E}_{CMW}^{\,*}(\vec{r})\vec{d}_{CBL}^{\,*} \cdot\vec{E}_{CBL}^{\,*}(\vec{r})\Omega_G(\vec{r}, t)\Omega_{HM-G}(\vec{r}, t)f_A(\vec{r}, t), \tag{11}$$

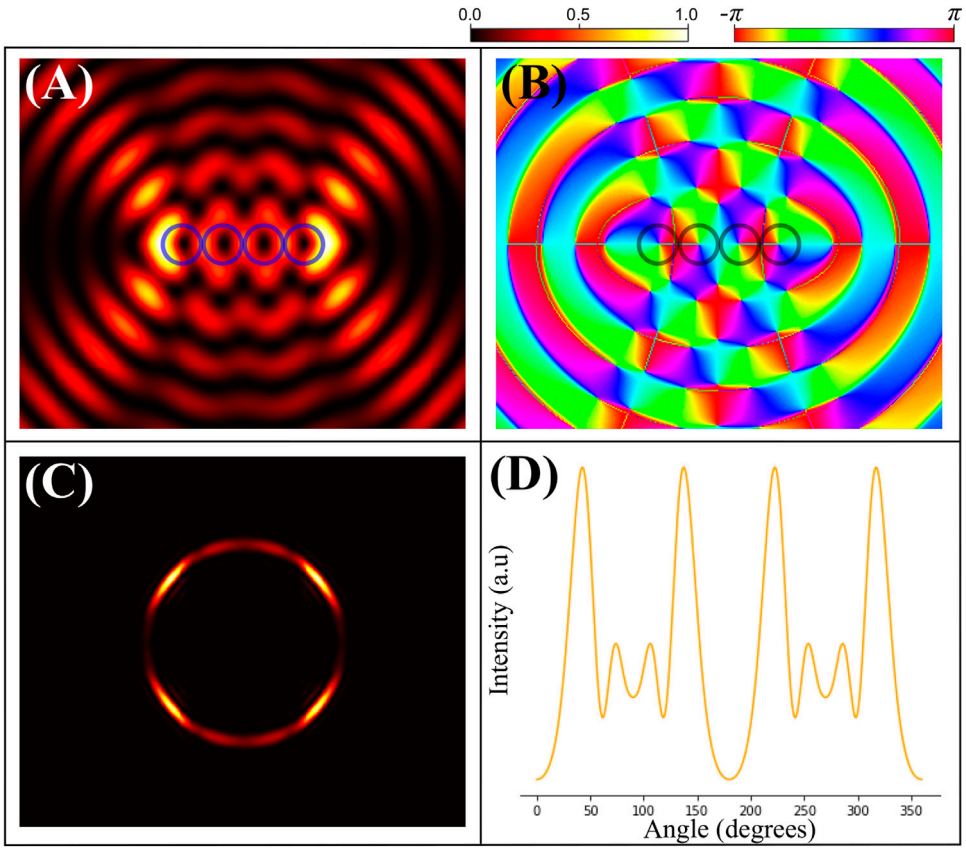

FIGURE 2 | Plots simulating a helical Mathieu–Gauss beam of order 4 (chosen to prepare HM-G). **(A)** Intensity profile; **(B)** spatial dependency of its phase. The blue circles on **(A)** and **(B)** enclose zero-field regions where optical vortices are expected. **(C)** Fourier ring formed at the focal length of the lens used for its experimental manipulation, and the orange curve in **(D)** illustrates the corresponding angular spectrum.

where $\vec{d}_{CMW}$ ($\vec{d}_{CBL}$) is the dipole moment of the $5D_{5/2} \rightarrow 6P_{3/2}$ ($6P_{3/2} \rightarrow 5S_{3/2}$) atomic transition and $f_A(\vec{r},t)$ is the atomic density; the Rabi frequencies of the pump beams, $\Omega_G(\vec{r},t)$ and $\Omega_{HM-G}(\vec{r},t)$, encode their space-time structure. For ideal monochromatic G and HM-G, the temporal integral yields the phase matching condition

$$\omega_G + \omega_{HM-G} = \omega_{CML} + \omega_{CBL} \tag{12}$$

with angular frequency ω_{CML} (ω_{CBL}) in the microwave (blue) region. Meanwhile, integration over the z-coordinate and the paraxial approximation gives rise to

$$(\mathbf{k}_G)_z + (\mathbf{k}_{HM-G})_z = (\mathbf{k}_{CML})_z + (\mathbf{k}_{CBL})_z. \tag{13}$$

As in [26], the transverse structure of G is a superposition of plane waves with $|\vec{k}_\perp|$ centered at zero and the transverse structure of HM-G centered at $|\vec{\kappa}_\perp|$ with a finite value. Photons of CBL have a wider wave-vector range than the microwaves, and thus, it may inherit the $k_\perp$ structure of HM-G. Consequently, the down-converted modes are expected to have a Gaussian-like transverse configuration. An important difference with experiments reported in [26] is the possibility that the *local* phase structure of the vortices could have been transferred to both CBL and CML. That may happen to photons in the vicinity of a phase singularity with a topological charge m since the Rabi frequency $\Omega_{HM-G}(\vec{r},t)$ is position-dependent. In such case, the $E^{\star}_{CML}(\vec{r})$ and $E^{\star}_{CBL}(\vec{r})$ electric fields exhibit a phase singularity where their topological charges m_{CBL} and m_{CML} satisfy

$$m_{HM-G} = m_{CMW} + m_{CBL}, \tag{14}$$

maximizing the integration of $|\mathfrak{F}[\vec{E}_{CMW}, \vec{E}_{CBL}]|$ in a neighborhood around each phase singularity of $\Omega_{HM-G}(\vec{r},t)$.

Since for Mathieu beams, the absolute value of the topological charge is either 1 or 0 (absence of phase singularity), it is expected that the phase singularities of the CBL light should add to either ±1 or zero. If $|m_{CBL}| > 1$, its complement would require a topological charge of even greater absolute value $|m_{CMW}| > |m_{CBL}|$ to guarantee the local phase-matching. Thus, dislocation lines in the pump, in the up-converted photons, and in the down-converted photons could evolve complex enough to compromise their stability. In a simpler scheme, vortices with a topological charge equal to that of the pump, Mathieu beams are transferred to the blue light. This is congruent with Ref. [26], where the Mathieu structure of even and odd modes is directly transferred to the CBL beam. It also extends to a local-space context, the

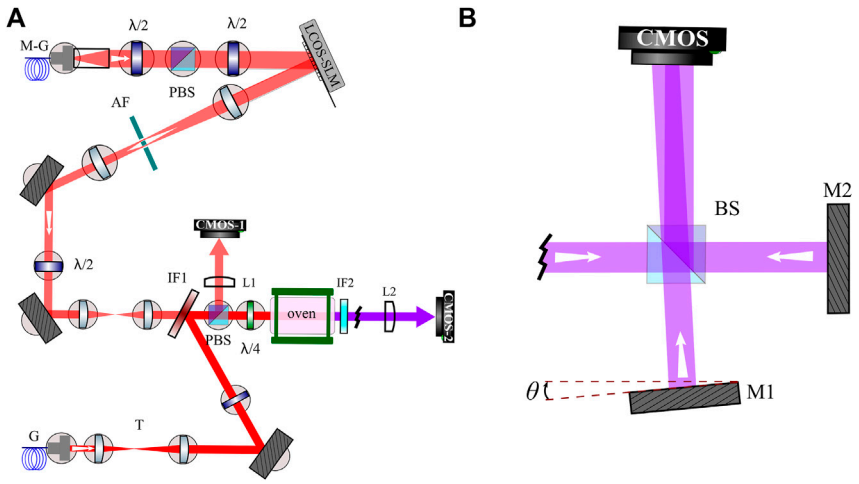

FIGURE 3 | Experimental setup to induce FWM in a hot atomic vapor of Rb^{87} with one helical Mathieu–Gauss (top) and a Gaussian beam (bottom). **(A)** Both pump beams are prepared and overlapped through the atomic sample whilst being heated by an oven. **(B)** Michelson–Morley interferometer that replaces the Fourier and configuration analysis setup for locating the optical vortices.

discussion presented in [18], which predicts that the topological charge of Laguerre–Gauss beams will preferably be transferred to the blue light for paraxial-pump beams satisfying the Boyd condition, unless the topological charge of those pump beams is large enough.

3 EXPERIMENT

To perform experiments, we used a similar apparatus as that reported in [26] with an additional interferometric module. Here, we describe only its main features and the Michelson–Morley arrangement by which the optical singularities were detected.

The experimental setup is schematized in **Figure 3**. Both HM-G and G pump beams are frequency-stabilized in separate spectroscopy setups which are not shown. Every data reported in this article were taken with G resonant to the $5S_{1/2} \rightarrow 5P_{3/2}$ transition ($\delta_1 = 0$); δ_2 was set to −16.2 MHz, optimizing the intensity of CBL on its Fourier plane within a ±20 MHz range. The top part of **Figure 3A** illustrates the optical arrangement for generating arbitrary Mathieu–Gauss beams with a phase-only SLM [33]. Their cross section has a long diameter of about 4 mm. This size is matched to the G beam with the help of telescope T1, as shown in the bottom part of **Figure 3A**. Experiments were performed by saturating the first FWM step with a power of 27 mW on G; HM-G carried 7 mW only. Both beams are overlapped on an interference filter F1 to co-propagate them across a heated spectroscopy cell. This guarantees the Boyd criteria for the efficiency in the FWM process The Fourier space of HM-G is imaged right before interacting with atoms by placing CMOS-I at the focal plane of lens L1. The CBL is equally monitored by focusing it with L2 on CMOS-2.

Figure 3B depicts the Michelson–Morley module added to analyze the phase of CBL. This interferometer is a variation of the simplest technique to detect an optical vortex: to interfere with the studied beam with an inclined plane wave, resulting in a fork-like interferogram. By counting the fork number in the resulting pattern and observing their relative orientation, the vortex order and its corresponding sign can be precisely assigned. We did not try to produce a blue plane wave to interfere with CBL because that requires an extra laser. Instead, we split the CBL, letting it to interfere with itself. Clear inference patterns can be readily observed by overlapping the center of one arm with the external field of the other, where the CBL-phase structure has its smallest variations [34].

The Michelson–Morley module is placed instead of lens L2 and CMOS-2 at the right end of **Figure 3A**—right after the interference filter IF2, which removes remnants of pumping light. Two arms with CBL are created by a 50:50 beam splitter cube. Each one of them is retro-reflected by its respective mirror (M1 and M2 in **Figure 3B**) in order to overlap them on a simple CMOS camera. For this interferometer to work, the arms should be slightly misaligned. The distance between them when impinging on the CMOS chip is controlled using a translation stage driving the angle θ of M1.

4 RESULTS

We characterized both electromagnetic fields by measuring their angular spectra from images of their Fourier plane to show that the structure of HM-G is transferred to CBL through the FWM process. This allows to formulate a compact expression for the two beams in terms of parameters that define the ideal Mathieu mode programmed to the SLM [26]. The analyses were performed for the illustrative example described in **Figure 2**. Its relevant parameters are shown in **Table1**. The interference patterns of CBL with itself confirmed that the full set of vortices, theoretically expected on the major axis of the Mathieu mode, are present in the generated light.

TABLE 1 | Consolidation of parameters measured from angular spectra of the M-G pump beam and the CBL; the parameters used for simulating the chosen illustrative mode, displayed in **Figure 2**, are shown for reference.

	SLM (theory)	HM-G	CBL
$\kappa_\perp$ (mm^{-1})	11	33.0 ± 0.34	33.2 ± 0.78
$\mathcal{I}_4^{(e)}$ (a.u.)	1.00	1.00 ± 0.06	0.99 ± 0.13
$\mathcal{I}_4^{(o)}$ (a.u.)	1.00	0.98 ± 0.08	1.00 ± 0.16
q	21.78	21.4 ± 0.65	21.1 ± 1.20
ϕ_0 (degrees)	0.00	−7.70 ± 0.27	−5.38 ± 0.51

4.1 Analysis in the Fourier Space

Fourier rings of CBL were imaged for an atomic-gas temperature ranging from 70 to 120°C. The data presented in this section were taken at 95°C because this is one of temperatures for which the angular spectrum of CBL yields a visibility that allows reliable identification of the parameters that mathematically describe the generated field.

Figure 4 depicts the Fourier analysis for both G-M (A) and CBL (B). Their transverse wave-numbers are given by the radius of the averaged ring scaled by $1/f\lambda$, where f is the focal length of the corresponding Fourier lens and λ is the wavelength of the light [35]. The measured values are $\kappa_\perp^{HM-G} = 33.0 \pm 0.34$ mm^{-1} (red ring) and $\kappa_\perp^{CBL} = 33.2 \pm 0.78$ mm^{-1} (blue ring); essentially, all the transverse momentum was inherited to the blue light through the FWM process, as expected. The angular spectra of both electromagnetic fields are analyzed at the right of **Figure 4**. There, blue dots are data extracted from the circle with radius $\kappa_\perp$for each case, and orange curves are the best fit to them with **Eq. 10**. Both graphs display a noise offset that was accounted for by adding a constant term to the adjusted function. **Table 1** shows the parameters yielding the best fit for the angular spectra of HM-G and CBL with a coefficient of reliability R^2 of 0.89 and 0.81, respectively. It is useful to first verify that $\mathcal{I}_4^{(e)} = |\mathcal{I}_4^{(o)}|$ in HM-G, as programed with the SLM. This is indeed the case within error bars as can be read from the second column, where both values normalized by $\mathcal{I}_4^{(e)}$ are shown. The full characterization of HM-G in the wave-vector space finishes by realizing that the fitted ellipticity parameter q (21.4 ± 0.65) agrees with its programed value in the SLM.

Evidence of an enhanced, spatial, and spectral coherence on the CBL has been observed [36]. This imposes an extra difficulty on aligning and overlapping HM-G with G to

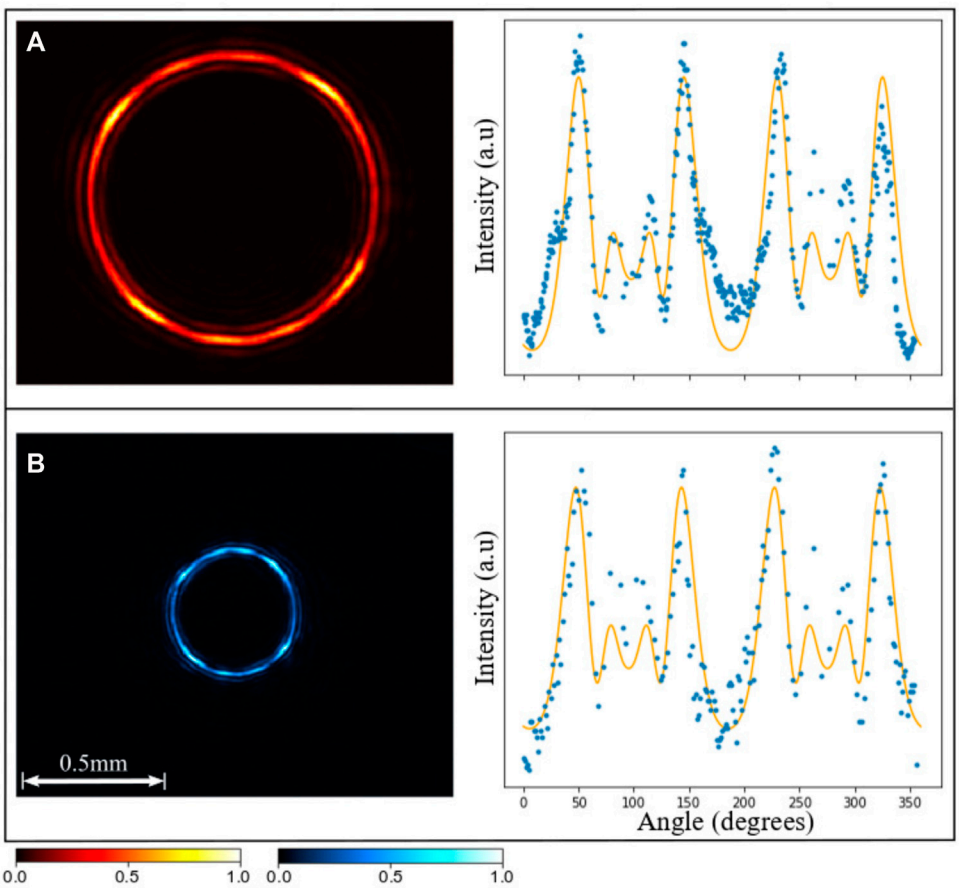

FIGURE 4 | Angular spectra of the HM-G pump beam and the CBL when Mathieu modes of order 4 were transferred from the red to the blue beam through FWM. On the left, **(A)** shows an image of HM-G taken using a CMOS camera at its Fourier plane, and on the right displays the best fit (orange) to the experimental data. The data corresponding to the CBL are depicted in **(B)**.

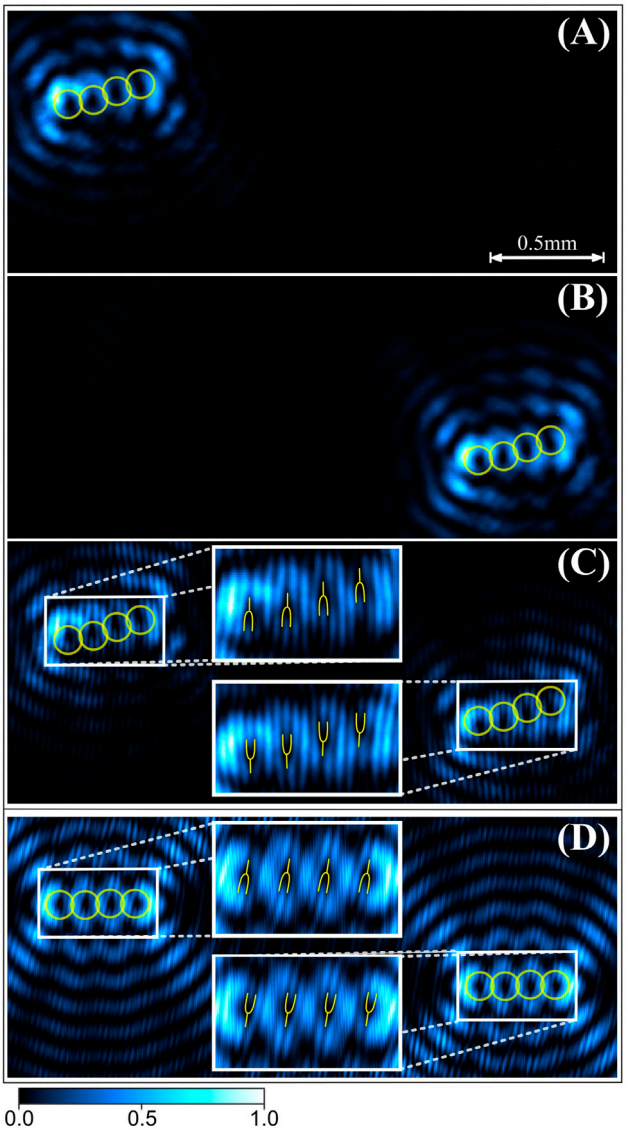

FIGURE 5 | Illustration of the phase analysis for the CBL generated with FWM. **(A)** and **(B)** display the intensity profile of both arms in the Michelson–Morley interferometer for spatial reference. **(C)** Image of the experimental interference pattern with its main features zoomed at the insets with white frame. **(D)** Pattern modeling the propagation of the CBL arms with their Fresnel integral throughout their respective optical paths.

generate balanced images of blue rings; we observed that normal incidence of the pump beams onto the input window of the spectroscopy cell should be slightly avoided. **Figure 4B** displays a sample of the best pictures that we could achieve for CBL-Fourier rings. The best-fit parameters of its angular spectrum are shown in the third column of **Table 1**. From there, one can corroborate that $\mathcal{I}_4^{(e)} = |\mathcal{I}_4^{(o)}|$ for CBL as well. Finally, q for this measurement is equal to both the ellipticity parameter programed in the SLM and its measurement from the angular spectrum of HM-G, within the experimental accuracy.

4.2 Analysis of the CBL Phase Structure

Optical vortices were detected on CBL with the Michelson–Morley interferometer depicted in **Figure 3B** and are congruent with the expectations derived from the theory, **Figure 2**. Power and the detuning of the pump beams were kept the same as for measurements in the Fourier space. We found high-visibility interference patterns at 82°C within the experimental temperature range. **Figure 5** displays a series of images illustrating the phase analysis carried out for the example mode chosen in this article. The image of each arm serves as a spatial reference in the interference pattern. They can individually be observed by blocking its counterpart, as shown in **Figures 5A,B**. There, the yellow circles enclose zero-field regions that are candidates to host phase singularities; ideal Mathieu modes of order 4 have four vortices on their mayor axis between their foci if $\mathcal{I}_n^{(e)} = |\mathcal{I}_n^{(o)}|$, shown in **Figure 2**. This was experimentally tested on CBL by letting both arms to interfere and by modeling their propagation.

The experimental interference pattern of CBL with itself is shown in **Figure 5C**. Insets with white frames enclose two regions where inline-phase singularities are expected. Each of these areas shows four forks witnessing four optical vortices. One can observe that the absolute value of the topological charge is equal to one in all cases since the interference fringes brake into two branches. In other words, we measured $m_{CBL} = m_{HM-G}$. Therefore, even though we did not characterize the topological structure of CMW, it is theoretically expected that it does not carry any phase singularity and be Gaussian-like. Note that the forks at each arm are orientated the other way around, meaning that the rows of optical vortices imaged from each arm have opposite helicity. This is a consequence of the optical path difference traveled by each beam due to the angle θ of M1. To corroborate the physical significance of these observations, the Fresnel integral was calculated throughout the optical path of both CBL beams from their respective mirrors to the CMOS chip. Details on this model are found in [37]. **Figure 5D** is an intensity plot obtained with these calculations. Comparison between **Figures 5C,D** certifies the theoretical expectancy of the features in the CBL-phase structure that were experimentally found. The small tilt of the major axis present in Mathieu–Gauss beams [33] can also be appreciated in **Figure 5C**. It has been attributed to the Gaussian contribution required for their experimental generation [22].

5 CONCLUSION

We demonstrated that non-trivial phase structures, composed of arrays of optical vortices, are transferable through FWM in atomic gases using a ladder-type double transition—that can up- and down-convert light. This was carried out by, respectively, exciting its first and second steps with Gaussian and Mathieu–Gauss beams. We confirmed that the HM-G pump beam was appropriately characterized by the parameters of an ideal helical Mathieu mode, as well as the generated CBL, by measuring their angular spectra in their respective Fourier planes.

For probing phase singularities, we successfully introduced Michelson–Morley interferometry to the analysis of light generated by FWM in atomic gases.

Measurements in the Fourier space showed that the transverse components $\kappa_{\perp}^{G-M} \approx \kappa_{\perp}^{CBL}$. Therefore, momentum perpendicular to the propagation of helical Mathieu modes is fully transferred from HM-G to CBL as well as happens individually for the odd and even cases [26]. During the same analysis, we showed that the ellipticity parameter q of the Mathieu modes is also transferred within our experimental accuracy. With Michelson–Morley interferometry, we verified that the zero-field regions on the semi-major axis of CBL carry the optical vortices of the mode that was fed to atoms by HM-G. We also observed that the topological charge of vortices on HM-G is equal to the topological charge of vortices on CBL. This testifies that the microwave field CMW should not be carrying OAM in this very context. Nevertheless, this situation should change if the pump beam G is imprinted with phase structure as well.

Our work is a step forward to classical applications requiring multiple vortices on light with frequencies hard to achieve such as free-space multiplexing with OAM [38]. In principle, our results can be extended to generate twin beams controllably carrying multiple phase singularities. Therefore, they also contribute to enhancing OAM-multiplexing with quantum light. This exciting application has been recently demonstrated [39]. It has been subsequently employed to perform OAM quantum teleportation, tripartite entanglement, and quantum dense coding in photon pairs with similar frequencies [40, 41, 42]. Therefore, our contribution may well be the key that opens access toward implementing these applications with differently colored, quantum-correlated light carrying several OAM channels in addition to remote preparation of highly structured optical states [27].

DATA AVAILABILITY STATEMENT

The raw data supporting the conclusion of this article will be made available by the authors, without undue reservation.

AUTHOR CONTRIBUTIONS

LM-L built the machine, in which experiments were carried out, analyzed data, and made all the figures for this article. JA-M built experimental prototypes to implement the techniques and developed their procedures of analysis. JB-O contributed to experimental-data collection and analysis. YT demonstrated FWM for the first time in the laboratory and showed that the Michelson–Morley interferometer is a suitable tool to analyze helical Mathieu modes. NA-T brought back the apparatus to a functioning status after 1 year of null experimental work in the laboratory due the SARS-Cov-2 pandemics. RJ contributed to invaluable expertise on quasi-invariant propagation beams and developed the theory contained in this manuscript. DSS is the principal investigator of the laboratory; he designed the experimental apparatus, shaped its scientific roadmap, and supervised all the instrumental developments involved.

FUNDING

We thank the Consejo Nacional de Ciencia y Tecnología (CONACyT) for supporting through the National Laboratories Program, under Grant Nos 280181, 293471, and 299057 and through the Basic Science Grant SEP-CONACyT No. 285387. LM-L and JA-M thank CONACyT for their postgraduate study fellowships. YT thanks DGAPA-UNAM for postdoctoral support. NA-T thanks SEP-CONACyT Grant No. 285387 and CTIC for posdoctoral support. We also thank DGAPA-UNAM for constant funding through PAPIIT under Grant Nos IN108018, IN103020, and IN106821 and PIIF-UNAM.

ACKNOWLEDGMENTS

We thank Rodrigo A. Guitiérrez-Arenas for his contributions on instrumentation development for this work; Ricardo Guitérrez-Jáuregui for discussions regarding this project; K. Volke-Sepulveda, Alejandro V. Arzola, and Pedro A. Quinto-Su for technical support on SLM programming.

REFERENCES

1. Darwin CG. Notes on the Theory of Radiation. *Proc R Soc Lond A* (1932) 136: 36–52. doi:10.1098/rspa.1932.0065
2. Beijersbergen MW, Allen L, van der Veen H, Woerdman JP. Astigmatic Laser Mode Converters and Transfer of Orbital Angular Momentum. *Opt Commun* (1993) 96:123–32. doi:10.1016/0030-4018(93)90535-d
3. Torres PJP, Torner PL. *Twisted Photons*. Singapore: John Wiley & Sons (2011).
4. Arnaut HH, Barbosa GA. Orbital and Intrinsic Angular Momentum of Single Photons and Entangled Pairs of Photons Generated by Parametric Down-Conversion. *Phys Rev Lett* (2000) 85:286–9. doi:10.1103/physrevlett.85.286
5. Mair A, Vaziri A, Weihs G, Zeilinger A. Entanglement of the Orbital Angular Momentum States of Photons. *Nature* (2001) 412:313–6. doi:10.1038/35085529
6. Molina-Terriza G, Torres JP, Torner L. Management of the Angular Momentum of Light: Preparation of Photons in Multidimensional Vector States of Angular Momentum. *Phys Rev Lett* (2002) 88:013601. doi:10.1103/PhysRevLett.88.013601
7. Barreiro JT, Wei T-C, Kwiat PG. Beating the Channel Capacity Limit for Linear Photonic Superdense Coding. *Nat Phys* (2008) 4:282–6. doi:10.1038/nphys919
8. Forbes A, Nape I. Quantum Mechanics with Patterns of Light: Progress in High Dimensional and Multidimensional Entanglement with Structured Light. *AVS Quan Sci.* (2019) 1:011701. doi:10.1116/1.5112027
9. Tabosa JWR, Petrov Dv. Optical Pumping of Orbital Angular Momentum of Light in Cold Cesium Atoms. *Phys Rev Lett* (1999) 83:4967–70. doi:10.1103/physrevlett.83.4967
10. Kuzmich A, Bowen WP, Boozer AD, Boca A, Chou CW, Duan L-M, et al.Generation of Nonclassical Photon Pairs for Scalable Quantum Communication with Atomic Ensembles. *Nature* (2003) 423:731–4. doi:10.1038/nature01714
11. Guo J, Feng X, Yang P, Yu Z, Chen LQ, Yuan CH, et al.High-performance Raman Quantum Memory with Optimal Control in Room Temperature Atoms. *Nat Commun* (2019) 10:148–6. doi:10.1038/s41467-018-08118-5
12. Zibrov AS, Lukin MD, Hollberg L, Scully MO. Efficient Frequency Up-Conversion in Resonant Coherent media. *Phys Rev A* (2002) 65. doi:10.1103/physreva.65.051801

13. Wolf J-P, Silberberg Y. Spooky Spectroscopy. *Nat Photon* (2016) 10:77–9. doi:10.1038/nphoton.2015.267
14. Lam M, Pal SB, Vogt T, Gross C, Kiffner M, Li W. Collimated UV Light Generation by Two-Photon Excitation to a Rydberg State in Rb Vapor. *Opt Lett* (2019) 44:2931. doi:10.1364/ol.44.002931
15. Downes LA, MacKellar AR, Whiting DJ, Bourgenot C, Adams CS, Weatherill KJ. Full-Field Terahertz Imaging at Kilohertz Frame Rates Using Atomic Vapor. *Phys Rev X* (2020) 10:011027. doi:10.1103/physrevx.10.011027
16. Akulshin AM, McLean RJ, Sidorov AI, Hannaford P. Coherent and Collimated Blue Light Generated by Four-Wave Mixing in Rb Vapour. *Opt Express* (2009) 17:22861–70. doi:10.1364/oe.17.022861
17. Vernier A, Franke-Arnold S, Riis E, Arnold AS. Enhanced Frequency Up-Conversion in Rb Vapor. *Opt Express* (2010) 18:17020–6. doi:10.1364/oe.18.017020
18. Offer RF, Stulga D, Riis E, Franke-Arnold S, Arnold AS. Spiral Bandwidth of Four-Wave Mixing in Rb Vapour. *Commun Phys* (2018) 1:84. doi:10.1038/s42005-018-0077-5
19. Walker G, Arnold AS, Franke-Arnold S. Trans-Spectral Orbital Angular Momentum Transfer via Four-Wave Mixing in Rb Vapor. *Phys Rev Lett* (2012) 108:243601. doi:10.1103/physrevlett.108.243601
20. Akulshin AM, Novikova I, Mikhailov EE, Suslov SA, McLean RJ. Arithmetic with Optical Topological Charges in Stepwise-Excited Rb Vapor. *Opt Lett* (2016) 41:1146. doi:10.1364/ol.41.001146
21. Chopinaud A, Jacquey M, Viaris de Lesegno B, Pruvost L. High Helicity Vortex Conversion in a Rubidium Vapor. *Phys Rev A* (2018) 97:063806. doi:10.1103/physreva.97.063806
22. Chávez-Cerda S, Padgett MJ, Allison I, New GHC, Gutiérrez-Vega JC, O'Neil AT, et al.Holographic Generation and Orbital Angular Momentum of High-Order Mathieu Beams. *J Opt B: Quan Semiclass. Opt.* (2002) 4:S52–S57. doi:10.1088/1464-4266/4/2/368
23. Durnin J, Miceli JJ, Eberly JH. Diffraction-free Beams. *Phys Rev Lett* (1987) 58:1499–501. doi:10.1103/physrevlett.58.1499
24. Dholakia K, Reece P, Gu M. Optical Micromanipulation. *Chem Soc Rev* (2008) 37:42–55. doi:10.1039/b512471a
25. Gutiérrez-López D, Maldonado-Terrón M, Hernández RJ, Vicuña-Hernández V, Ramírez-Alarcón R, Cruz-Ramírez H, et al.Spatial Control of Spontaneous Parametric Down-Conversion Photon Pairs through the Use of Apertured Bessel-Gauss Pump Beams. *Phys Rev A* (2019) 100:013802. doi:10.1103/physreva.100.013802
26. Mendoza-López LA, Acosta-Montes JG, Ángeles-Aguillón IF, Sierra-Costa D, Torres YM, Jáuregui R, et al.Generalized Angular Momentum Transfer to Up-Converted Photons via Four-Wave Mixing in Atomic Gases. *Phys Rev Res* (2021) 3:033170. doi:10.1103/physrevresearch.3.033170
27. Cameron AR, Cheng SWL, Schwarz S, Kapahi C, Sarenac D, Grabowecky M, et al.Remote State Preparation of Single-Photon Orbital-Angular-Momentum Lattices. *Phys Rev A* (2021) 104:L051701. doi:10.1103/physreva.104.l051701
28. Olver FWJ, Lozier DW, Boisvert RF, Clark CW. *The NIST Handbook of Mathematical Functions*. Cambridge, New York, Melbourne, Madrid, Cape Town, Singapore, Saõ Paulo, Delhi, Dubai, Tokyo: Cambridge Univ. Press (2010).
29. Boyer CP, Kalnins EG, Miller W. Symmetry and Separation of Variables for the Helmholtz and Laplace Equations. *Nagoya Math J* (1976) 60:35–80. doi:10.1017/s0027763000017165
30. Rodríguez-Lara BM, Jáuregui R. Dynamical Constants for Electromagnetic fields with Elliptic-Cylindrical Symmetry. *Phys Rev A* (2008) 78:S52S57. doi:10.1103/physreva.78.033813
31. Dartora CA, Zamboni-Rached M, Nóbrega KZ, Recami E, Hernández-Figueroa HE. General Formulation for the Analysis of Scalar Diffraction-free Beams Using Angular Modulation: Mathieu and Bessel Beams. *Opt Commun* (2003) 222:75–80. doi:10.1016/s0030-4018(03)01564-5
32. Gutiérrez-Vega JC, Bandres MA. Helmholtz-Gauss Waves. *J Opt Soc Am A* (2005) 22:289–98. doi:10.1364/josaa.22.000289
33. Hernández-Hernández RJ, Terborg RA, Ricardez-Vargas I, Volke-Sepúlveda K. Experimental Generation of Mathieu-Gauss Beams with a Phase-Only Spatial Light Modulator. *Appl Opt* (2010) 49:6903. doi:10.1364/ao.49.006903
34. White AG, Smith CP, Heckenberg NR, Rubinsztein-Dunlop H, McDuff R, Weiss CO, et al.Interferometric Measurements of Phase Singularities in the Output of a Visible Laser. *J Mod Opt* (1991) 38:2531–41. doi:10.1080/09500349114552651
35. Goodman JW. Introduction to Fourier Optics. In: JW Goodman, editor. *Introduction to Fourier Optics*. 3rd ed. Englewood, CO: Roberts & Co. Publishers (2005).
36. Akulshin AM, Budker D, McLean RJ. Parametric Wave Mixing Enhanced by Velocity-Insensitive Two-Photon Excitation in Rb Vapor. *J Opt Soc Am B* (2017) 34:1016. doi:10.1364/josab.34.001016
37. Mendoza-López LA. *Análisis de luz generada vía mezclado de cuatro ondas con densidad de momento angular*. Ciudad de México: Master's thesis, Universidad Nacional Autónoma de México (2020).
38. Wang J, Yang J-Y, Fazal IM, Ahmed N, Yan Y, Huang H, et al.Terabit Free-Space Data Transmission Employing Orbital Angular Momentum Multiplexing. *Nat Photon* (2012) 6:488–96. doi:10.1038/nphoton.2012.138
39. Pan X, Yu S, Zhou Y, Zhang K, Zhang K, Lv S, et al.Orbital-Angular-Momentum Multiplexed Continuous-Variable Entanglement from Four-Wave Mixing in Hot Atomic Vapor. *Phys Rev Lett* (2019) 123:070506. doi:10.1103/physrevlett.123.070506
40. Liu S, Lou Y, Jing J. Orbital Angular Momentum Multiplexed Deterministic All-Optical Quantum Teleportation. *Nat Commun* (2020) 11:3875. doi:10.1038/s41467-020-17616-4
41. Li S, Pan X, Ren Y, Liu H, Yu S, Jing J. Deterministic Generation of Orbital-Angular-Momentum Multiplexed Tripartite Entanglement. *Phys Rev Lett* (2020) 124:083605. doi:10.1103/physrevlett.124.083605
42. Chen Y, Liu S, Lou Y, Jing J. Orbital Angular Momentum Multiplexed Quantum Dense Coding. *Phys Rev Lett* (2021) 127:093601. doi:10.1103/physrevlett.127.093601

Conflict of Interest: The authors declare that the research was conducted in the absence of any commercial or financial relationships that could be construed as a potential conflict of interest.

frontiers | Frontiers in Physics

TYPE Original Research
PUBLISHED 19 August 2022
DOI 10.3389/fphy.2022.921499

OPEN ACCESS

EDITED BY
Omar Magana-Loaiza,
Louisiana State University, United States

REVIEWED BY
Freddy Fernandes Guimaraes,
Universidade Federal de Goiás, Brazil
Bo-Han Wu,
University of Arizona, United States

*CORRESPONDENCE
Zhenhuan Yi,
yzh@tamu.edu
Marlan O. Scully,
scully@tamu.edu

SPECIALTY SECTION
This article was submitted to Quantum Engineering and Technology, a section of the journal Frontiers in Physics

RECEIVED 15 April 2022
ACCEPTED 12 July 2022
PUBLISHED 19 August 2022

CITATION
Yi Z, Begzjav TK, Ariunbold GO, Zheltikov AM, Sokolov AV and Scully MO (2022), Multiple pathway quantum beat spectroscopy.
Front. Phys. 10:921499.
doi: 10.3389/fphy.2022.921499

Multiple pathway quantum beat spectroscopy

Zhenhuan Yi[1]*, Tuguldur Kh. Begzjav[1,2], Gombojav O. Ariunbold[2,3], Aleksei M. Zheltikov[1], Alexei V. Sokolov[1,4] and Marlan O. Scully[1,4,5]*

[1]Texas A and M University, College Station, TX, United States, [2]National University of Mongolia, Ulaanbaatar, Mongolia, [3]Mississippi State University, Starkville, MS, United States, [4]Baylor University, Waco, TX, United States, [5]Princeton University, Princeton, NJ, United States

We investigate quantum beats by monitoring cooperative emission from rubidium vapor and demonstrate correlated beats via coupled emission channels. We develop a theoretical model, and our simulations are in good agreement with experimental results. The results pave the way for advanced techniques measuring interactions between atoms that are excited to high energy levels.

KEYWORDS

ultrafast spectroscopy, quantum beat, rubidium, quantum interference, quantum coherence

1 Introduction

Quantum coherence plays important roles in many advances in quantum detection and control techniques in the recent two decades, such as coherent anti-Stokes Raman scattering (CARS) spectroscopy [1, 2], multidimensional Fourier transform spectroscopy [3], wave packet control of atoms and molecules [4–6], and quantum interference control of photocurrent [7], due to the fact that optical interference can reveal the quantum pathways in which the system evolves. Quantum computers also heavily rely on coherent manipulation of quantum states, for e.g., in atomic, ionic, and superconducting circuit qubits [8–10]. These systems use dipole–dipole interactions to simulate many-body physics. Thus, it is important to measure the interactions of atomic/ionic systems at different energy states. Recent works using double-quantum two-dimensional coherent spectroscopy were able to detect long-range dipole–dipole interactions in low-density atomic vapors [11]. It has also been demonstrated that by comparing the shape, including broadening and sidebands, of the Fourier spectra of measured quantum beat patterns to theoretical models, the number of atoms involved in dipole–dipole interactions can be characterized for an excited atomic ensemble [12]. Most importantly, this method provides a possible route to measure dipole–dipole interactions at many highly excited states. Therefore, improving quantum beat measurements for highly excited atomic systems is of great interest.

Many of these quantum beating experiments [12–15] were carried out in pump–probe configurations. Typically, a laser pulse is split into two with different intensities; the stronger one is used as the pump pulse and the other as the probe. The delay between the

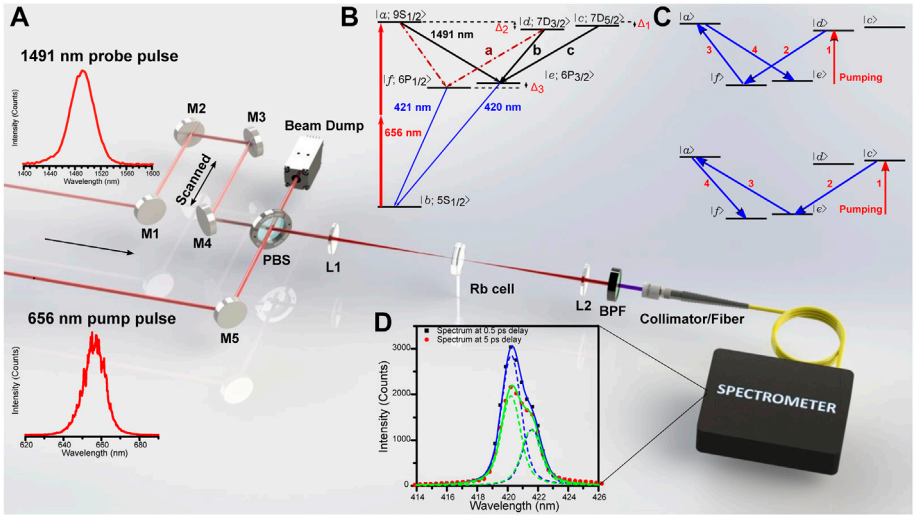

FIGURE 1
(A) Experimental schematics for observing the multichannel quantum beats. The pump (656 nm) and the probe (1491 nm) laser pulses were collinearly combined and focused into the rubidium (Rb) cell. Normalized spectra of the input pulses are shown as they are generated from OPAs. M1–M5 are mirrors. PBS is a Pellicle beamsplitter. BPF is a band-pass filter centered at 420 nm with full width at half maximum (FWHM) of 10 nm. **(B)** Simplified energy level diagram of ^{87}Rb. Broadband pump pulses excite atoms from 5*S* to both 9*S* and 7*D* levels; probe pulses couple 9*S* and 7*D* levels to 6*P* levels. **(C)** Illustrations of fourth-order quantum paths, which result in exchanging transition probabilities of the two 6*P* fine structure levels and beat pattern's envelope oscillations as discussed in the text. **(D)** Spectra of the emission (black and red dots) measured at a delay time of 0.5 and 5 ps between pump and probe pulses; two distinguishable lines (dashed lines) at 420 and 421 nm are fitted to each spectrum. The solid lines are the sum of the fitted Voigt profiles.

pump and probe pulses is scanned to obtain a beat pattern. At the density of atoms (or molecules) at which quantum beats are observed, the first few or ten picoseconds of the coherent optical signals exhibit exponential decay envelopes. This is attributed to superfluorescence (SF) processes, where the single-pass gain is large enough to overcome dephasing in a population inverted system, and a build-up polarization results in a burst of emission [16, 17]. In this work, we present experimental data to determine a time scale for this process, based on our previous studies of SF processes in the same atomic system and other systems [18, 31]. Furthermore, because we used two beams at different wavelengths for the pump and drive/probe pulses, which effectively couple much lower energy levels, we were able to see some transitions which are weak or negligible in other experiments, e.g., in [19].

We investigate multichannel quantum beats *via* the 420 nm and 421 nm radiation from an atomic vapor of ^{87}Rb, and relevant energy levels are shown in Figure 1B. The atoms are two-photon excited from 5*S* to both 9*S* and 7*D* levels by ultrashort laser pulses with a broadband spectrum centered at 656 nm, and Δ's are angular frequency differences between energy levels. The broadband drive pulses centered at 1491 nm couple the fine structure levels of 9*S* and 7*D* to those of 6*P*. According to selection rules, all transitions from 9*S* and 7*D* to 6*P* are dipole-allowed, except the $7D_{5/2} \rightarrow 6P_{1/2}$ transition. The sum rule [20] tells us that the transition intensity of the three labeled ones from 7*D* to 6*P* in the figure is $a : b : c = 5 : 1 : 9$. If we imagine that transition *b* is absent, one can see that when the delay between pump and drive pulses is scanned, the beat frequency $\Delta_1/2\pi$ can be seen on the 420 nm transition, while the 421 nm transition can show the beat frequency of $\Delta_2/2\pi$. Furthermore, since the two channels are coupled through levels 9*S* (and weakly via $7D_{3/2}$), multi-photon processes, as shown in Figure 1C, are revealed through the beat frequency of $(\Delta_2 - \Delta_1)/2\pi$. All these happen in a typical SF time scale of ~ 20 picoseconds. In the following sections of this article, we will discuss these aspects in detail. In Sections 2, 3, we describe the experimental setup and results. Section 4 is devoted to a theoretical model of multichannel beat processes. An approximate formula for beat intensity is derived using the fourth-order time-dependent perturbation theory. We summarize the experimental and theoretical results in the last section.

2 Experimental methods

The experimental setup is shown in Figure 1A. Femtosecond laser pulses with wavelengths centered at 656 and 1491 nm were collinearly focused into a thin rubidium vapor cell. The cell is made of sapphire which allows a high temperature operation. It has a cylindrical shape with a total length of 5.3 mm, two 1.7-mm-thick windows, and a diameter of 1 inch. Rb vapor fills the

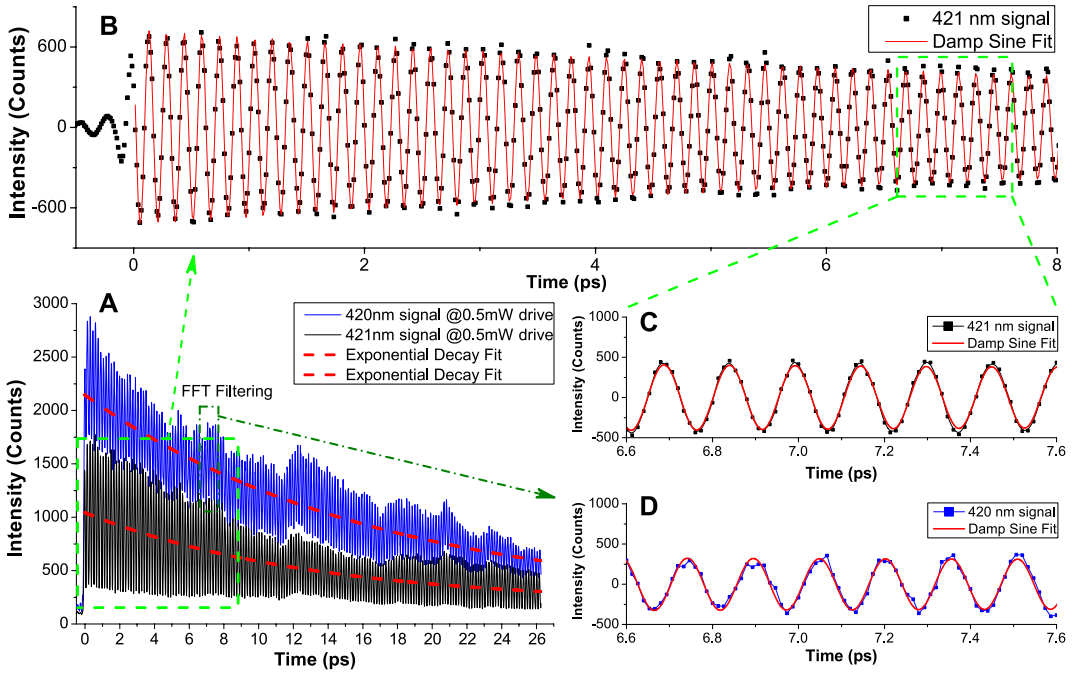

FIGURE 2
Experimental data with fitted functions. **(A)** Long-range scanned data with a time resolution of 0.0133 ps. Solid lines represent the measured data, and dashed red lines are fitted exponential decay curves. The fitted curves give an average decay time of 16.14 ps. **(B)** Fast Fourier transform (FFT) filtered 421 nm data (black dots) fitted to a damped sine curve (red line) in a 10 ps time window. The DC offset is removed by the FFT filtering. **(C)** Zoomed-in window as shown in the green dashed box. **(D)** Data of 420 nm signal (blue dot and line) and fitted damped sine curve (red line) in the same time window as **(C)**.

1.9-mm-long space sandwiched between the windows. The generated signal was analyzed using a spectrometer (HR4000, Ocean Optics). The pump (656 nm) and drive (1491 nm) laser pulses were generated from two optical parametric amplifiers (OperA, Coherent) pumped by 800 nm, 30 fs laser pulses from a Ti:sapphire femtosecond laser system (Legend, Coherent) with a 1-kHz repetition rate. Both pulses were linearly polarized, with the same polarization. The pulse energy of each beam was controlled using a reflective-type continuous variable neutral density filter. The probe beam was retro-reflected by a pair of mirrors mounted on a digitally controlled translation stage (Newport) to precisely adjust the time delay between pump and drive pulses. Both beams were collinearly combined by a pellicle beamsplitter (PBS) and were focused using a lens with 200 mm focal length into the Rb cell. The cold reservoir of the cell was kept at 214 °C, and the number density of ^{87}Rb atoms was estimated to be $1.3 \times 10^{15}\, cm^{-3}$ [21].

3 Experimental results and discussion

The spectra of the coherent emission in the forward direction are shown in Figure 1D. They were obtained with an average pump power at 2.0 mW and 0.5 mW of the drive at two different delay times between pump and drive pulses. As we scan the delay, two peaks clearly change their intensities; thus, we fit each spectrum by double peaks of Voigt profiles. In the fitting, the two peaks share the same line widths, while the positions and intensities of two peaks plus a constant baseline are independent parameters. Both spectra show fitted peaks at 420.2 and 421.6 nm which match the exact values of the transitions [22] within the calibration accuracy (0.1 nm) of our spectrometer. The fitted spectral width of the Voigt profiles is 1.5 nm; thus, it is not limited by the resolution (0.35 nm) of our spectrometer. A similar spectrum was taken at every step while the translation stage was scanned.

To resolve the beat frequencies, we used a small step size of 2 μm, which is equivalent to 0.0133 ps time delay. In order to see a large time scale decay curve, we also scanned with a 10 times larger step size, corresponding to 0.133 ps per step. A sample of the typical data scanned with a smaller step size is shown in Figure 2A. These data are fitted by a single exponential decay curve, and on average, we get a 16.14 ps decay time constant which closely matches to the delay time of the SF signal (17.5 ps) from our previous work [18]. There are two time constants associated with SF processes: the collective damping time τ_r governs the SF pulse width, and the delay time τ_D tells how much time the system takes to evolve before emitting an SF pulse. Our data suggest that τ_D is a qualitative measure of the decay time of the

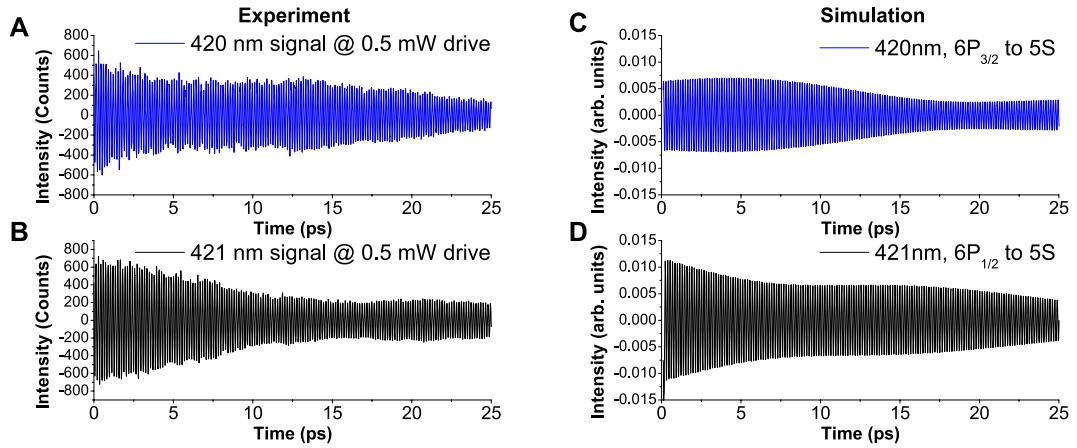

FIGURE 3
Slow varying envelopes of the beats of 420 and 421 nm signals. **(A)** Blue and **(B)** black are experimental data after an FFT high-pass filtering used to remove the DC and exponential decay components from the raw data. **(C)** Blue and **(D)** black are numerical simulations for the corresponding transitions to **(A)** and **(B)**, both labeled with wavelength and color-coded to match the experimental results.

beating pattern. A good match between the two time scales is reasonable because amplified spontaneous emission (ASE) rises from the population inversion between upper levels (9*S* and 7*D* levels) and intermediate levels (6*P*, and 8*P*, 7*P*, 5*P*) after the atoms are optically pumped. If there is enough single-pass gain (in other words, enough number of excited atoms within a wavelength range), the emission will evolve into SF [16, 17]. Coherence in the atomic ensemble builds up, and after some delay time, a burst of light is emitted from the atoms. This argument rises naturally as many quantum beat experiments mentioned previously rely on the detection of the SF or yoked SF [23] signal(s).

To extract a clear beat pattern, we performed a fast Fourier transform (FFT) filtering which filters the decay and the dc offset components. A typical sample of the processed data is shown in Figure 2B. To find the beat frequency, we fit the data to a damped sine function of the form $A_0 + A_1 e^{-t/\tau_0} \sin(2\pi f t)$, where τ_0 is the decay time to be numerically fit. For the 420 nm signal, we get an average beat frequency of 6.517 THz, and for the 421 nm signal, the average is 6.563 THz, with a difference of 46.4 ± 2.8 GHz between them. In the literature, the calculated fine splitting of 7D of Rb is 45.18 ± 0.3 GHz [22]. If we zoom in the data points in Figures 2C, D, we see the effect of the weak transition *b* shown in the energy diagram in Figure 1B. The 421 nm transition has only two quantum paths from 9*S* and 7*D*, and the data (Figure 2C) follow closely to the fitted curve. As a comparison, the 420 nm transition has three upstream quantum paths; even though transition *b* is relatively weak compared to the other two, it is enough to dither some of the data points off the fitted sine trace as shown in Figure 2D.

After an FFT filtering of the longer scan data shown in Figure 2A, the beat pattern shows an overall envelope with two features: an exponential decay and an oscillation with a frequency of 46 GHz, which matches to the fine structure splitting of 7D. Figure 3 exhibits the experimental results together with simulations demonstrating both features. The exponential decay of this envelope is carried from the overall decay of the signals. The reason of this oscillation is understood as follows. By closely inspecting the energy diagram (Figure 1), it is obvious for the 420 nm signal to carry a frequency of 46 GHz, since both levels of 7*D* are involved in its quantum path. However, questions arise are: how can the 421 nm signal also carry this frequency? Is it from the coupling via 9S? To answers these questions, we employ the following theoretical model.

4 Theoretical model and interpretations

For the 6-level system as shown in Figure 1B, the atom–field effective interaction Hamiltonian can be written as [24, 25]:

$$\begin{aligned} V(t) = -\hbar\big(&\Omega_{eff}|a\rangle\langle b| + \Omega_{eff}e^{-i\Delta_1 t}|c\rangle\langle b| \\ &+ \Omega_{eff}e^{-i\Delta_2 t}|d\rangle\langle b| + \Omega_{ae}|a\rangle\langle e| \\ &+ \Omega_{af}e^{i\Delta_3 t}|a\rangle\langle f| + \Omega_{ce}e^{-i\Delta_1 t}|c\rangle\langle e| \\ &+ \Omega_{df}e^{-i(\Delta_2-\Delta_3)t}|d\rangle\langle f| + \Omega_{de}e^{-i\Delta_2 t}|d\rangle\langle e| \\ &+ h.c.\big), \end{aligned} \tag{1}$$

where we assume Gaussian pulses such that $\Omega_{eff} = \Omega_p^{(0)} \exp(-t^2/\alpha_p^2)$is the pump laser effective Rabi frequency, $\Omega_{ij} = \Omega_{ij}^{(0)} \exp(-(t-\tau)^2/\alpha_c^2)$ is the drive pulse Rabi frequency which couples *i* and *j* states, τ is the delay time between the probe and the pump pulses, and $\alpha's$ are pulse durations. Because the pulses are very short compared to the SF time scale, we essentially treat them in the delta function limit in our calculation. The notations we use for detunings are $\Delta_1 = 40.99 \times 10^{12}\text{s}^{-1}$, the energy difference between $9S^{1/2}$ and $7D^{5/2}$;

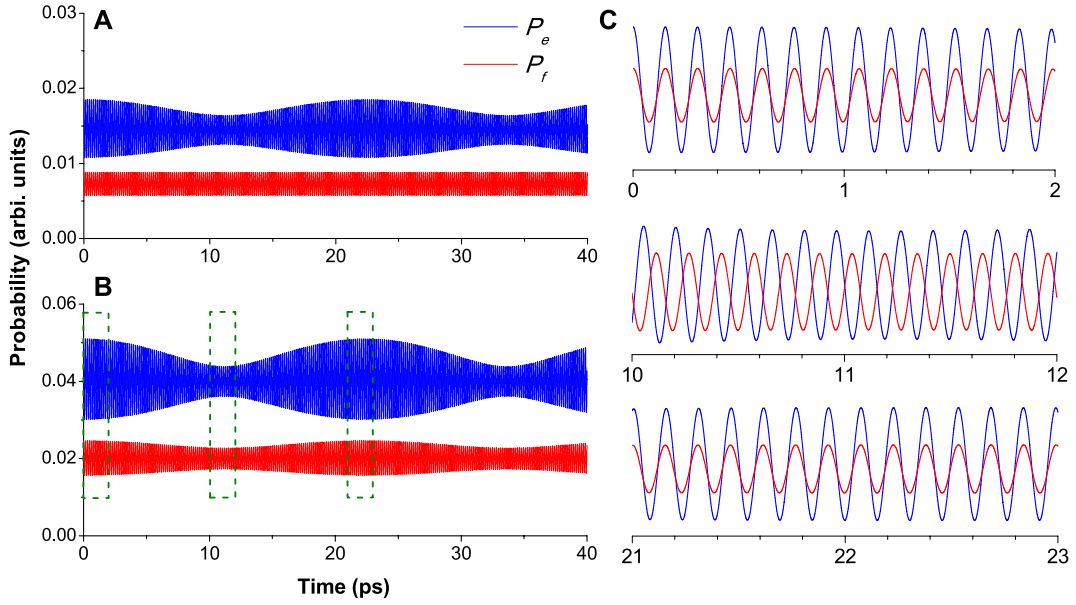

FIGURE 4
(A) Probabilities of finding atoms on level $|e\rangle$ (P_e)and level $|f\rangle$ (P_f) plotted from analytical expressions up to second-order terms. **(B)** Same probabilities plotted with the expressions up to fourth-order terms. The envelope modulation of P_f is a result of multi-photon (>3) interaction between levels $|c\rangle$ and $|f\rangle$ because single-photon transition is forbidden. **(C)** Probabilities zoomed in 2-ps windows, and the curves have been offset to show a relative phase shift due to different beat frequencies of the signals. Parameters used for the plots are: $\alpha_p\Omega_p^{(0)} = 0.2$, $\alpha_c\Omega_{ae}^{(0)} = 0.6$, $\Omega_{af}^{(0)} = \Omega_{ae}^{(0)}/\sqrt{2}$, $\Omega_{ce}^{(0)} = 0.2\Omega_{ae}^{(0)}$, $\Omega_{df}^{(0)} = \Omega_{ce}^{(0)}\sqrt{5/9}$, and $\Omega_{de}^{(0)} = \Omega_{ce}^{(0)}\sqrt{1/9}$. Relative transition dipole moments are estimated by the sum rule [20].

$\Delta_2 = 41.27 \times 10^{12}\text{s}^{-1}$, the energy difference between $9S^{1/2}$ and $7D^{3/2}$; and $\Delta_3 = 14.61 \times 10^{12}\text{s}^{-1}$, the energy difference between $6P^{3/2}$ and $6P^{1/2}$. Our goal is to find the probability of finding atoms in the $|e\rangle$ and $|f\rangle$ states using the time-dependent perturbation theory. The second-order perturbation terms explain the beat frequencies $\Delta_1/2\pi$ and $\Delta_2/2\pi$ but lack to tell the envelope beat in the 421 nm signal. Therefore, we use the perturbation theory up to the fourth-order terms. The approximate solution can be written in the following form:

$$\begin{aligned} P_e &= |e_0 + e_1 e^{i\Delta_1\tau} + e_2 e^{i\Delta_2\tau}|^2, \\ P_f &= |f_0 + f_1 e^{i\Delta_1\tau} + f_2 e^{i\Delta_2\tau}|^2, \end{aligned} \tag{2}$$

where e_j and f_j ($j = 0, 1, 2$) are constants. e_2 and f_1 are explicitly written as:

$$\begin{aligned} e_2 = {} & \pi\alpha_p\alpha_c\Omega_{ed}^{(0)*}\Omega_p^{(0)} \\ & + \pi^2\alpha_p\alpha_c^3\Big(\Omega_{ea}^{(0)*}\Omega_{ae}^{(0)}\Omega_{ed}^{(0)*}\Omega_p^{(0)} + \Omega_{ea}^{(0)*}\Omega_{af}^{(0)}\Omega_{fd}^{(0)*}\Omega_p^{(0)} \\ & \quad + \Omega_{ec}^{(0)*}\Omega_{ce}^{(0)}\Omega_{ed}^{(0)*}\Omega_p^{(0)} + \Omega_{ed}^{(0)*}\Omega_{de}^{(0)}\Omega_{ed}^{(0)*}\Omega_p^{(0)} \\ & \quad + \Omega_{ed}^{(0)*}\Omega_{df}^{(0)}\Omega_{fd}^{(0)*}\Omega_p^{(0)}\Big) \\ & + 3\pi^2\alpha_p^3\alpha_c\Omega_{ed}^{(0)*}\Omega_p^{(0)}\Omega_p^{(0)*}\Omega_p^{(0)}, \end{aligned} \tag{3}$$

$$f_1 = \pi^2\alpha_p\alpha_c^3\Big(\Omega_{fa}^{(0)*}\Omega_{ae}^{(0)}\Omega_{ec}^{(0)*}\Omega_p^{(0)} + \Omega_{fd}^{(0)*}\Omega_{de}^{(0)}\Omega_{ec}^{(0)*}\Omega_p^{(0)}\Big), \tag{4}$$

where we change the indices order in the complex conjugate of the Rabi frequency such that $(\Omega_{ij}^{(0)})^* = \Omega_{ji}^{(0)*}$. In this notation, we can interpret the terms in Eqs. 3 and 4 with ease. For example, the term $\Omega_{ea}^{(0)*}\Omega_{ae}^{(0)}\Omega_{ed}^{(0)*}\Omega_p^{(0)}$represents the fourth-order process as pumping atoms from the ground state $|b\rangle \rightarrow |d\rangle \rightarrow |e\rangle \rightarrow |a\rangle \rightarrow |e\rangle$, which is one of the final states.

We plot the probability of finding atoms on level $|e\rangle$ (P_e) and level $|f\rangle$ (P_f) with parameters shown in Figure 4. For conditions $e_1 \gg e_2$ and $f_1 \ll f_2$, one can verify that probabilities P_e and P_f oscillate at angular frequencies Δ_1 and Δ_2, respectively. Therefore, e_1 and f_2 terms in Eq. 2 give fast oscillations, as shown in resolved time windows in Figure 4C. Moreover, because the frequencies are different, we can also see that the relative phase of the beat oscillation shifts as the delay time increases. The expression which only keeps up to second-order terms is plotted in Figure 4A, where the envelope modulation of P_f is absent; while the plot using expression with fourth-order terms clearly shows the modulation on P_f and a larger modulation depth on P_e. We conclude that the e_2 and f_1 terms in Eqs. 3 and 4 cause the envelope modulation shown in the analytical results (Figure 4B) and the experimental results (Figure 3). Furthermore, the main reasons for the envelope oscillation are the fourth-order processes coupled through the $|a\rangle$ state ($9S_{1/2}$) as well as other processes in Eqs. 3 and 4. To see this more clearly, let us set $\Omega_{de}^{(0)} = 0$ because $|d\rangle \rightarrow |e\rangle$ transition intensity is only 1/9 of $|c\rangle \rightarrow |e\rangle$ and 1/5 of $|d\rangle \rightarrow |f\rangle$ transition intensities. Then, Eqs. 3 and 4 become $e_2 = \pi^2\alpha_p\alpha_c^3\Omega_{ea}^{(0)*}\Omega_{af}^{(0)}\Omega_{fd}^{(0)*}\Omega_p^{(0)}$and $f_1 = \pi^2\alpha_p\alpha_c^3\Omega_{fa}^{(0)*}\Omega_{ae}^{(0)}\Omega_{ec}^{(0)*}\Omega_p^{(0)}$, which are symmetrically

exchanging the excitation probability from $|d\rangle$ ($|c\rangle$) to $|e\rangle$ ($|f\rangle$) (Figure 1D). These fourth-order processes coupled through the $|a\rangle$ state ($9S_{1/2}$) are the main reason for envelope oscillation in the 421 nm signal and a deeper modulation on the 420 nm signal.

5 Conclusion

In this work, we demonstrate that the beat pattern of the 421 nm signal is much less disturbed by other quantum pathways, and it is potentially a better candidate for the technique described in Ref. [12] to characterize dipole–dipole interactions. In general, $F = 1/2$ levels have less coupled upper levels due to selection rules; thus, they can be used to obtain cleaner beat patterns for sensing dipole–dipole interactions. In addition, this technique requires a long time scan (~ 100ps) in order to get enough spectral resolution after a Fourier transform. Our experimental data show persistence for a longer scan range despite the decay of the signal. Because for a weak atomic excitation, both theoretical [26] and experimental [27] works showed that the population on the excited states can survive for hundreds of picoseconds.

It is also possible to detect the beat pattern by monitoring the transmission of the infrared probe [14] as well as X-ray absorption [28], as long as different quantum pathway interferences at a common final state are realized [24, 29]. Controls of the beat pattern and thus the quantum path have been studied in our group by shifting the pump wavelength [15] or adding a control pulse [4]. In the present case, a shift of the pump beam central wavelength would tune the amplitudes and initial phase of the beat pattern. While our current system is based on OPAs, new laser sources can provide an extended wavelength range to cover more transition wavelengths and give more control of the sources, such as different frequency generation sources that extend to mid-infrared and a versatile single-laser platform that combines a short-pulse laser source with a tunable broadband wavelength converter based on a highly non-linear photonic-crystal fiber (PCF), which was recently demonstrated for single-beam dual-color two-photon spectroscopy [30].

In conclusion, we investigate coherent emissions at 420 and 421 nm in ^{87}Rb. We observed quantum beats at different frequencies on these two emissions as we scan the delay between pump and drive pulses. The profiles were measured, and numerical simulations based on a theoretical model are compared with the experimental results. Our results suggest that the SF delay time is a good measure of the exponential decay of the beating envelope. With the help of the time-dependent perturbation method, a higher order (five-photon) process was identified from the beat envelope of the 421 nm emission. The results pave the way for detecting dipole–dipole interactions of atoms at highly excited states.

Data availability statement

The original contributions presented in the study are included in the article/Supplementary Material; further inquiries can be directed to the corresponding authors.

Author contributions

ZY, GA, and MS conceived the work; ZY conducted the experiment and collected the data; ZY, GA, and AS analyzed the data; TB, ZY, AZ, and MS developed the theoretical model and simulations. TB wrote the code. All authors wrote the manuscript.

Funding

We gratefully acknowledge support of the Air Force Office of Scientific Research (Award No. FA9550-20-1-0366 DEF), the National Science Foundation (Grant No. PHY-2013771), and the Robert A. Welch Foundation (Award A-1261, A-1547, and A-1801). TB thanks the funding from the National University of Mongolia (P2021-4180).

Acknowledgments

We would like to thank Anatoly A. Svidzinsky and Moochan Kim for their helpful discussions.

Conflict of interest

The authors declare that the research was conducted in the absence of any commercial or financial relationships that could be construed as a potential conflict of interest.

Publisher's note

Supplementary material

The Supplementary Material for this article can be found online at: https://www.frontiersin.org/articles/10.3389/fphy.2022.921499/full#supplementary-material

References

1. Pestov D, Murawski RK, Ariunbold GO, Wang X, Zhi M, Sokolov AV, et al. Optimizing the laser-pulse configuration for coherent Raman spectroscopy. *Science* (2007) 316:265–8. doi:10.1126/science.1139055

2. Traverso AJ, Hokr B, Yi Z, Yuan L, Yamaguchi S, Scully MO, et al. Two-photon infrared resonance can enhance coherent Raman scattering. *Phys Rev Lett* (2018) 120:063602. doi:10.1103/physrevlett.120.063602

3. Li H, Bristow AD, Siemens ME, Moody G, Cundiff ST. Unraveling quantum pathways using optical 3D Fourier-transform spectroscopy. *Nat Commun* (2013) 4: 1390. doi:10.1038/ncomms2405

4. Yuan L, Pestov D, Murawski RK, Ariunbold GO, Zhi M, Wang X, et al. Tracking molecular wave packets in cesium dimers by coherent Raman scattering. *Phys Rev A* (2012) 86:023421. doi:10.1103/physreva.86.023421

5. Brinks D, Hildner R, van Dijk EMHP, Stefani FD, Nieder JB, Hernando J, et al. Ultrafast dynamics of single molecules. *Chem Soc Rev* (2014) 43:2476–91. doi:10.1039/c3cs60269a

6. Svidzinsky AA, Eleuch H, Scully MO. Rabi oscillations produced by adiabatic pulse due to initial atomic coherence. *Opt Lett* (2017) 42:65. doi:10.1364/ol.42.000065

7. Wang K, Muniz RA, Sipe JE, Cundiff ST. *Phys Rev Lett* (2019) 123:067402. doi:10.1103/physrevlett.123.067402

8. Ebadi S, Wang TT, Levine H, Keesling A, Semeghini G, Omran A, et al. Quantum phases of matter on a 256-atom programmable quantum simulator. *Nature* (2021) 595:227–32. doi:10.1038/s41586-021-03582-4

9. Egan L, Debroy DM, Noel C, Risinger A, Zhu D, Biswas D, et al. Fault-tolerant control of an error-corrected qubit. *Nature* (2021) 598:281–6. doi:10.1038/s41586-021-03928-y

10. Song C, Xu K, Li H, Zhang Y-R, Zhang X, Liu W, et al. Generation of multicomponent atomic Schrödinger cat states of up to 20 qubits. *Science* (2019) 365:574–7. doi:10.1126/science.aay0600

11. Yu S, Titze M, Zhu Y, Liu X, Li H. Long range dipole-dipole interaction in low-density atomic vapors probed by double-quantum two-dimensional coherent spectroscopy. *Opt Express* (2019) 27:28891. doi:10.1364/oe.27.028891

12. Shen F, Gao J, Senin AA, Zhu CJ, Allen JR, Lu ZH, et al. Many-body dipole-dipole interactions between excited Rb atoms probed by wave packets and parametric four-wave mixing. *Phys Rev Lett* (2007) 99:143201. doi:10.1103/physrevlett.99.143201

13. Blanchet V, Nicole C, Bouchene M-A, Girard B. Temporal coherent control in two-photon transitions: From optical interferences to quantum interferences. *Phys Rev Lett* (1997) 78:2716–9. doi:10.1103/physrevlett.78.2716

14. Zhu CJ, Xiao Y, Senin AA, Gao J, Eden JG, Varzhapetyan TS, et al. Quantum beating in Rb at 18.3 THz (608cm˜{− 1}) detected by parametric six-wave mixing and sum-frequency generation in LiIO_ {3}. *Phys Rev A* (2007) 75:053405. doi:10.1103/physreva.75.053405

15. Ariunbold GO, Sautenkov VA, Scully MO. Switching from a sequential transition to quantum beating in atomic rubidium pumped by a femtosecond laser. *J Opt Soc Am B* (2011) 28:462. doi:10.1364/josab.28.000462

16. Maki JJ, Malcuit MS, Raymer MG, Boyd RW, Drummond PD. Influence of collisional dephasing processes on superfluorescence. *Phys Rev A* (1989) 40: 5135–42. doi:10.1103/physreva.40.5135

17. Yuan L, Hokr BH, Traverso AJ, Voronine DV, Rostovtsev Y, Sokolov AV, et al. Theoretical analysis of the coherence-brightened laser in air. *Phys Rev A* (2013) 87:023826. doi:10.1103/physreva.87.023826

18. Yi Z, Jha PK, Yuan L, Voronine DV, Ariunbold GO, Sinyukov AM, et al. Observing the transition from yoked superfluorescence to superradiance. *Opt Commun* (2015) 351:45–9. doi:10.1016/j.optcom.2015.04.035

19. Ricconi B. *Quantum beat observations in rubidium vapor*. Urbana, IL: UIUC (2012).

20. Woodgate GK. *Elementary atomic structure*. 2nd ed. Oxford: Clarendon Press (1980).

21. Nesmeyanov ANGR. *Vapor pressure of the chemical elements*. Amsterdam: Elsevier (1963).

22. Sansonetti JE. Wavelengths, transition probabilities, and energy levels for the spectra of rubidium (Rb I through Rb XXXVII). *J Phys Chem Reference Data* (2006) 35:301–421. doi:10.1063/1.2035727

23. Brownell JH, Lu X, Hartmann SR. Yoked superfluorescence. *Phys Rev Lett* (1995) 75:3265–8. doi:10.1103/physrevlett.75.3265

24. Scully MO, Zubairy MS. *Quantum optics*. Cambridge ; New York: Cambridge University Press (1997).

25. Zubairy AHMS, Zubairy MS. Validity of the effective Hamiltonian in the two-photon atom-field interaction. *Phys Rev A* (1992) 45:4951–9. doi:10.1103/physreva.45.4951

26. Svidzinsky AA, Chang J-T, Scully MO. Exact solution of gradient echo memory and analytical treatment of gradient frequency comb. *Phys Rev A* (2010) 81:053821. doi:10.1103/PhysRevA.81.053821

27. Xia H, Svidzinsky AA, Yuan L, Lu C, Suckewer S, Scully MO. *Phys Rev Lett* (2012) 109:093604. doi:10.1103/physrevlett.109.093604

28. Guimarães F, Gelmukhanov F, Cesar A, Ågren H. Quantum wave packet revivals in IR + X-ray pump–probe spectroscopy. *Chem Phys Lett* (2005) 405:398. doi:10.1016/j.cplett.2005.02.061

29. Drühl MOK, Drhl K. Quantum eraser: A proposed photon correlation experiment concerning observation and "delayed choice" in quantum mechanics. *Phys Rev A* (1982) 25:2208–13. doi:10.1103/physreva.25.2208

30. Chebotarev AS, Lanin AA, Raevskii RI, Kostyuk AI, Smolyarova DD, Bilan DS, et al. Single-beam dual-color alternate-pathway two-photon spectroscopy: Toward an optical toolbox for redox biology. *J Raman Spectrosc* (2021) 52: 1552–60. doi:10.1002/jrs.6183

31. Wang K, Wang Y, Wang J, Yi Z, Kulatilaka WD, Sokolov AV, et al. Femtosecond pump-probe studies of atomic hydrogen superfluorescence in flames. *Appl Phys Lett* (2020) 116:201102. doi:10.1063/5.0001924

frontiers | Frontiers in Physics

TYPE Review
PUBLISHED 12 September 2022
DOI 10.3389/fphy.2022.892519

OPEN ACCESS

EDITED BY
Roberto de J. León-Montiel,
National Autonomous University of Mexico, Mexico

REVIEWED BY
Yin Cai,
Xi'an Jiaotong University, China
Che-Ming Li,
National Cheng Kung University, Taiwan

*CORRESPONDENCE
Yuanyuan Chen,
chenyy@xmu.edu.cn
Lixiang Chen,
chenlx@xmu.edu.cn

SPECIALTY SECTION
This article was submitted to Quantum Engineering and Technology, a section of the journal Frontiers in Physics

RECEIVED 09 March 2022
ACCEPTED 09 August 2022
PUBLISHED 12 September 2022

CITATION
Chen Y, Hong L and Chen L (2022), Quantum interferometric metrology with entangled photons.
Front. Phys. 10:892519.
doi: 10.3389/fphy.2022.892519

Quantum interferometric metrology with entangled photons

Yuanyuan Chen*, Ling Hong and Lixiang Chen*

Department of Physics and Collaborative Innovation Center for Optoelectronic Semiconductors and Efficient Devices, Xiamen University, Xiamen, China

Quantum interferences of entangled photons have engendered tremendous intriguing phenomena that lack any counterpart in classical physics. Hitherto, owing to the salient properties of quantum optics, quantum interference has been widely studied and provides useful tools that ultimately broaden the path towards ultra-sensitive quantum metrology, ranging from sub-shot-noise quantum sensing to high-resolution optical spectroscopy. In particular, quantum interferometric metrology is an essential requisite for extracting information about the structure and dynamics of photon-sensitive biological and chemical molecules. This article reviews the theoretical and experimental progress of this quantum interferometric metrology technology along with their advanced applications. The scope of this review includes Hong–Ou–Mandel interferometry with ultrahigh timing resolution, entanglement-assisted absorption spectroscopy based on a Fourier transform, and virtual-state spectroscopy using tunable energy-time entangled photons.

KEYWORDS

quantum entanglement, Hong–Ou–Mandel interference, spectral and temporal domains, biphoton wavefunction, quantum metrology, entanglement-assisted absorption spectroscopy

1 Introduction

Quantum entanglement is a non-classical phenomenon that the quantum state of each individual particle cannot be described independently of the state of the others, whose nature reveals the most fascinating and unexpected aspects of the quantum world [1, 2]. For example, the non-classical correlation of such entangled particles would not be diminished even when they are spatially separated by arbitrary distances. Naturally, quantum entanglement is an essential prerequisite for a variety of quantum experiments in the field of fundamental tests of quantum physics, such as the investigation of the Einstein–Podolsky–Rosen (EPR) paradox and the violation of Bell's inequalities [3–5], and practical applications, such as quantum information processing [6, 7]. The exploitation of quantum entanglement in these specific scenarios has great potential to outperform the schemes based on classical physics. As an example in metrology, while an individual particle exhibits an inherent uncertainty, the joint correlation between entangled photons can be exempt from such limitation. More specifically, the arriving

time of the individual photons is completely random, but the entangled photons always arrive simultaneously. These myriad and significant implications of quantum entanglement make them compelling for use in quantum optical metrology [8–12].

Quantum interference of entangled photons leads to many counterintuitive results, which can be considered an absolute necessity in the quantum mechanic's toolkit. Thereinto, Hong–Ou–Mandel (HOM) interference, the fact that two identical photons that arrive simultaneously on different input ports of a beam splitter would bunch into a common output port, is a prototypical example of quantum interference [13]. Its interference visibility, namely, the bunching probability, is directly related to photons' level of indistinguishability. The definition of indistinguishability is on the bases of various parameters in all degrees of freedom, such as polarization, frequency, time, path, and orbital angular momentum. This quantum effect enables a wide range of quantum information processing tasks, in particular for the measurements of optical delays and spectroscopy with the requirements for ultrahigh resolution, precision and accuracy, and experimental robustness against detrimental noise [14–17].

In the context of the applications in both metrology and sensing, the precise and demanding measurements are most likely performed as optical interference, including but not limited to Ramsey interferometry in atomic spectroscopy [18], x-ray diffraction in crystallography [19], and optical interferometry in gravitational-wave studies [20, 21]. Quantum mechanics indicates that the fundamental shot noise limit of the phase uncertainty in optical metrology based on classical resources is $\delta\phi \geq 1/\sqrt{N}$, where N is the number of systems used in measurement. For quantum entanglement, this standard limit can be beat as the fundamental precision limit reaches $\delta\phi \geq 1/N$ by using a maximally entangled N-photon state, i.e., the well-known Heisenberg limit [22, 23]. Thus, quantum interferometric metrology with entangled photons promises ultrahigh precision and accuracy in the phase measurement that may arise from optical delay [16, 17], spatially structured photon [24], and dephasing time [25].

Additionally, while conventional spectroscopy based on classical light is limited by shot noise, absorption spectroscopy with single photons can achieve a precision that is beyond the shot-noise limit and even near the ultimate quantum limit [26]. Therefore, quantum light provides a powerful tool to extract the spectroscopic information of target materials by using a single-photon monochromator [27] or tunable frequency-correlated photons [26], which may be particularly relevant for photon-sensitive biological and chemical samples [25]. In order to tackle the experimental issues, quantum Fourier spectroscopy is presented as an alternative route [14, 28, 29]. In analogy to classical Fourier transform between time and frequency domains, the spectral and temporal degrees of freedom of biphoton wavefunction can also be connected by a Fourier transform [30]. Thus, quantum interferometric spectroscopy enables us to extract the spectroscopic information from the temporal pattern of quantum interference, but without the usual requirement for flexible single-photon monochromator or paired photons with tunable and narrow spectral distribution.

As an alternative route toward temporal measurement and spectroscopy, quantum interferometric metrology with entangled photons provides great advantages in resolution, precision, and time efficiency. Typically, the conventional interferometric approaches based on classical light, such as Mach–Zehnder interferometer, are known as first-order interference, which is extremely subject to environmental noise and photon loss. On the contrary, the HOM interference based on quantum light is not affected by variations in the optical phase, even when the fluctuations of path length difference are on the order of the wavelength [31]. This feature has resulted in proposals for quantum interferometric metrology with provable advantages in the robustness against noise and loss [32, 33], such as the cancellation of some deleterious dispersion effects [31, 34]. Although photon wave packets are generally broadened and delayed when they transmit through the dispersive optical elements, the corresponding dispersion is balanced in both arms of the HOM interferometer. Assisted by coincidence measurement made with entangled photon pairs, the observed interference pattern can be free of such dispersive behavior [35, 36]. These results may indicate a new direction toward fully harnessing quantum interference in practical quantum metrology.

In this review, our aim is to present the theoretical and experimental progress in the investigation of quantum interference with entangled photons and their applications in the field of quantum metrology. Emphasis is placed on the preparation of energy-time entanglement and its relevant applications in temporal measurement and spectroscopy.

This review is structured as follows: In Section 2, we discuss the creation of quantum entanglement, which is used as the probe in quantum interferometric metrology, in particular, the exploitation of energy-time entanglement. In Section 3, we review the experimental implementation and practical applications of HOM interferometry with ultrahigh timing resolution, regarding the enhancement of HOM interferometry by using discrete frequency entanglement and applications in the exploration of superluminal speeds of structured light and dephasing time of the molecular properties in biology and chemistry. In Section 4, we review the quantum interferometric spectroscopy with quantum entanglement and its applications in single-photon and two-photon absorption spectroscopy. Section 5 contains the conclusion and an outlook.

2 Entanglement source

Since this work focuses on the quantum interferometric metrology with entangled photons, we first introduce the

concept and generation of quantum entanglement, whose specific properties enable the intriguing quantum interference that goes beyond the possibilities of classical physics.

In the set of a quantum system consisting of n subsystems, the Hilbert space of the whole system is the tensor product of the subsystem spaces, namely, $H = \otimes_{l=1}^{n} H_l$. As a direct result, the basis can be written as a superposition state in the form of

$$|\Psi\rangle = \Sigma_{i_1,\ldots,i_n} c_{i_1,\ldots,i_n} |i_1\rangle \otimes |i_2\rangle \otimes \cdots \otimes |i_n\rangle, \tag{1}$$

where $|i_{1,\ldots,n}\rangle$ represents the specific state of the individual subsystems. We consider a more general case as a multipartite system A_1, A_2, . . ., A_m. Typically, their many-body states can be divided into two classes: entangled states and separable states. One calls a state of m systems entangled if it cannot be written as a convex combination of product in the form of

$$|\Phi_{A_1,A_2,\ldots,A_m}\rangle \neq |\Phi_{A_1}\rangle \otimes |\Phi_{A_2}\rangle \otimes, \ldots, \otimes |\Phi_{A_n}\rangle. \tag{2}$$

In contrast, if the state can be decomposed into the tensor products of subsystems, one calls it separable [37–39]. Intuitively, the entangled state is a prototypical quantum phenomenon that lacks any counterpart in classical physics or simulation by classical correlations [1, 40–42]. This work focused on the two-photon entanglement in the bipartite systems with a Hilbert space $H = H_1 \otimes H_2$. The complete Bell basis in this state space can be expressed by the well-known Bell states as

$$\begin{aligned} |\phi^{\pm}\rangle &= \frac{1}{\sqrt{2}} (|00\rangle \pm |11\rangle) \\ |\psi^{\pm}\rangle &= \frac{1}{\sqrt{2}} (|01\rangle \pm |10\rangle). \end{aligned} \tag{3}$$

These Bell states have interesting properties [43–45].

This intriguing quantum entanglement is an enabling resource for a large number of practical applications, including but not limited to quantum information processing [46–51], quantum metrology [8–12], and quantum simulation [52–55]. Therefore, an efficient source of entangled photons has long been hailed as an essential prerequisite in the quantum mechanic's toolkit. Among these available technologies, the spontaneous parametric down-conversion (SPDC) process in nonlinear materials is most commonly used in practice, which provides advantages in fiber coupling efficiency, entangled photon pair generation rates, and entanglement fidelity and flexibility [56–61]. In an SPDC process, a pump photon with high energy would spontaneously decay into signal and idler photons, which can be tailored to exhibit entanglement in various photonic degrees of freedom. For example, as the signal and idler photons are created simultaneously, the time entanglement is an inherent property of the down-converted photons generated by the SPDC process. The spontaneous down conversion ensures the time correlation between signal and idler photons, while the coherent temporal modes of pump lasers enable the nonlocal correlation. Thus, the time entanglement has been verified through the violation of Bell inequality by using the Franson interferometer [62, 63] and enabling the applications in quantum information processing [64–66]. In addition, since the frequency bandwidth of the pump laser is much narrower than that of the down-converted photons, the frequency entanglement arises quite naturally as a direct result of energy conservation. More specifically, the central frequencies of down-converted signal, idler, and pump photons satisfy the energy conservation as $\omega_s + \omega_i = \omega_p$, which directly indicates the spectral correlation of entangled photons. Backed by the coherent spectral modes of pump lasers that enable the nonlocal correlation, the violation of Bell inequality in the frequency domain has been verified [67].

2.1 Generation of quantum entanglement by spontaneous parametric down conversion

In particular, the quasi-phase matching in the SPDC process has a strict requirement for polarization states of pump, signal, and idler photons. Thus, polarization entanglement can be generated using elaborate configurations such as polarization Sagnac interferometer and crossed-crystal scheme. In order to implement a polarization entanglement source with ultrahigh brightness, we use the SPDC process with collinear type-0 quasi-phase matching, which has resulted in the highest photon pair generation rates reported to date [68]. However, the spatial modes of down-converted photons overlap completely, these type-0 sources typically require wavelength distinguishability to route photons into distinct spatial modes for independent manipulation. Consequently, these frequency-distinguishable signal and idler photons are inapplicable for quantum information process applications that require indistinguishable photons, such as HOM interference. This leads to a question of the utmost importance: How can we generate identical entangled photons that are separated in opposite spatial modes with ultrahigh brightness. By superimposing four pair-creation possibilities on a polarization beam splitter, pairs of identical photons are separated into two spatial modes as a direct result of time-reversed HOM interference and without the usual requirement for wavelength distinguishability or noncollinear emission angles [69]. More specifically, while the typical HOM interference states the fact that identical photons that arrive simultaneously on different input ports of a beam splitter would bunch into a common output port, time-reversed HOM interference states that the superposition of two-photon quantum states that arrive simultaneously on difference input ports of a beam splitter would deterministically anti-bunch into distinct output ports. This intriguing interference effect enables the deterministical separation of identical photons into distinct spatial modes without any requirement of photons' distinguishability and phase stability. The resultant polarization entanglement is in the form of

$$|\Psi_p^+\rangle = \frac{1}{\sqrt{2}}(|HV\rangle + |VH\rangle), \quad (4)$$

where $|H\rangle$ and $|V\rangle$ represent the horizontal and vertical polarization, respectively. By combining the benefits of the phase-stable polarization Sagnac sources and highly-efficient crossed-crystal sources, we generate wavelength-degenerate photon pairs around the center wavelength of 810 nm with a Bell-state fidelity of 99.2% and detect a pair rate of 160 kcps per mW of pump power. Furthermore, we believe that our source can yield entangled photon rates in excess of 10^7 pairs per second for pump powers readily attainable using compact laser diodes. These polarization-entangled photons have been widely used in HOM interferometry, where polarization correlation is used to deterministically route paired photons into distinct spatial modes such that these identical photons can arrive on different input ports of a beam splitter.

To fulfill the requisites of specific applications, ultrabroadband biphotons can yield a high flux of nonoverlapping biphotons with ultrahigh brightness, which is essential for making quantum entanglement in nonclassical applications such as entangled-photon microscopy, quantum spectroscopy, and optical coherence tomography. To tackle this issue, adaptive modulation in quasi-phase-matched nonlinear gratings that have a linearly chirped wave vector is used to generate ultrabroadband biphotons with a spectral bandwidth of 300 nm, which results in the observation of ultranarrow HOM dip with a full width at half maximum of 7.1 fs [70]. Another approach to control the spectral structure of photon pairs is based on the SPDC process in microstructured fibers. Specifically, by fabricating fibers with design dispersion, the photons' wavelengths, joint spectrum, and quantum entanglement can, thus, be manipulated [71]. In particularly, photon pairs with no spectral correlations are produced that allow direct heralding of single photons in pure-state wave packets without filtering. As the theoretical analysis and preliminary tests suggest that 94.5% purity is possible with a much longer fiber, an experimental purity of (85.9 ± 1.6)% has been achieved.

Additionally, photon pairs entangled in multiple properties have remarkable advantages, such as increasing the information capacity for quantum communication [72–74], implementing the complete Bell state measurements for superdense coding or larger quantum states can be transmitted in quantum teleportation [46, 75], enhancing the fidelity of mixed entangled states in entanglement purification [76, 77], and increasing the state space for multiphoton entanglement and quantum computing [78, 79]. Hence, it is of great significance to design wieldy and practical strategies to harness hyperentanglement. In analogy to polarization entanglement based on time-reversed HOM interference. we use the experimental configuration to generate and characterize the hyperentanglement in polarization and discrete frequency degrees of freedom [80], which can be written as

$$|\Psi_p^+\rangle \otimes |\Psi_\omega^-\rangle = \frac{1}{2}(|HV\rangle + |VH\rangle) \otimes (|\omega_1\omega_2\rangle - |\omega_2\omega_1\rangle). \quad (5)$$

In the characterization process, we first measure two-photon correlation in two mutually orthogonal polarization bases, yielding visibilities that imply lower bounds on the Bell-state fidelity and concurrence as $F_p \geq 0.979$ and $C_p \geq 0.958$ in the polarization degree of freedom. However, as a result of the difficulty of a mutually unbiased measurement in the frequency domain, the verification of entanglement in the discrete frequency subspace is more elaborate. While the nonlocal measurement of the frequency-entangled states is difficult without the assistance of a nonlinear optical process and a time-resolved measurement, we use spatial beating in HOM interference to quantify the frequency entanglement. By scanning the time of arrival of one of the photons incident on the HOM interferometer, the interference pattern manifests itself in sinusoidal oscillations of the interference fringes within a Gaussian envelope as a function of relative time delay [81]. This coincidence probability can be modeled as

$$p_c(\tau) = \frac{1}{2} - \frac{V_\omega}{2} cos(\mu\tau + \phi_\omega)\left(1 + |\frac{2\tau}{\tau_c}|\right) \quad for \quad |\tau| < \frac{\tau_c}{2}, \quad (6)$$

where V_ω is the interference visibility, τ is the relative arrival time delay of two photons at the beam splitter, τ_c is the single-photon coherence time that equals the base-to-base envelope width, and $\mu = |\omega_1 - \omega_2|$ is the detuning of two well-separated frequency bins. Thus, under the assumption that energy is exactly conserved in the SPDC process, the lower bounds on the Bell-state fidelity and concurrence are $F_p \geq 0.971$ and $C_p \geq 0.942$ in the frequency degree of freedom. These measured high fidelities in both the polarization and frequency subspace indicate the presence of hyperentanglement, which allows proof that high-dimensional entanglement has indeed been produced in our setup *via* hyperentanglement. Different from the general HOM dip, quantum interference of frequency entangled photons exhibits periodic oscillation within the coherence time envelope. This feature provides an alternative route toward ultra-precise HOM interferometry using superpositions of two well-separated and entangled discrete frequency modes and coincidence detection on the bi-photon beat note [17].

2.2 Generation of quantum entanglement by atomic four-wave mixing

In addition to the widely used SPDC process, atomic four-wave mixing is an alternative route toward the creation of entanglement with high efficiency and brightness [82]. Up to date, a large wide range of theoretical research works and experimental implementations have been explored, including

the generation and verification of biphotons entangled in polarization [83], orbital angular momentum [84], and time-frequency [85]. In this work, we focus on the energy-time entanglement of narrow-band biphotons that is used for quantum interferometric metrology. For example, the direct characterization of energy-time entanglement is produced from spontaneous four-wave mixing in cold atoms, where the Stokes and anti-Stokes two-photon temporal correlation is measured by using commercially available single-photon detectors with nanosecond temporal resolution, and their joint spectral intensity is characterized by using an optical cavity with a narrow linewidth of 72 KHz. As a direct result, the joint frequency-time uncertainty product of 0.063 ± 0.0044 is verified, which violates the separability criterion and satisfies the continuous variable Einstein–Podolsky–Rosen steering inequality [85]. Thus, the energy-time entanglement generated by using the atomic four-wave mixing can provide a significant advantage in enhancing the resolution, precision, and accuracy in quantum metrology.

Additionally, as a direct result of the ultranarrow bandwidth, the quantum entanglement generated by using the atomic four-wave mixing has the potential to be used in the storage of quantum qubits. For example, the entanglement of a 795 nm light polarization qubit and an atomic Rb spin-wave qubit for a storage time of 0.1 s is observed by measuring the violation of Bell's inequality [86, 87]. On the other hand, these narrowband photons can be used in the measurement of absorption spectroscopy of biological and chemical molecules, and the detection of trace molecular species [88, 89].

2.3 High-dimensional entanglement by adaptive modulation

In addition to two-dimensional entanglement, high-dimensional entanglement is currently one of the most prolific fields in quantum information processing and quantum metrology [42, 72–74, 90, 91]. For example, photon pairs entangled in high dimensions provide the advantages of improving noise resilience and speeding up certain tasks in photonic quantum computation [65, 92, 93]. Although several physical properties of photons can be used to directly encode high-dimensional entanglement, such as orbital angular momentum, time-energy and path, the exploitation of high-dimensional spatial coding has strict requirements on the quality of optical wave-fronts and shaping for generation and measurement. In this work, we focus on time-energy entanglement because it is intrinsically suitable for long-distance transmission in fiber and free space and quantum spectroscopy. As an essential prerequisite, the versatile manipulation and characterization of frequency entanglement, however, poses an ongoing challenge. In particular, the required number of measurements for the task of full quantum state tomography of high-dimensional entanglement in a large state space would increase exponentially versus the dimensions, which is one of the fundamental but important problems concerning entanglement. We use spatial beating of HOM interference with polarization-frequency hyperentangled photons to discretize continuous and broadband spectra into a series of narrow frequency bins [94]. Since the incident entangled photons is in the form of polarization-frequency hyperentanglement, the HOM interference transforms the state into

$$|\psi\rangle_{hyper} = \frac{1}{2}\left[(|H_3V_4\rangle + |V_3H_4\rangle) \otimes |\psi\rangle_{\omega}^{-} + |H_3V_3\rangle + |V_4H_4\rangle) \otimes |\psi\rangle_{\omega}^{+}\right], \quad (7)$$

where $|\psi\rangle_{\omega}^{-}$ ($|\psi\rangle_{\omega}^{+}$) represents the frequency-entangled state produced in opposite (identical) spatial modes. It is obvious that the bi-photon components $|\psi\rangle_{\omega}^{+}$ would diminish the visibility, which significantly limits its applicability in quantum interference. In order to tackle this issue, we eliminate the detrimental bunched photon events by exploiting the anti-correlation in the polarization state, i.e., using polarizers to filter a single non-vanishing term $|\psi\rangle_{\omega}^{-}$. Due to the normalized coincidence probability that expressed as

$$P(\tau) = \frac{1}{4}\iint d\omega_1 d\omega_2 f(\omega_1, \omega_2)|1 - e^{i(\omega_1-\omega_2)\tau}|^2, \quad (8)$$

where $f(\omega_1, \omega_2)$ is the Gaussian spectral amplitude function that fulfills the normalized condition, it indicates that the anti-bunched photons are entangled in the frequency domain as

$$|\psi\rangle = \sum_{j=1}^{m/2} A_j\left(\alpha_j|\omega_j\omega_{m-j}\rangle - e^{i\phi_j}\alpha_{m-j}|\omega_{m-j}\omega_j\rangle\right), \quad (9)$$

where m denotes the number of dimensions, A_j is a probability amplitude, ϕ_j is a phase-offset, $\alpha_j^2 = p_j$, $\alpha_j^2 + \alpha_{m-j}^2 = 1$, p_j is a balance parameter, and $\omega_j + \omega_{m-j} = \omega_p$ that satisfy the energy conservation. Moreover, we also show that the HOM interference can be used to characterize high-dimensional frequency entanglement, namely, the measurements of fringe spacing of the observed interference pattern allow us to extract specific parameters for quantifying the high-dimensional entanglement. Thus, the generation and characterization of two-, four-, and six-dimensional frequency entangled qubits are theoretically and experimentally investigated, allowing for the estimation of entanglement dimensionality in the whole state space. These results indicate that the spectral and temporal domains of biphoton wave functions can be linked by using HOM interference, which provides an alternative platform for the implementation of quantum interferometric spectroscopy.

The generation, manipulation, and detection of photons that are entangled in frequency, time, and polarization degrees of freedom provide powerful tools for a variety of practical

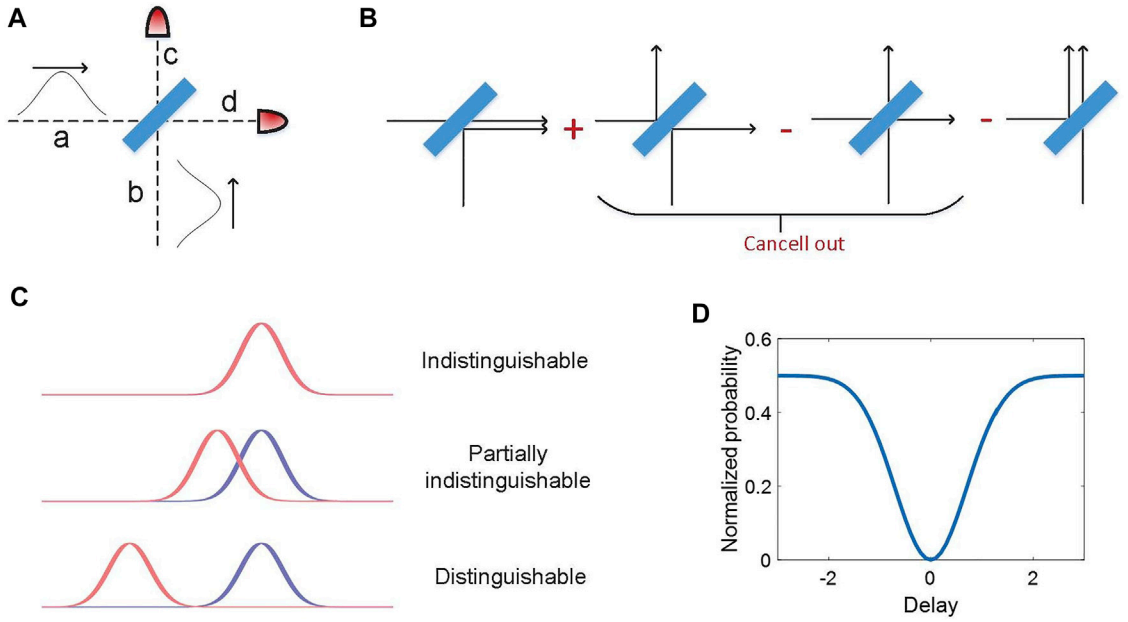

FIGURE 1
(A) Two photons interfere on a beam splitter. After the interaction on the beam splitter, the photons in opposite spatial modes are detected by single photon detectors. **(B)** Diagram showing four different cases for two photons to interact on a balanced beam splitter, wherein the relative phase is revealed by the signs. If these two photons are completely indistinguishable, the second and third terms can be cancelled out. **(C)** Taking temporal distinguishability into consideration, it is allowed to tune the level of distinguishability by changing the time delay between two photons with finite bandwidths. **(D)** The coincidence probability of HOM interference as a function of the relative time delay. Typically, the coincidence counts are identified by using two single-photon detectors at opposite spatial modes c and d, which can be normalized to fit Eq. 15.

applications. Next, we present several prototypical applications in quantum metrology by using these entangled states.

3 Hong–Ou–Mandel interferometry with ultrahigh timing resolution

Hong–Ou–Mandel interference was first experimentally verified by Chunk Ki Hong, Zhe Yu OU, and Leonard Mandel in 1987 [13]. It shows a quantum phenomenon that identical photons arriving simultaneously on different input ports of a beam splitter would bunch into a common output port as a direct result of bosonic nature. We consider a basic model of two-photon HOM interference, as shown in Figure 1A. The incident two-photon state can be expressed as

$$|\Psi_{in}\rangle_{ab} = \hat{a}^{\dagger}\hat{b}^{\dagger}|vac\rangle = |1\rangle_a|1\rangle_b, \tag{10}$$

where $\hat{a}^{\dagger}$ and $\hat{b}^{\dagger}$ are creation operators in mode a and b, $|vac\rangle$ denotes the vacuum state. Then these photons arrive at a beam splitter simultaneously. The evolution of a state on the beam splitter with reflectivity η can be modelled with a unitary operator $\hat{U}_{BS}$, which acts on the creation operators as follows

$$\begin{aligned} \hat{a}^{\dagger} &\rightarrow \sqrt{1-\eta}\hat{c}^{\dagger} + \sqrt{\eta}\hat{d}^{\dagger} \\ \hat{b}^{\dagger} &\rightarrow \sqrt{\eta}\hat{c}^{\dagger} - \sqrt{1-\eta}\hat{d}^{\dagger}. \end{aligned} \tag{11}$$

Thus, the combined two-photon state interferes on the beam splitter, and the corresponding output state is

$$\begin{aligned} |\Psi_{out}\rangle_{cd} = \hat{U}_{BS}|\Psi_{in}\rangle_{ab} &= \left(\sqrt{1-\eta}\,\hat{c}^{\dagger} + \sqrt{\eta}\,\hat{d}^{\dagger}\right)\left(\sqrt{\eta}\,\hat{c}^{\dagger} - \sqrt{1-\eta}\,\hat{d}^{\dagger}\right)|vac\rangle \\ &= \left(\sqrt{\eta(1-\eta)}\,\hat{c}^{\dagger}\hat{c}^{\dagger} + \eta\hat{c}^{\dagger}\hat{d}^{\dagger} - (1-\eta)\hat{d}^{\dagger}\hat{c}^{\dagger} - \sqrt{\eta(1-\eta)}\,\hat{d}^{\dagger}\hat{d}^{\dagger}\right)|vac\rangle. \end{aligned} \tag{12}$$

For a typically balanced beam splitter, $\eta = 1/2$, and the output state is transformed to

$$|\Psi_{out}\rangle_{cd} = \frac{1}{2}\left(\hat{c}^{\dagger}\hat{c}^{\dagger} + \hat{c}^{\dagger}\hat{d}^{\dagger} - \hat{d}^{\dagger}\hat{c}^{\dagger} - \hat{d}^{\dagger}\hat{d}^{\dagger}\right)|vac\rangle, \tag{13}$$

whose visualization is shown as Figure 1B. Since two photons are completely indistinguishable after the beam splitter, it indicates that the second and third terms in Eq. 13 can be cancelled out. Thus, Eq. 13 is simplified to

$$|\Psi_{out}\rangle_{cd} = \frac{1}{\sqrt{2}}\left(\hat{c}^{\dagger}\hat{c}^{\dagger} - \hat{d}^{\dagger}\hat{d}^{\dagger}\right)|vac\rangle. \tag{14}$$

In the experimental implementation of HOM interference, we choose to detect the coincidence probability between the opposite spatial modes, which corresponds to the events that entangled

photons bunched into different output ports of the beam splitter. Thus, quantum theory predicts that the coincidence probability of HOM interference would decrease to zeros when and only when the two incident photons are completely indistinguishable, i.e., the well-known HOM dip.

Next, let us consider the distinguishability in the temporal degree of freedom. Since the distribution of single photons in the temporal domain is within a wavepacket, its coherence time refers to the time over which the photon may be considered coherent, which means that its average phase is predictable. By controlling the imbalance between two paths of the HOM interferometer, a relative time of arrival of one of the photons incidents on the beam splitter can be introduced and parameterized by the time delay τ. This manipulation of the temporal delay between the entangled photons is able to tune their level of distinguishability, which corresponds to two indistinguishable photons, partially distinguishable photons and distinguishable photons, as shown in Figure 1C. As a direct result of the coherence time of single photons, the HOM interference probability manifests itself as a Gaussian envelope, as a function of the relative time delay τ, where its coincidence probability can be modelled in the form of

$$P(\tau) = \frac{1}{2}\left[1 - exp\left(-\sigma^2\tau^2\right)\right], \tag{15}$$

where σ is relevant to single photon coherence time that equals to the base-to-base envelope width, as shown in Figure 1D [62, 81, 95–97].

3.1 Robust Hong–Ou–Mandel interferometry for measuring optical delays

Since the single-photon coherence time is in the order of subpicosecond, HOM interferometry has been widely used in the characterization of single photon source [98–101], quantum metrology [14, 15, 32], and quantum information processing [96, 102–104]. For example, while the speed of light in a vacuum is constant, the phase and group velocities of light beams have been changed because they have finite transverse sizes [24]. In other words, the modification of the axial component of the wave vector arises from the transverse spatial confinement of the field. Generally speaking, the magnitude of the wave vector for the light with center wavelength of λ is $k_0 = 2\pi/\lambda$, which is related to its Cartesian components $\{k_x, k_y, k_z\}$ in the form of

$$k_x^2 + k_y^2 + k_z^2 = k_0^2. \tag{16}$$

It is obvious that the optical modes of finite transverse spatial extent have nonzero k_x and k_y, and the resultant $k_z < k_0$ leads to a corresponding modification of both the phase and group velocities of the light. Let us consider the Bessel beam with a description of a mode within a circular waveguide, which is a prototypical example of a structured beam. In free space, Bessel beams can be prepared by using an axicon that converts a plane wave into conical phase fronts, which is characterized by a single radial component of the wave vector as k_r. As a direct result, the axial component of the wave vector is obtained as $k_z = k_0 - k_r^2/2k_0$. This means the phase velocity and group velocity along z direction reads

$$\begin{aligned} v_\phi &= c\left(1 - \frac{k_r^2}{2k_0^2}\right)^{-1}, \\ v_{g,z} &= c\left(1 - \frac{k_r^2}{2k_0^2}\right). \end{aligned} \tag{17}$$

By changing the beam's transverse spatial structure, a relative delay in their arrival time is introduced. However, the reported superluminal speeds achieved with the various approaches in free space have been to data 1.00022c [105], 1.00012c [106], 1.00015c [107] and 1.111c in plasma [108]. Reports on measured subluminal speeds have been lacking and limited to delays to several micrometers over a propagation distance of ~ 1 meter. This indicates that the verification of the modification of the phase and group velocities has the requirement for precise metrology with ultrahigh resolution. With the assistance of a two-photon HOM interferometer, a reduction in the group velocity of photons in both a Bessel beam and photons in a focused Gaussian beam is measured, where the delay in the magnitude of micrometers is generated between time-correlated photon pairs as shown in Figures 2A–C. Since the superliminal and subluminal speeds are changed by a very small factor, it is not easy to measure the optical delay resulting from the changes in the speed of light. To tackle this issue, a sensor with ultrahigh resolution and precision is required, namely, HOM interferometry provides a good candidate for this measurement. As shown in Figure 2B, paired photons are created by using the SPDC process in the nonlinear BBO crystal, which are routed into a balanced beam splitter from different input ports. One photon is used as a reference temporal signal, and its paired photon is transferred to structured photons using a spatial light modulator. After the transmission for a certain distance that introduces a relative path delay as a direct result of superluminal and subluminal speed, this structured photon is transferred back to Gaussian mode that enables the coupling of single mode fiber. Thus, the observation of HOM interference dip reveals the time delay, as shown in Figure 2C. Therefore, the HOM interferometer is suitable for the application in measuring optical delays between different paths even when the relative time delay reaches the magnitude of attosecond [16].

In the context of quantum metrology, the simultaneous measurement of both the spatial and temporal degrees of freedom has long been hailed as an absolute necessity in quantum imaging. Since the quantum interference pattern is determined by photons' level of distinguishability in all degrees of freedom, both the spatial and temporal properties can make contributions to the final measurement results. Inversely, it is

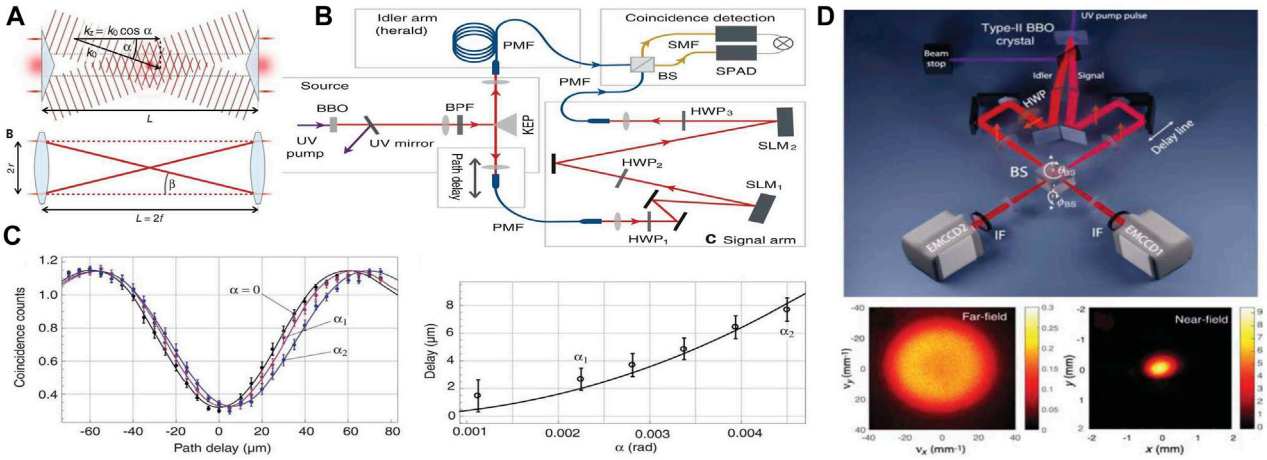

FIGURE 2
(A) Bessel beam can be created with an axicon, producing conical phase fronts of angle α. A ray entering a confocal telescope at radius r will travel an additional distance proportional to $\cos^{-1}\beta$. **(B)** Experimental setup for measuring the time delay arising from spatially structure of photons by using a ultra-precise HOM interferometry. **(C)** Experimental observation of the time delay for a Bessel beam. From ref. [24]. Reprinted with permission from AAAS.**(D)** Experimental setup for imaging spatiotemporal biphoton states with a HOM interferometer. Reprinted with permission from [109]. Copyright (2021) American Chemical Society.

allowed to extract the corresponding information from quantum interference results, which inspires various applications including but not limited to quantum imaging and sensing. In particular, with the combination of spatially-resolved detection implemented by single-photon cameras, quantum interference is a powerful tool for simultaneously measuring spatial and temporal information. For example, by detecting coincidence events with intensified scientific complementary metal-oxide-semiconductor cameras [109], spatiotemporal HOM interference of biphoton states is also experimentally observed, as shown in Figure 2D. Analogously, HOM interference in both spatial and temporal degrees of freedom enable us to implement a variety of applications in the field of quantum imaging, such as full-field quantum state tomography [110]. While this work focuses on the spectral and temporal domain in quantum interference, the overall scheme could also be extended to other degrees of freedom, such as orbital angular momentum, where the precise measurement of quantum information still poses a significant challenge.

In addition, the interference pattern of HOM interferometry is determined by the relative phase between two photons but is irrelevant to the global phase of single photons. Consequently, HOM interferometry can be used in applications with the requirements of dispersion cancellation, robustness against noise, and photon loss [31, 111]. For example, highly entangled states and N00N states are notoriously vulnerable to losses, which leads to the difficulty in sharing them between remote locations and recombining them for exploiting interference effects. In order to tackle this challenge, the reversed HOM interference effect is used to prepare a high-fidelity two-photon N00N state shared between two parties connected by a lossy optical medium [32]. Additionally, detector side channel attack is a notoriously hard problem in quantum key distribution. By using HOM interference between two photons coming from users, measurement device–independent quantum cryptography has been experimentally implemented. While this work focuses on the HOM interference of entangled photons created by using the SPDC process, the visibility of HOM interference is determined by the photons' indistinguishability. In other words, if and only if the two-photon incident on a balanced beam splitter is indistinguishable in all degrees of freedom, quantum interference can be observed. The Bell state measurement based on quantum interference can passively reveal the information of the incident entanglement between the quantum state from users. Although the measurement device knows the public Bell state measurement results, it has no knowledge about the transmitted information such that the measurement device–independent quantum key distribution can be implemented. Backed by this technology, a long-distance quantum key distribution over, say, 400 km still has the potential to remain secure even with seriously flawed detectors [112–115].

3.2 Hong–Ou–Mandel interferometry on a biphoton beat note

In the context of applications in HOM interferometry for measuring the optical delays between different paths, the

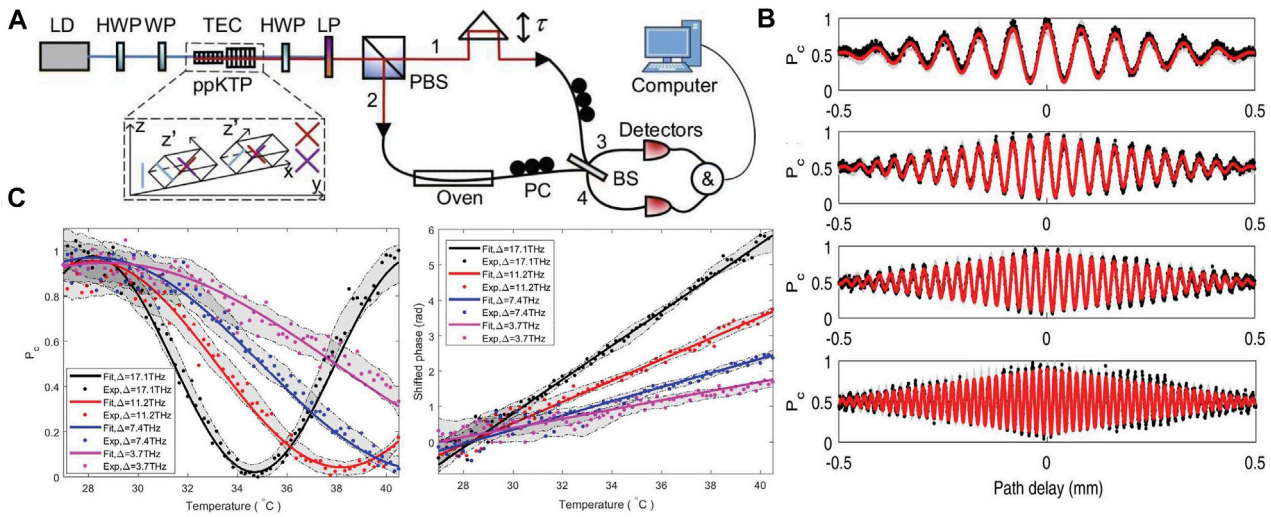

FIGURE 3
(A) Experimental setup for temperature sensor through the beating of frequency entanglement. **(B)** Two-photon HOM interference of frequency entanglement with various different frequency detunings such as 3.65 THz (7.98 nm) at a temperature of 30˚C, 7.35 THz (16.08 nm) at a temperature of 50˚C, 11.18 THz (24.45 nm) at a temperature of 70˚C, and 17.08 THz (37.35 nm) at a temperature of 100˚C. **(C)** Experimental demonstration of thermal characteristics of jacket optical fiber by using frequency-entangled photons with various different frequencies. P_c is the normalized probability of HOM interference as expressed in Eq. 6 [17].

engineered attosecond resolution HOM interferometry by using statistical estimation theory has been experimentally implemented [16]. The ultimate limit on the precision of measurement by using quantum interference of two identical photons can be calculated as the quantum Cramér-Rao bound, which is tied to a particular quantum probe state and has the statement as

$$\delta\tau = \frac{1}{N^{1/2}}\frac{1}{2\sigma}, \tag{18}$$

where N denotes the number of independent experimental trials [16, 116, 117]. Furthermore, backed by a measurement and estimation strategy based on Fisher information analysis, the precision of HOM interferometry achieves few-attosecond scale resolutions in a dual-arm geometry. It has also been proved that the HOM measurement can recover the quantum Cramér-Rao bound, which confirms that this measurement strategy is optimal [116, 118]. However, it is obvious that the quantum Cramér-Rao bound of HOM interferometry is significantly limited by single photon coherence time. Thus, it has been a broad consensus that great precision in the measurement requires that photons are prepared with a large bandwidth; in particular, ultra-broadband photon sources have long been hailed as a vital prerequisite for ultra-precise HOM interferometry. For example, the precision of this scheme can be increased by using shorter nonlinear crystals in the SPDC process.

We embark on an alternative scheme for ultra-precise HOM interferometry by using two well-separated frequencies embedded in a quantum entanglement [17], namely, discrete color entanglement that can be written as

$$|\Psi\rangle = \frac{1}{\sqrt{2}}\int d\Omega f(\Omega)\left[e^{i(\Delta+2\Omega)\tau}a_1^\dagger(\omega_1^0+\Omega)a_2^\dagger(\omega_2^0-\Omega)\right.$$
$$\left.-a_1^\dagger(\omega_2^0+\Omega)a_2^\dagger(\omega_1^0-\Omega)\right]|vac\rangle \tag{19}$$

where ω_1^0 and ω_2^0 are central frequencies of down-converted photons, $\Delta = \omega_1^0 - \omega_2^0$ is the difference frequency of two well-separated frequency bins, $f(\Omega)$ represents the joint spectral intensity that fulfils the normalization condition as $\int d\Omega|f(\Omega)|^2 = 1$, and $|vac\rangle$ is the vacuum state as shown in Figure 3A. Therefore, the quantum Cramér-Rao bound for this state on the estimation of time delays in HOM interferometry is written as

$$\delta\tau_\omega = \frac{1}{N^{1/2}}\frac{1}{\left(\Delta^2+4\sigma^2\right)^{1/2}}, \tag{20}$$

where $\sigma = \sqrt{\langle\Omega^2\rangle - \langle\Omega\rangle^2}$ is the RMS (root mean square) bandwidth of down-converted photons, which is also relevant to their coherence lengths, as shown in Figure 3B. In order to demonstrate the viability principle of employing our HOM sensor, we performed a proof of concept experiment in which we estimate the time delay due to linear expansion of a jacket optical fiber. The created photon pairs are separated by using polarization correlation and arrive simultaneously on different input ports of a balanced beam splitter. Analogously, the photon in spatial mode 1 is used as a reference temporal signal, and its partner photon is also coupled into a single-mode fiber that is

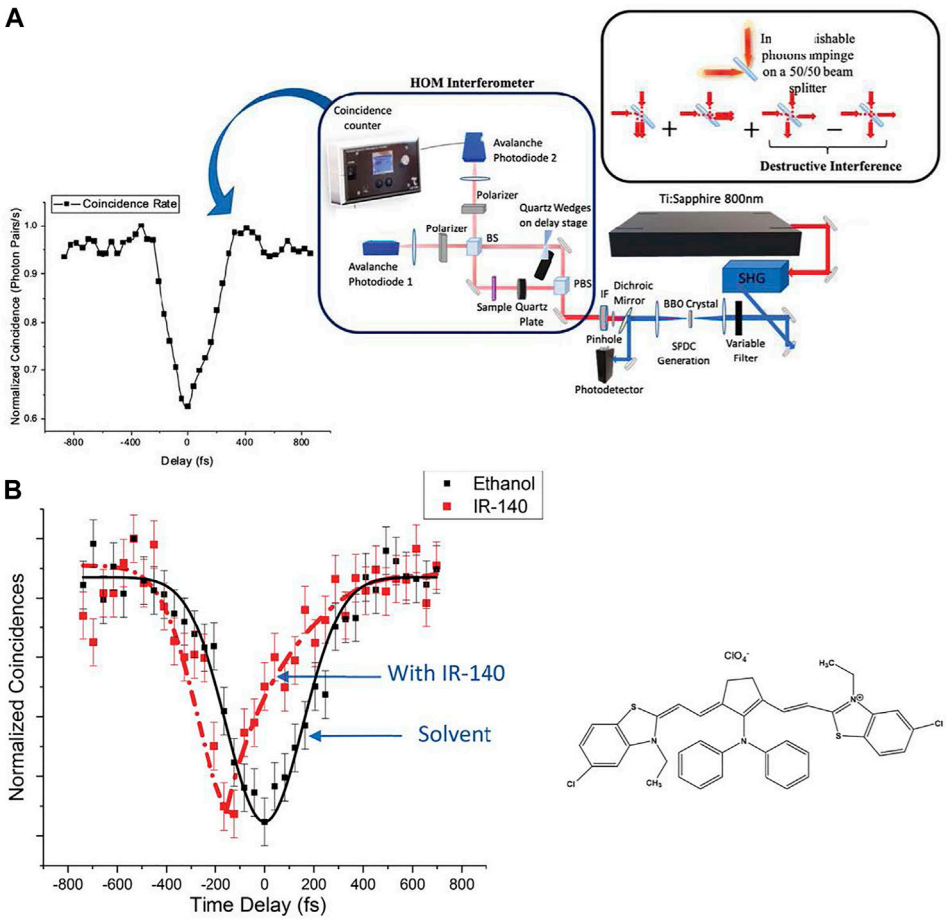

FIGURE 4
(A) Experimental setup for measuring the dephasing time of photons arising from its interaction with a molecular sample by using a HOM interferometer. **(B)** The presence of a simple refractive or birefringent material in the interferometer pathway can lead to polarization mode dispersion which degrades entanglement and causes temporal delays in the order of 100 fs. As a direct result, the normalized coincidence probability as a function of the scanning time is shifted by a time delay that corresponds to the dephasing time [25].

heated by a temperature controllable oven. Build on the properties of silica fibers, the optical path would be related to the temperature. Two polarization controllers are used to compensate for polarization distinguishability. As shown in Figure 3C, the normalized probability of HOM interference and shifted phase can be expressed as a function of temperature. Moreover, according to the classical estimation theory, we also prove that the measurement strategy based on HOM interferometer can also recover the quantum Cramér-Rao bound in the case of zero loss and perfect visibility. By evaluating the Fisher information for the interference probabilities, we can determine the optimal working points and also demonstrate the experimental feasibility of this approach by detecting thermally-induced delays in an optical fiber, as shown in Figure 3C. These results prove that the use of frequency entanglement in HOM interferometry for quantum sensing can avoid some stringent conditions, such as the requirement for large bandwidth entanglement sources. Backed by these theoretical predictions and experimental verifications, both a wider single-photon frequency bandwidth and a larger difference frequency of color-entangled states can increase its achievable resolution and sensitivity.

3.3 Hong–Ou–Mandel interferometry for applications in biology and chemistry

In addition, since the quantum light with extremely low energy is suitable for interacting with those photon-sensitive samples, the HOM interferometry based on entangled photons can also provide a useful tool to study molecular properties such as dephasing time. Unlike other interferometric approaches based on first-order interference and simple measurement of intensity, HOM interference is not affected by variation in the

relative optical phase and is strongly robust against experimental noise and channel loss. For example, a dephasing time of the organic molecular of as low as 102 fs upon coherent excitation and quantum interference with a path of entangled photons in the interferometer is extracted by using HOM interferometry as shown in Figure 4 [25]. Without inserting any molecular sample in the optical path, a well-known HOM interference pattern that agrees well with the theoretical prediction can be observed. By inserting a molecular sample IR-140 dye in the optical path, it is obvious that the observed HOM dip overall becomes narrower and gains an asymmetry on the right side, as shown in Figure 4B. Moreover, the center of the HOM dip with the sample is shifted to the left compared to the dip with the solvent. These measurement results allow extracting the information pertaining to the linear susceptibility and absorption of the studied sample. Additionally, HOM interference can be used to characterize the coherence properties of single photon source and the distinguishability of emitted single photons, which would pave the way toward quantum applications. Thereinto, single photons emitted by a single molecule are prepared for quantum networks. For example, single organic molecules that are optimized by an atomic Faraday filter are experimentally presented to create single photons whose properties have been verified by performing a number of nonclassical HOM interference measurements [119]. Thus, quantum interference has been proved to be an essential approach in the fields of biology and chemistry.

4 Entanglement-assisted quantum spectroscopy

Absorption spectroscopy has long been hailed as an essential prerequisite for characterizing the optical properties of materials, chemicals and biological samples [10, 28, 120, 121]. Typically, a sample's absorption spectroscopy is obtained by comparing the spectrum and intensity of the incident light and those of the transmitted light after the interaction with the target sample. While absorption spectroscopy is generally implemented by using classical light, quantum light provides an alternative route toward quantum spectroscopy with high precision and robustness against deleterious noise.

4.1 Absorption spectroscopy using quantum light

While conventional laser absorption spectroscopy is significantly limited by shot-noise due to the fundamental Poisson-distribution of photon number in laser radiation [122, 123], quantum light provides an alternative route toward precise absorption spectroscopy. In addition, quantum spectroscopy with the assistance of coincidence detection can further enhance the measurement resolution as a direct result of a high signal-to-noise ratio. We consider a general case where paired photons are prepared by using the SPDC process. The down-converted photons are separated into opposite spatial modes, referring to signal and idler photons. After the interaction between one of the paired photons with the target sample, a single-photon monochromator is used to filter the photons at a specific frequency bin. The measured number of coincidence events corresponds to the intensity of absorption at this frequency. By scanning the monochromator, the whole absorption spectrum can be achieved. In this process, the single photon count is $S_{s,i} = \eta_{s,i}P$, where P is the number of photon pairs generated by the entanglement source, $\eta_{s,i}$ represents the quantum efficiency of the detectors at signal and idler channel, respectively. Thus, the expected number of two-fold coincidence is proportional to the probability of joint detection in the opposite spatial modes as

$$R(\omega_s) = \eta_s\eta_i P. \tag{21}$$

The accidental coincidence counts arises from the overlap of uncorrelated photon counts within the coincidence window Δt, which can be calculated by

$$R_N = N_sN_i\Delta t + S_sN_i\Delta t + N_sS_i\Delta t, \tag{22}$$

where N_s and N_i are the number of noise photon counts in the signal and idler channel. In conventional transmission spectroscopy, the transmission spectrum is obtained directly from single photon counts, and its signal-to-noise ratio for the transmission spectroscopy is given by $SNR_T = \eta_sP/N_s$. For the quantum spectroscopy based on coincidence detection, the signal-to-noise ratio is given by $SNR_Q = R(\omega_s)/R_N = \eta_s\eta_iP/N_sN_i\Delta t$, where it is assumed that $N_sN_i \gg S_sN_i$ or N_sS_i. The contrast of these two signal-to-noise ratios is written as $SNR_Q/SNR_T = \eta_i/N_i\Delta t$, which indicates that quantum spectroscopy can provide provable advantages by using high-efficient, low-noise single-photon detectors, and the narrow coincidence window. This scheme has been used to measure the spectroscopic propertied of the YAG: Er^{3+} crystals [124] and plasmonic nanostructures [27], which proves the advantages of quantum spectroscopy based on coincidence detection in experiments as shown in Figure 5A. Since the entangled photons typically contain many frequencies, namely, a large bandwidth, a grating and spatial filter are used as a tunable monochromator to select out a specific frequency, which can enhance the spectral resolution. Thus, the dynamic range is limited by the frequency shape and bandwidth of entangled photons. As an alternative method, frequency-correlated and tunable entanglement sources are presented to perform quantum absorption spectroscopy with precision beyond the shot-noise limit and near the ultimate quantum limit, as shown in [26]. The use of type-II PPKTP crystal enables the generation of frequency-entangled photons with a narrow bandwidth, where the central frequency can be controlled

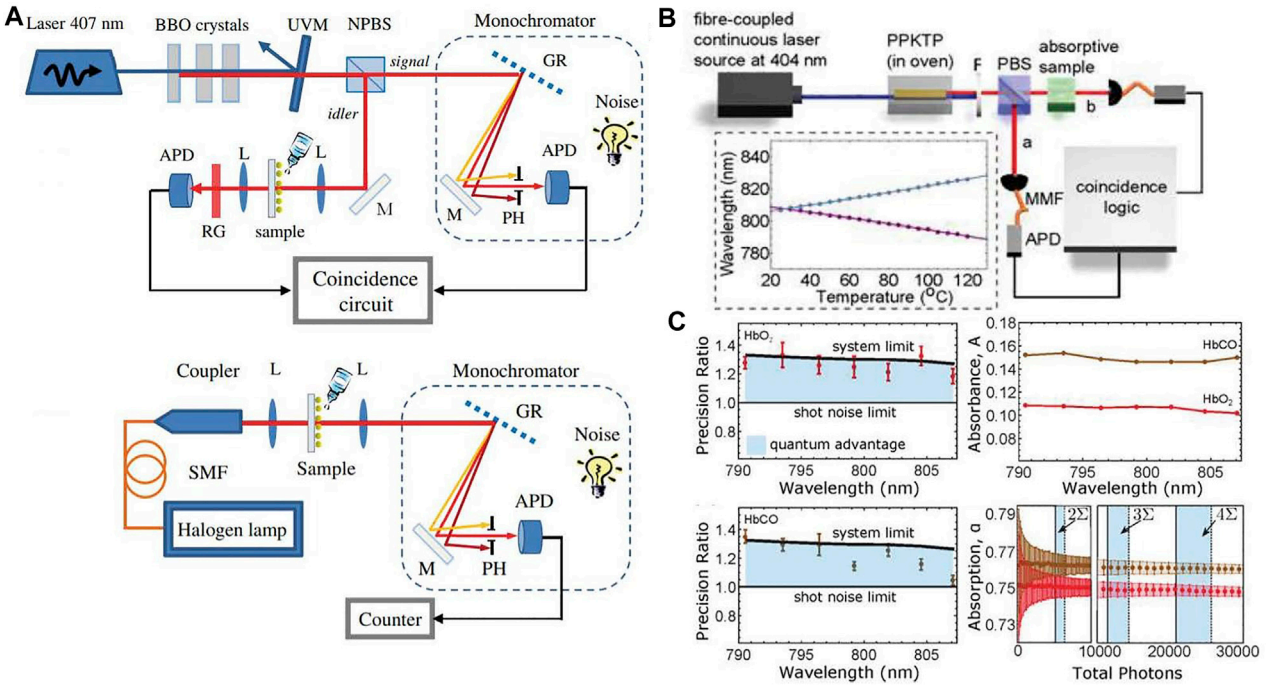

FIGURE 5
(A) Quantum spectroscopy setup based on coincidence detection of entangled photons and single photon monochromator for selecting out a specific frequency, and the conventional transmission spectroscopy by using classical light [27]. **(B)** Experimental setup for sub-shot-noise spectroscopy by using tunable frequency-entangled photons. **(C)** Sub-shot-noise absorbance spectra ofHbO2 and HbCO [26].

by tuning the phase to match the temperature of the PPKTP crystal. Thus, by scanning the phase matching temperature, the absorption spectroscopy of the studied sample is achieved without any requirement of frequency filters. These theoretical and experimental investigations show that single photons are the optimal probes for absorption spectroscopy, and quantum-enhanced spectroscopy can achieve great performance that is beyond classical physics.

4.2 Entanglement-assisted absorption spectroscopy

However, the excess noise and thermal loss channel can make changes in the transmission ratio, the conventional method is susceptible to experimental imperfection, which limits its precision and resolution. In addition, since the resolution is determined by the bandwidth of down-converted photons, it has been a broad consensus that single photons with narrow frequency bandwidth enable us to obtain a higher spectral resolution. In contrast, generating spectrally narrow photons would reduce the brightness of the entanglement source, which inversely imposes an ultimate limit on the precision. In order to tackle this issue, entanglement-assisted absorption spectroscopy is presented [34]. It uses a source of multichromatic frequency-entangled photon pairs prepared by the SPDC process as the probe, and the photon detection after optical parametric amplification is used at the receiver side. Consequently, a maximum likelihood estimation strategy on the statistical analysis is sufficient for extracting the spectral distribution. This scheme has been theoretically proved that it can achieve an error probability orders of magnitude lower even than the optimal classical systems. In particular, it is also robust against noise and loss as a direct result of the optical parametric amplifier on entangled photons. Nevertheless, the complexity and efficiency in the experimental implementation of optical parametric amplifiers still face significant technological challenges.

Then, we present a robust and efficient entanglement-based absorption spectroscopy by using one of the entangled photons to interact with the target absorptive sample and exploiting the HOM interference at the detection side as shown in Figure 6 [125]. In our experiment, we use a pair of type-0 PPKTP crystals that are pumped with a ultra-narrow pump, broadband frequency entanglement arises quite naturally following the energy conservation. In order to tackle the issue of separating indistinguishable photons to distinct spatial modes, the two nonlinear crystals are placed in horizontal and vertical direction such that the emission $|H\rangle \rightarrow |HH\rangle$ in the first crystal and $|V\rangle \rightarrow |VV\rangle$ in the second crystal are generated

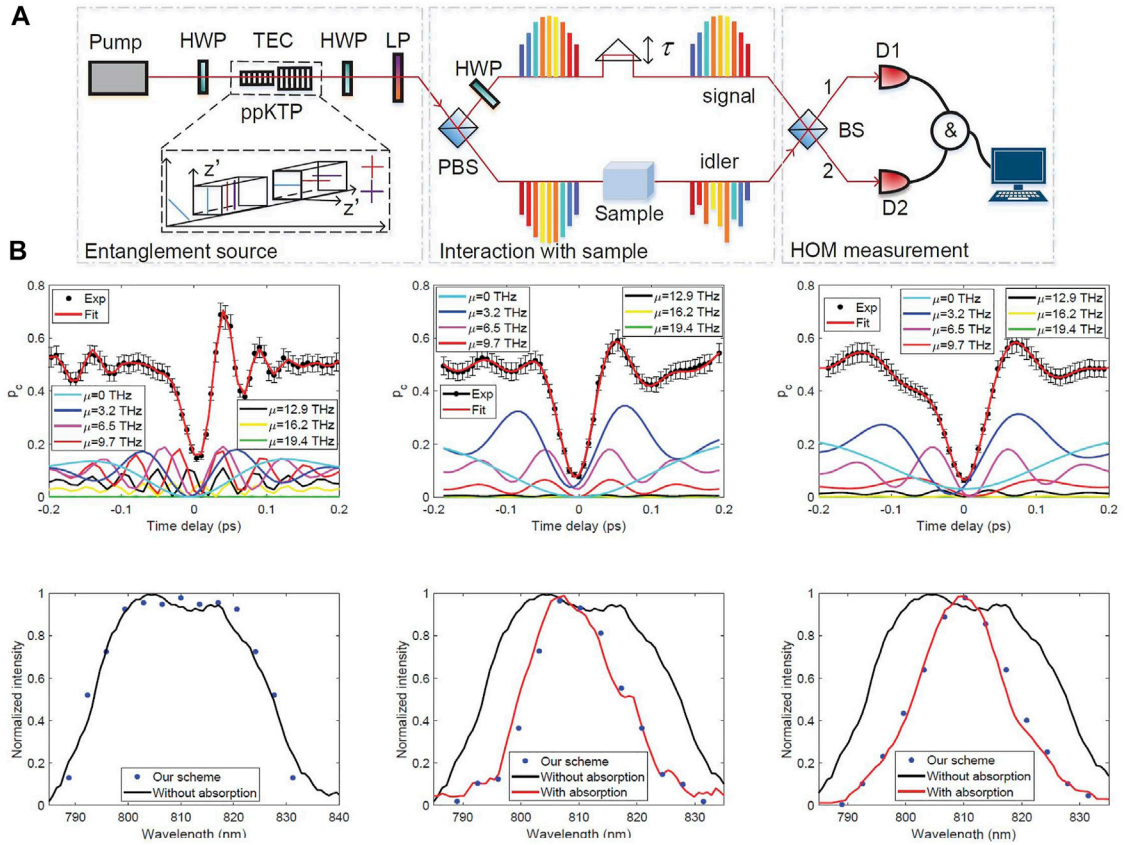

FIGURE 6
(A) Experimental setup for entanglement-assisted absorption spectroscopy by using HOM interference. **(B)** The experimental reconstruction of the spectra of two optical microcavities at resonance wavelengths of 806 and 810 nm. The colorful lines represent the interference patterns of sub-entanglement with various frequency detunings. Since the whole spectra are sampled by averaging them within each of m = 13 frequency bins, and they satisfy the strict energy conservation as a direct result of the exploitation of the pump with ultranarrow frequency linewidth, the resultant 7 pairs of subentanglement with frequency detunings μ = 0 THz, μ = 3.2*THz*, μ = 6.5 THz, μ = 9.7 THz, μ = 12.9 THz, μ = 16.2 THz and μ = 19.4 THz. Reprinted with permission from ref. [125]. Copyright (2022) by the American Physical Society.

with equal probability. Then, a half wave plate and a polarizing beam splitter are used to route paired photons into two input ports of a HOM interferometer. The nonclassical interference of frequency entanglement is observed by scanning the relative arriving time of paired photons. As shown in Eq. 6, the oscillation period in the interference pattern is determined by the frequency detuning. It is allowed to extract the spectral distribution from the HOM interference results by directly using nonlinear curve fitting. For an instructive means of understanding, this approach can be considered as a quantum version of spectral analysis, which decomposes the complex periodic vibration into a series of simple harmonic motions. Accordingly, the absorption spectra can be obtained from this spectral decomposition. As shown in Figure 6B, the observed HOM interference exhibits asymmetric patterns, which is relevant to the specific spectral distribution. By comparing the spectrum before and after inserting the studied samples (the black and red curves), it is able to extract the corresponding information about the absorptive spectroscopy. This entanglement-based absorption spectroscopy with the assistance of HOM interference has the potential to provide advantages in the robustness against detrimental noise and the measurement precision and accuracy.

Beyond its application appeal, our approach indicates a fundamental link between spectral and temporal degrees of freedom of biphoton wavefunction [94]. As the normalized coincidence probability of HOM interference is expressed as Eq. 8, which equals to

$$P(\tau) = \frac{1}{2}\left[1 + \iint d\omega_s d\omega_i |f(\omega_s, \omega_i)|^2 exp(i\Delta\tau)\right], \quad (23)$$

and it corresponds to the second-order correlation function in the form of

$$G(\tau) = 1 - 2P(\tau) = \iint d\omega_s d\omega_i |f(\omega_s, \omega_i)|^2 exp(i\Delta\tau)\Big], \quad (24)$$

which can be considered as a two-photon temporal signal. The difference-frequency spectrum intensity of biphoton state can be defined as

$$F(\Delta) = \frac{1}{2}\int d\tau G(\tau) exp(i\Delta\tau). \tag{25}$$

It is obvious that the second-order temporal correlation and the difference-frequency spectrum intensity can be connected by performing a Fourier transform. As a direct result, this approach has a variety of potential applications, such as quantum interferometric spectroscopy [29, 30, 128] and spectral-domain quantum coherence tomography [97, 129].

4.3 Two-photon absorption by using entangled photons

Additionally, quantum interference with entangled photons also provides a powerful tool toward two-photon absorption spectroscopy, which has been widely used in many disciplines, including but not limited to photoluminescene polymer and light-harvesting photosynthetic complexes [130, 131]. While laser light is typically used in absorption spectroscopy, quantum light provides new and exciting avenues in this regime [34, 132–134]. Remarkably, as a prototypical example of quantum light that lacks any counterpart in classical physics, the exploitation of entangled photon pairs in two-photon absorption enables the observation of many fascinating phenomena, such as linear dependence of two-photon absorption rate on the photon flux [135, 136], inducing disallowed atomic transitions [137], manipulation of quantum pathways of matter [138, 139], and control in molecular processes [140]. However, the experimental implementation of entangled two-photon absorption spectroscopy has two major technical challenges. First, it has the requirement for performing multiple experiments with two-photon states bearing different temporal correlations. Second, it has the requirement for prior knowledge of the absorbing medium's lowest-lying intermediate energy level. In order to tackle this issue, a tunable frequency entanglement source and a HOM interferometer with controllable delay are used to detect the two-photon absorption signal [126]. The central frequencies of down-converted photons prepared by the SPDC process can be tuned by changing the temperature for phase matching in the nonlinear crystal. As discussed in Section 2, the frequency entanglement used in this two-photon absorption spectroscopy is in the form of Eq. 5. One advantage of the exploitation of type-II PPKTP crystal in the process of entanglement generation is that the central frequencies of down-converted photons can be controlled by tuning the phase match temperature. Thus, the nondegeneracy of the signal and idler photons wavelengths is parameterized by the temperature as

$$\mu(T) = \omega_i^0(T) - \omega_i^s(T), \tag{26}$$

where $\omega_{s,i}^0(T)$ represents the temperature-dependent central frequencies of the photon wave packet. The controllable delay between paired photons carries all information about the electronic level structure of the absorbing medium, which can be revealed by a single Fourier transformation. As a result, the two-photon absorption signal can be expressed as

$$P_{g\to f}(\tau, T) = \frac{|\delta\left(\frac{\Delta_+}{2\pi}\right)|^2}{4\pi\hbar^2\varepsilon_0^2c^2A^2}\frac{\omega_i^0(T)\omega_i^s(T)}{T_e}\Big|\sum_{j=1} D^{(j)}\left\{\frac{1-e^{-i\left[\varepsilon_j-\omega_i^0(T)\right](2T_e-\tau)}}{\varepsilon_j-\omega_i^0(T)} + \frac{1-e^{-i\left[\varepsilon_j-\omega_s^0(T)\right](2T_e-\tau)}}{\varepsilon_j-\omega_s^0(T)}\right\}\Big|^2. \tag{27}$$

This result indicates that the absorption properties of the sample can be tuned by appropriately controlling the time and frequency properties of the entangled photon pairs, as shown in Figure 7A. Up to date, the linear dependence of entangled two-photon absorption rate as a function of photon-pair rate has been experimentally proved, which enables the estimation for the concentration-dependent entangled two-photon absorption cross section for Rhodamine 6G [127, 136]. The signature of energy-time entanglement and polarization dependence in the fluorescence rate has also been investigated, which demonstrates a strong dependence of the signal on the interphoton delay that reflects the coherence time of the entangled biphoton wave packet, as shown in.

5 Discussion

We have reviewed the non-classical phenomena as quantum interference of entangled photons, which has enabled a wide range of fundamental tests of quantum physics and pioneering applications such as quantum metrology. A number of important applications have been highlighted, such as HOM-based sensors for enhanced timing resolution and robust entanglement-assisted absorption spectroscopy. The scope of this review is limited to energy-time entanglement, which can be readily prepared by the SPDC process in a nonlinear crystal. Thus, the hyperentanglement in temporal and spectral degrees of freedom arises quite naturally as a direct result of energy conservation. Since the quantum interference pattern is determined by the level of photons' distinguishability, the temporal and spectroscopic information can be extracted from interference patterns by using maximum likelihood estimation or Fourier transform. Additionally, the correlation of entangled photons has great potential to be used in studying the structure of complex molecular systems. By tuning the different frequencies and relative time delay between paired photons, both the spectral and temporal properties of two-photon absorption in a molecular sample are investigated. Therefore, quantum interferometric metrology with entangled photons provides a powerful tool to extract the temporal and spectroscopic information about the dynamics and structures of complex systems, ranging from spatially structured photons, optical materials, and biological and chemical samples, which is particularly relevant to those photon-sensitive samples.

Armed with quantum interferometric metrology based on entangled photons, these new techniques would inspire the

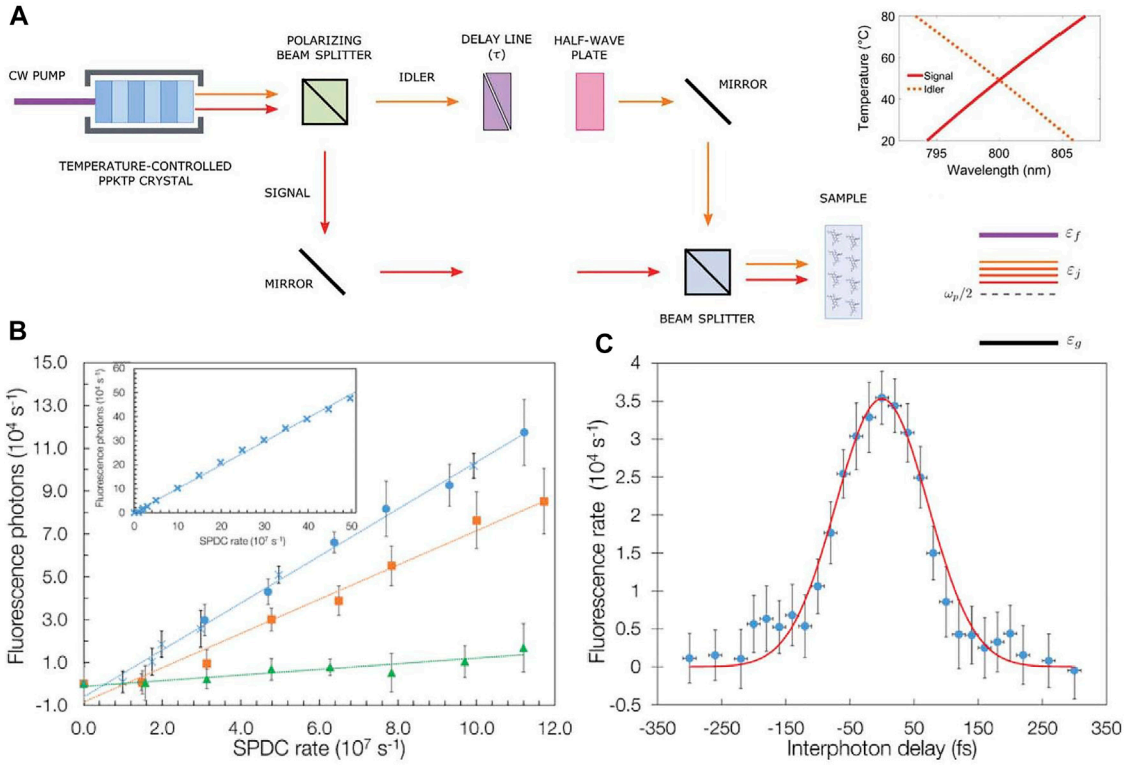

FIGURE 7
(A) Experimental illustration of temperature-controlled quantum nonlinear spectroscopy. Reprinted with permission from ref. [126]. Copyright (2022) by the American Physical Society. **(B)** Experimental measured fluorescence rate of entangled two-photon absorption as a function of the SPDC photon-pair flux for different Rh6G concentrations in ethanol: 110 mmol/L (blue circles); 4.5 mmol/L (orange squares), and 38 μ mol/l (green triangles). **(C)** Temporal dependence of fluorescence rate of entangled two-photon absorption for a 110 mmol/L Rh6G ethanol solution and an SPDC flux of 4.2×10^7 pairs/s, as a function of the inter-photon delay. Reprinted with permission from ref. [127]. Copyright (2022) by the American Physical Society.

development of quantum information processing and quantum metrology to reach a higher level. We also expect the techniques reviewed in this work can be applicable for more scenarios in future quantum applications and make near-term experimental demonstration possible.

Author contributions

YC and L H wrote the manuscript under the supervision of LC. All authors contributed to the final version of the manuscript.

Funding

This work is supported by the National Natural Science Foundation of China (NSFC) (12034016, 12004318, and 61975169), the Fundamental Research Funds for the Central Universities at Xiamen University (20720190057 and 20720210096), the Natural Science Foundation of Fujian Province of China (2020J05004), the Natural Science Foundation of Fujian Province of China for Distinguished Young Scientists (2015J06002), and the program for New Century Excellent Talents in University of China (NCET-13-0495).

Conflict of interest

The authors declare that the research was conducted in the absence of any commercial or financial relationships that could be construed as a potential conflict of interest.

The handling editor RL-M declared a shared affiliation with the authors YC and LC at the time of review.

Publisher's note

All claims expressed in this article are solely those of the authors and do not necessarily represent those of their affiliated

organizations, or those of the publisher, the editors, and the reviewers. Any product that may be evaluated in this article, or claim that may be made by its manufacturer, is not guaranteed or endorsed by the publisher.

References

1. Horodecki R, Horodecki P, Horodecki M, Horodecki K. Quantum entanglement. *Rev Mod Phys* (2009) 81:865–942. doi:10.1103/RevModPhys.81.865

2. Raimond JM, Brune M, Haroche S. Manipulating quantum entanglement with atoms and photons in a cavity. *Rev Mod Phys* (2001) 73:565–82. doi:10.1103/RevModPhys.73.565

3. Giustina M, Mech A, Ramelow S, Wittmann B, Kofler J, Beyer J, et al. Bell violation using entangled photons without the fair-sampling assumption. *Nature* (2013) 497:227–30. doi:10.1038/nature12012

4. Rauch D, Handsteiner J, Hochrainer A, Gallicchio J, Friedman AS, Leung C, et al. Cosmic bell test using random measurement settings from high-redshift quasars. *Phys Rev Lett* (2018) 121:080403. doi:10.1103/PhysRevLett.121.080403

5. Chen L, Ma T, Qiu X, Zhang D, Zhang W, Boyd RW. Realization of the einstein-podolsky-rosen paradox using radial position and radial momentum variables. *Phys Rev Lett* (2019) 123:060403. doi:10.1103/PhysRevLett.123.060403

6. Pan JW, Chen ZB, Lu CY, Weinfurter H, Zeilinger A, Żukowski M. Multiphoton entanglement and interferometry. *Rev Mod Phys* (2012) 84:777–838. doi:10.1103/RevModPhys.84.777

7. Bennett CH, DiVincenzo DP. Quantum information and computation. *nature* (2000) 404:247–55. doi:10.1038/35005001

8. Giovannetti V, Lloyd S, Maccone L. Quantum metrology. *Phys Rev Lett* (2006) 96:010401. doi:10.1103/PhysRevLett.96.010401

9. Giovannetti V, Lloyd S, Maccone L. Advances in quantum metrology. *Nat Photon* (2011) 5:222–9. doi:10.1038/nphoton.2011.35

10. Taylor MA, Bowen WP. Quantum metrology and its application in biology. *Phys Rep* (2016) 615:1–59. doi:10.1016/j.physrep.2015.12.002

11. Joo J, Munro WJ, Spiller TP. Quantum metrology with entangled coherent states. *Phys Rev Lett* (2011) 107:083601. doi:10.1103/PhysRevLett.107.083601

12. Riedel MF, Böhi P, Li Y, Hänsch TW, Sinatra A, Treutlein P. Atom-chip-based generation of entanglement for quantum metrology. *Nature* (2010) 464:1170–3. doi:10.1038/nature08988

13. Hong CK, Ou ZY, Mandel L. Measurement of subpicosecond time intervals between two photons by interference. *Phys Rev Lett* (1987) 59:2044–6. doi:10.1103/PhysRevLett.59.2044

14. Su ZE, Li Y, Rohde PP, Huang HL, Wang XL, Li L, et al. Multiphoton interference in quantum fourier transform circuits and applications to quantum metrology. *Phys Rev Lett* (2017) 119:080502. doi:10.1103/PhysRevLett.119.080502

15. Georgi P, Massaro M, Luo KH, Sain B, Montaut N, Herrmann H, et al. Metasurface interferometry toward quantum sensors. *Light Sci Appl* (2019) 8:70–7. doi:10.1038/s41377-019-0182-6

16. Lyons A, Knee GC, Bolduc E, Roger T, Leach J, Gauger EM, et al. Attosecond-resolution hong-ou-mandel interferometry. *Sci Adv* (2018) 4:eaap9416. doi:10.1126/sciadv.aap9416

17. Chen Y, Fink M, Steinlechner F, Torres JP, Ursin R. Hong-ou-mandel interferometry on a biphoton beat note. *Npj Quan Inf* (2019) 5:43–6. doi:10.1038/s41534-019-0161-z

18. Ramsey NF. The method of successive oscillatory fields. *Phys Today* (1998) 21:25–30. doi:10.1063/1.2914161

19. Bragg WH, Bragg WL. "The reflection of x-rays by crystals," Proceedings of the Royal Society of London. Series A, Containing Papers of a Mathe-matical and Physical Character. The Royal Society London (1913) 88:428–38. doi:10.1098/rspa.1913.0040

20. Barish BC, Weiss R. Ligo and the detection of gravitational waves. *Phys Today* (1999) 52:44–50. doi:10.1063/1.882861

21. Abbott BP, Abbott R, Adhikari R, Ajith P, Allen B, Allen G, et al. Ligo: The laser interferometer gravitational-wave observatory. *Rep Prog Phys* (2009) 72:076901. doi:10.1088/0034-4885/72/7/076901

22. Holland M, Burnett K. Interferometric detection of optical phase shifts at the heisenberg limit. *Phys Rev Lett* (1993) 71:1355–8. doi:10.1103/PhysRevLett.71.1355

23. Zhou S, Zhang M, Preskill J, Jiang L. Achieving the heisenberg limit in quantum metrology using quantum error correction. *Nat Commun* (2018) 9:78. doi:10.1038/s41467-017-02510-3

24. Giovannini D, Romero J, Potoček V, Ferenczi G, Speirits F, Barnett SM, et al. Spatially structured photons that travel in free space slower than the speed of light. *Science* (2015) 347:857–60. doi:10.1126/science.aaa3035

25. Eshun A, Gu B, Varnavski O, Asban S, Dorfman KE, Mukamel S, et al. Investigations of molecular optical properties using quantum light and hong–ou–mandel interferometry. *J Am Chem Soc* (2021) 143:9070–81. doi:10.1021/jacs.1c02514

26. Whittaker R, Erven C, Neville A, Berry M, O'Brien J, Cable H, et al. Absorption spectroscopy at the ultimate quantum limit from single-photon states. *New J Phys* (2017) 19:023013. doi:10.1088/1367-2630/aa5512

27. Kalashnikov DA, Pan Z, Kuznetsov AI, Krivitsky LA. Quantum spectroscopy of plasmonic nanostructures. *Phys Rev X* (2014) 4:011049. doi:10.1103/PhysRevX.4.011049

28. De Oliveira N, Roudjane M, Joyeux D, Phalippou D, Rodier JC, Nahon L. High-resolution broad-bandwidth fourier-transform absorption spectroscopy in the vuv range down to 40 nm. *Nat Photon* (2011) 5:149–53. doi:10.1038/nphoton.2010.314

29. Mukai Y, Arahata M, Tashima T, Okamoto R, Takeuchi S. Quantum fourier-transform infrared spectroscopy for complex transmittance measurements. *Phys Rev Appl* (2021) 15:034019. doi:10.1103/PhysRevApplied.15.034019

30. Jin RB, Shimizu R. Extended wiener–khinchin theorem for quantum spectral analysis. *Optica* (2018) 5:93–8. doi:10.1364/OPTICA.5.000093

31. Okano M, Okamoto R, Tanaka A, Ishida S, Nishizawa N, Takeuchi S. Dispersion cancellation in high-resolution two-photon interference. *Phys Rev A (Coll Park)* (2013) 88:043845. doi:10.1103/PhysRevA.88.043845

32. Ulanov AE, Fedorov IA, Sychev D, Grangier P, Lvovsky A. Loss-tolerant state engineering for quantum-enhanced metrology via the reverse hong–ou–mandel effect. *Nat Commun* (2016) 7:11925–6. doi:10.1038/ncomms11925

33. Oszmaniec M, Augusiak R, Gogolin C, Kołodyński J, Acin A, Lewenstein M. Random bosonic states for robust quantum metrology. *Phys Rev X* (2016) 6:041044. doi:10.1103/PhysRevX.6.041044

34. Shi H, Zhang Z, Pirandola S, Zhuang Q. Entanglement-assisted absorption spectroscopy. *Phys Rev Lett* (2020) 125:180502. doi:10.1103/PhysRevLett.125.180502

35. Steinberg AM, Kwiat PG, Chiao RY. Dispersion cancellation in a measurement of the single-photon propagation velocity in glass. *Phys Rev Lett* (1992) 68:2421–4. doi:10.1103/PhysRevLett.68.2421

36. Larchuk TS, Teich MC, Saleh BEA. Nonlocal cancellation of dispersive broadening in mach-zehnder interferometers. *Phys Rev A (Coll Park)* (1995) 52:4145–54. doi:10.1103/PhysRevA.52.4145

37. Doherty AC, Parrilo PA, Spedalieri FM. Distinguishing separable and entangled states. *Phys Rev Lett* (2002) 88:187904. doi:10.1103/PhysRevLett.88.187904

38. Lewenstein M, Sanpera A. Separability and entanglement of composite quantum systems. *Phys Rev Lett* (1998) 80:2261–4. doi:10.1103/PhysRevLett.80.2261

39. Gao J, Qiao LF, Jiao ZQ, Ma YC, Hu CQ, Ren RJ, et al. Experimental machine learning of quantum states. *Phys Rev Lett* (2018) 120:240501. doi:10.1103/PhysRevLett.120.240501

40. Vedral V. Quantum entanglement. *Nat Phys* (2014) 10:256–8. doi:10.1038/nphys2904

41. Fickler R, Lapkiewicz R, Plick WN, Krenn M, Schaeff C, Ramelow S, et al. Quantum entanglement of high angular momenta. *Science* (2012) 338:640–3. doi:10.1126/science.1227193

42. Erhard M, Krenn M, Zeilinger A. Advances in high-dimensional quantum entanglement. *Nat Rev Phys* (2020) 2:365–81. doi:10.1038/s42254-020-0193-5

43. Terhal BM, DiVincenzo DP, Leung DW. Hiding bits in bell states. *Phys Rev Lett* (2001) 86:5807–10. doi:10.1103/PhysRevLett.86.5807

44. Tittel W, Brendel J, Zbinden H, Gisin N. Quantum cryptography using entangled photons in energy-time bell states. *Phys Rev Lett* (2000) 84:4737–40. doi:10.1103/PhysRevLett.84.4737

45. Ghosh S, Kar G, Roy A, Sen A, Sen U. Distinguishability of bell states. *Phys Rev Lett* (2001) 87:277902. doi:10.1103/PhysRevLett.87.277902

46. Hu XM, Guo Y, Liu BH, Huang YF, Li CF, Guo GC. Beating the channel capacity limit for superdense coding with entangled ququarts. *Sci Adv* (2018) 4: eaat9304. doi:10.1126/sciadv.aat9304

47. Harrow A, Hayden P, Leung D. Superdense coding of quantum states. *Phys Rev Lett* (2004) 92:187901. doi:10.1103/PhysRevLett.92.187901

48. Jennewein T, Simon C, Weihs G, Weinfurter H, Zeilinger A. Quantum cryptography with entangled photons. *Phys Rev Lett* (2000) 84:4729–32. doi:10.1103/PhysRevLett.84.4729

49. Ursin R, Tiefenbacher F, Schmitt-Manderbach T, Weier H, Scheidl T, Lindenthal M, et al. Entanglement-based quantum communication over 144 km. *Nat Phys* (2007) 3:481–6. doi:10.1038/nphys629

50. Yin J, Li YH, Liao SK, Yang M, Cao Y, Zhang L, et al. Entanglement-based secure quantum cryptography over 1, 120 kilometres. *Nature* (2020) 582:501–5. doi:10.1038/s41586-020-2401-y

51. Aspelmeyer M, Böhm HR, Gyatso T, Jennewein T, Kaltenbaek R, Lindenthal M, et al. Long-distance free-space distribution of quantum entanglement. *Science* (2003) 301:621–3. doi:10.1126/science.1085593

52. Georgescu IM, Ashhab S, Nori F. Quantum simulation. *Rev Mod Phys* (2014) 86:153–85. doi:10.1103/RevModPhys.86.153

53. Trabesinger A. Quantum simulation. *Nat Phys* (2012) 8:263. doi:10.1038/nphys2258

54. Gerritsma R, Kirchmair G, Zähringer F, Solano E, Blatt R, Roos C. Quantum simulation of the Dirac equation. *Nature* (2010) 463:68–71. doi:10.1038/nature08688

55. Houck AA, Türeci HE, Koch J. On-chip quantum simulation with superconducting circuits. *Nat Phys* (2012) 8:292–9. doi:10.1038/NPHYS2251

56. Law C, Eberly J. Analysis and interpretation of high transverse entanglement in optical parametric down conversion. *Phys Rev Lett* (2004) 92:127903. doi:10.1103/PhysRevLett.92.127903

57. Zhang H, Jin XM, Yang J, Dai HN, Yang SJ, Zhao TM, et al. Preparation and storage of frequency-uncorrelated entangled photons from cavity-enhanced spontaneous parametric downconversion. *Nat Photon* (2011) 5:628–32. doi:10.1038/nphoton.2011.213

58. Eibl M, Gaertner S, Bourennane M, Kurtsiefer C, Żukowski M, Weinfurter H. Experimental observation of four-photon entanglement from parametric down-conversion. *Phys Rev Lett* (2003) 90:200403. doi:10.1103/PhysRevLett.90.200403

59. Zhong HS, Li Y, Li W, Peng LC, Su ZE, Hu Y, et al. 12-photon entanglement and scalable scattershot boson sampling with optimal entangled-photon pairs from parametric down-conversion. *Phys Rev Lett* (2018) 121:250505. doi:10.1103/PhysRevLett.121.250505

60. Wagenknecht C, Li CM, Reingruber A, Bao XH, Goebel A, Chen YA, et al. Experimental demonstration of a heralded entanglement source. *Nat Photon* (2010) 4:549–52. doi:10.1038/nphoton.2010.123

61. Guo X, Zou CL, Schuck C, Jung H, Cheng R, Tang HX. Parametric down-conversion photon-pair source on a nanophotonic chip. *Light Sci Appl* (2017) 6: e16249. doi:10.1038/lsa.2016.249

62. Xie Z, Zhong T, Shrestha S, Xu X, Liang J, Gong YX, et al. Harnessing high-dimensional hyperentanglement through a biphoton frequency comb. *Nat Photon* (2015) 9:536–42. doi:10.1038/nphoton.2015.110

63. Thew RT, Acín A, Zbinden H, Gisin N. Bell-type test of energy-time entangled qutrits. *Phys Rev Lett* (2004) 93:010503. doi:10.1103/PhysRevLett.93.010503

64. Steinlechner F, Ecker S, Fink M, Liu B, Bavaresco J, Huber M, et al. Distribution of high-dimensional entanglement via an intra-city free-space link. *Nat Commun* (2017) 8:15971–7. doi:10.1038/ncomms15971

65. Ecker S, Bouchard F, Bulla L, Brandt F, Kohout O, Steinlechner F, et al. Overcoming noise in entanglement distribution. *Phys Rev X* (2019) 9:041042. doi:10.1103/PhysRevX.9.041042

66. Jogenfors J, Elhassan AM, Ahrens J, Bourennane M, Åke Larsson J. Hacking the bell test using classical light in energy-time entanglement based quantum key distribution. *Sci Adv* (2015) 1:e1500793. doi:10.1126/sciadv.1500793

67. Guo X, Mei Y, Du S. Testing the bell inequality on frequency-bin entangled photon pairs using time-resolved detection. *Optica* (2017) 4:388–92. doi:10.1364/OPTICA.4.000388

68. Wengerowsky S, Joshi SK, Steinlechner F, Hübel H, Ursin R. An entanglement-based wavelength-multiplexed quantum communication network. *Nature* (2018) 564:225–8. doi:10.1038/s41586-018-0766-y

69. Chen Y, Ecker S, Wengerowsky S, Bulla L, Joshi SK, Steinlechner F, et al. Polarization entanglement by time-reversed hong-ou-mandel interference. *Phys Rev Lett* (2018) 121:200502. doi:10.1103/PhysRevLett.121.200502

70. Nasr MB, Carrasco S, Saleh BEA, Sergienko AV, Teich MC, Torres JP, et al. Ultrabroadband biphotons generated via chirped quasi-phase-matched optical parametric down-conversion. *Phys Rev Lett* (2008) 100:183601. doi:10.1103/PhysRevLett.100.183601

71. Cohen O, Lundeen JS, Smith BJ, Puentes G, Mosley PJ, Walmsley IA. Tailored photon-pair generation in optical fibers. *Phys Rev Lett* (2009) 102:123603. doi:10.1103/PhysRevLett.102.123603

72. Ding Y, Bacco D, Dalgaard K, Cai X, Zhou X, Rottwitt K, et al. High-dimensional quantum key distribution based on multicore fiber using silicon photonic integrated circuits. *Npj Quan Inf* (2017) 3:25–7. doi:10.1038/s41534-017-0026-2

73. Sit A, Bouchard F, Fickler R, Gagnon-Bischoff J, Larocque H, Heshami K, et al. High-dimensional intracity quantum cryptography with structured photons. *Optica* (2017) 4:1006–10. doi:10.1364/OPTICA.4.001006

74. Mirhosseini M, Magaña-Loaiza OS, O'Sullivan MN, Rodenburg B, Malik M, Lavery MP, et al. High-dimensional quantum cryptography with twisted light. *New J Phys* (2015) 17:033033. doi:10.1088/1367-2630/17/3/033033

75. Graham TM, Bernstein HJ, Wei TC, Junge M, Kwiat PG. Superdense teleportation using hyperentangled photons. *Nat Commun* (2015) 6:7185–9. doi:10.1038/ncomms8185

76. Hu XM, Huang CX, Sheng YB, Zhou L, Liu BH, Guo Y, et al. Long-distance entanglement purification for quantum communication. *Phys Rev Lett* (2021) 126: 010503. doi:10.1103/PhysRevLett.126.010503

77. Ecker S, Sohr P, Bulla L, Huber M, Bohmann M, Ursin R. Experimental single-copy entanglement distillation. *Phys Rev Lett* (2021) 127:040506. doi:10.1103/PhysRevLett.127.040506

78. Deng FG, Ren BC, Li XH. Quantum hyperentanglement and its applications in quantum information processing. *Sci Bull (Beijing)* (2017) 62:46–68. doi:10.1016/j.scib.2016.11.007

79. Ciampini MA, Orieux A, Paesani S, Sciarrino F, Corrielli G, Crespi A, et al. Path-polarization hyperentangled and cluster states of photons on a chip. *Light Sci Appl* (2016) 5:e16064. doi:10.1038/lsa.2016.64

80. Chen Y, Ecker S, Bavaresco J, Scheidl T, Chen L, Steinlechner F, et al. Verification of high-dimensional entanglement generated in quantum interference. *Phys Rev A (Coll Park)* (2020) 101:032302. doi:10.1103/PhysRevA.101.032302

81. Ramelow S, Ratschbacher L, Fedrizzi A, Langford N, Zeilinger A. Discrete tunable color entanglement. *Phys Rev Lett* (2009) 103:253601. doi:10.1103/PhysRevLett.103.253601

82. Yun S, Wen J, Xu P, Xiao M, Zhu SN. Generation of frequency-correlated narrowband biphotons from four-wave mixing in cold atoms. *Phys Rev A (Coll Park)* (2010) 82:063830. doi:10.1103/PhysRevA.82.063830

83. Gulati GK, Srivathsan B, Chng B, Cerè A, Kurtsiefer C. Polarization entanglement and quantum beats of photon pairs from four-wave mixing in a cold ^{87}Rb ensemble. *New J Phys* (2015) 17:093034. doi:10.1088/1367-2630/17/9/093034

84. Pan X, Yu S, Zhou Y, Zhang K, Zhang K, Lv S, et al. Orbital-angular-momentum multiplexed continuous-variable entanglement from four-wave mixing in hot atomic vapor. *Phys Rev Lett* (2019) 123:070506. doi:10.1103/PhysRevLett.123.070506

85. Mei Y, Zhou Y, Zhang S, Li J, Liao K, Yan H, et al. Einstein-podolsky-rosen energy-time entanglement of narrow-band biphotons. *Phys Rev Lett* (2020) 124: 010509. doi:10.1103/PhysRevLett.124.010509

86. Dudin YO, Radnaev AG, Zhao R, Blumoff JZ, Kennedy TAB, Kuzmich A. Entanglement of light-shift compensated atomic spin waves with telecom light. *Phys Rev Lett* (2010) 105:260502. doi:10.1103/PhysRevLett.105.260502

87. Ding DS, Jiang YK, Zhang W, Zhou ZY, Shi BS, Guo GC. Optical precursor with four-wave mixing and storage based on a cold-atom ensemble. *Phys Rev Lett* (2015) 114:093601. doi:10.1103/PhysRevLett.114.093601

88. Farrow RL, Rakestraw DJ. Detection of trace molecular species using degenerate four-wave mixing. *Science* (1992) 257:1894–900. doi:10.1126/science.257.5078.1894

89. Thiel C. *Four-wave mixing and its applications*. Washington DC: Faculty of Washington (2008).

90. Dada AC, Leach J, Buller GS, Padgett MJ, Andersson E. Experimental high-dimensional two-photon entanglement and violations of generalized bell inequalities. *Nat Phys* (2011) 7:677–80. doi:10.1038/nphys1996

91. Bavaresco J, Valencia NH, Klöckl C, Pivoluska M, Erker P, Friis N, et al. Measurements in two bases are sufficient for certifying high-dimensional entanglement. *Nat Phys* (2018) 14:1032–7. doi:10.1038/s41567-018-0203-z

92. Doda M, Huber M, Murta G, Pivoluska M, Plesch M, Vlachou C. Quantum key distribution overcoming extreme noise: Simultaneous subspace coding using high-dimensional entanglement. *Phys Rev Appl* (2021) 15:034003. doi:10.1103/PhysRevApplied.15.034003

93. Xu F, Shapiro JH, Wong FN. Experimental fast quantum random number generation using high-dimensional entanglement with entropy monitoring. *Optica* (2016) 3:1266–9. doi:10.1364/OPTICA.3.001266

94. Chen Y, Ecker S, Chen L, Steinlechner F, Huber M, Ursin R. Temporal distinguishability in hong-ou-mandel interference for harnessing high-dimensional frequency entanglement. *Npj Quan Inf* (2021) 7:167–7. doi:10.1038/s41534-021-00504-0

95. Legero T, Wilk T, Hennrich M, Rempe G, Kuhn A. Quantum beat of two single photons. *Phys Rev Lett* (2004) 93:070503. doi:10.1103/PhysRevLett.93.070503

96. Kobayashi T, Ikuta R, Yasui S, Miki S, Yamashita T, Terai H, et al. Frequency-domain hong-ou-mandel interference. *Nat Photon* (2016) 10:441–4. doi:10.1038/nphoton.2016.74

97. Vanselow A, Kaufmann P, Zorin I, Heise B, Chrzanowski HM, Ramelow S. Frequency-domain optical coherence tomography with undetected mid-infrared photons. *Optica* (2020) 7:1729–36. doi:10.1364/OPTICA.400128

98. Senellart P, Solomon G, White A. High-performance semiconductor quantum-dot single-photon sources. *Nat Nanotechnol* (2017) 12:1026–39. doi:10.1038/nnano.2017.218

99. He YM, He Y, Wei YJ, Wu D, Atatüre M, Schneider C, et al. On-demand semiconductor single-photon source with near-unity indistinguishability. *Nat Nanotechnol* (2013) 8:213–7. doi:10.1038/nnano.2012.262

100. Kim JH, Cai T, Richardson CJ, Leavitt RP, Waks E. Two-photon interference from a bright single-photon source at telecom wavelengths. *Optica* (2016) 3:577–84. doi:10.1364/OPTICA.3.000577

101. Ollivier H, Thomas S, Wein S, de Buy Wenniger IM, Coste N, Loredo J, et al. Hong-ou-mandel interference with imperfect single photon sources. *Phys Rev Lett* (2021) 126:063602. doi:10.1103/PhysRevLett.126.063602

102. Stobińska M, Buraczewski A, Moore M, Clements W, Renema JJ, Nam S, et al. Quantum interference enables constant-time quantum information processing. *Sci Adv* (2019) 5:eaau9674. doi:10.1126/sciadv.aau9674

103. Zhang Y, Roux FS, Konrad T, Agnew M, Leach J, Forbes A. Engineering two-photon high-dimensional states through quantum interference. *Sci Adv* (2016) 2:e1501165. doi:10.1126/sciadv.1501165

104. Zhang Y, Agnew M, Roger T, Roux FS, Konrad T, Faccio D, et al. Simultaneous entanglement swapping of multiple orbital angular momentum states of light. *Nat Commun* (2017) 8:632–7. doi:10.1038/s41467-017-00706-1

105. Bonaretti F, Faccio D, Clerici M, Biegert J, Di Trapani P. Spatiotemporal amplitude and phase retrieval of bessel-x pulses using a hartmann-shack sensor. *Opt Express* (2009) 17:9804–9. doi:10.1364/OE.17.009804

106. Bowlan P, Valtna-Lukner H, Lõhmus M, Piksarv P, Saari P, Trebino R. Measuring the spatiotemporal field of ultrashort bessel-x pulses. *Opt Lett* (2009) 34:2276–8. doi:10.1364/OL.34.002276

107. Kuntz K, Braverman B, Youn S, Lobino M, Pessina E, Lvovsky A. Spatial and temporal characterization of a bessel beam produced using a conical mirror. *Phys Rev A (Coll Park)* (2009) 79:043802. doi:10.1103/PhysRevA.79.043802

108. Alexeev I, Kim K, Milchberg H. Measurement of the superluminal group velocity of an ultrashort bessel beam pulse. *Phys Rev Lett* (2002) 88:073901. doi:10.1103/PhysRevLett.88.073901

109. Devaux F, Mosset A, Moreau PA, Lantz E. Imaging spatiotemporal hong-ou-mandel interference of biphoton states of extremely high schmidt number. *Phys Rev X* (2020) 10:031031. doi:10.1103/PhysRevX.10.031031

110. Ibarra-Borja Z, Sevilla-Gutiérrez C, Ramírez-Alarcón R, Cruz-Ramírez H, U'Ren AB. Experimental demonstration of full-field quantum optical coherence tomography. *Photon Res* (2020) 8:51–6. doi:10.1364/PRJ.8.000051

111. Aguilar G, Piera R, Saldanha P, de Matos Filho R, Walborn S. Robust interferometric sensing using two-photon interference. *Phys Rev Appl* (2020) 14:024028. doi:10.1103/PhysRevApplied.14.024028

112. Lo HK, Curty M, Qi B. Measurement-device-independent quantum key distribution. *Phys Rev Lett* (2012) 108:130503. doi:10.1103/PhysRevLett.108.130503

113. Liu Y, Chen TY, Wang LJ, Liang H, Shentu GL, Wang J, et al. Experimental measurement-device-independent quantum key distribution. *Phys Rev Lett* (2013) 111:130502. doi:10.1103/PhysRevLett.111.130502

114. Yin HL, Chen TY, Yu ZW, Liu H, You LX, Zhou YH, et al. Measurement-device-independent quantum key distribution over a 404 km optical fiber. *Phys Rev Lett* (2016) 117:190501. doi:10.1103/PhysRevLett.117.190501

115. Curty M, Xu F, Cui W, Lim CCW, Tamaki K, Lo HK. Finite-key analysis for measurement-device-independent quantum key distribution. *Nat Commun* (2014) 5:3732–7. doi:10.1038/ncomms4732

116. Albarelli F, Friel JF, Datta A. Evaluating the holevo cramér-rao bound for multiparameter quantum metrology. *Phys Rev Lett* (2019) 123:200503. doi:10.1103/PhysRevLett.123.200503

117. Gammelmark S, Mølmer K. Fisher information and the quantum cramér-rao sensitivity limit of continuous measurements. *Phys Rev Lett* (2014) 112:170401. doi:10.1103/PhysRevLett.112.170401

118. Braunstein SL, Caves CM. Statistical distance and the geometry of quantum states. *Phys Rev Lett* (1994) 72:3439–43. doi:10.1103/PhysRevLett.72.3439

119. Rezai M, Wrachtrup J, Gerhardt I. Coherence properties of molecular single photons for quantum networks. *Phys Rev X* (2018) 8:031026. doi:10.1103/PhysRevX.8.031026

120. Van Loon JC. *Analytical atomic absorption spectroscopy*. New York: Elsevier (1980). doi:10.1016/B978-0-127-14050-6.X5001-3

121. Velasco-Velez JJ, Wu CH, Pascal TA, Wan LF, Guo J, Prendergast D, et al. The structure of interfacial water on gold electrodes studied by x-ray absorption spectroscopy. *Science* (2014) 346:831–4. doi:10.1126/science.1259437

122. Wolfgramm F, Vitelli C, Beduini FA, Godbout N, Mitchell MW. Entanglement-enhanced probing of a delicate material system. *Nat Photon* (2013) 7:28–32. doi:10.1038/nphoton.2012.300

123. Taylor MA, Janousek J, Daria V, Knittel J, Hage B, Bachor HA, et al. Biological measurement beyond the quantum limit. *Nat Photon* (2013) 7:229–33. doi:10.1038/nphoton.2012.346

124. Kalachev A, Kalashnikov D, Kalinkin A, Mitrofanova T, Shkalikov A, Samartsev V. Biphoton spectroscopy of yag: Er3+ crystal. *Laser Phys Lett* (2007) 4:722–5. doi:10.1002/lapl.200710061

125. Chen Y, Shen Q, Luo S, Zhang L, Chen Z, Chen L. Entanglement-assisted absorption spectroscopy by hong-ou-mandel interference. *Phys Rev Appl* (2022) 17:014010. doi:10.1103/PhysRevApplied.17.014010

126. León-Montiel RJ, Svozilík J, Torres JP, U'Ren AB. Temperature-controlled entangled-photon absorption spectroscopy. *Phys Rev Lett* (2019) 123:023601. doi:10.1103/PhysRevLett.123.023601

127. Tabakaev D, Montagnese M, Haack G, Bonacina L, Wolf JP, Zbinden H, et al. Energy-time-entangled two-photon molecular absorption. *Phys Rev A (Coll Park)* (2021) 103:033701. doi:10.1103/PhysRevA.103.033701

128. Barkai E, Jung Y, Silbey R. Time-dependent fluctuations in single molecule spectroscopy: A generalized wiener-khintchine approach. *Phys Rev Lett* (2001) 87:207403. doi:10.1103/PhysRevLett.87.207403

129. Yepiz-Graciano P, Martínez AMA, Lopez-Mago D, Cruz-Ramirez H, U'Ren AB. Spectrally resolved hong–ou–mandel interferometry for quantum-optical coherence tomography. *Photon Res* (2020) 8:1023–34. doi:10.1364/PRJ.388693

130. Hamm P. *Principles of nonlinear optical spectroscopy: A practical approach or: Mukamel for dummies*, 41. Zurich, Switzerland: University of Zurich (2005). p. 77.

131. Hamm P, Zanni M. *Concepts and methods of 2D infrared spectroscopy*. Cambridge, UK: Cambridge University Press (2011). doi:10.1017/cbo9780511675935

132. Schmidt PO, Rosenband T, Langer C, Itano WM, Bergquist JC, Wineland DJ. Spectroscopy using quantum logic. *Science* (2005) 309:749–52. doi:10.1126/science.1114375

133. Sánchez Muñoz C, Frascella G, Schlawin F. Quantum metrology of two-photon absorption. *Phys Rev Res* (2021) 3:033250. doi:10.1103/PhysRevResearch.3.033250

134. Prajapati N, Niu Z, Novikova I. Quantum-enhanced two-photon spectroscopy using two-mode squeezed light. *Opt Lett* (2021) 46:1800–3. doi:10.1364/OL.418398

135. Javanainen J, Gould PL. Linear intensity dependence of a two-photon transition rate. *Phys Rev A (Coll Park)* (1990) 41:5088–91. doi:10.1103/PhysRevA.41.5088

136. Landes T, Allgaier M, Merkouche S, Smith BJ, Marcus AH, Raymer MG. Experimental feasibility of molecular two-photon absorption with isolated time-frequency-entangled photon pairs. *Phys Rev Res* (2021) 3:033154. doi:10.1103/PhysRevResearch.3.033154

137. Muthukrishnan A, Agarwal GS, Scully MO. Inducing disallowed two-atom transitions with temporally entangled photons. *Phys Rev Lett* (2004) 93:093002. doi:10.1103/PhysRevLett.93.093002

138. Roslyak O, Mukamel S. Multidimensional pump-probe spectroscopy with entangled twin-photon states. *Phys Rev A (Coll Park)* (2009) 79:063409. doi:10.1103/PhysRevA.79.063409

139. Schlawin F, Dorfman KE, Fingerhut BP, Mukamel S. Suppression of population transport and control of exciton distributions by entangled photons. *Nat Commun* (2013) 4:1782–7. doi:10.1038/ncomms2802

140. Shapiro M, Brumer P. Generation and control of chains of entangled atom-ion pairs with quantum light. *Phys Rev Lett* (2011) 106:150501. doi:10.1103/PhysRevLett.106.150501

Advantages of publishing in Frontiers

OPEN ACCESS
Articles are free to read for greatest visibility and readership

FAST PUBLICATION
Around 90 days from submission to decision

HIGH QUALITY PEER-REVIEW
Rigorous, collaborative, and constructive peer-review

TRANSPARENT PEER-REVIEW
Editors and reviewers acknowledged by name on published articles

Frontiers
Avenue du Tribunal-Fédéral 34
1005 Lausanne | Switzerland

Visit us: www.frontiersin.org
Contact us: frontiersin.org/about/contact

REPRODUCIBILITY OF RESEARCH
Support open data and methods to enhance research reproducibility

DIGITAL PUBLISHING
Articles designed for optimal readership across devices

FOLLOW US
@frontiersin

IMPACT METRICS
Advanced article metrics track visibility across digital media

EXTENSIVE PROMOTION
Marketing and promotion of impactful research

LOOP RESEARCH NETWORK
Our network increases your article's readership